Advanced optical signatures of single, wurtzite GaN quantum dots:

From fundamental exciton coupling mechanisms towards tunable photon statistics and hybrid-quasiparticles

vorgelegt von
Diplom-Physiker
Gordon Callsen
geb. in Berlin

Von der Fakultät II - Mathematik und Naturwissenschaften
der Technischen Universität Berlin
zur Erlangung des akademischen Grades

Doktor der Naturwissenschaften
Dr. rer. nat.

genehmigte Dissertation

Promotionsausschuss:

Vorsitzender: Prof. Dr. Michael Lehmann
Gutachter: Prof. Dr. Axel Hoffmann
Gutachter: Prof. Dr. Matthew Phillips
Gutachterin: Prof. Dr. Janina Maultzsch
Gutachter: Prof. Dr. Bernard Gil

Tag der wissenschaftlichen Aussprache:
08. Mai 2015

Berlin 2015

Zusammenfassung

Die vorliegende Arbeit behandelt die optischen Signaturen von einzelnen, in AlN eingebetteten, hexagonalen GaN Quantenpunkten. Die durchgeführten Experimente sind die Basis für eine Vielzahl von neuartigen Beobachtungen, welche nicht nur für dieses spezielle Quantenpunktsystem von Interesse sind, sondern von generellem Wert für die gesamte Quantenpunkt Community. Die dargestellte Analyse der Wechselwirkung zwischen Exzitonen in Quantenpunkten und geladenen Defekten als auch Phononen ermöglicht dabei letztendlich sogar die erstmalige Demonstration von quantenoptischen Bauteilkonzepten im ultravioletten (UV) Spektralbereich. Hierbei ist besonders eine optisch getriebene Zwei-Photonquelle auf Basis der Biexzitonkaskade hervorzuheben, deren vielversprechende Photonstatistik bis zu einer Temperatur von 50 K nachweisbar ist. Weitergehende Untersuchungen dieser Biexzitonkaskade führen letztendlich zur Beschreibung von sogenannten Hybrid-Quasipartikeln im Rahmen dieser Arbeit mit weitreichenden Konsequenzen für eine Vielzahl von exzitonbasierten Quantenlichtquellen.

Der erste Teil dieser Doktorarbeit befasst sich mit der Präparation von multiexzitonischen Zuständen. Dank der Verbindung von leistungsdichteabhängigen und zeitaufgelösten mikro-Photolumineszenz Messungen ist es möglich eine ganze Vielfalt an neuartigen multiexzitonischen Komplexen zu identifizieren. Die Bestimmung von Relaxationszeiten stellt hierbei eine Beobachtung mit direkt anwendungsbezogenen Konsequenzen dar. Des Weiteren wird nachgewiesen, dass der anfängliche Ladungsträgereinfang von Auger- und damit nicht von Multiphononprozessen dominiert wird. Letztere stellen erst bei der folgenden Quantenpunkt-internen Relaxation den limitierenden Faktor dar, ein Effekt der auch als „Phononflaschenhals“ beschrieben wird. Die Anwendung als auch die erweiterte, grundlegenden Untersuchung von hexagonalen GaN Quantenpunkten wird von einem als „spektrale Diffusion“ bekannten Effekt limitiert, der zu einer starken Emissionslinienverbreiterung führt. Eine Statistik dieser Linienbreiten für Hunderte von einzelnen GaN Quantenpunkten ermöglicht die indirekte Bestimmung des mittleren defektinduzierten elektrischen Feldes, dessen Fluktuationen die Linienverbreiterung bedingen. Eine weiterführende statistische Analyse zur Kopplung zwischen Exzitonen und longitudinal-optischen (LO) Phononen führt zur Bestimmung der zugehörigen Huang-Rhys Faktoren als auch LO-Phononenergien für eine hohe Quantenpunktzahl, woraus sich eine erstmalige Abschätzung des Exziton-LO-Phonon Wechselwirkungsvolumens ergibt.

Dank dieser umfangreichen, optischen Analyse von einzelnen GaN Quantenpunkten ist es sogar möglich die optische Signatur der zugehörigen Biexzitonkaskade über einen großen Spektralbereich zu erfassen. Für einen Übergangsenergiebereich beobachtet man hierbei ein einzigartiges Gleichgewicht zwischen Ein- und Zwei-Photonprozessen beim Zerfall des Biexzitons, welches mittels Temperatur und Anregungsleistung sogar steuerbar ist. Gerade die Zweiphotonemission ist auf Grund ihrer Temperaturstabilität bis 50 K ein vielversprechender Kandidat für zukünftige Anwendungen. Interessanterweise ermöglicht auch gerade dieser spezielle Fall der biexzitonischen Komplexe die erstmalige Beschreibung einer ganzen neuen Klasse von Hybrid-Quasipartikeln, welche bisher unbekannte Spinkonfigurationen aufweisen. Eine Analyse der optischen Eigenschaften dieser Hybrid-Quasipartikel zeigt ein ungewöhnliches Zerfallsverhalten auf, welches gerade auch die besondere Rolle der „dunklen“ Exzitonen in GaN Quantenpunkten im Rahmen dieser Arbeit hervorhebt.

Abstract

The present work treats the fundamental optical signatures of individual, hexagonal GaN quantum dots embedded in AlN. The conducted experiments established the basis for numerous, novel observations, which are not only of interest for this particular quantum dot system, but also of general value for the entire quantum dot community. The presented analysis of the interaction in between quantum dot excitons and charged defects, as well as phonons, culminates in the first-time demonstration of quantum-optical device concepts for the ultraviolet (UV) spectral range. Here, a highlight is constituted by an optically pumped two-photon source based on the biexciton cascade, which maintains its highly promising photon statistics up to a temperature of 50 K. Further in-detail studies of this biexciton cascade even lead to the description of so-called hybrid-quasiparticles in this work, with prominent consequences for a wide range of exciton-based quantum light sources.

The first part of this thesis is dedicated to the preparation of multiexcitonic states. Based on the conjunction of excitation power dependent and time-resolved micro-Photoluminescence, an entire zoo of multiexcitonic complexes is identified for the first time. Here, the determination of relaxation times presents an observation with direct consequences for applications. Furthermore, it is demonstrated that the initial carrier capture process is predominantly realized by Auger-processes that dominate any multi-phonon contributions. However, in terms of intra-quantum dot carrier relaxation, it is exactly these multi-phonon processes that present the limiting factor, a phenomenon known as the "phonon-bottleneck" effect. As the emission of these excitons in hexagonal GaN is affected by "spectral diffusion", a strong emission line widths broadening occurs, which still limits future applications but also any more fundamental analysis. A line width statistic is obtained by analyzing hundreds of individual GaN quantum dots, allowing an indirect determination of the average, defect-induced electric field, whose fluctuations originate the line widths broadening. A continuative statistical analysis is given for the coupling between excitons and longitudinal-optical (LO) phonons. As a result, the corresponding Huang-Rhys factors and LO-phonon energies are extracted for an elevated number of quantum dots. Finally, a microscopic parameter, known as the exciton-LO-phonon interaction volume was approximated for the first time, based on the presented detailed statistical analysis.

Due to this extended, optical analysis of individual GaN quantum dots it was possible to characterize the optical traces of the biexciton cascade over a wide spectral range. Here, for a certain transitional range, a unique balance between one- and two-photon processes is observed, which arises from the biexciton decay and can be tuned means of temperature and excitation density. Especially the two-photon emission is a promising candidate for future applications as its temperature stability is demonstrated up to 50 K. Interestingly, the particular case of biexcitonic complexes also forms the basis for the description of an entire new class of hybrid-quasiparticles with so far unknown spin configurations. An extended analysis of the optical properties of these hybrid-quasiparticles presents highly unconventional decay characteristics, demonstrating the outmost importance of the dark-excitons in hexagonal GaN quantum dots based on the present thesis.

Contents

1 Introduction

The advent of research on quantum dots (QDs) representing truly zero-dimensional structures, dates back to the early 1980s. In 1982 Arakawa and Sakaki [1] described the superior physical properties of such structures of ultimate dimensionality in comparison to thitherto most extensively studied two-dimensional and bulk structures. However, the fundamental concept that describes the benefits of a reduction in dimensionality already dates back to the year of 1976, as documented by a patent issued to Dingle and Henry [2]. What followed was an almost unrivaled rise in research activities, as evidenced by an increasing number of publications and funding proposals dedicated to QDs. The endless list of benefits ascribed to QDs like e.g. low laser threshold currents [3], improved temperature stability [1], wide modulation bandwidths [4], and later on, efficient single, as well as entangled photon generation [5, 6] was from the early on directly connected to numerous, highly promising applications ranging from basic lighting to quantum cryptography. In this light QDs appeared as the "Holy Grail" of semiconductor physics at that time.

However, despite the evident long time period already dedicated to the research on QDs, their physical properties, related device concepts, growth, and modeling are nowadays still actively debated topics. Based on all the physical advantages of zero-dimensional structures one would expect their occurrence in numerous every-day devices, which is surprisingly not the common case yet. Severe growth issues, difficulties in controlling their size and shape, as well as simple cost issues still hinder a triumphal procession of QDs in industry. However, epitaxially grown QDs and even colloidal QDs [7] still continue their progression towards numerous real-world applications, representing a strong motivation for future research in these fields. Finally, resembling the Arthurian tale, it appears that the physicists' voyage of exploration in this "QD quest" turns out as the most valuable result. While the broad, every-day life application has not been found for QDs yet, the dedicated research covering more than 35 years originated numerous discoveries and fundamental insight into the physics of such nanostructures.

For already many years the world of epitaxial QD research, which also resides within the focus of this thesis, is divided based on the existing QD material systems. Here, mainly e.g. arsenide- [8], selenide- [9], sulfide- [10], and phosphide-based [11] QDs originate a major share of the conducted research, but also silicon nano clusters

remain highly debated [12]. As it cannot be the entitlement of this thesis to establish a broad literature overview regarding all these material systems, the given references should only serve as unbiased reading suggestions representing a selection from several thousands of articles and numerous review articles. As the nucleation and formation of epitaxial QDs is a strain-driven process [13], sufficient differences regarding the lattice constants are a key requirement for their growth. Both could be achieved from the beginning for the listed material groups, however, this was not the only motivation for their utilization. Their bulk material counterparts or related quantum well (QW) structures were already commonly known as brilliant, direct-bandgap emitters, providing a strong motivation for their application in the field of QDs. However, despite the successful application of many of these material systems in e.g. light emitting diodes (LEDs) and laser diodes (LDs), the temperature stability of the underlying luminescence was not always fully satisfying. For bulk materials the matter of the emission temperature stability is, among other things, governed by the absolute exciton binding energies, which range from just several meV for arsenides [14], towards the room temperature equivalent and beyond for selenides and sulfides [15].

Interestingly, in parallel to the rise of the QDs another material class, known as the nitrides, has increasingly been investigated. Just recently the underlying research activities even culminated in the Nobel Prize in physics (2014) for three Japanese researchers (Isamu Akasaki, Hiroshi Amano, Shoji Nakamura) and their distinct commitment to nitride research [16]. It is not only that novel frequency regimes can be addressed based on such nitride structures [17], also the accompanying temperature stability is most striking for selected compounds like e.g. $Al_XGa_{1-X}N$ due to huge exciton binding energies [18]. Hence, it is only natural to apply the entire class of nitride materials, which have already proven as outstandingly efficient for LED and LD structures, for the growth of nitride-based QDs.

While basic bulk GaN and AlN already exhibit fairly stable and brilliant emission characteristics upon rise of temperature, the implementation of such structures for QDs even further emphasizes these benefits. If e.g. wurtzite GaN QDs are embedded in AlN of the same crystal structure, huge band offsets occur, raising promising prospects for the temperature stability of resulting excitonic QD emission [19, 20]. The first reports regarding the growth of such hexagonal GaN QDs originate from the mid 1990s. Here, Tanaka et al. [21] established the GaN QD growth by metal organic chemical vapor phase epitaxy (MOCVD), while Daudin et al. presented the successful GaN QD segregation by molecular beam epitaxy (MBE) in 1997 [22]. Obviously, also several other nitride-based QDs can successfully be grown as e.g. InGaN QDs embedded in GaN [23, 24] or even AlGaN QDs embedded in AlN [20]. However, the present introduction will proceed with tightening its focus towards

pure GaN QDs embedded in AlN, as they represent the main topic of the thesis in hand.

Generally, the straightforward analysis of ensembles of GaN QDs was feasibly from the early on [25–30], while the following characterization of single GaN QDs [31] scaled with the growth progress aiming for lower QD densities. An interim highlight regarding the growth and analysis of single GaN QDs was achieved by Kako et al. by presenting UV single photon emission up to a temperature of 200 K [32], which could recently even be advanced towards 300 K [33]. In parallel to this experimental progression, also the theoretical description of nitride based QDs started to rapidly evolve [34–36]. However, advanced reports on a most important *combination* of both, experiment and theory are scarce [37–39] and directly substantiate the motivation for the present thesis to demonstrate advanced optical signatures of GaN QDs far beyond state-of-the-art reports in literature.

1.1 Objectives and thesis structure

It is the aim of this thesis to introduce the reader to an entire new level of detail regarding the spectroscopy of single, wurtzite GaN QDs embedded in AlN. Generally, the two common spectroscopic approaches, namely *ensemble* and *single* QD spectroscopy are associated with a well-balanced number advantages but also disadvantages. While ensemble QD spectroscopy always facilitates general results that are valid for the entire sample, single QD spectroscopy allows more detailed insight, which, however, commonly lacks any generality. Physical insight based on just a handful of QD micro-Photoluminescence (μ-PL) spectra, just always remains questionable if QD size and shape exhibit significant deviations for one and the same sample, as it is highly common for any so far fabricated GaN QD sample. In this thesis, the advantages of both techniques are combined by conducting fully automated μ-PL measurements for hundreds of single QDs, reaching towards a statistically valid analysis. Hence, general physical conclusions can be derived featuring an unrivaled level of detail. However, such ambitious aims come at high experimental costs, especially as the single QD spectroscopy focusses on the ultraviolet (UV) spectral range.

Based on the corresponding, extended experimental data sets comprising hundreds of individual μ-PL spectra it is feasible to obtain a most valuable and detailed, direct comparison to theory. As a result, it can be shown that common theoretical conceptions developed for other QD systems (e.g. arsenides) fail to predict most of the optical properties derived for hexagonal GaN QDs. However, by combining an in-detail spectroscopic analysis with truly elaborated modeling [38, 40] exclusively established for nitride QDs, it becomes feasible to advance towards a new level of understanding regarding excitons inherent in GaN QDs.

Following this introduction, Chap. 2 describes the applied experimental techniques. However, not all the experimental details are described in order to limit the extent of this thesis and to focus on the main results. The fundamental concepts of the applied techniques are considered as common knowledge and can be studied in the basic literature [41, 42]. An identical conception is pursued in Chap. 3, introducing the general reader to the basic modeling that is applied and further developed throughout this thesis. First, a brief introduction is given for the crystal structure, the band structure, and the phonon dispersion of bulk nitrides as e.g. GaN and AlN. Subsequently, a formalism is introduced that allows the approximation of excitons in nitride QDs. Here, again, not all the details are provided but substantial references are provided for the interested reader. As a result, a straightforward accessible theoretical introduction is achieved that enables a more general understanding of the theoretical challenges without the burden of an exaggerated level of detail. Addi-

tional theoretical concepts are developed throughout this thesis as soon as needed in order to explain the experimental data. It is the general concept of this thesis to focus on the experimental results and not on complicated theoretical descriptions that can possibly not even be approved by the final, most supreme judge; the experiment.

Exactly these experimental results are treated in Chap. 4 - 8 along with a direct application of some of the theoretical concepts developed in Chap. 3. Here, Chap. 4 introduces the reader to the first application of the experimental techniques described in Chap. 2. After a brief introduction to the ensemble PL signature of wurtzite GaN QDs, the basic μ-PL spectra of single QDs are treated. Excitation power dependent μ-PL spectroscopy is applied as a rudimental tool to approach an identification of excitonic complexes inherent to GaN QDs. While the continuous wave excitation suggests the observation of excitons and biexcitons in a single QD, the high power pulsed excitation reveals a surprising diversity of excitonic complexes, which has so far never been observed before. By combining a time-resolved analysis (μ-TRPL) with the excitation power dependent data, a most suggestive emission line identification is obtained. Here, extended excitonic complexes in access of the biexciton, namely tri-excitons, quart-excitons, and so fourth are observed along with some of their excited-state counterparts. In addition, radiative decay times and relaxation times are analyzed for various excitonic complexes originating from a single GaN QD, which further strengthens the emission line identification. In this context, a phonon bottleneck effect regarding the intra-QD relaxation is observed, evoking straightforward consequences for device applications with focus on high speed applications.

Moreover, the interaction between excitons inherent to GaN QDs and a fluctuating charge environment, or even a phonon bath, is discussed in Chap. 5 and 6. First, the extensively discussed phenomenon of a prominent emission line widths broadening is discussed and finally traced back to large relative excitonic dipole moments and high defect concentrations exhibiting charge fluctuations. Not only that the directly related field strength can be approximated for the first time in this context, also the phenomenon itself is demonstrated to serve as a useful tool for the emission line identification. Again, all the information derived is founded on the analysis of hundreds of individual QDs, while the novel emission line width identification method is confirmed for more than 10 QDs. Relying on a similar statistical analysis of μ-PL spectra even provides direct access to the coupling between excitons in a QD and longitudinal-optical (LO) phonons. Never before it has ever been feasible to analysis the exciton-LO-phonon coupling for hundreds of individual GaN QDs. As a result, unique scaling behaviors of the characteristic Huang-Rhys factors and LO-phonon energies are derived. The explanation of these trends features the introduction of a straightforward, experimentally motivated approximation yielding

a spheric exciton-LO-phonon interaction volume as a first indirect measure of the interaction range. Again, to the best knowledge of the author of this thesis, such an approximation based on a statistical analysis of QD spectra has never been presented before. Ultimately, not only detailed insight into physics is obtained, also experimental advances are introduced within the scope of the present thesis.
After a solid emission line identification is established in Chap. 4 - 6, Chap. 7 turns towards the interplay between excitonic and biexcitonic emission with focus on the resulting photon statistics. At this point, the reader is introduced to tunable photon statistics, which strongly depend on the actual structure of the biexciton cascade. Not only that the biexciton binding energy serves as a viable tuning parameter, also the influence of temperature and excitation power achieve tractability of the photon statistics. As a result, an optically driven two-photon source is experimentally demonstrated and theoretically described based on an advanced modeling of the biexciton cascade's quantum-state tomography. Commonly applied rate equation models neglect the influence of such parameters as the biexciton binding energy, emphasizing the outstanding importance of the provided results. The described photon source is a viable candidate for advanced quantum light sources beyond single photon sources, with strong perspectives for quantum cryptography and imaging.
The particular case of the biexciton as a simplistic representative of a multiexciton already introduced in Chap. 4, is finally treated in full detail in Chap. 8. By combining sophisticated spectroscopy with state-of-the-art theory [40], an entire new class of, so-called, hybrid-quasiparticles is established. The presented experimental results contradict any biexciton modeling ever applied for wurtzite GaN QDs, because parallel hole spins contribute to the biexciton complex for certain QD height intervals. As a direct consequence, highly unconventional polarization dependencies are observed along with most particular μ-PL temperature series. Subsequently, an in-detail analysis of the μ-PL data does not only allow the determination of the excitonic bright- and dark-bright splitting but even the excitonic dark-state splitting becomes accessible. By presenting the associated temperature-dependent correlation signature of the biexciton cascade for a certain GaN QD, the overall model of hybrid-quasiparticles can be confirmed based on the observation of a spin-blockade cascade that is activated upon rise of temperature.
Finally, all the findings and conceptions derived from Chap. 4 - 8 are recapitulated in Chap. 9, which closes with some future-orientated final remarks providing a strong motivation for further research on the highly interesting system of wurtzite GaN QDs embedded in AlN.

2 Experimental techniques

It is the purpose of this chapter to provide an overview regarding the applied experimental techniques. A significant fraction of the entire thesis will deal with Photoluminescence (PL) and especially micro-Photoluminescence (μ-PL) measurements conducted with an experimental setup that was exclusively build by the author and his students for analyzing single nitride quantum dots (QDs). Its versatility, high light throughput, and mechanical as well as thermal stability constitute the constructed μ-PL system as unique. Possible measurements comprise a list of various μ-PL techniques, including time-resolved measurements, polarization- and excitation power dependent μ-PL, as well as correlation spectroscopy of truly single QDs. Especially the accessible wavelength range scaling from the ultraviolet (UV) to the green constitutes the main experimental challenges as special care must e.g. be taken regarding suitable optics. The present chapter briefly introduces the reader to the μ-PL system but further details can be found in the Appendix on page 148.

Within the scope of this thesis most frequently analyzed GaN QD samples were grown by the group of Prof. Dr. Y. Arakawa from the Tokyo University. Only Chap. 5.3 introduces the first results of a different type of wurtzite GaN QD sample, demonstrating recent growth advances in the group of Prof. Dr. A. Strittmatter from the Otto-von-Guericke-University, Magdeburg. Additional experimental techniques such as transmission electron microscopy (TEM) were performed by Dr. T. Markurt in the group of Dr. M. Albrecht at the Institut für Kristallzüchtung, Berlin as detailed in Chap. 6, page 74.

2.1 GaN quantum dot specimen

In the following the growth procedure by low-pressure metal-organic vapor deposition is described for a self-assembled wurtzite GaN QD sample that is most frequently analyzed throughout this manuscript. After growth of a 100 nm thick layer of AlN at 1180 °C on top of an n-type 6H-SiC [0001] substrate, the GaN QDs were segregated at a temperature of 975 °C, followed by a growth interruption under NH_3 flow in order to facilitate the QD formation process. Subsequently, an $\approx$ 5 - 10 nm thick low temperature (975 °C) AlN spacer was grown, before the final 100 nm thick

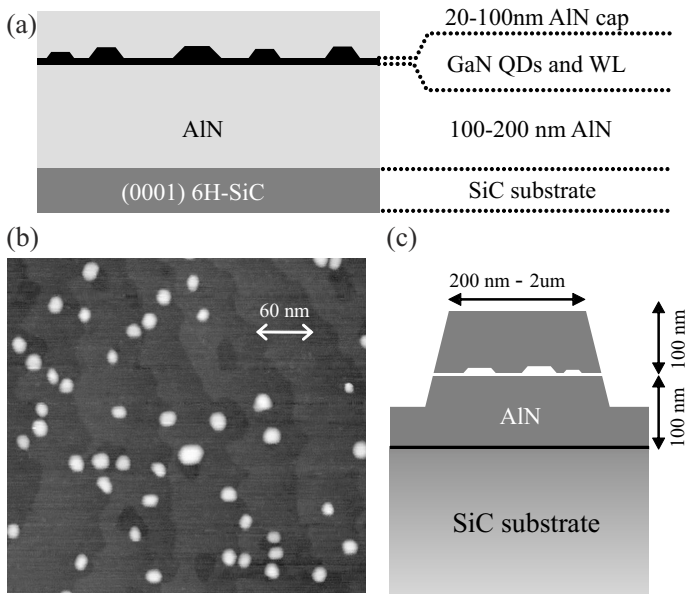

Figure 2.1: (a) Sample structure of the analyzed GaN QD specimen illustrating the SiC substrate, the AlN matrix material and the GaN QDs along with their wetting layer (WL). (b) Atomic force microscopy (AFM) image of an uncapped QD sample that reveals the hexagonal shape and the density of the individual QDs. (c) Patterning of the sample with a mesa structure enables single QD spectroscopy based on the μ-PL method. Partially adopted from Ref. [43].

AlN capping layer was deposited (1180 °C). The corresponding sample structure is illustrated in Fig. 2.1a and more detailed growth conditions can be found elsewhere [29, 32, 44]. The resulting QDs are segregated with a density of $\approx 6 \times 10^9$ cm^{-2} and exhibit a hexagonally shaped basal plane, cf. Fig. 2.1b. Additionally, the sample was processed with a mesa structure (diameters down to 200 nm) as depicted in Fig. 2.1c. Such patterning by ion-assisted plasma etching allows the optical investigation of single GaN QDs in the UV-enhanced μ-PL system described in Sec. 2.2. Further details regarding the QD dimensions and the interface quality in between the QD and the matrix material can be found in Chap. 6, page 86, while Ref. [45] treats the particular interrelation between growth parameters and the QD dimensions as well as their shape.

Exclusively Chap. 5.3, page 72 introduces the outstanding optical signature of wurtzite GaN QDs based on a deviating growth procedure enabling emission line width scaling in the range of 500 µeV. These QDs result from GaN layer growth by metal-organic vapor phase epitaxy with a V/III ratio of 30 in an AIXTRON 200/4 RF-S reactor on 2" c-plane AlN/sapphire templates. After deposition of a few monolayers of GaN for 10 s at 960 °C, a growth interruption without ammonia supply was applied for 30 s in order to initiate the formation of GaN QDs. Subsequently, the entire structure was capped by AlN at 1195 °C.

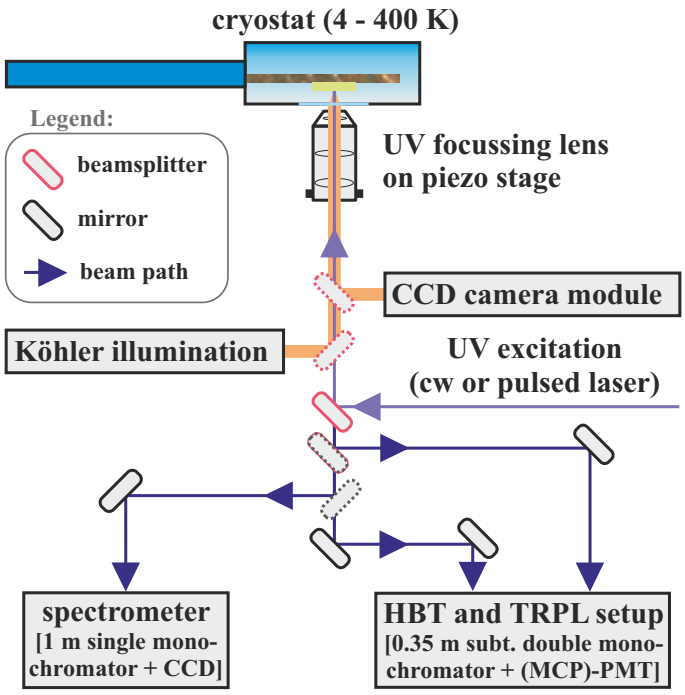

Figure 2.2: Scheme of the micro-Photoluminescence setup enhanced for the ultraviolet spectral (UV) spectral range in a nutshell. Dashed contour lines symbolize flip-mounted optics, whereas solid contours show optics that are constantly present in the beam path. The laser beam excites the sample in a backscattering configuration and a luminescence mapping is achieved by either moving the focussing lens (piezo stage) or the cryostat itself (motorized stage). The advanced detection capabilities comprise common continuous wave techniques but also time resolved and correlation measurements. More details can be found in the text along with an explanation of the acronyms and in the Appendix on page 148.

2.2 Advanced micro-Photoluminescence setup

A scheme of the UV-enhanced experimental setup can be found in Fig. 2.2. For the sake of simplicity only a simplified sketch of the entire experimental setup is shown, which summarizes the underlying method but omits all the more sophisticated experimental details. The specimen of interest is placed in a helium-flow microscopy cryostat ST-500 manufactured by Janis, enabling a temperature variation from approx. 4 - 400 K. The laser light used for the UV excitation is guided towards a beamsplitter before it is focused on the specimen's surface by a microscope lens with sufficient transmission characteristics in the UV spectral range (e.g. microspot lens by Thorlabs, 20x magnification, numerical aperture 0.4). Consequently, the generated luminescence light is collected by the same microscope lens and is guided towards the detection section of the experimental setup via a beamsplitter and several mirrors. A customized Köhler illumination along with a charge-coupled device (CCD) camera module allow an imaging of the sample surface as further

described in chapter 5, page 62 and applied in Ref. [46].

The bottom part of Fig. 2.2 indicates the detection section that is either represented by a single monochromator (Spex 1704, 1 m focal length, various gratings) equipped with a UV-enhanced CCD array, or by a subtractive double monochromator (McPherson 2035, 0.35 m focal length, various gratings). Flip mirrors in the beam path allow the user to chose the detection method of interest. While the first detection path mainly suits basic μ-PL techniques (excitation power and polarization-dependent measurements), the second beam path is used for time-resolved μ-PL (μ-TRPL) or correlation spectroscopy, while even μ-PLE measurements are feasible (not shown in this thesis). A Hanburry-Brown & Twiss (HBT) setup is integrated into the beam path allowing auto- and cross-correlation measurements due to the possibility to independently drive the stages of the subtractive double monochromator. Generally, the application of such a subtractive double-monochromator is also beneficial for μ-TRPL measurements with a multichannel plate (MCP) photomultiplier (Hamamatsu, S20 cathode), allowing a time resolution of down to ≈ 30 ps that can further be improved by deconvolution techniques [47]. The most significant optical path length differences introduced by single monochromators get automatically compensated in the double subtractive monochromator configuration, allowing superior time resolution in addition to the benefit of a reduced stray light level. For the correlation measurements photosensor modules (Hamamatsu H10721-210 with an improved shielding) with a individual time resolution $\lesssim 200$ ps were used due to their superior quantum efficiency provided by an ultra-alkali cathode in comparison to the S-20 cathode of the MCP-photomultiplier (MCP-PMT). As the achievable time resolution depends, among other things, on the laser, the modelocker adjustment, the optical path length differences, and the amplifier gain in case of the photosensor modules, it was necessary to record a laser response function for each set of time-resolved measurements. A similar approach was applied in order to determine the biphoton time resolution of the HBT setup based on a pulsed ps-laser allowing pulsed auto-correlation measurements.

As such excitation sources, either continuous wave (cw) or pulsed lasers were used. The 325 nm emission of a HeCd laser (Omnichrome Series 74) and the 244 nm and 256 nm lines of a frequency doubled Ar^{2+}-ion laser (Coherent, Innova 300 FreD) provided the most commonly applied cw excitation. For the μ-TRPL measurements a mode-locked Nd:YAG laser (Coherent Antares 76s) was frequency-quadrupled yielding an excitation wavelength of 266 nm at a repetition rate of 76 MHz and an average temporal pulse width of 55 ps, which limited the achievable time resolution. Standard photon counting techniques were applied for recording the luminescence decays or correlation functions with a SPC-130 photon counting card by Becker&Hickl.

In order to record excitation power dependent and polarization angle dependent μ-

PL spectra, motorized filter wheels and $\lambda/2$-plates were introduced into the excitation and/or detection beam paths. A mapping of the sample's surface can be achieved by operating a closed-loop 3-axes piezo stage that holds the microscope lens (1 nm step resolution, reproducibility over the entire scan range of 100 µm is better than 10 nm). However, also the entire cryostat can be moved by a 2-axes motorized stage with a step resolution of ≈ 200 nm, allowing a fast mapping over large sample areas. Generally, the mapping across the sample yields either polychromatic (CCD detection) or monochromatic mapscans (PMT detection). The latter type of mapscans is the key to long integration times as applied for auto- and crosscorrelation measurements over several days. The thermal and mechanical stability of the entire μ-PL system facilitates a sufficient ($\approx 90\,\%$) overlap between the laser focus spot (diameter of ≈ 300 nm) and the smallest mesa structures (200 nm diameter) for around an hour. Afterwards an automated mapping routine must be applied in order to automatically readjust the system, allowing integration times well in access of 24 hours, which are just limited by the coolant consumption. In addition, various sets of optics were purchased for this fully customized system, allowing the user a rapid and reproducible modification of the setup without the need of any severe realignment. Please see the Appendix 12, page 148 for further details.

3 Fundamentals and theoretical background

It is the aim of this chapter to provide a basic understanding of the theoretical modeling that finally generates an understanding of the optical signature related to individual hexagonal GaN QDs embedded in AlN. Generally, upon optical excitation of such nanostructures, an electronic excitation constituting an electron and a hole occupies the QD, which is known as an exciton if multi-particle interactions are considered. The following theoretical concepts approximate such a two-particle state of an exciton by either separable particle wavefunctions that take the most significant fraction of the interactions into account, or even by their linear combinations as described within the configuration interaction (CI) model. In this sense, the resulting wavefunctions are "two-particle" wavefunctions, which are applied throughout the entire manuscript in order to explain the optical finger prints of individual GaN QDs derived from μ-PL spectra. Based on such an approximation of an exciton it is straightforwardly feasible to derive a large variety of basic parameters as e.g. the exciton dipole moment, the biexciton binding energy, and the exciton-phonon coupling strength, all of which are also accessible by means of μ-PL spectroscopy. As this is an experimentally focused thesis it is not the aim of the author to provide all the details of these calculations, which are instead the topic of a more theoretically focused thesis by G. Hönig [48]. Nevertheless, a basic understanding of the origin of the applied wavefunctions is provided in the following, as this is necessary in order to understand all the occurring experimental particularities presented in the subsequent chapters. Additional theoretical concepts are further detailed in the corresponding chapters as soon as required for a more sophisticated interpretation of the measurements.

However, before the origin of the wavefunctions is explained, more fundamental properties of the materials that constitute the QDs and their enclosing need to be introduced. Here, the focus resides on a basic introduction of the wurtzite crystal structure and its particular polarization fields, the band structure and valence band ordering of GaN and AlN, as well as the first order phonon modes native to the wurtzite lattice. Nowadays such basic properties of group-III nitrides can be considered as common knowledge as a large variety of review articles and books address these topics. Nevertheless, the following chapter starts with a brief introduction in

order to subsequently develop more elaborated concepts, which are required in order to approach the multitude of experimental results presented in Chap. 4-8.

All contour plots from this chapter and Chap. 4, page 39 that show the electric potential distribution based on polarization charges, or occupation probability densities of an electron or a hole inherent to single GaN QDs were computed by G. Hönig. The corresponding code was developed at the Technische Universität Berlin for more over a decade and contains significant contributions from Dr. O. Stier, Prof. Dr. M. Grundmann, Dr. A. Schliwa, Dr. M. Winkelnkemper, G. Hönig, and others.

3.1 Fundamental properties of GaN and AlN

Both, GaN and AlN preferentially crystalize in the wurtzite structure, which also forms the basis for the analyzed QDs. Generally, the crystallization of GaN and AlN can also yield the metastable cubic phase [49], or under high ambient pressures the rocksalt configuration [50,51]. Even though the successful growth of cubic GaN QDs embedded in AlN can be demonstrated [52–55], the growth remains a tremendously challenging task. Stabilization of the cubic phase is an exceptionally non-trivial endeavor for group-III nitrides and constitutes a strong motivation for the wurzite growth of these materials, despite undesired phenomena such as the quantum-confined Stark effect (see Sec. 3.7, page 37). The rocksalt configuration of GaN and AlN originates from the application of high pressures and is indeed highly interesting from a physical point of view [56], but has so far not achieved any relevance regarding nanostructures, which are mostly still based on the wurtzite configuration of nitrides.

3.1.1 Crystal structure and polarization fields

The wurtzite structure as a representative of a hexagonal system consists of two hexagonal close-pack layers that obey an ABAB stacking. Consequently, the space group of the wurtzite structure is C_{6v}^4, which is homomorphic to the point group C_{6v} [42]. Naturally, each of the layers A and B exhibits an hexagonal symmetry regarding the included atoms (Ga and N or Al and N in each layer A and B), which is the origin of the C_3 rotational symmetry of the zinc-blende crystal, thus the cubic modification. Both crystal modification exhibit a tetrahedral bonding just with different stacking sequences, which are exclusively governed by the cohesive energy of the crystal. The bonds themselves are of the sp^3 type and the bond angles between the nearest neighbors exhibit an angle of 109.47° in the ideal wurtzite structure [42]. Here, in such an ideal wurtzite crystal the ratio of the lattice constants amounts to

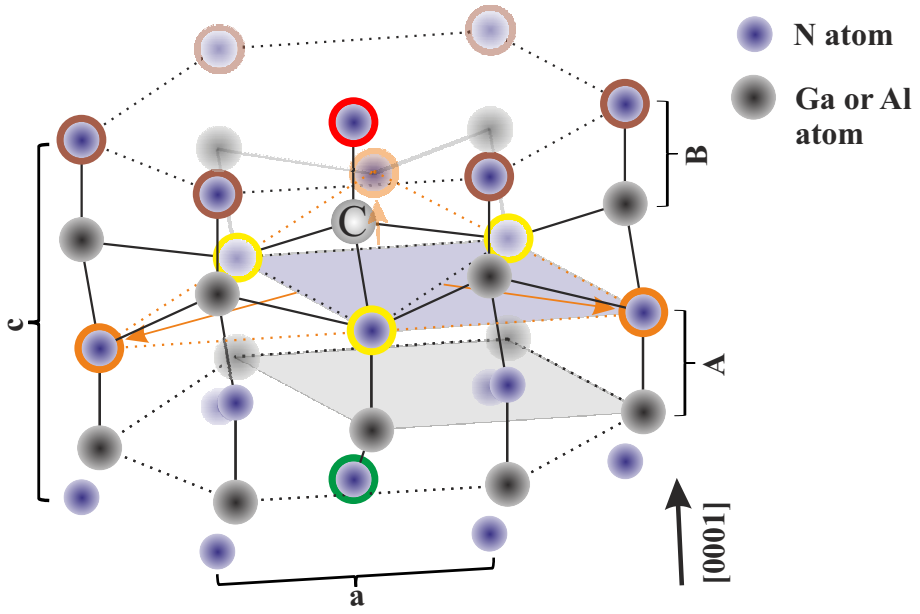

Figure 3.1: Schematic illustration of the wurzite structure (not to scale) focussing on the nearest and second nearest neighbors of the designated (C) metal atom (grey) surrounded by the tetrahedrally coordinated nitrogen atoms (blue). The nitrogen-polar crystal section shown, illustrates the AB stacking sequence as well as the c and a lattice constants. Four first-neighbor atoms are highlighted (red and yellow) along with ten second-neighbor atoms (orange, brown, and green), exhibiting different distances in regard to C. Please see the text for further details.

$c/a = \sqrt{8/3} = 1.633$ with an ideal internal cell parameter $u = 8/3 = 0.375$. However, based on various experimental methods it is known, that none of these theoretical cell parameters matches the experimental values for GaN and AlN [57, 58].

In the ideal wurtzite structure, the two hexagonal close-pack layers of metal and nitrogen atoms are shifted by 3/8 of the c lattice constant with respect to each other along any arbitrary anion-cation bond, which is not orientated in parallel to the c-axis. Fig. 3.1 illustrates a nitrogen-polar wurtzite lattice consisting of an A and a B stack along with one additional nitrogen layer. The wurzite structure lacks any symmetry plane perpendicular to the c-axis, while three of these symmetry planes exist in parallel to the c-axis. Hence, due to the reduced symmetry in comparison to e.g. the cubic structure, the wurzite structure requires a strict distinction between the c-axis and its antiparallel counterpart. As a result, even the ideal wurtzite structure triggers the occurrence of a polarization along the c-axis. Ambacher et al. provided an intuitive analysis of the related charge asymmetries in the wurtzite lattice as summarized in the following paragraph based on Ref. [59].

The designated metal atom (C) shown in Fig. 3.1 is surrounded by four nearest neighbor nitrogen atoms. Three of these nearest neighbors (yellow) commonly ex-

hibit identical bond length and angles if, e.g., no application of any uniaxial stress component is assumed. The fourth nearest neighbor (red) only exhibits an identical distance to C in comparison to the other three nearest neighbors, if the ideal wurtzite structure is considered. In that case, these four nearest neighbors originate an evenly distributed charge distribution around C based on identical bond lengths and angles. However, the entire symmetry is heavily altered as soon as the second nearest neighbors of C are considered. The nitrogen plane in the B-stack shown in Fig. 3.1 contains six second-neighbor nitrogen atoms (brown), while the top-nitrogen layer of the A-stack beneath contributes three second nearest neighbors (orange with arrows). Please note how these three second-neighbors are distributed around C in accordance to the C_3 rotational symmetry of the corresponding atomic plane (orange dashed lines). However, exactly one second nearest neighbor atom (green) of the metal atom C resides in the nitrogen plane beneath the A stack as shown in Fig. 3.1. This distance (metal atom C $\rightarrow$ "green" nitrogen atom in Fig. 3.1) is shorted by around 13 % [59] in regard to the other second nearest neighbor bond length, demonstrating a fulminant asymmetry of the ideal wurtzite that breaks the charge neutrality and results in a polarization field along the c-axis known as the spontaneous polarization or also pyroelectricity. However, the precise determination of the pyroelectricity of the bulk material remains a challenging task as numerous occurring dipole moments must be taken into account as described by Bernardini et al. [60] based on density functional calculations in the local density approximation. Any deviation from the ideal wurtzite structure, as it is the case for the GaN and AlN lattice, heavily alters this pyroelectricity and even introduces piezoelectricity, cf. Sec. 3.2.1. Naturally, the displacement of atoms from their position in an ideal wurtzite structure as e.g. induced by strain (also internal strain common to the non-ideal wurtzite lattice [61]) strongly varies the charge distribution in the entire crystal based on strongly ionic metal-nitrogen bonds. As a result, the piezo- and pyroelectric fields in the close vicinity of nanostructures reflect their particular shape as illustrated in Sec. 3.2.1.

3.1.2 Band structure and valence band ordering

Wurtzite GaN and AlN exhibit their valence band maxima and conduction band minima at the Γ point, thus, both are direct semiconductors. The antibinding 4s states of gallium and the antibinding 3s states of aluminium originate the conduction band in GaN and AlN, while the binding 2p states of nitrogen form the upper valence bands. The crystal field [62] induces a splitting of the uppermost valence bands at the Γ-point of the Brillouin zone with either Γ_1 or Γ_5 symmetry following the Koster notation [63]. Furthermore, the spin-orbit interaction originates a further splitting of the valance bands in GaN and AlN. Here, a particular difference

between GaN and AlN becomes evident as the symmetry ordering of their upmost valence bands is reversed. GaN exhibits three upper valence bands with a Γ_9, Γ_7, Γ_7 symmetry ordering, while the ordering of the two upmost valence band symmetries is reversed in AlN yielding a Γ_7, Γ_9, Γ_7 ordering [62, 64] similar to the case of ZnO [65]. Precisely these three valence bands are also commonly described as the A, B, and C valence band in any wurtzite semiconductor. The conduction band itself exhibits Γ_7 symmetry in GaN and AlN. In order to describe the optical properties of the GaN QDs it is sufficient to consider the close vicinity of the Γ-point, rendering a k·p approach an ideal choice as introduced in Sec. 3.2.

3.1.3 First order phonon modes

As the wurtzite structure features $n = 4$ atoms in the primitive unit cell, $3n = 12$ first order phonon modes are expected, constituting the common 3 acoustical modes along with 9 optical modes. The entire set of phonon modes can be described based on group theoretical considerations [66] yielding the following irreducible representation:

$$\Gamma = 2A_1(1) + 2B_1(1) + 2E_1(2) + 2E_2(2). \tag{3.1}$$

Here, the number in brackets denotes the one- or twofold degeneracy. The acoustical modes native to the wurtzite lattice comprise one non-degenerate A_1 mode and a twofold degenerate E_1 mode, while the other 9 optical modes are commonly labeled as

$$\Gamma_{opt} = A_1(1) + B_1^{low}(1) + B_1^{high}(1) + E_1(2) + E_2^{low}(2) + E_2^{high}(2). \tag{3.2}$$

Fig. 3.2 illustrates the atomic displacement of all these 9 optical modes. The A_1 and B_1 modes exhibit oscillations parallel to the c-axis of the wurtzite crystal and the E_1 and E_2 modes contain perpendicular orientated atomic displacements. The B_1 oscillations are Raman-forbidden, leaving 6 first-order Raman modes behind that can straightforwardly be observed by means of Raman spectroscopy [61, 67]. However, in this thesis the A_1 and E_1 modes are of main interest as they are polar modes, which features a strong coupling to optical excitations like e.g. excitons. As depicted in Fig. 3.2 the A_1 mode originates from an oscillation of the metal against the nitrogen lattice parallel to the c-axis, finding its perpendicular counterpart in the E_1 mode. Hence, an oscillating polarization accompanies the A_1 and E_1 modes in the lattice, originating a strong electron- and exciton-phonon coupling [68, 69] as further discussed in Chap. 6, page 74.

The polarization fields native to the wurtzite structure lift the degeneracy of the A_1 and E_1 modes, yielding a longitudinal-optical (LO) and transversal-optical (TO)

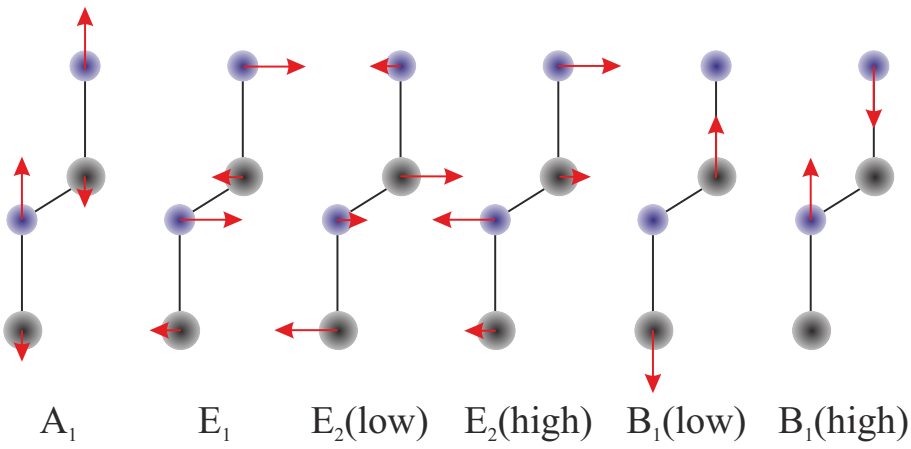

Figure 3.2: Schematic illustration of the ion displacement that occurs in a wurtzite material as soon as an optical phonon mode is excited. For the case of GaN or AlN, the metal atoms are depicted by grey spheres, while the nitrogen atoms are illustrate by purple complements. The length of the depicted arrows is proportional to the most dominant displacement. The sub-lattice of the nitrogen atoms predominantly contributes to the A_1, E_1, B_1^{high}, and E_2^{high} modes, while the B_1^{low} and E_2^{low} vibrations are strongly influenced by the oscillation of the metal atoms. The A_1 and E_1 modes are polar in contrast to their B_1 and E_2 counterparts.

mode. The energy of the LO modes naturally exceeds the corresponding TO values, because the macroscopic electric field acts as an additional restoring force for the ion oscillation [70], an effect that can in principle easily be understood and mimicked by the well-known plate capacitor [42].

3.2 From single- to multi-particle states

The applied 8-band k·p modeling for wurtzite material based QDs represents the extension of an implementation that was previously successfully applied for various zincblende QD systems [71–74]. The inclusion of strain effects, the piezoelectric and pyroelectric polarization, as well as the spin-orbit and crystal-field splitting ensures realistic wavefunctions as approved by a direct comparison to optical data. The application of the full 8×8 Hamiltonian accounts for the coupling between the valence and conduction bands, yielding a successful theoretical description even for wurtzite materials with smaller bandgaps like InN if compared to GaN and AlN [35]. Generally, atomistic tight-binding approaches are still only of limited value due to the experimentally confirmed sheer size of GaN QDs comprising up to 100k atoms, rendering the presented 8-band k·p formalism inevitable and most valuable.

3.2.1 Strain state and built-in electric field calculations

The particular strain distribution induced by embedding a wurtzite GaN QD in its matrix material AlN, does not only affect the electronic states via the electronic deformation potentials, but also by the strain-induced piezoelectric polarization. Generally, in c-plane grown GaN QDs the biaxial stress is large and amounts up to several GPa (for details please see Chap. 6, page 74). In combination with huge piezoelectric constants that are common to wurtzite GaN and AlN [75], one obtains a significant influence regarding the electronic states, if e.g. compared to arsenide-based QDs. In addition to the piezoelectric polarization, the spontaneous (pyroelectric) polarization needs to be considered. For wurtzite GaN QDs both polarization types exhibit the same order of magnitude in contrast to e.g. the case of InGaN/GaN QDs [35]; a balance that is straightforwardly governed by the difference of the pyroelectric polarization constants [60].
As a first step, the strain field in the model QDs and their vicinity is calculated using a continuum mechanical approach as described in Refs. [76, 77]. The applied QD dimensions and further parameters are, as far as possible, derived from experiments, cf. Chap. 6.4, page 86. Generally, the total polarization $\boldsymbol{P}$ for the case of a wurtzite type semiconductor is given by the following Eq. 3.3.

$$\boldsymbol{P} = \boldsymbol{P}_{PZ} + \boldsymbol{P}_{SP} \tag{3.3}$$

Here, $\boldsymbol{P}_{PZ}$ symbolizes the strain-induced piezoelectric polarization, while $\boldsymbol{P}_{SP}$ is its pyroelectric counterpart. $\boldsymbol{P}_{SP}$ only exhibits one significant component along the [0001] direction and is taken from Ref. [78] for GaN and AlN, while the corresponding $\boldsymbol{P}_{PZ}$ values can directly be derived based on the strain tensor [79]. Consequently, the entire polarization charge density $\rho(\boldsymbol{r})$ can be described by

$$\rho(\boldsymbol{r}) = -\nabla \cdot \boldsymbol{P}(\boldsymbol{r}), \tag{3.4}$$

directly resulting the electrostatical potential $V_{static}(\boldsymbol{r})$ via the Poisson equation

$$\epsilon_0 \nabla \cdot [\epsilon_r(\boldsymbol{r}) \nabla V_{static}(\boldsymbol{r})] = \rho(\boldsymbol{r}). \tag{3.5}$$

It is exactly this potential $V_{static}(\boldsymbol{r})$ that will finally be included in the Hamilton operator described in the following Sec. 3.2.2 in order to derive e.g. single-particle wavefunctions. Fig. 3.3 displays $V_{static}(\boldsymbol{r})$ for two model QDs in a color-coded contour plot, exhibiting the shape of a truncated, hexagonal pyramid with a diameter of 16 nm and a height of 1.2 nm, respectively 2.4 nm. The QDs' shape and their dimensions are confirmed by scanning transmission electron (STEM) and atomic force microscopy (AFM) as described in Chap. 2, page 16) and 6, page 74. Fig. 3.3a and b nicely illustrate how a negativ potential is formed at the QD bottom (red →

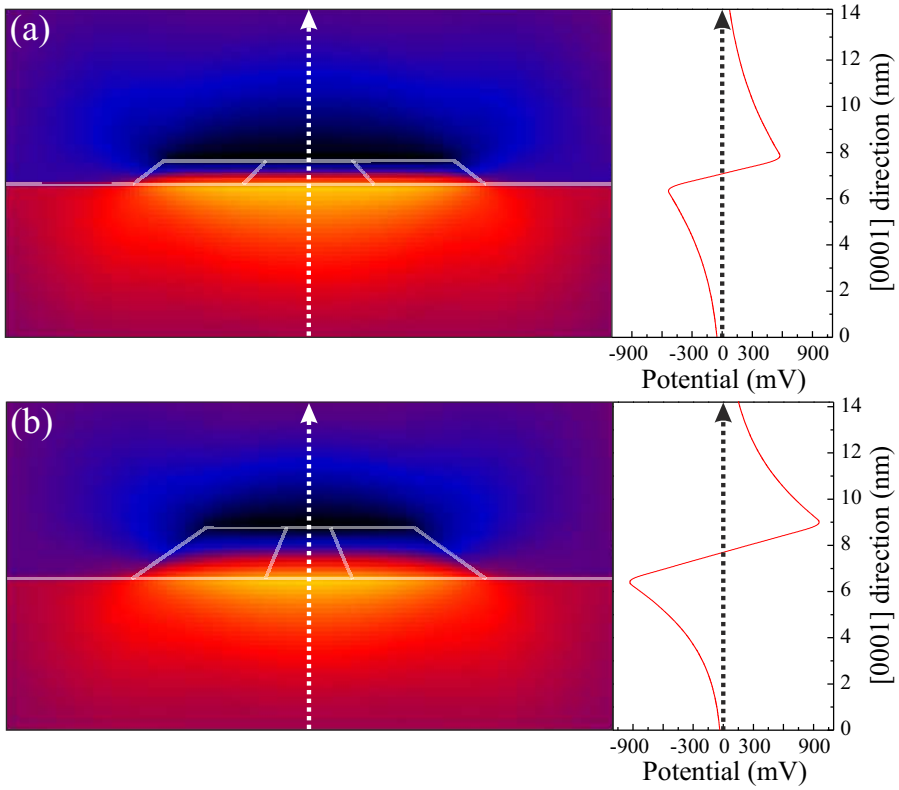

Figure 3.3: Color-coded contour plot of the electrostatical potential $V_{static}(\boldsymbol{r})$ based on the piezo- and pyroelectric field P introduced in Eq. 3.3 (left). The QD shown in (a) exhibits a height of 1.2 nm and a width of 16 nm, while the height of the QD shown in (b) is doubled with the diameter remaining constant. A profile plot (right) that quantifies the electrostatical potential along the [0001] direction (dashed arrows) is shown next to the corresponding color-coded plot. Following this direction, a negativ potential occurs at the bottom of the QD (red → yellow), which is nullified at QD half-height, before it reverses its sign towards the QD top (blue → black).

yellow), while the QD top area is dominated by a positiv potential (blue → black). Hence, upon excitation of such a QD with an electron-hole pair forming an exciton, the upper QD section is attractive for electrons, while holes should accumulate at the QD bottom as confirmed in the following Sec. 3.2.2.

3.2.2 Single-particle states

The electronic states and energy levels of a bulk semiconductor can in principle straightforwardly be derived by solving the Schödinger equation

$$H_0\psi = \left[\frac{\boldsymbol{p}^2}{2m_0} + V(\boldsymbol{r})\right]\psi = E\psi \tag{3.6}$$

with the Hamiltonian H_0, the electronic wavefunction ψ, the total energy E, the momentum operator $\boldsymbol{p}$, the free electron mass m_0, and the lattice potential $V(\boldsymbol{r})$ depending on the position vector $\boldsymbol{r}$ as shown in Fig. 3.3. However, in a heterostructure like a GaN QD embedded in AlN the crystal composition, the strain, and the field situation varies depending on $\boldsymbol{r}$, rendering approximations in order to solve Eq. 3.6 inevitable. Gershoni et al. [80] describe such an approximation known as the k·p method, comprising envelope functions for the three topmost valence bands and the lowest conduction band in the close vicinity of the Brillouin zone center close to $\boldsymbol{k} = 0$. In each homogenous region of the complex structure of interest the wavefunction itself is assumed to obey the following form:

$$\Psi(\boldsymbol{r}) = \sum_n U_n(\boldsymbol{r})F_n(\boldsymbol{r}) \tag{3.7}$$

Here, $U_n(\boldsymbol{r})$ are the zone center Bloch waves for the particular local material of the heterostructure as selected by $\boldsymbol{r}$ and the underlying global structure (e.g. QD shape, dimensions, stratification in a device structure, etc.). The summation additionally encompasses the envelope functions $F_n(\boldsymbol{r})$ and includes the Bloch wavefunctions for the conduction band minimum as well as the three valence band maxima, each contributing two spin orientations. Hence, an eponymous set of *eight* coupled differential equations can be derived

$$\sum_n H(\boldsymbol{r},k)_{mn}F_n(\boldsymbol{r}) = EF_m(\boldsymbol{r}). \tag{3.8}$$

Solving this set of equations is directly related to the application of correct boundary conditions at the interfaces of the computational domains that finally guarantee envelope function continuity and current conservation as summarized by Baraff et al. in Ref. [81]. As a result of the given sub-selection of bands, the state ψ is composed of eight projections on four bands as described by

$$\psi = (c^{\uparrow}, v_A^{\uparrow}, v_B^{\uparrow}, v_C^{\uparrow}, c^{\downarrow}, v_A^{\downarrow}, v_B^{\downarrow}, v_C^{\downarrow})^T. \tag{3.9}$$

In this basis the Hamiltonian H can be denoted in the block matrix form given by

$$\begin{pmatrix} G(\boldsymbol{k}) & \Gamma \\ -\Gamma^* & G^*(\boldsymbol{k}) \end{pmatrix} \tag{3.10}$$

with G and Γ presenting 4x4 matrixes each, while the asterisk denotes the complex conjugate. The detailed structure of these matrixes is not of interest in this experimentally oriented manuscript and is given for zinc-blende crystal in Ref. [80], while, among others, Winkelnkemper et al. have reported the wurtzite-specific parts in Ref. [35,82]. A list of all parameters contributing to $G^{(*)}(\boldsymbol{k})$ and $\Gamma^{(*)}$ is given in Ref. [40], including a sign correction for one of the piezoelectric constants [38, 75, 83]. Finally, the single-particle states of the holes and electrons are computed by an algorithm that derives all required eigenvalues. Hereunto, the computational domain that encompasses the entire heterostructure is separated into cubes with a side length of $\approx 0.2\,\mathrm{nm}$. The underlying C and Fortran 90 code was continuously developed at the Technische Universität Berlin [74, 82, 84] and its results can seed the multi-particle state calculations as described in the following section.

Fig. 3.4 illustrates the resulting occupation probability densities $|\psi|^2$ in a normalized, color-coded contour plot for the same two model QDs already depicted in Fig. 3.3, comprising a diameter of 16 nm and a height of 1.2 nm, respectively 2.4 nm. The color coding was applied to normalized $|\psi|^2$ distributions in order to ease the visibility of the charge carrier distribution along the QD by applying the full color range. However, the corresponding profile plots along the [0001] direction allow to compare the deviating $|\psi|^2$ of the electron and the hole across all model QDs, cf. Fig. 3.5. This was achieved by a rather arbitrary normalization of each profile plot to the sum of all hole $|\psi|^2$ values along the [0001] direction that originate from the flatter QD (any normalization is suitable if kept constant for all contour plots). Fig. 3.4a nicely illustrates the generally stronger localization of the hole due its large effective mass, if compared to its counterpart, the electron. As soon as the QDs flatten, the electron occupation probability density extends over the QD diameter, approaching the quantum well case. However, as soon as the QD height is increased, the spatial carrier localization is enhanced as directly noticeable by a comparison of Fig. 3.3a and b. Please also note the horizontal grey dashed lines, which connect the QD contours with the profile plots. These lines allow the observation that a certain section of the electron and hole occupation probability density resides outside of the QD material in the matrix material, an effect that will be of tremendous importance for the physical discussion presented in Chap. 6, page 74 treating the exciton-LO-phonon coupling.

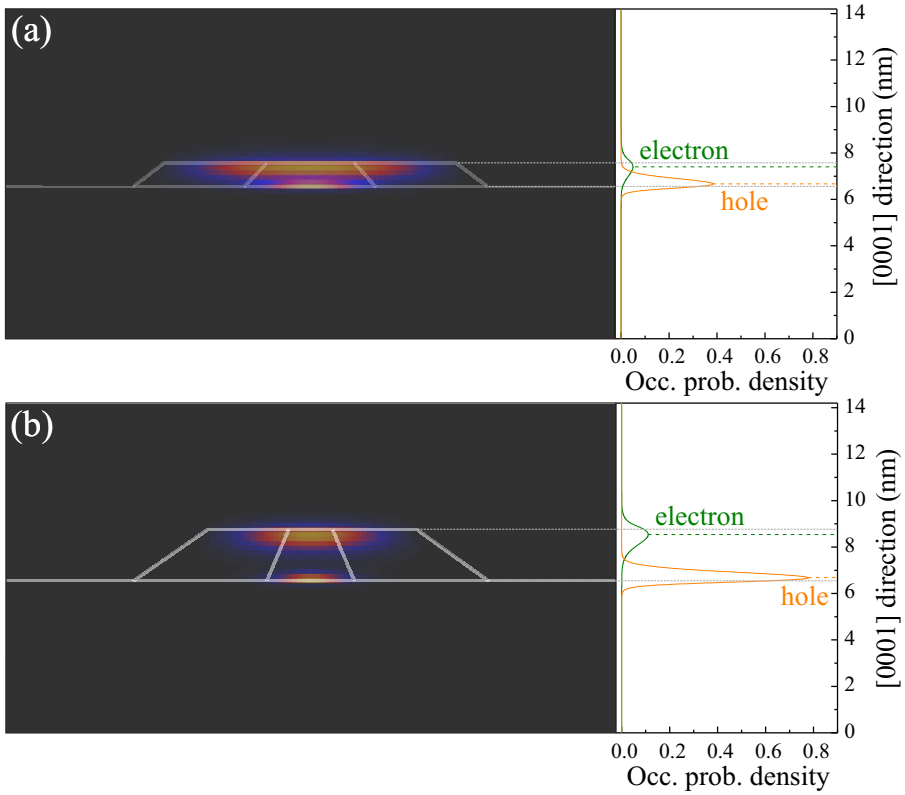

Figure 3.4: Normalized, color-coded contour plots showing the occupation probability density $|\psi|^2$ of single-particle wavefunctions occurring in wurtzite GaN QDs embedded in AlN. The model QD structures (truncated, hexagonal pyramids) are sketched by the grey contour-lines, describing a QD height of 1.2 nm (a) or 2.4 nm (b) and a constant QD diameter of 16 nm, which is identical to the QD dimensions applied in Fig. 3.3. Profile plots along the [0001] direction through the QDs' centers individually show $|\psi|^2$ for an electron and a hole. In order to allow a quantitative comparison between the individual $|\psi|^2$ dependencies, all of them were normalized to the sum of all hole $|\psi|^2$ values along the [0001] direction of the flatter QD shown in (a).

3.2.3 Multi-particle states

The challenging task of a most realistic simulation dedicated to multi-particle states is commonly solved by the configuration-interaction (CI) method, which takes few-particle effects into account. In addition to the direct Coulomb interaction of electron(s) and hole(s), these are the exchange interaction and correlation effects. However, the accuracy of the CI method scales with the number of bound single-particle states (see Sec. 3.2.2), whose number is especially limited e.g. for InGaN QDs embedded in GaN [35, 82]. However, for wurtzite GaN QDs embedded in AlN a sufficient number of bound single-particle states exists due to large bandgap offsets. Nevertheless, the direct application of the CI method on single-particle states remains

challenging due to the renormalization of the wavefunctions. Hence, even though the CI method based on single-particle states has proven as an efficient technique for InAs/GaAs QDs exhibiting negligible renormalization effects, its application for wurtzite, c-plane GaN QDs requires an improved set of basis states.
Such improved basis states can e.g. be derived by the Hartree or the Hartree-Fock method, yielding more realistic multi-particle states if used for seeding the CI scheme as the final computational step. The Hartree method accounts for all mean Coulomb interactions in a multi-particle state leading to a renormalization of the single-particle wavefunctions under the influence of the strong pyro- and piezoelectric fields in nitride QDs. As a result, a multi-particle wavefunction is obtained that already allows the description of excitonic complexes to a certain degree. However, already the following ansatz for the multi-particle wavefunction in the Hartree approximation $\Psi^{Hartree}$ reveals a prominent deficiency of the Hartree method:

$$\Psi^{Hartree} = \prod_i \psi_i(\boldsymbol{r}) \tag{3.11}$$

In this simplistic ansatz $\Psi^{Hartree}$ is described by a product of orthonormalized single-particle wavefunction ψ_i. Hence, in the Hartree approximation two wavefunctions that describe fermions in one and the same quantum mechanical system can indeed be identical, in most striking contrast to the Pauli exclusion principle. The consideration of the spin-related exchange interaction, which also takes this most fundamental physical exclusion principle into account, is achieved in a more advanced ansatz applied in the Hartree-Fock approximation. Here, the multi-particle wavefunction Ψ^{HF} is given by

$$\Psi^{HF}(t_1, t_2, ..., t_A) = \frac{1}{\sqrt{A!}} \begin{vmatrix} \psi_1(t_1) & \psi_1(t_1) & ... & \psi_1(t_A) \\ \psi_2(t_1) & \psi_2(t_2) & ... & \psi_2(t_A) \\ ... & ... & ... & ... \\ \psi_A(t_1) & ... & ... & \psi_A(t_A) \end{vmatrix}, \tag{3.12}$$

with A indicating the number of participating one particle states ψ_A, depending on a set of coordinates t_i that is composed of the position vector $\boldsymbol{r}$ and the spin σ. Each row of the determinant in Eq. 3.12 can be interpreted as the occupation of one of the single-particle states $\psi_1, \psi_2, ..., \psi_A$ with one of the contributing particles $i = 1, 2, ..., A$. Consequently, Ψ^{HF} describes an antisymmetric multi-particle wavefunction as an exchange of two rows or columns of the, so-called, Slater determinant alters its sign, in contrast to the product form of $\Psi^{Hartree}$ cf. Eq. 3.11. Naturally, this antisymmetry now complies with the Pauli exclusion principle, as the exchange of two identical rows or columns can only change the sign of the Slater determinant

by nullifying the entire multi-particle state Ψ^{HF}.

The precise modality for introducing the Coulomb interaction in the Hartree, and both, the Coulomb and exchange interaction in the Hartree-Fock approximation, resides beyond the scope of this thesis and can be found elsewhere [48]. Nevertheless, the calculation scheme for both approximations is from a structural point of view identical and starts with the single-particle states that are fed into a self-consistent calculation loop. In this loop, the Hartree energy $E^{Hartree}$ or the Hartree-Fock energy E^{HF} are calculated based on the Coulomb, or both, the Coulomb and exchange interaction. As a result, new single-particle states are obtained that can again serve as initial states for the iterative loop. Finally, the sequently ameliorated particle states are not significantly altered anymore and the output of the calculation loop yields converged, so-called, multi-particle states that consider, in the best case, the particular strain state of the QD, the piezo- and pyroelectric field, as well as the Coulomb and exchange interaction. The described cycle identifies the applied calculation scheme as a variational method that minimizes the energy functional by approaching $\delta_{\psi} E^{Hartree/HF} = 0$.

However, even the ansatz from Eq. 3.12 cannot yield a fully valid description of two-particles systems as excitons, because only the occupied states are considered and the final solution still obeys a separable form. A truly exact solution is only obtained if all $(N \rightarrow \infty)$ occupation possibilities are considered, each contributing its own Slater determinant to a linear combination of Hartree-Fock states:

$$\Psi = \sum_{n=1}^{N} c_n \Psi_n^{HF}(t_1, t_2, ..., t_N) \tag{3.13}$$

The corresponding CI Hamiltonian can be found in Ref. [48] and it incorporates on its main diagonal the energies that were obtained by the Hartree-Fock iteration method. All off-diagonal matrix elements originate from configuration combinations with non-vanishing Coulomb and exchange interaction terms. Hence, the CI method strongly benefits from the application of a "few" Hartree-Fock states that already include the majority of interactions except of the configuration interaction.

As a direct result of the Hartree-Fock approach, Fig. 3.5 shows the fully converged $|\psi|^2$ distributions for an electron and a hole. The same two model QDs that were already depicted in Fig. 3.3 and 3.4, comprising a diameter of 16 nm and a height of 1.2, respectively 2.4 nm, are again depicted by grey lines. By comparing Fig. 3.4 with Fig. 3.5 an increased localization of the electron can be observed at a first glance. Although this effect is most prominent for the electron that occupies the flatter QD shown in Fig. 3.5a, it is also noticeable for the corresponding hole, even in the higher QD illustrated in Fig. 3.5b. The profile plots from Fig. 3.5 allow a quantitative comparison to Fig. 3.4 as the same normalization procedure was

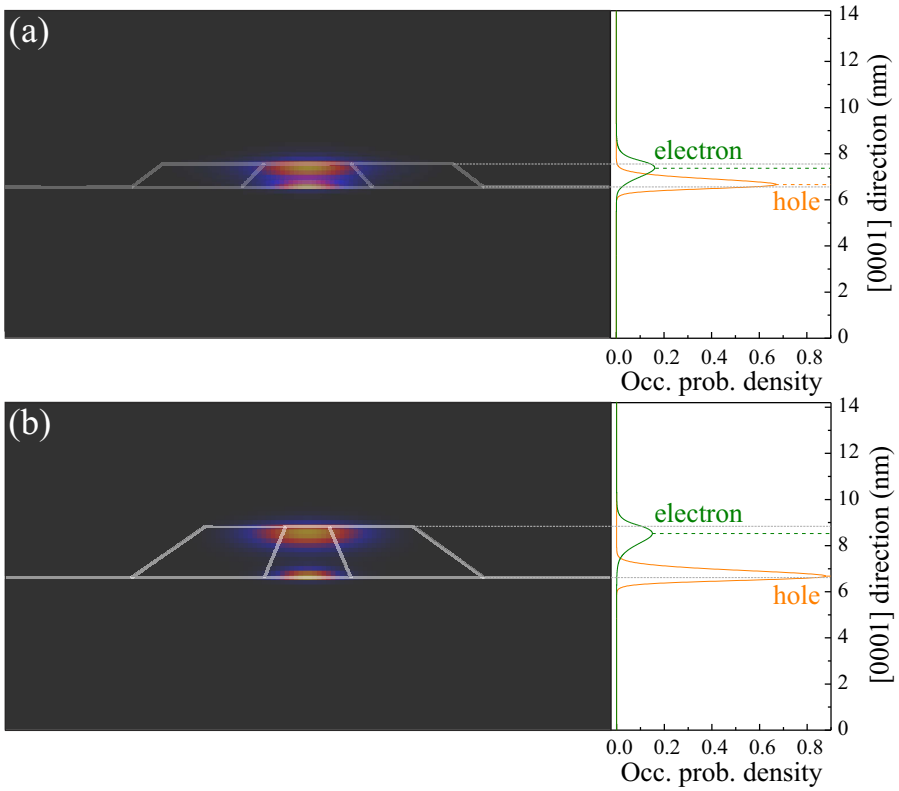

Figure 3.5: Normalized, color-coded contour plots showing the electron and hole occupation probability densities $|\psi|^2$ in wurtzite GaN QDs embedded in AlN based on the Hartree-Fock approach. The model QD structures (truncated pyramids) are sketched by the grey lines describing a QD height of 1.2 nm (a) or 2.4 nm (b) and a constant QD diameter of 16 nm, which is identical to the QD dimensions applied in Fig. 3.3 and 3.4. Profile plots along the [0001] direction through the QDs' centers individually show $|\psi|^2$ for an electron and a hole. In order to allow a quantitative comparison between the individual $|\psi|^2$ dependencies, all of them were normalized to the sum of all hole $|\psi|^2$ values along the [0001] direction of the flatter QD.

applied based on the sum of all hole $|\psi|^2$ values along the [0001] direction belonging to the flatter QD. Please note that the illustration shown in Fig. 3.5 represents the best way for illustrating an approximation of an exciton in a QD in real space based on Hartree-Fock wavefunctions. Any approximations beyond Hartree-Fock, as e.g. the inclusion of CI cannot straightforwardly be illustrated anymore. Here, the illustration of a large contour plot set would be the only feasible solution for an illustration, comprising an electron and/or a hole in a multitude of fixed positions and the corresponding $|\psi|^2$ distribution for the opposing charge carrier. Clearly, the benefit of such an illustration is questionable. Hence, it is more valuable to reside to a characteristic number, the total complex interaction energy, which serves as a fingerprint for the excitonic complex inherent to the individual GaN QD. Naturally,

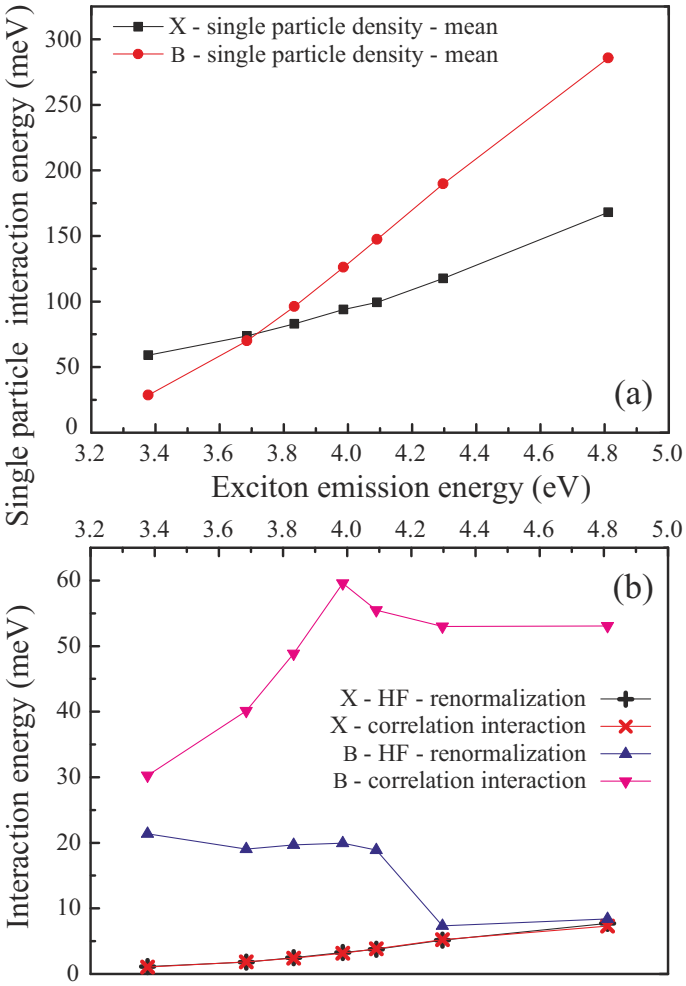

Figure 3.6: (a) Mean Coulomb and exchange interaction energies of the exciton (X) and biexciton (B) based on single-particle states plotted against the X emission energy that already takes all interaction effects into account. For such a correct description the renormalization and correlation energies of the X and the B complex have to be considered as shown in (b). As long as the resulting total B interaction energy (sum of all three interaction contributions) exceeds twice the total X interaction energy minus its dark-bright state splitting [40], the B exhibits a binding nature and appears at lower energies in regard to X in μ-PL spectra.

such total complex interaction energies also strongly depend on the applied modeling procedure taking a certain, computational time limited, subset of interactions into account.

By computing the total complex interaction energy [48], the in Fig. 3.4 and 3.5 depicted changes regarding the occupation probability density are directly quantified. It is exactly this pivotal number that finally dictates the spectral position of the excitonic complexes, which can be probed by means of μ-PL spectroscopy. Fig. 3.6a shows the single-particle interaction energy of either one or two bound electron hole pairs, known as an exciton (X) and a biexction (B). The calculation of these interaction energies is based on the wavefunctions that were described in Sec. 3.2.2 and 3.2.3. However, Fig. 3.6b now facilitates a separation of the renormalization and correlation effects. As soon as the QD size is decreased within experimentally determined limits (see Chap. 2), the interaction energy continuously rises with the exciton emission energy due to a reduced electron-hole separation.

Clearly, the mean Coulomb and exchange interaction between the particles has the

largest impact on the interaction energies as shown in Fig. 3.6. However, the determination of these energies based on single-particle states represents only the simplest approximation, which cannot bear a direct comparison to experiments. Hence, an improved set of basis states must be obtained as introduced in Sec. 3.2.3 based on an iterative Hartree-Fock calculation that takes the mean Coulomb and the exchange interaction into account. As a direct result, one obtains an overall increase of the particle interaction energies by the values plotted in Fig. 3.6b that are labeled with HF renormalization. Subsequently, a correlation interaction scheme can directly be applied based on the Hartree-Fock basis states, yielding an additional increase of the interaction energies as summarized in Fig. 3.6b. Here, quite particular trends appear for the renormalization- and correlation-induced energy components of the B complex in strong contrast to the continuous trend from Fig. 3.6a. The precise origin for this behavior is given in Chap. 8 and is based on a lateral separation of the hole states in the B complex, leading to a novel, so called hybrid-biexciton with a particular hole-spin alignment [40]. Generally, all particle interaction energies of the X and B complexes shown in Fig. 3.6 are plotted against an X emission energy that already takes the entire set of interactions into account. Since elongated QD structures were modeled in accordance to the experiment [37], the average of the bright X states was applied for determining the X emission energy.

3.3 Quantum-confined Stark effect

A more simplified but also very descriptive explanation of the charge carrier separation in c-plane grown wurtzite GaN QDs embedded in AlN is based on the model of the quantum-confined Stark effect (QCSE) [64, 85, 86]. Generally, the fundamental Stark effect describes the shift of molecular or atomic spectral lines under the influence of an electric field, thus, representing the analogon to the Zeeman effect, which describes the same physical phenomenon just under the influence of a magnetic field. One distinguishes between the linear and the quadratic Stark effect, depending on wether a dipole moment already exists without the presence of an electric field (inherent dipole moment) or a dipole is induced upon the application on an electric field (induced dipole moment). The terminology of the *quantum-confined* Stark effect is frequently used in the field of semiconductor physics and trivially relates to the quantum-confinement of the particles that constitute the dipole moment but does not introduce any deviating new conceptions.

As outlined in Sec. 3.2.1 and motivated in Fig. 3.3, any c-plane interface between GaN and AlN introduces a significant accumulation of charges [87]. Hence, as soon as two interfaces oppose each other as it is the case in a quantum well, quantum wire, or in a QD, huge electric fields of the order of several MV/cm occur across the

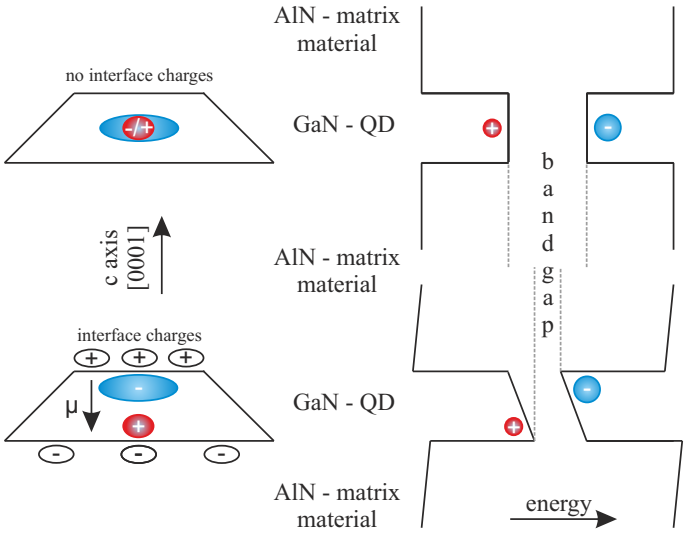

Figure 3.7: Scheme of the quantum-confined Stark Effect (QCSE) in a single GaN quantum dot (QD) embedded in its matrix material AlN. If the natural occurrence of interface charges is neglected then no tilting of the bands occurs, allowing the electron (blue) and the hole (red) in the QD to overlap (top). However, as soon as interface charges are considered (bottom) the bands tilt, leading to a red-shift of the emission and increased excitonic lifetimes due to a spatial carrier separation that also originates enhanced excitonic dipole moments μ. Please note that the underlying band parameters are not drawn to scale.

nanostructure. Even without the sophisticated 8-band k·p calculations presented in Sec. 3.2.2, one can straightforwardly understand the occurring charge carrier separation, which was illustrated e.g. in Fig. 3.4. Here, Fig. 3.7 (left) shows the initial situation of the charge distribution at the GaN/AlN interfaces of the QD with and without the occurrence of large piezo- and pyroelectric fields. Positive interface charges accumulate at the QD top interface, while their negative counterparts populate the QD's bottom region. As a result of the inherent electric field, the band structure is heavily altered as illustrated in Fig. 3.7 (right). In a first approximation, the conduction and valence band incline, thus reducing their effective energetic separation. Hence, the spatial separation of an electron and hole decreases their energetic spacing, an effect that can directly be witnessed in e.g. PL spectra by a strong redshift of the related luminescence in regard to the fundamental bandgap of the underlying material. Without the presence of these surface charges, the electron and hole that occupy the QD would not spatially separate (only valid in this simplistic approach) and the band structure exhibits the typical, simplified well shape in all spatial directions. Experimentally, the QCSE cannot only be witnessed by a redshift of the luminescence, but also by increased radiative lifetimes due to a reduction of the charge carrier overlap. Hence, it is only natural that the QCSE holds a most determining role for any real-world light applications, as a high photon

output usually resides in the center of interest. However, this is not necessarily the case for applications in quantum cryptography, as long excitonic lifetimes can ease the manipulation of the related quantum-states.

4 Basics of single GaN quantum dot spectroscopy

It is the purpose of this chapter to introduce the reader to some common optical signatures of single, wurtzite GaN QDs embedded in an AlN matrix. First, the ensemble spectra of the QD sample that is predominantly analyzed throughout this thesis are introduced, directly motivating the need for single QD spectroscopy by means of the μ-Photoluminescence (μ-PL) technique. Based on such an analysis of truly single QDs the identification of the inherent excitonic complexes becomes feasible. However, no experimental technique by itself allows and undoubtful identification of each individual, excitonic emission line. Hence, a number of vital experimental parameters as e.g. the excitation power, the temperature, the polarization angle, and the excitation wavelength can be varied in our setup in order to study the effect on the μ-PL spectra. Consequently, by comparing the experimental spectra with theoretical results derived from rate equations and/or multi-particle 8-band k·p calculations, one can indeed finally determine the physical origin of each emission line. In this chapter the excitation power will be varied representing the most directly accessible parameter that can be well approached by basic rate equation models. Additionally, the variation of temperature and polarization angle is discussed in Chap. 8, while the variation of the excitation wavelength remains a task for future work. Interestingly, regarding e.g. arsenide-based QDs a detailed understanding has already been achieved for the variation of all these experimental parameters. However, for wurtzite GaN QDs an emission line identification is much more challenging because QD size variations heavily alter the lateral confinement of holes and electrons. Hence, in this chapter the focus lies on a wurtzite GaN QD of constant size, which emits at $\approx 3.5\,\mathrm{eV}$ in good agreement with the maximum of the ensemble PL emission, rendering such QD common for the analyzed sample as it can most frequently be observed by μ-PL. Finally, this chapter extends the concept of basic excitation power dependent measurements towards the high excitation regime. Here it is feasible to obtain novel observations beyond the currently in the literature reported research level, as an entire zoo of multiexcitonic excitons is observed and can even extensively be probed by means of time-resolved μ-PL spectroscopy.

4.1 Ensemble spectroscopy of GaN QDs

Fig. 4.1 illustrates low-excitation ensemble spectra recorded at 6 K and 300 K for the GaN QD sample of interest, cf. Chap 2, page 16. The overall luminescence consists of several peaks belonging to the emission of GaN QD sub-ensembles of discretely varying QD height. Each peak is labelled by the number of monolayers (MLs) that constitute the overall QD height including a wetting layer thickness of 1 ML. The inset of Fig. 4.1 depicts the relation between the QD sub-ensemble emission energy and the number of contributing MLs as derived from the multi-particle calculations outlined in Chap. 3, page 21. Upon rise of temperature the ensemble spectrum broadens from $\approx$310 meV (6 K) to $\approx$440 meV (300 K), which is accompanied by a broadening of the individual sub-ensemble peaks. At a temperature of 300 K the identification of the sub-ensembles peaks related to more than 8 MLs becomes challenging as the PL signal is overlaid by LO-phonon replica of 1st and 2nd order with a distinct spacing of 95(2) meV in regard to the zero phonon line, the ensemble maximum. Interestingly, the observed LO-phonon energy resides in between the LO-phonon energies of bulk GaN [61] and AlN [67], an observation that will be clarified based on an extended μ-PL study in Chap. 6, page 74. Also the exciton-LO-phonon interaction strengths seems to be fairly strong, as it can already clearly be observed on a linear intensity scale in Fig. 4.1. However, any quantitative analysis is challenging due to the spectral overlap with the QD sub-ensemble peaks.
Also the cause of the sub-ensemble peak broadening mechanism evident in Fig. 4.1 is difficult to determine based on the presented ensemble PL spectra. Clearly, a strong contribution of acoustic phonons is expected upon rise of temperature, but the detailed effect of a coupling between excitons and phonons can only be studied in more detail based on single QD spectra as introduced in Chap. 4.2, page 40.

4.2 Spectroscopy of individual QDs under continuous wave excitation

The most common optical traces of a single, wurtzite GaN QD embedded in AlN under continuous wave (cw) excitation are shown in Fig. 4.2. The depicted scaling behavior of all emission lines with rising excitation power strongly supports their identification as expressed by the corresponding labelling. In the following this labelling is already anticipated in order to increase the accessibility of the text. At low excitation powers ($\leq 0.02\,\mathrm{kW/mm^2}$) the excitonic emission (X) dominates the spectrum along with a comparably faint contribution of an excited-state (X^*). Upon rise of excitation power the biexcitonic emission (B) becomes more dominant and even exceeds the excitonic intensity for the highest illustrated excitation power.

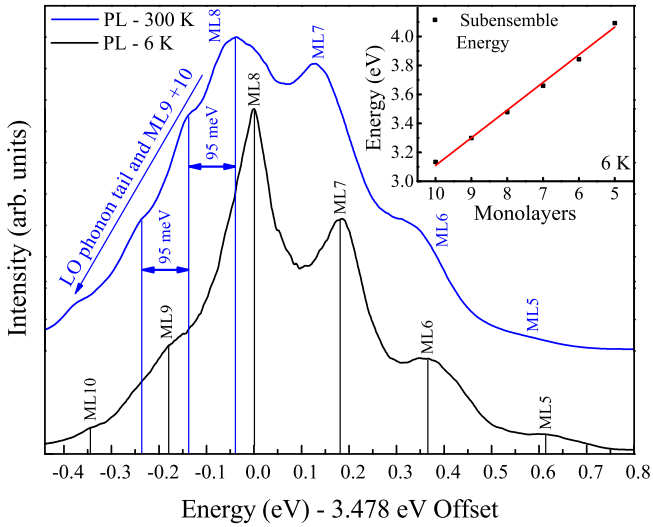

Figure 4.1: Low-excitation ensemble PL spectra of the QD sample that is predominantly analyzed throughout this thesis recorded at 6 K (black) and 300 K (blue). Individual peaks related to QD sub-ensembles of discretely varying QD heights are evident and are consequently labeled with the number of contributing monolayers (MLs). Upon rise of temperature a spectral broadening can be observed that is accompanied by the appearance of LO-phonon replica related luminescence already noticeable on the applied linear scaling.

Also phonon-assisted one-LO-phonon replica can be noticed on the Stokes-side of the X and B emissions, cf. Fig. 4.2. As shown in the inset of Fig. 4.2, this LO-phonon emission band consisting of X' and B' directly mirrors the splitting between X and B, supporting the emission line identification. Interestingly, the particular LO-phonon energy for this QD equals around 98 meV, exceeding the LO-phonon energy extracted from the ensemble spectra of Fig. 4.1 (95 meV). Such a rather minor discrepancy of 3 meV could be attributed to a particular strain state of the analyzed individual QD or could also originated from the temperature variation [88]. However, in Chap. 6 (page 74) a clear trend will be derived for this LO-phonon energy. Based on the analysis of >200 single QD spectra it can be shown that the LO-phonon energy increases with rising QD emission energy, an effect that is directly related to the particular nature of the exciton-LO-phonon coupling in such strongly polar, wurtzite GaN QDs.

In order to analyze the particular scaling behavior of all emission lines in Fig. 4.2 with rising excitation power, it is a good first approach to apply Gaussian fitting functions in order to extract the peak areas. The application of Gaussian fit functions is validated by the strong contribution of a phenomenon known as spectral diffusion [46, 89], originating the observed emission line width as treated in Chap. 5, page 62. Please note the astonishingly large inhomogenous emission line widths noticeable in

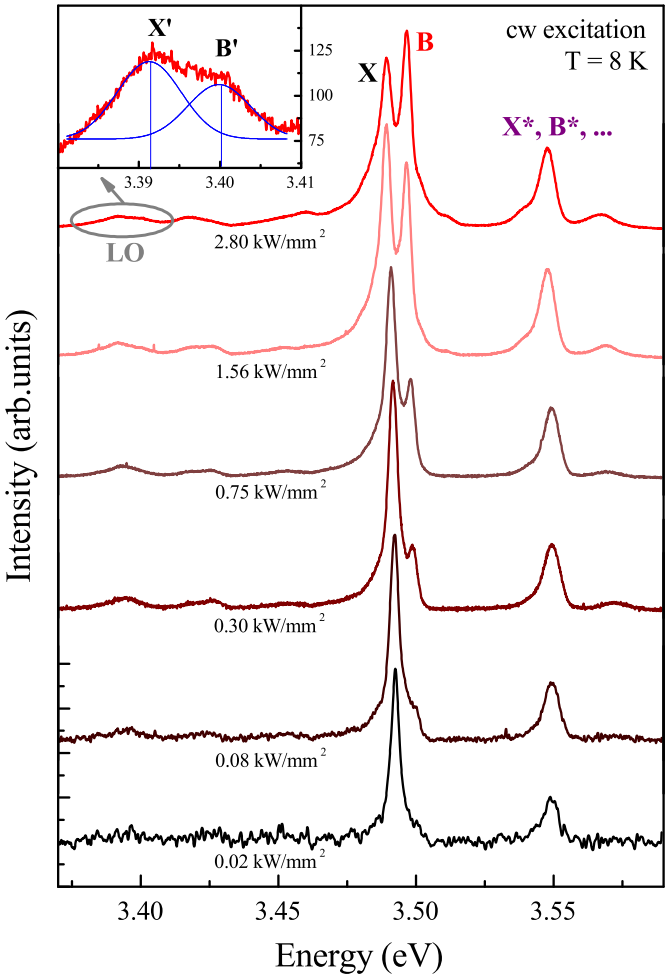

Figure 4.2: At low excitation power and cryogenic temperatures (8 K) the excitonic emission (X) of the single GaN QD emitting at around 3.5 eV dominates the μ-PL spectrum. Upon rise of excitation power an excited (X*) and the biexcitonic (B) complex become more evident along with a pronounced LO-phonon sideband. This Stokes-shifted luminescence mirrors the spectral separation of the X and B emission (inset with Gaussian fits applied to the spectrum) supporting its identification. The illustrated spectra were extracted from an excitation power variation series of over 20 μ-PL spectra, whose corresponding main peak areas are evaluated in Fig. 4.3.

Fig. 4.2, which will be discussed in more detail in Chap. 5, page 62. All extracted peak areas for X, X*, B and the LO-phonon replica of X are summarized in Fig. 4.3. The evolution of the peak area (I_n) with excitation power (P) can be described by a multiexcitonic model of a single QD as outlined in Ref. [43, 45], assuming independent, excitonic recombination probabilities. As a direct result the following fit function is obtained:

$$I_n^{cw}(P) = I_0 \cdot \left(\frac{P}{P_0}\right)^n \cdot exp\left(-\frac{P}{P_0}\right) \tag{4.1}$$

Here, I_0 and P_0 serve the normalization as fitting parameters and n expresses the number of excitonic decay channels that is assumed to scale with the exciton number. However, Eq. 4.1 is only exactly valid for $n \leq 2 \in \mathbb{N}$ as it harks back to the Poisson distribution [43]. However, from an experimental point of view it has been proven as effective to apply $n \leq 2 \in \mathbb{R}$ in Eq. 4.1 for the fitting procedure in order to reveal multiexcitonic luminescence contributions. For the particular case of X and B one has to simultaneously fit the data from Fig. 4.3 with shared fit parameters

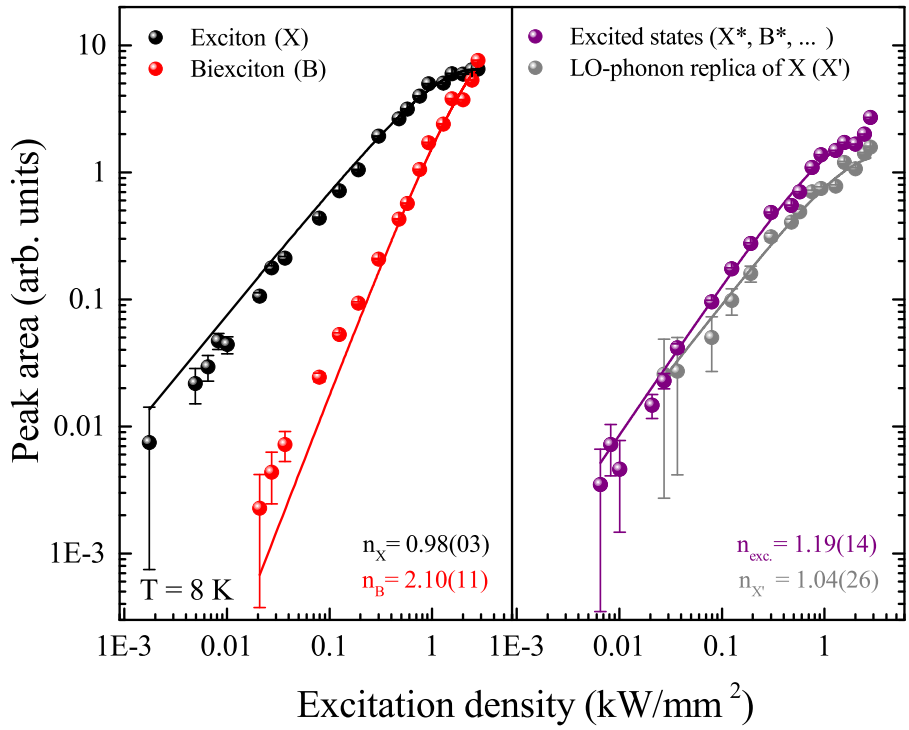

Figure 4.3: Varying the excitation power over more than 3 orders of magnitude reveals deviating scaling behaviors for the emission lines introduced by Fig. 4.2. The plotted peak areas were extracted from a Gaussian fitting routine. The depicted solid lines represent the results of a fitting procedure based on a basic rate equation model [43, 45]. As a result, the number of excitonic decay channels n is extracted for the complexes X', X, B, and X* supporting their identification. Numbers in parentheses indicate the error.

as long as no significantly deviating loss mechanisms are assumed for both excitonic complexes [40]. As a result, $n_X^{cw} = 0.98(03)$ and $n_B^{cw} = 2.10(11)$ are obtained in good agreement with the expected theoretical values of 1 and 2 for the exciton and the biexciton in the underlying model (further fit parameters: $I_0 = 17.51(50)$, $P_0 = 2.63(10)$ kW/mm^2). Hence, at an excitation power of $\approx 2.6\,$kW/mm^2 an average exciton occupation number of $\mu = 1$ is reached marking the fits intersection point in Fig. 4.3 (left) as further described in Ref. [43, 45]. The scaling behavior for X* and X' were analyzed by separate fitting functions yielding $n_{X*}^{cw} = 1.19(14)$ and $n_{X'}^{cw} = 1.04(26)$ as shown in Fig. 4.3 (right). The scaling parameters n for X and X' are equal within the errors, which further supports the identification of X' as the one-LO-phonon replica of X. The generation of phonons involved in the emission process of X' is clearly not hindered due to their bosonic nature. However, it should be noted for the inset of Fig. 4.2 that even though the B intensity has already surpassed the X intensity at an excitation power of $2.90\,$kW/mm^2 this is not yet the case for the phonon replica B' regarding X'. This observation presents a strong moti-

vation for future work analyzing the coupling between extended excitonic complexes and LO-phonons in order to understand the underlying selectivity. The transition X^* seems to surpass the scaling behavior of X suggesting underlying luminescence contributions of e.g. multiexcitons. However, in order to study such higher order multiexcitons that can even emit at several spectral positions [90], the excitation power must be increased without damaging the sample. This task can readily be achieved by a pulsed ps-laser that delivers high excitation powers within the pulse duration and a sufficient time frame in between the pulses in order to achieve a heat distribution across the sample, thus lowering the chances for any laser-induced damage.

4.3 Spectroscopy of individual QDs under pulsed excitation

Under cw excitation the damage threshold for the analyzed wurtzite GaN QDs is reached as soon as excitation powers approaches the low kW/mm^2 range. Hence, all cw μ-PL spectra previously introduced in Fig. 4.2 are still reproducible, while the application of higher cw excitation powers permanently alters the μ-PL spectra mainly regarding overall signal loss. It can be expected that the conducted mesa-structuring limits the achievable cw excitation powers as the heat transport is lowered by etching away most of the QDs' surrounding material. Also the structuring process itself introduces a rougher and therefore larger surface area that provokes additional absorption and potential luminescence channels in the matrix material (AlN), even if the excitation occurs below its bandgap as it is the common case in this thesis. Hence, any high excitation effects as, e.g., higher order excitonic complexes remain mostly obscured under cw excitation conditions.

Here, the application of a pulsed laser systems providing long ps pulses (55 ps) and a sufficiently high repetition rate (76 MHz) constitutes a blessing. Not only that higher peak excitation powers can be reached, also time-resolved measurements become feasible. In the following it is demonstrated how excitation powers of up to almost the MW/mm^2 range can be approached without any sample damage to occur. At the same time an entire zoo of multiexcitonic particles is discovered, allowing a precise determination of all the occurring time constants due to the application of a pulsed laser and suitable detectors, cf. Chap. 2, page 16.

Fig. 4.4 depicts a direct comparison of the μ-PL spectra that are recorded under low and high excitation based on a cw or a pulsed laser enabling quasi-resonant excitation below the AlN bandgap in the QDs wetting layer states. At low cw excitation powers only the excitonic (X) emission is noticeable that gets accompanied by the biexcitonic (B) emission as soon as the excitation power rises. However, already in this high power, cw μ-PL spectrum additional optical traces at the high energy side of B

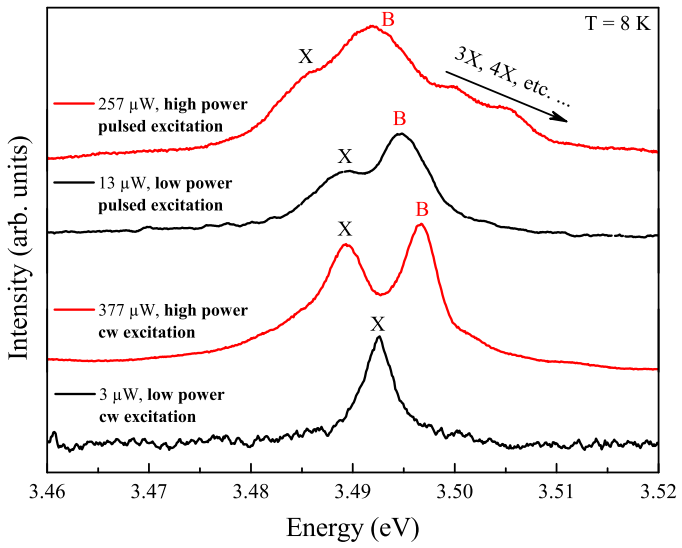

Figure 4.4: Comparison of low and high power continuous wave (cw) and pulsed excitation of the same QD previously introduced in Fig. 4.2. Here, cw and quasi-cw excitation power values are stated for the sake of straightforward accessibility for spectroscopists. At the highest cw excitation level, the biexciton (B) has just surpassed the exciton (X) regarding its intensity, a situation that cannot even be reversed in the spectrum of lowest pulsed excitation power (55 ps pulse widths, 76 MHz repetition rate) with an integration time of 1200 s. Upon further rise of excitation power additional peaks of a multiexcitonic origin (e.g. 3X, 4X) appear. Please see the text for further details.

start to appear. If the identical QD is now excited with a pulsed laser system, two emission lines, namely X and B, are already present at the lowest experimentally accessible excitation power. Please note that the corresponding low power μ-PL spectrum for the case of pulsed excitation exhibits an integration time of already 1200 s! The quasi-cw excitation powers stated in Fig. 4.4 are supposed to facilitate an improved accessibility for any reader with a spectroscopic background and can easily be translated into the corresponding excitation densities based on Fig. 4.2 and the following Fig. 4.5. The under high, cw excitation hardly noticeable features in the high energy flank of B become directly noticeable if the high, pulsed excitation regime is approached, cf. Fig. 4.4. In the following exactly these luminescence traces will be attributed to multiexcitonic emissions, like e.g. tri-excitons (3X), quart-excitons (4X), and complexes of even higher order.

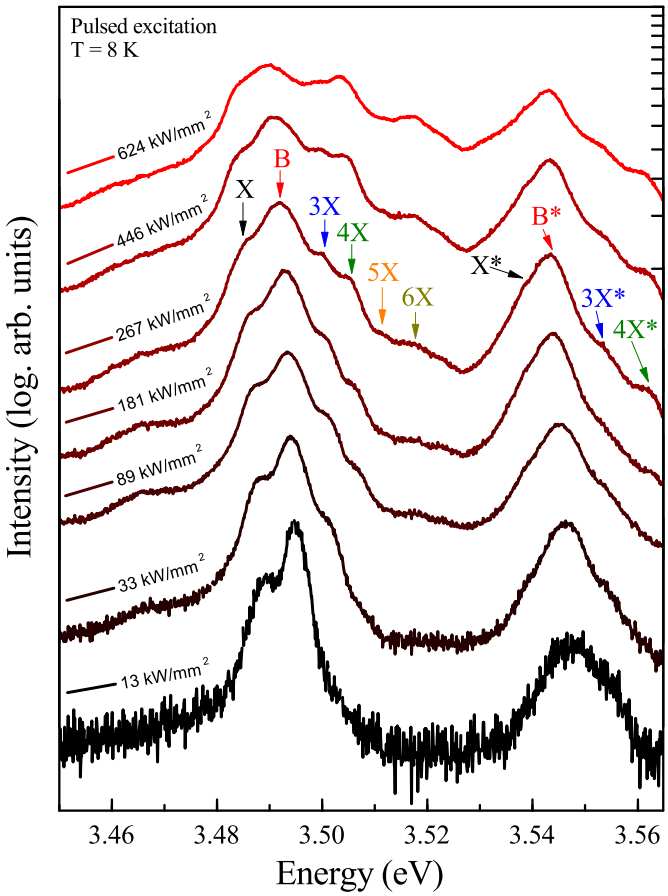

Figure 4.5: Excitation power series of the same QD previously introduced in Fig. 4.2 and 4.4 under pulsed excitation. Upon rise of excitation power various multiexcitonic emissions appear in addition to the exciton (X) and the biexciton (B), such as the tri- (3X), quart- (4X), quint- (5X), and sext-exciton (6X). Approximately 53 meV higher in energy a similar peak pattern appears, which can be attributed to the corresponding excited-states (*). The μ-PL spectrum for an excitation power of 267 kW/mm^2 equals the high excitation spectrum shown in Fig. 4.4.

4.3.1 Generation of multiexcitons under high excitation

Selected μ-PL spectra of the pulsed excitation power series are shown in Fig. 4.5. At the lowest depicted excitation power the B transition is noticeable, which has already surpassed the intensity of X. In addition, similar to the observation for Fig. 4.2, an excited-state luminescence band at around 3.55 eV is noticeable. Upon rise of excitation power, the peak maxima ratio of X and B remains constant, while additional peaks appear in the high energy flank of the B emission. These peaks are tentatively labeled following their order with 3X - 6X towards higher energies. Interestingly, the entire set of these peaks gains in intensity if compared to X and B upon rise of excitation power, already presenting a strong motivation for a multiexcitonic origin. Most intriguingly, a similar peak pattern can be observed in the emission band at around 3.55 eV, just always at comparably higher excitation powers. Here, the overlapping individual underlying peaks are labeled with X*, B*, 3X*, and 4X* referring to their potential excited-state (*) origin.

Based on an energy splitting of 53 meV between X and X*, not only an individual excited hole can contribute to the emission of X*. Single-particle calculations by Winkelnkemper et al. [91] predict a hole level spacing for wurtzite GaN QDs

embedded in AlN of ≈ 10 meV for the presented emission range, in agreement with the common A-B valence band splitting of GaN [62, 92, 93]. Please note that this splitting corresponds to the spacing between S - A (VB) and S - B (VB) depicted in the later on introduced level schemes in Fig. 4.10, page 56. Consequently, it is feasible to assume that at least one excited electron contributes to the emission of X*. Based on calculations, the first excited electronic state resides ≈ 130 meV above the corresponding ground-state at an emission energy of around 3.5 eV for a QD aspect ratio of 0.2 [91]. This value decreases to ≈ 25 meV [91] as soon as the QD aspect ratio is lowered towards 0.1, while keeping the emission energy constant. Hence, the measured value of 53 meV for the splitting between X and X* indeed points towards the participation of at least one excited electron, originating from the $P_{x,y}$ state, cf. Fig. 4.10. Conclusively, it can be derived that the particular QD from Fig. 4.5 exhibits an aspect ratio in between 0.1 and 0.2. This observation is in good agreement with the conclusions presented in Chap. 8, page 118, as also the energetic splitting between X and B of -7.1(2) meV, known as the biexciton binding energy E^B_{bind}, is common for the derived aspect ratio interval. Additionally, this aspect ratio interval can directly be confirmed by various microscopic techniques as outlined in Ref. [45] and Chap. 6.4, page 86.

In order to determine these binding energies E_{bind} for all the observed excitonic complexes, i.e. their energetic spacings in regard to X, a careful peak fitting based on Gaussian (see Chap. 5, page 62) fit functions must be undertaken. At a medium excitation power of 267 kW/mm^2 all transitions are well noticeable and allow a tentative fitting as shown in Fig. 4.6, which, however is increasingly hindered at higher excitation powers due to an increased emission line widths broadening. Fig. 4.6 shows an energy scale relativ to the X emission energy of 3.4849 eV in order to allow a direct reading of the complexes' binding energies. Table 4.1 on page 58 summarizes all resulting absolute and relative peak energies exhibiting their uncertainty in the last digit shown.

However, already the fitting of the μ-PL spectrum shown in Fig. 4.6, which exhibits the most pronounced peak signatures, represents a challenging task. As introduced in Chap. 5, page 62, a clear trend should be noticeable regarding the individual emission line widths that scale with the relative dipole moment ratios of the excitonic complexes. Hence, at a first glance, higher excitonic complexes should exhibit more narrow emission lines, a condition that can already not be satisfied by the fitting routine shown in Fig. 4.6. The fit is clearly over-parametrized but still represents the only feasible approach in order to extract the emission line positions. As a result, a peak area determination for all excitation power steps is hindered as no fitting routine can be established that simultaneously fits the entire series of μ-PL spectra with a consistent set of parameters and corresponding trends. Hence,

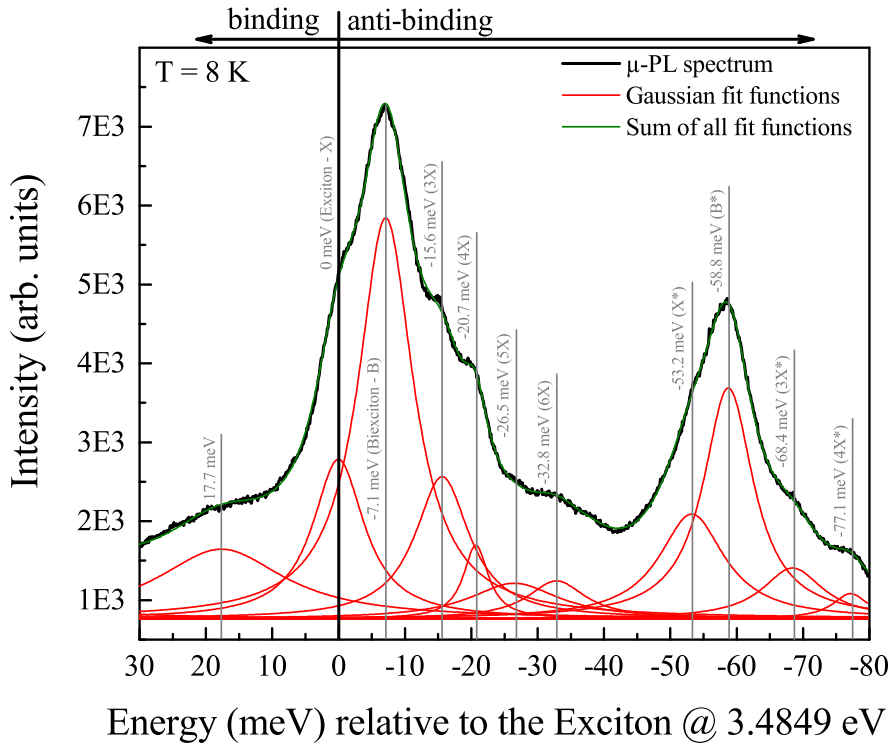

Figure 4.6: Assignment of all excitonic emission noticeable in Fig. 4.5 at an excitation power of 267 kW/mm^2. The μ-PL spectrum is plotted relative to the exciton emission energy of 3.4849 eV in order to display differential energies, known as the "binding" energies of the corresponding complexes. All assigned transitions appear on the high energy side of X and thus represent anti-binding complexes. A fit by Gaussian fit functions (individual: red, sum: green) yielding the emission energies represents a challenging task because all emission lines are broadened by spectral diffusion and hence overlap.

it is necessary to recede to a manual peak height determination in order to still compare the deviating scaling behavior of the multiexciton-related intensities with rising excitation power. Naturally, such a basic comparison of the scaling behavior regarding peak maxima is of interest, as it represents a well established indicator that can finally lead to a solid emission line identification if further indicators as e.g. radiative lifetimes are considered. The peak situated at 17.7 meV in Fig. 4.6 cannot be assigned to a multiexcitonic complex, but it could arise from the coupling of excitons and acoustic phonons [68].

Fig. 4.7 displays the peak maxima of the excitonic complexes introduced in Fig. 4.5 over rising excitation density (pulsed). Both, X and B exhibit within the error identical scaling factors ($n_X^{pulsed} \approx n_B^{pulsed}$), meaning that these two excitonic complexes have reached saturation as feasible for the case of pulsed excitation [43]. As soon as the order of the excitonic complexes is further increased, the corresponding scaling factor n rises along with the number of participating excitonic decay channels.

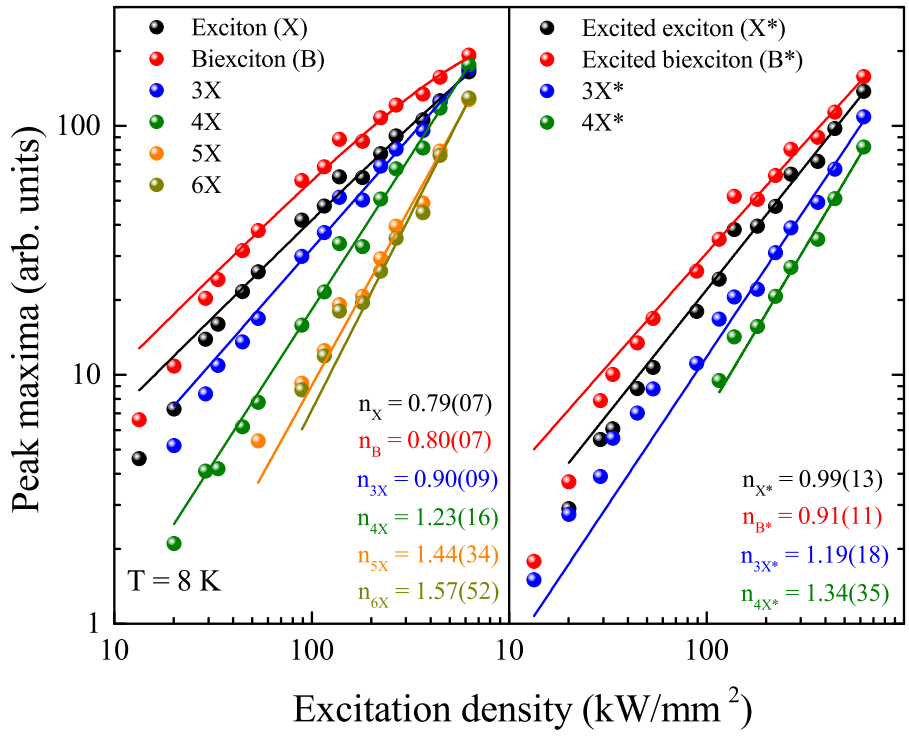

Figure 4.7: Varying the excitation power by almost 2 orders of magnitude under pulsed excitation conditions reveals deviating scaling behaviors for the emission lines indicated in Fig. 4.5. It proofs necessary to recede to a peak maxima determination, as a peak area determination is hindered by strong emission line overlap, cf. Fig. 4.6. The depicted solid lines represent the outcome of a fitting procedure based on a basic rate equation model [43, 45]. As a result, the particular scaling behavior of all excitonic complexes (X - 6X ground-state excitons / X* - 4X* excited-state excitons) is extracted and expressed by n, supporting their identification. Numbers in parentheses indicate the error.

Please see Tab. 4.1 on page 58 for a compilation of all n values related to pulsed excitation, which were extracted from the fits shown in Fig. 4.7. Here, Tab. 4.1 also lists the scaling factors of the excited multiexcitons originating from an identical fitting procedure. Generally, a multiexcitonic state is generated upon pulsed excitation, which subsequently decays in a cascade process, while emitting one photon per intermediated multiexcitonic state until the ground-state (empty QD) is reached. The evolution of the associated intensity (I_n) with pulsed excitation power (P) can also be described by a basic and most commonly applied multiexcitonic model, as introduced in Ref. [43]. Again, if independent recombination probabilities are assumed, the following Eq. 4.2 holds:

$$I_n^{pulsed}(P) = I_0 \cdot \left(1 - \frac{\Gamma(n, P/P_0)}{\Gamma(n)}\right) \tag{4.2}$$

However, for the above given reasons, I_n is now not based on peak areas anymore, but on less error-prone peak maxima. Here, $\Gamma(n, P/P_0)$ and $\Gamma(n)$ denote the incomplete and complete gamma functions, while I_0 and P_0 are fitting parameters similar to the cw case described by Eq. 4.1. Not only that the sole determination of the scaling parameters n for the case of pulsed excitation is far from sufficient for an identification of the excitonic transitions, also the related error is significant, cf. Fig. 4.7. Hence, time-resolved measurements that come along with the overall benefits of a pulsed excitation source can be utilized in order to approach a more solid identification of the multiexcitons observed in the recorded μ-PL spectra.

4.4 Time-resolved analysis of multiexcitons

Fig. 4.8 introduces the time-resolved optical response of the ground-state multiexcitons originating from the identical QD previously analyzed in Sec. 4.2 and 4.3 that emits at an energy of around 3.5 eV. All decays can be fitted by a biexponential model based on a convoluted fitting routine [47] that accounts for the instruments response function with a temporal FWHM of ≈ 55 ps. Generally, within the experimental limits no rise-time can be extracted from any of the transients shown in this Sec. 4.4, meaning that the rise is always as fast as inflicted by the system response function. Hence, the initial fill process of the QDs should take place on a sub- to few-ps timescale [94, 95] and must at least be faster than the rise-time of the system response function (laser transient) with 40(13) ps. The accessible upper limit for the rise-time can even further be reduced by deconvolution techniques [47] down to ≈ 5 ps. After this fast QD excitation the inherent excitonic complexes start to decay. All transients shown in Fig. 4.8 have a rapid decay component in common, whose associated decay times τ_{rel} exhibit quite a particular, discontinuous evolution with rising number of excitonic decay channels (X - 6X). Finally it will exactly be this observation that provides strong support for the entire emission line identification. After this initial rapid decay, a significantly longer decay dominates the transients, with the corresponding τ_{rad} scaling from 7.73 ns for X, over 4.36 ns for B, down to e.g. even 1.97 ns for 6X as summarized in Tab. 4.1. Please note that the errors stated in Tab. 4.1 only describe fitting errors but do not account for any effects that arise from the prominent peak overlay shown in Fig. 4.6, which could only be further addressed by an overall improved sample quality.

Such an excitonic decay time in the ns regime at an emission energy of around 3.5 eV is indeed common for the analyzed type of wurtzite GaN QDs embedded in AlN. For a similar emission energy, Kako et al. report a radiative decay time of 8.5 ns for a single wurtzite GaN QD [32], while the average radiative decay time obtained from an ensemble of QDs emitting at ≈ 3.5 eV scales in between 3 - 5 ns

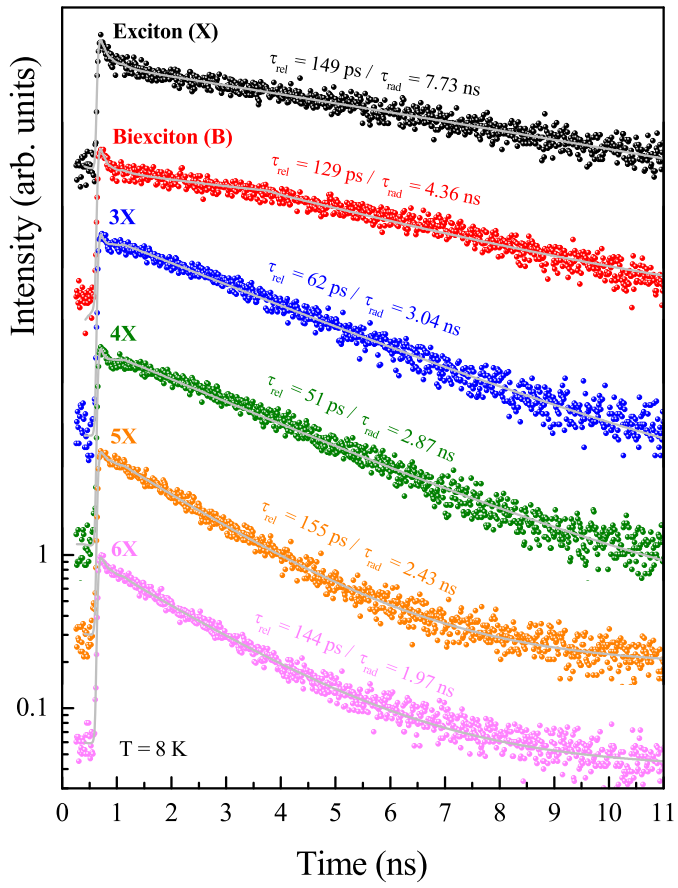

Figure 4.8: Time-resolved analysis of the ground-state excitonic emissions from Fig. 4.5. All transients can be approximated by a fit based on a biexponential decay (solid, grey line). Following a time-resolution limited rise [40(13) ps], first, all complexes predominantly decay with rates that correspond to the individual time constants τ_{rel}. In the following the decay is dominated by individual radiative lifetimes τ_{rad}. Upon rise of contributing exciton number, the number of radiative decay channels increases as expressed by a reduction of τ_{rad}, while τ_{rel} exhibits a more complex scaling behavior. Please see the text for further details

[27]. Similar ensemble TRPL measurements were performed by the author of this thesis (not shown), yielding a good agreement with these already published values that strongly scale with the QD height [27] due to the quantum-confined Stark effect. Hence, the longer time constant τ_{rad} indeed corresponds to the radiative decay time of the individual GaN QD analyzed in Fig. 4.8.

The second time constants τ_{rel}, however, corresponds to the intra-QD carrier relaxation time as described by Mukai and Sugawara for the case of individual InGaAs/GaAs QDs [96]. A theoretical description of the related mostly biexponential decays constitutes a radiative decay and an intra-QD relaxation component that can be described by the random initial occupation (RIO) approach. In Sec. 4.4.2 the basic assumptions of this model will be outlined based on Ref. [96]. As a result, not only the initial fast decay will be motivated, but also the particular evolution of τ_{rel} and τ_{rad} with rising decay channel number (see Fig. 4.8) becomes plausible.

After the excitation by a laser pulse, a nanostructure like a QD is usually *rapidly* populated with carriers, as expressed by a capture time τ_{cap} (not accessible with the experimental setup available) and approved by the measured rise-time limitation ($\rightarrow \tau_{cap} < 5\,\text{ps}$). As a result, random electronic levels of the QD are initially

filled with carriers (fast), rendering a complex multiexcitonic population a common starting point for the following intra-QD relaxation (slower) and the final radiative recombination processes (slowest) that consequently empty the QD. Please note that this classification in three different process velocities is naturally not always valid and strongly varies, among other things, with the excitation conditions, the temperature, and the particular QD material. Generally, the basic assumption of a random initial occupation is always valid as soon as the optically excited carrier density is sufficiently high. As a result, the initial fast occupation of the QDs with carriers, as expressed by τ_{cap}, is no longer predominantly governed by electron-phonon interaction, but by Auger relaxation [95]. Exactly these two basic relaxation mechanisms are discussed in the following Sec. 4.4.1 because they establish the basis for the entire RIO model subsequently described in Sec. 4.4.2.

4.4.1 Relaxation mechanisms - towards an initial occupation

Generally, in a first approximation it is important to distinguish between two groups of carrier relaxation processes, leading to the initial carrier population in the QD forming, e.g., a multiexcitonic excitation in its excited-state. The first group of relaxation processes characterized by τ_{cap} must be very efficient, as the large energy gaps (several hundreds of meV) between the electronic matrix material states (or wetting layer states depending on the excitation conditions) and the bound-QD states can rapidly be overcome as approved by the lack of any, within the experimental limits measurable, rise-time ($< 5\,\mathrm{ps}$), cf. Fig. 4.8. After these initial charge carrier capture processes have occurred, various *excited* multiexcitonic states are created inside of the QDs, which can now further relax towards their multiexcitonic ground-states with an average rate inverse to τ_{rel}. The main difference between these two relaxation groups now is that the initial population of the QDs occurs, while a large carrier concentration is present. This large carrier concentration is directly evoked by the high excitation level achieved by a laser pulse approaching the $\mathrm{GW/mm^2}$ regime. As the high carrier concentration rapidly decays after the optical excitation, the following relaxation processes of the multiexcitonic states in the QDs occur, while a significantly lower number of free carriers is present. It is exactly this optically induced free carrier concentration that dominates the final dynamics leading to $\tau_{cap} < \tau_{rel}$.

As long as a large free carrier concentration is present, the carrier relaxation is predominantly governed by Auger processes (electron-electron scattering) and electron-phonon scattering acts as a minor contribution [94, 95]. Hence, an initial charge carrier occupation is established within a time frame described by τ_{cap}. However, as soon as the free carrier concentration diminishes after the initial excitation, the electron-phonon scattering becomes the most prominent but less efficient relaxation

mechanism. This is directly confirmed by the experiment because τ_{rel} enters the tens to hundreds of ps regime [97] in contrast to τ_{cap}, cf. Tab. 4.1. Hence, the well-established phonon-bottleneck effect [95,98,99] does not exhibit a dominant effect on τ_{cap}, but rather affects the relaxation time τ_{rel} describing the intra-QD relaxation. Similar observations have been reported by numerous research groups for the case of In(Ga)As/GaAs QDs [98, 100, 101], but no data has so far ever been reported for the case of wurtzite GaN QDs. Generally, the energetic level spacings inside of wurtzite GaN QDs embedded in AlN (compare Sec. 4.3.1) are large in comparison to the native acoustical and optical phonon energies [88], similar to the case of the carrier relaxation from the matrix material states into the QD states. Single phonon processes are by far not sufficient in order to surmount these energy gaps. Hence, only multi-phonon processes can still contribute in order to facilitate a relaxation of the initially predominantly excited multiexcitonic states [102]. In this sense both, the intra-QD relaxation *and* the initial carrier capture process suffer from the well-known phonon bottleneck effect. The Auger relaxation, however, overcompensates this effect for the initial carrier capture and causes the observation of rather fast rise-times [103, 104]. The unique balance between phonon- and electron-induced relaxation (electronic muliti-phonon relaxation vs. Auger relaxation) is directly altered by the number of free carriers, which tunes the corresponding relaxation times from the sub- to few-ps regime (τ_{cap}) towards the tens to hundreds of ps (τ_{rel}) range. It is only natural to assume that a multitude of individual relaxation times yield the finally by μ-TRPL accessible values, even for the case of single QD spectroscopy. However, the individual time components cannot be resolved, rendering any in the following reported τ_{rel} values averaged numbers.

4.4.2 The random initial occupation model

Following the fast relaxation of the carriers into the QD (capture process) an excitonic occupation is established, constituting a random number of charge carriers that randomly occupy the QD's energy levels. In order to simplify the entire problem of a subsequent, multiexcitonic decay, only a simple two-level system is assumed, which features a ground and an excited-state as shown in the scheme of Fig. 4.9. Following this scheme, the corresponding rate equations can be derived [96], which describe the time evolution of all total carrier numbers ($N_{AA}(t)$, $N_{AB}(t)$, $N_{ABC}(t)$, etc.). It represents a strong simplification to assume that all relaxation and radiative decay channels shown in Fig. 4.9 exhibit the same rates as expressed by the inverse of τ_{rel} and τ_{rad}. However, based on this reduction only two averaged rates, namely the relaxation and the radiative recombination rate, finally dominated the measurable decay.

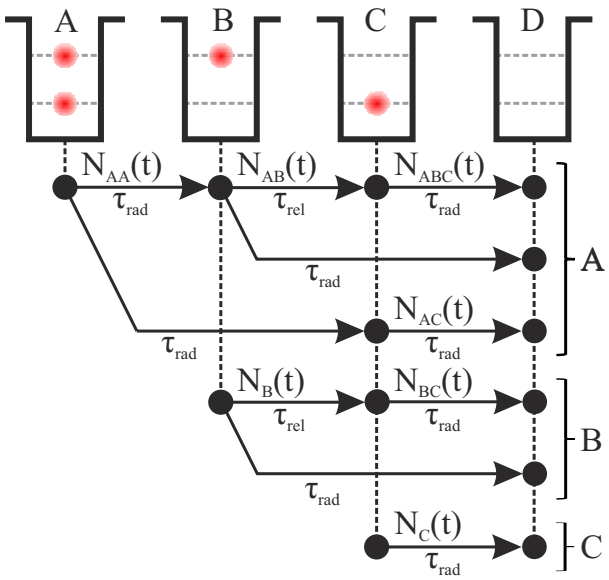

Figure 4.9: Fundamental scheme of the random initial occupation model (RIO) as described by Mukai and Sugawara [96], assuming independent excitonic recombinations. The illustration depicts all four initial occupation possibilities (A - D) in a two-level scheme in addition to the related relaxation and radiative recombination paths. All corresponding total carrier numbers are denoted with N, while the relaxation and radiative recombination times are described by τ_{rel} and τ_{rad}, already constituting a drastic simplification for modeling a multiexcitonic decay.

The total number of carriers in the excited-state is described by

$$N_{exc}(t) = N_A(t) + N_B(t), \tag{4.3}$$

with

$$N_B(t) = N_{B,0}(t)e^{-\left(\frac{1}{\tau_{rel}}+\frac{1}{\tau_{rad}}\right)t} \tag{4.4}$$

and $N_A(t) = N_{AA}(t) + N_{AB}(t)$. An in detail analysis of the rate equations yields

$$N_{AA}(t) = N_{A,0}e^{-\frac{2t}{\tau_{rad}}} \tag{4.5}$$

and

$$N_{AB}(t) = e^{-\left(\frac{1}{\tau_{rel}}+\frac{1}{\tau_{rad}}\right)t}\int_0^t \frac{N_{AA}(s)}{\tau_{rad}}e^{\left(\frac{1}{\tau_{rel}}+\frac{1}{\tau_{rad}}\right)s}ds \tag{4.6}$$

with the parametrization s. The total number of ground-state carriers is then denoted by

$$N_{GS}(t) = N_{ABC}(t) + N_{AC}(t) + N_{BC}(t) + N_C(t), \tag{4.7}$$

while the individual expressions for the participating summands can be found in Ref. [96]. However, if one assumes $\tau_{rel} \ll \tau_{rad}$ than the first three carrier numbers from Eq. 4.7 can be neglected, yielding a decay time of τ_{rad} for the ground-state, while the excited-state decays with $\tau_{rad}/2$. However, as soon as τ_{rel} cannot be neglected anymore as confirmed by the experiment, more complicated decay trends are observable, which can be approximated by the biexponential fit functions deployed in Fig. 4.8. Hence, even for the excitonic emission of a single QD a biexponential decay behavior is observed if τ_{rel} is sufficiently large in comparison to τ_{rad}. Even though Fig. 4.9 represents a strong simplification regarding the overall exciton picture, the herein depicted decay channels B facilitate a straightforward understanding of the biexponential decay. An excitonic luminescence is not only simply fed by its initial purely, excitonic population (see C, occupied ground-state), but is also supported by phonon-limited relaxation processes from the excited-state(s). However, in a multi-excitonic picture this entire matter becomes a highly complex issue. Not only that various individual radiative rates occur, also the relaxation rates towards the various electronic levels will strongly vary. Generally, the feature-rich phonon density of polar modes [88], which exhibit a strong coupling to excitons in individual, wurtzite GaN QDs (compare Chap. 6, page 74), allows the prediction of particular resonances regarding τ_{rel}. However, a precise identification of these resonances will be challenging as not only the individual QD size, but also the order of the excitonic complexes indirectly tunes the energetic spacings in regard to the phonon energies via the various occupied electronic levels. Furthermore, Nakayama and Arakawa [105] predict a margin of a few tens of meV for the corresponding energy conservation due to the time-energy uncertainty, which will broaden any observable resonances, clearly hindering a more detailed identification by experiments. Nevertheless, it is most valuable to sketch the measured excitonic complexes in a simple single-particle picture (strong simplification). In the following it is this simplification that facilitates an analysis of the evolution of τ_{rad} and τ_{rel} with rising number of electron-hole pairs.

4.4.3 Radiative recombination and relaxation of multiexcitons

Fig. 4.10a shows the occupation probability densities of electrons and holes in their ground- and excited-states (single-particle states) inherent to a wurtzite GaN QD. In contrast to Fig. 3.4, page 31, this illustration represents a top view, nicely illustrating the S- or P-type character of the corresponding wavefunctions. Generally, the carrier overlap is reduced by the quantum-confined Stark effect for the ground- and the excited electron and hole states. However, a non-negligible charge carrier overlap even exists for excited-states as derived from calculations (not shown), while the ground-state transitions always exhibit the highest decay possibilities. However, despite their reduced charge carrier overlap, excited-state transitions can experimen-

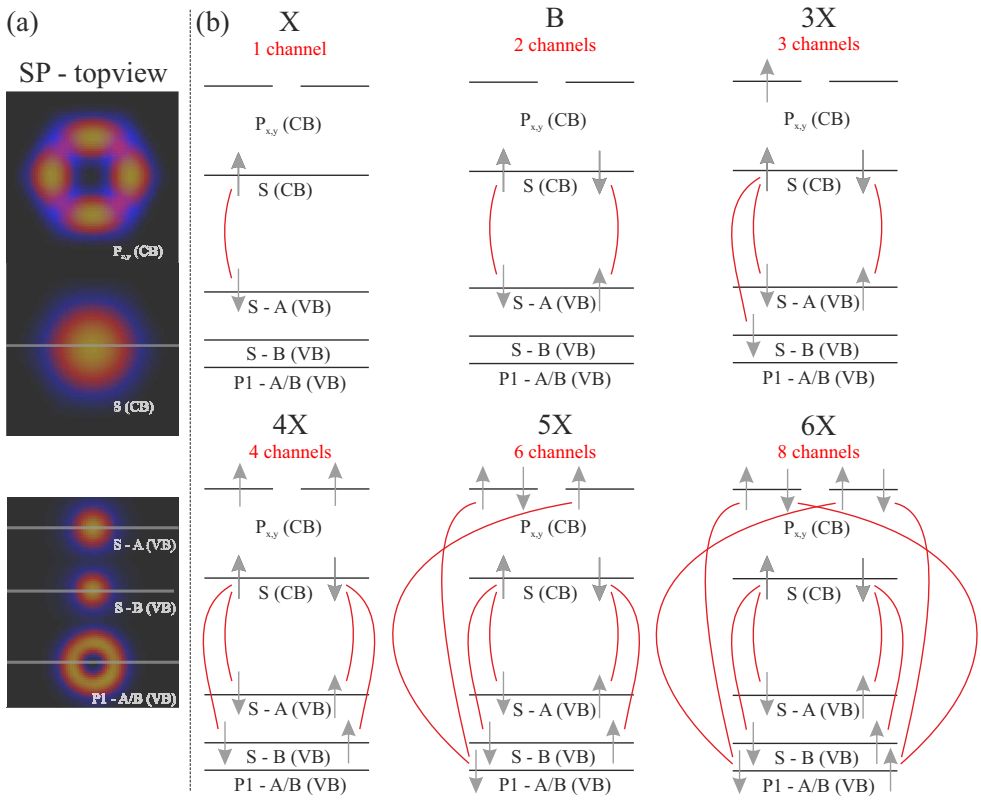

Figure 4.10: (a) Simplified level schemes (not to scale) for a wurtzite GaN quantum dot embedded in AlN overlaid by color-coded single-particle (SP) occupation probability densities. The conduction band (CB) contributes three energy levels with predominant S or $P_{x,y}$ character for the electrons, while the holes occupy three states with predominant S or P1 character with contributions from either the A or the B valence band (VB) of GaN, or both (A/B). (b) Upon occupation with electron-hole pairs various decay channels with deviating decay possibilities contribute to the overall emission. Please see the text for further details.

tally be observed in basic μ-PL spectra as introduced in Fig. 4.6, page 48. Naturally, it is highly desirable to obtain theoretical predictions for the energetic spacings in between the multitude of emission lines show in this Fig. 4.6. However, any detailed calculations beyond single-particle states (see Fig. 4.10a), as described in Sec. 3.2.3, page 31, are an extremely challenging task. Already the inclusion of a second exciton represents the limit for the applied calculations discussed in Chap. 8, page 118. Hence, the modeling of higher excitonic complexes (e.g. 3X, etc.) is hindered in the present, extended GaN QD structures, because the corresponding iteration loops of the calculations lack a sufficient convergence, even on extremely potent multi-core equipment (status of early 2015). Generally, the theoretical treatment of multi-excitonic states is feasible to a certain degree [90, 106], but most calculations are only performed for extremely small structures in strong contrast to the experimental results, cf. Chap. 2, page 16. Hence, it is necessary to recede towards basic

level schemes of multiexcitons [107] as shown in Fig. 4.10b in order to gain insight into the particular scaling behavior of τ_{rad} and τ_{rel} with rising exciton number as summarized in Tab. 4.1, page 58.

Fig. 4.10b illustrates the level schemes for X, B, 3X, 4X, 5X, and 6X. The complexes X and B still emit at only one discrete energy, but 3X is the first complex that predominantly emits at two energy positions, similar to 4X, as long as any fine structure splitting is still neglected [37]. The red lines depicted in Fig. 4.10b always illustrate the most pronounced transitions based on a careful analysis of the corresponding transition dipole matrix elements (not shown). Generally, the excitonic complexes 3X and 4X already have a populated $P_{x,y}$(CB) state but corresponding transition probabilities are low as only holes with S-like symmetry are available. Hence, the number of decay channels is not additionally increased by $P_{x,y}$(CB) electrons for 3X and 4X as depicted in Fig. 4.10b. Nevertheless, 3X and 4X are the first complexes that constitute holes from an S-like state that originates from the B valence band of GaN. The first more significant contribution that arises from the excited electron states [$P_{x,y}$(CB)] occurs for the 5X and 6X complex. Here, a P1-like hole state gets populated exhibiting a mixed (A/B) character that increases the transition dipole matrix elements in regard to electrons occupying the $P_{x,y}$(CB) level. As a result, the number of predominantly contributing decay channels starts to rise in a non-linear fashion if compared to the number of excitons involved. Naturally, the radiative decay rate is enhanced with rising decay channel number as expressed by a lowering of τ_{rad} with rising exciton number, cf. Tab. 4.1. For the case of X and B, the corresponding τ_{rad} values approach a ratio of 2:1 [7.73(28) ns vs. 4.36(09) ns], which is almost *ideal* in the sense of contributing decay channels. However, this ratio is also inflicted by the particular spin dynamics of the excitonic complexes with focus on the excitonic dark states [108–110]. Hence, τ_{rad} approximately scales with the number of excitonic decay channels for these two complexes X and B. However, this relation is lifted for higher excitonic complexes, mainly due to the reduced charge carrier overlap introduced by the excited-states. Nevertheless, τ_{rad} continuously diminishes from X $\rightarrow$ 6X but is also clearly affected by the emission line overlap observed in Fig. 4.6. Most intriguingly this continuous decrease is not observed for the case of τ_{rel}. Tab. 4.1 summarizes the τ_{rad} and τ_{rel} values for all analyzed multiexcitonic complexes along with the corresponding scaling factors n and the complex binding energies.

However, regarding τ_{rel} an astonishing and very suggestive agreement can be found by comparing Fig. 4.10b with the corresponding τ_{rel} column from Tab. 4.1. First, for the case of X and B, τ_{rel} marginally diminishes from 149(31) ps to 129(31) ps, simply meaning that an increased carrier number naturally introduces more relaxation channels. However, as soon as a new electronic level is occupied for 3X and

Table 4.1: Set of essential parameters derived from the excitation power dependent and time-resolved μ-PL measurements for various multiexcitonic complexes from the exciton (X), over the biexciton (B), up to the sext-exciton (6X). The corresponding excited-state transitions are labeled with an asterisk (*). The assignment column is supposed to evaluate the reliability of the peak attribution based on the experimental evidence. If no error is stated in parentheses then the uncertainty resides in the last significant digit. Please see the text for further details.

Label:	Energy: (eV)	E_{bind}: (meV)	n^{cw}:	n^{pulsed}:	τ_{rel}: (ps)	τ_{rad}: (ns)	Assign.
X	3.4849	-	0.98 (03)	0.79(07)	149(31)	7.73(28)	++
B	3.4920	-7.1	2.10(11)	0.80(07)	129(31)	4.36(09)	++
3X	3.5005	-15.6	-	0.90(09)	62(30)	3.04(05)	+
4X	3.5056	-20.7	-	1.23(16)	51(27)	2.87(05)	+
5X	3.5114	-26.5	-	1.44(34)	155(17)	2.43(11)	0
6X	3.5177	-32.8	-	1.57(52)	144(38)	1.97(04)	0
X*	3.5381	-53.2	1.19(14)†	0.99(13)	473(63)	2.97(06)	+
B*	3.5437	-58.8	1.19(14)†	0.91(11)	420(48)	2.53(06)	+
3X*	3.5533	-68.4	-	1.19(18)	383(35)	1.77(04)	0
4X*	3.5620	-77.1	-	1.34(35)	379(53)	1.73(02)	0

† Mixed contributions of X* and B*.

4X, which is mainly the S-like hole state originating from the B valence band of GaN [$P_{x,y}$(CB) does not significantly contribute to the emission], τ_{rel} significantly drops to 62(30) ps, respectively 51(27) ps. Please note how τ_{rel} again is only marginally reduced regarding 3X and 4X, in-line with the same observation for X and B. Interestingly, τ_{rel} leaps towards 155(17) ps and 144(38) ps for the case of 5X and 6X, again exhibiting only a minor reduction if both values are compared to each other. Finally, τ_{rel} does not only scale with the number of electron-hole pairs, but is heavily altered as soon as new electronic levels are occupied. This observation precisely presents a strong motivation for the provided emission line assignment. A microscopic origin for the increase of τ_{rel} towards 5X and 6X cannot be given, however, it should be noted that only in this case two new electronic levels are occupied with electrons *and* holes, which both significantly contribute to the final emission. As the carrier relaxation depends on two carrier types exhibiting totally different energy spacings, which also requests different multi-phonon cascade processes, it is only naturally to expect longer τ_{rel} values. However, also relaxation resonances could occur as soon as certain intra-QD energy spacings match typical multiples of host phonon energies of GaN or AlN [61, 67, 88, 111, 112]. Clearly this prediction constitutes a strong motivation for future work that well resides beyond the scope of this thesis.

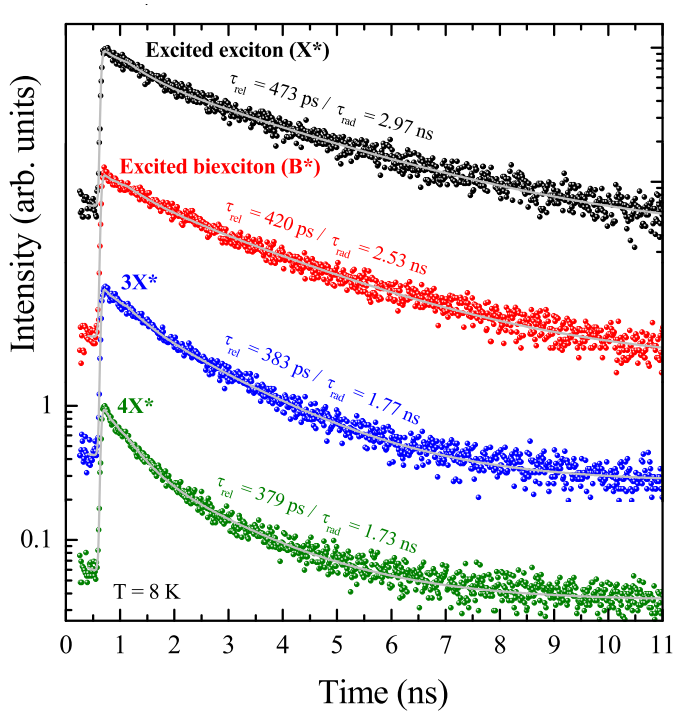

Figure 4.11: Time-resolved analysis of the excited (*) excitons shown in Fig. 4.5. All transients are fitted based on a biexponential model (solid, grey line). Following a time-resolution limited rise [40(13) ps], first, all complexes predominantly decay with the time constant τ_{rel}. Subsequently, the decay is dominated by the radiative lifetime τ_{rad}. Upon rise of exciton number, the number of radiative decay channels increases as expressed by a reduction of τ_{rad}, while τ_{rel} also diminishes.

Fig. 4.11 shows the temporal evolution for the excited-state luminescence X*, B*, 3X* and 4X*. As all luminescence features from the μ-PL spectrum shown in Fig. 4.6 are strongly spectrally broadened, none of the solely by the additional occupation of hole levels induced decay components (3X, 4X) can directly be observed. However, excited excitons that constitute the $P_{x,y}(CB)$ level can be witnessed, allowing the time-resolved analysis of them due to larger energy splittings. Again, X*, B*, 3X* and 4X* exhibit biexponential decay characteristics and no rise-time can be resolved, cf. Fig. 4.11. All τ_{rad} values that belong to excited-states are reduced in comparison to their ground-state counterparts. As the number of decay channels is not straightforwardly altered, the relaxation of the exited excitons towards their ground-states must diminish the experimentally accessible τ_{rad} values. In contrast to τ_{rad}, the τ_{rel} values of the excited excitons are enhanced if compared to their ground-state equivalents, but still follow the already described particular scaling behavior depending on the electronic levels involved. An explanation of the overall larger τ_{rel} values for excited excitons could be a more efficient feeding of the ground-states by relaxation in contrast to the excited-states, which even exhibit relaxation processes as their loss channels. Please note that Fig. 4.10 predicts negligible transition rates between the $P_{x,y}$(CB) electrons and holes with s-like symmetry. Hence, in order to explain the occurrence of the excited state luminescence (X*, B*, 3X* and 4X*) at lower excitation powers in comparison to 5X and 6X (see Fig. 4.5), it is feasible to assume a dominant contribution of the P1-like holes states for all excited-state transitions.

As a result, not only the electrons but also the holes occupy excited-states, rendering the stated average splitting between the ground- and the excited-states ($\approx 53\,\mathrm{meV}$) a twofold affected number (see Sec. 4.3.1, page 46). An in detail description by a sophisticated rate equation model would be needed in order to gain a deeper understanding of the experimentally witnessed dynamics. Nevertheless, the presented analysis of multiexcitons in wurtzite GaN QDs still represents one of the most extended analysis of its kind [113, 114] to date, as both, the theoretical treatment and the related experiments encounter a number of outstanding challenges as described within this chapter.

4.5 Summary

In this chapter the reader is first briefly introduced to the characteristic ensemble luminescence of the wurtzite GaN QD sample that is mainly analyzed throughout the entire manuscript. A structured emission is observed in the ensemble luminescence spectrum, which is related to the emission of sub-ensembles of GaN QDs exhibiting varying heights. Based on a comparison to multi-particle 8-band k·p calculations, each sub-ensemble can be related to a particular number of monolayers, yielding the average height of the QDs that contribute to the luminescence. First traces of exciton-LO-phonon coupling were witnessed in an ensemble PL spectrum but any further quantification of the coupling strengths is hindered by spectrally overlapping luminescence contributions. This observation presents a strong motivation for μ-PL spectroscopy of single, wurtzite GaN QDs as presented in Chap. 6, page 74. In a brief analysis some common spectral features of a GaN QD emitting at $\approx 3.5\,\mathrm{eV}$ are analyzed by means of excitation power dependent μ-PL spectroscopy. As a result, strong indication for the observation of excitonic and biexcitonic emission along with their one-LO-phonon replica is obtained, which is additionally complemented by the observation of an excited-state luminescence. This picture is completely altered as soon as the pulsed excitation of the identical QD resides within focus. Not only that such pulsed excitation enables time-resolved μ-PL spectroscopy, also the regime of high excitation in single QDs can be accessed. Here, an entire zoo of ground- and excited-state excitonic particles is observed. This chapter presents the first evidence for excitonic complexes beyond the biexction up to the sext-exciton (6X). In addition the excited-states of these multiexcitons can be observed, substantiating the given emission line assignment. As any suitable theoretical predictions for these multiexcitons fail due to the sheer size of the wurtzite GaN QDs, it is necessary to recede towards basic, but intriguingly intuitive level schemes, i.e. a single-particle picture. Based on the random initial occupation model introduced by Mukai and Sugawara [96], it is feasible to not only explain the actively debated biexponential

decay behavior of multiexcitons but also a biexponential decay of a single exciton. Hence, for the first time, radiative decay *and* relaxation times for multiexcitons inherent to wurtzite GaN QDs are reported providing deep insight into fundamental relaxation mechanisms in QDs, which are governed by a weighted balance of Auger electron and phonon contributions.

After this first spectroscopic analysis of excitonic complexes of various kind, the astonishingly large inhomogenous emission line width of single GaN QDs, mostly residing in the meV range, will be analyzed in the following chapter. Here, the focus will be extended to a larger variety of QD sizes exhibiting different emission line widths. However, it will be shown that not only the QD size influences the emission line width but also the particular nature of the underlying excitonic complex. Exactly this particular emission line broadening rendered an even more detailed analysis of the multiexcitonic complexes presented in this chapter a challenging task. Hence, it is only natural to analyze the origin of this limiting factor in order to develop effective countermeasures that will promote future GaN QD sample growth endeavors aiming towards reduced emission line widths.

5 Emission energy dependent line widths broadening

A statistical analysis of emission line widths broadening in wurtzite GaN QDs embedded in AlN is presented in this chapter. Generally, luminescence traces of single, wurtzite GaN QDs exhibit remarkably broad emission lines in the meV range [31]. This well-known feature [32, 68, 86, 115–117] introduced in Chap. 4 is particularly surprising given the long radiative lifetimes of wurtzite GaN QDs embedded in AlN ranging from the ns to the μs regime [27, 118] pointing to homogenous emission line widths down to the μeV range. In the following chapter it will be shown that this apparent emission line width discrepancy of over three orders of magnitude is predominantly caused by a phenomenon known as *spectral diffusion*, as supported by the observation of a unique scaling behavior between the median emission line widths and the QDs' emission energies. All experimental results are further substantialized by the advanced 8-band k·p calculations [48] previously introduced in Chap. 3, page 21. Such calculations allow to determine strong excitonic dipole moments native to wurtzite GaN QDs that cause their particular vulnerability to spectral diffusion. Based on the presented conjunction between experimentally determined emission line widths and theoretically derived excitonic dipole moments, one can estimate the electric field strength induced by charged defects that causes spectral diffusion in wurtzite GaN QDs with $\approx 2\,\mathrm{MV/m}$. Even a novel emission line identification method can be established based on the occurrence of deviating emission line widths for various excitonic complexes. A direct comparison of relative excitonic dipole moment ratios determined by theory and experimentally observed emission line widths ratios facilitates a straightforward method for the identification of e.g. excitonic and biexcitonic emission origins. Furthermore, ongoing progress regarding the growth of wurtzite GaN QDs has nowadays already led to significant advances concerning achievable line widths as demonstrated at the end of this chapter, closing with reporting a record emission line width for single, planar, wurtzite GaN QDs embedded in AlN of $\approx 440(5)\,\mu$eV.

The results from this chapter are partially published in Refs. [38, 46]. The 8-band k·p wavefunctions were derived by G. Hönig, yielding the excitonic dipole moments and related ratios [48], while Dr. C. Kindel provided a set of emission line widths.

5.1 Phenomenon of spectral diffusion

The detailed understanding of fundamental parameters characterizing a quantum light source like, e.g. complex binding energies [36, 75, 115, 119] and fine structure splittings [32,37,39,120–122] is crucial for the design of any real-world device. However, inhomogenous emission line width broadening due to e.g. spectral diffusion can make such task a tough challenge. The general phenomenon of spectral diffusion was first described in nuclear magnetic resonance experiments [123, 124] and was then applied to light-emitting systems such as rare-earth ions [125], nitrogen vacancies in diamond [126], and semiconductor QDs [89, 127, 128]. For the particular case of an epitaxial semiconductor QD the emitter is situated in a semiconductor matrix material containing defects that stochastically trap and release charges and hence generate a fluctuating Coulomb field [38]. As a consequence an exciton inherent to the QD senses the charged defects in the matrix material mediated by a basic electrostatic interaction, evoking a continuous change of the associated emission energy. If the typical time scale associated to these charge fluctuations is shorter than the integration time of the detection system, then the natural line width is obscured and an inhomogeneous emission line width broadening is observed. However, this effect is not only noticeable in μ-PL spectra but also in second order correlation functions [129], causing a bunching phenomenon at $\tau \neq 0$ as further discussed in Chap. 8.

5.1.1 Basic emission line widths analysis

Fig. 5.1b, page 64 shows the exemplary emission of several wurtzite GaN QDs by means of a μ-PL spectrum obtained from a 200 nm wide mesa structure marked in Fig. 5.1a recorded at a temperature of 8 K. Interestingly, the luminescence lines become much narrower with increasing emission energy. While at low emission energies ($\approx$ 3.6 eV) broad emission lines with full widths at half maximum (FWHM) of the order of 10 meV are observed, a pronounced narrowing appears towards higher emission energies ($\approx$ 4.0 eV) reaching FWHM of $\approx$ 2 meV. At the selected excitation power of 0.1 kW/mm^2 almost all dominantly observed emission lines exhibit an excitonic character with linearly scaling power dependencies [115,119] as e.g. introduced by Fig. 4.3, page 43 and a corresponding fine structure splitting [43]. Therefore, the influence of charged and neutral multi-excitonic complexes [38, 107, 114] with deviating excitonic dipole moments and emission line widths is, first of all, neglected in the following analysis and subsequently separately introduced as an extremely helpful tool for the emission line identification in Sec. 5.2.

Fig. 5.2a shows the extracted FWHM values (grey dots) of $>$ 200 individual, wurtzite GaN QDs over a wide emission range from 3.4 eV to 4.2 eV. In order to obtain the illustrated FWHM distribution the μ-PL setup described in Chap. 2.2, page 18 has

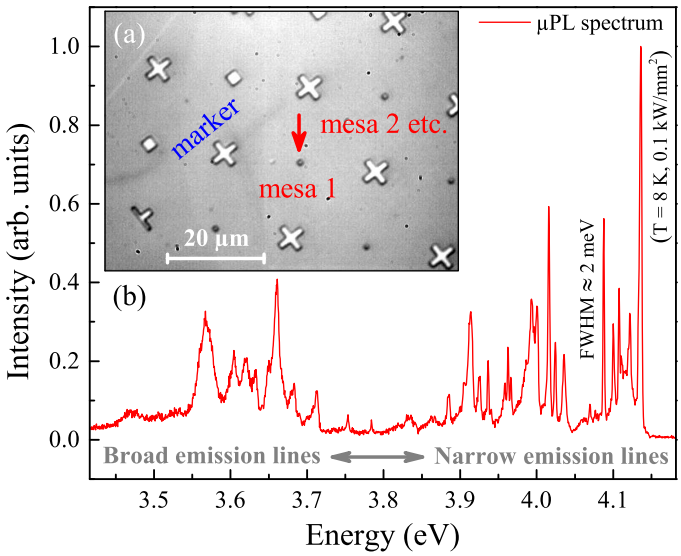

Figure 5.1: (a) Optical microscope image of the specimen's surface showing some cross-shaped marker and round mesa structures. The red arrow marks the mesa structure that yielded the μ-PL spectrum shown in (b) exhibiting luminescences of several GaN QDs recorded at a temperature of 8 K. Please note the broad emission line widths of the order of 10 meV at around 3.6 eV compared to very narrow emission line widths with ≈ 2 meV at around 4.0 eV. Adopted from Ref. [46].

tracked, focussed and measured hundreds of mesa structures distributed over the specimen's surface. All FWHM values illustrated in Fig. 5.2a were obtained from μ-PL spectra similar to Fig. 5.1b based on a peak fitting routine applying Gaussian fit functions [89]. Now the statistical confirmation for the emission line widths trend previously hinted by Fig. 5.1b is obtained. The average (median) excitonic line width indeed becomes much smaller for larger QD emission energies.

The median of the line width is more than halved from 8.2 meV at an emission energy of 3.45 eV down to 3.3 meV at 4.15 eV. Here, the median values are considered, since they are generally more resilient to single large outliers than the mean value. Furthermore, the distribution of line widths at a fixed emission energy appears to be asymmetric with a sharp lower limit for small line widths and a long tail for large line widths as also observed for GaAs/AlGaAs QDs [130]. A detailed analysis of this particular assymmetry will be published elsewhere.

5.1.2 Excitonic dipole moments: experiment vs. theory

The measured trend of a decreasing emission line width towards higher emission energies can qualitatively be understood by analyzing the intrinsic excitonic electric dipole moments of wurtzite GaN QDs. For such calculations Hartree-Fock wavefunctions are applied (see Chap. 3, page 21), which were determined by 8-band k·p calculations, including the effects of strain, pyro-, as also piezoelectricity, spin-orbit, and crystal field interaction along with renormalization effects caused by the mean particle interactions [37, 38]. The correspondingly modeled GaN QDs embedded in AlN have the shape of truncated hexagonal pyramids with a constant aspect ratio (AR) of 0.2 (or 0.1) as supported by atomic force [45] as well as TEM microscopy [32] (see Chap. 6, page 74), and vary in height from 2.4 - 1.2 nm, respectively 2.0 - 1.2 nm. Two exemplary QDs are illustrated in Fig. 5.2b along with the resulting isosurfaces of the electron (blue) and hole (red) occupation probability densities. The dipole moment of the excitonic bright states was determined by summing up the Hartree-Fock state densities of the electrons and the holes with appropriate signs. The resulting dipole moments are illustrated in Fig. 5.2b and show a strong reduction of the dipole moment of the excitonic bright states with decreasing QD height at a constant AR and hence increasing emission energy. The calculated excitonic dipole moments are altered by a factor of around 3 over the entire QD emission interval shown in Fig. 5.2b. In contrast, variations in the QD's AR within the experimentally determined limits of 0.1 - 0.2 [45] yield maximal dipole moment variations of only 15 % for QDs emitting between 3.3 eV and 4.3 eV, cf. Fig. 5.2b. Also variations in a volume maintaining QD elongation of up to 20 % [37,117] change the calculated excitonic dipole moment for large towards small QDs by maximal 20 % down to negligible 0.5 %, clearly emphasizing the importance of the QD height. It is also exactly this QD height that tunes the radiative decay time of excitons in wurtzite GaN QDs over several orders of magnitude [27].

After having analyzed the influence of the QD geometry one can now estimate the weighting between the fundamental interactions additionally incorporated in the calculations of the realistic wavefunctions. Renormalization effects included in the Hartree-Fock calculations (exchange and Coulomb interaction) yield excitonic dipole moment variations between 2 - 5 %. Interestingly, such renormalization effects account for almost identical excitonic dipole moment variations as induced by correlation effects [38]. Hence, the built-in electron-hole separation altered by the QD geometry is the most dominant factor for the calculated excitonic dipole moment dependencies shown in Fig. 5.2b.

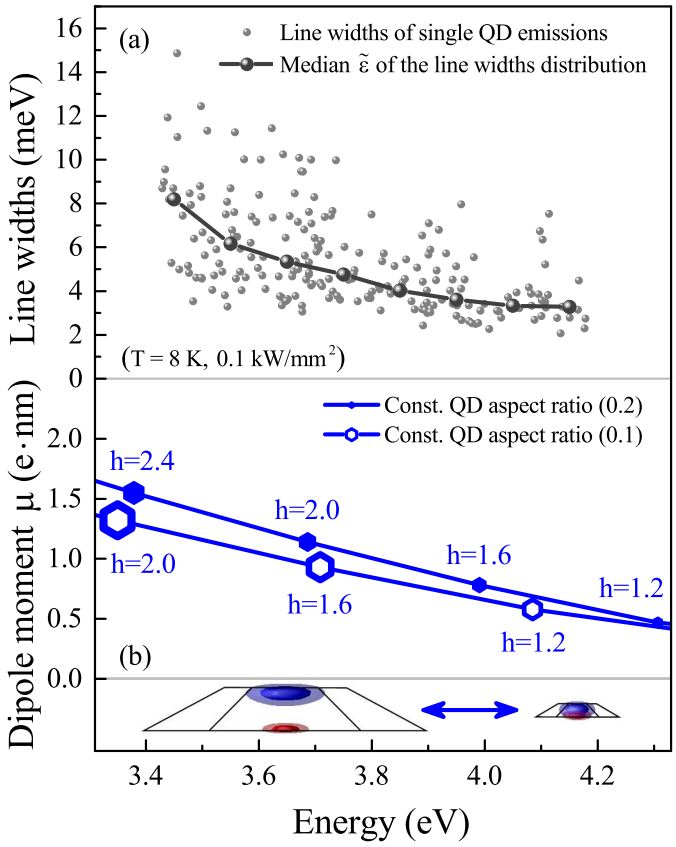

Figure 5.2: (a) Line widths (FWHM) of single QD emissions originating from >200 spectra measured with the μ-PL system described in Chap. 2, page 16. With rising emission energy a reduction of the median line widths $\tilde{\varepsilon}$ is observed with lowest values of ≈ 2 meV. (b) A corresponding decreasing trend is found for the calculated excitonic dipole moments μ for two QD aspect ratios (0.1 and 0.2). The symbol size in (b) scales with the QD diameter. The QD schemes illustrate the isosurfaces of the electron (blue) and hole (red) occupation probability densities. Adopted from Ref. [46].

5.1.3 Emission line widths statistics

It is found that the observed median emission line widths $\tilde{\varepsilon}$ are proportional to the QDs' internal dipole moments μ as illustrated in Fig. 5.2. The link between μ and $\tilde{\varepsilon}$ can be understood within the framework of the linear quantum-confined Stark effect (QCSE) [85,86] introduced in Sec. 3.7, page 37 and spectral diffusion [38,129]. The strong built-in electric field in the order of MV/cm [34] in wurtzite GaN/AlN QDs causes a spatial separation of the electron and hole centers of masses on the order of nanometers, resulting in dipole moments scaling between e.g. 1.55 e·nm and 0.47 e·nm for an AR of 0.2 (QD height of 2.4 - 1.2 nm), cf. Fig. 5.2b. Generally, any external electric field $\vec{F}$ causes exciton emission energy shifts ΔE due to the linear QCSE [24]:

$$\Delta E(t) = \vec{\mu} \cdot \vec{F(t)} \tag{5.1}$$

If the electric field is time-dependent and fluctuates statistically around a mean value, then the exciton emission energy will follow this fluctuation. For fluctuations faster than the detector integration time one observes inhomogeneously broadened, Gaussian-like emission lines instead of Lorentzian shaped and only homogeneously broadened QD emissions [38]. The standard deviation of the exciton energy

$\sigma_{\Delta E}$ now trivially relates to the FWHM ε of a Gaussian-shaped emission line by $\varepsilon = 2\sqrt{2\ln 2} \cdot \sigma_{\Delta E}$. If it is assumed that the overall strength of the field fluctuations is the same for all investigated QDs then $\tilde{\varepsilon}$ is indeed directly proportional to μ, precisely matching the observation depicted in Fig. 5.2. This argumentation is further strengthened by the observation of a decreasing absolute slope of the calculated excitonic dipole moment trend towards larger emission energies that is in agreement with the measured evolution of the slope related to the median emission line widths. The conjunction of $\sigma_{\Delta E}$ and the theoretically derived μ now facilitates a consistent estimation of the average electric field strengths resulting in e.g. $\approx 2\,\mathrm{MV/m}$ for the entire data set under the assumption of a QD AR of 0.2. Such AR of 0.2 is experimentally most frequently observed in contrast to more rarely occurring, rather flat QDs with an AR of 0.1. Hence, in a first approximation, any singly charged defect situated directly above or below the GaN QD center at a distance of $\approx 8\,\mathrm{nm}$ could cause the determined electric field strength. As a direct consequence, an energetic shift of the excitonic emission line would be induced, which exhibits the same order of magnitude as the emission line width. It is particularly likely that charges might be trapped in the interface region above or below the QDs. A 5 - 10 nm thick AlN capping layer was deposited after the growth of the QDs at a comparably low growth temperature of 975 °C in order to preserve the QD formation (see Chap. 2, page 16). Hence, such an AlN layer will be defect-rich with a high density of charge trapping sites. However, the interface region between the QD bottoms and the underlying AlN matrix material is also a veritable candidate for charge trapping sites as the presence of strain and e.g. material intermixing may contribute to an additional defect formation. Interestingly, a sophisticated analysis by means of scanning transmission electron microscopy (STEM) presented in Sec. 6.4, page 86 even suggests the sidewall facets of the QDs as a viable region for such charge fluctuations.

A detailed stochastical analysis of *how* a distribution of fluctuating charges induces a distribution of line widths resides beyond the scope of this thesis and will be published elsewhere. Finally, it is the giant built-in dipole moment μ that causes the observed huge emission line widths and results in the general high sensitivity of nitride QDs to a fluctuating charge environment. Even extreme QD geometry variations like a change in the AR of 0.1 to 0.2 as shown in Fig. 5.2b cannot explain the observed broad emission line widths distribution. This observation is especially true for smaller wurtzite GaN QDs ($\approx 4\,\mathrm{eV}$), whose excitonic dipole moment is less affected by QD geometry changes, clearly revealing spectral diffusion as most dominating origin for the occurring FWHM.

The presented line widths broadening phenomenon in nitride QDs stands in contrast to less polar e.g. zincblende arsenide QDs. Here, generally smaller excitonic dipole moments occur [131, 132] and the observed emission line widths are typically on

the order of μeV, three orders of magnitude smaller than in nitrides [89, 133]. This observation provides a strong motivation for the growth of GaN QDs on less-polar substrates or even the analysis of cubic GaN QDs [55], naturally yielding lower single QD emission line widths due to the presence of smaller excitonic dipole moments. Another option for such a beneficial reduction of the excitonic dipole moment is the growth of even smaller wurtzite GaN QDs [134] with emission energies beyond 4 eV as shown in the following Chap. 5.3. However, the apparent line width differences between e.g. mature arsenide- and rather novel nitride-based QD systems are not exclusively caused by varying excitonic dipole moments, but also by still deviating point and extended structural defect concentrations in the matrix material.

Based on the μ-PL analysis one can further determine that the characteristic timescale of spectral diffusion is not larger than a few, detector-limited, tens of milliseconds at a temperature of 8 K for most of the analyzed GaN QDs. The identification of the physical origin related to the charged defects causing the electric field fluctuations remains a task for future work. However, the most relevant defects prove to be of an energetically shallow nature as already a rise of the temperature towards 20 K causes an increase of spectral diffusion and spectral jittering effects in the μ-PL spectra, the latter taking place on a time scale of a few hundreds of ms. For comparison, the characteristic spectral diffusion timescale τ_{SD} was first exemplarily measured for selenide QDs and yielded $\tau_{SD} \approx 4$ ns [129]. In contrast, recent $g^{(2)}$-correlation function measurements [39] have shown that the low-ns regime can mostly be excluded as the timescale for spectral diffusion in similar selected, high quality, wurtzite GaN QDs embedded in AlN. Only particular GaN QDs exhibit τ_{SD} values in the mid-ns regime (25 ns) as recently described in Ref. [40]. Additionally, cathodoluminescence experiments on InGan QDs pointed towards larger τ_{SD} values on the order of ms to s in nitrides [24]. Though, the fundamentally different excitation mechanisms in photo- and cathodoluminescence hinder a truly direct comparison between the determined τ_{SD} values.

Furthermore, this chapter demonstrated that the experimental trend for the emission line widths from Fig. 5.2a is still predominantly evoked by spectral diffusion [38] and not by an exciton acoustic phonon interaction via e.g. a deformation potential and piezoelectric coupling [135]. Generally, the elastic and inelastic interaction of acoustic phonons with the charge carriers inherent to the QD influence the overall emission line shape and line width [136]. Even though the entire exciton acoustic phonon coupling strength scales with the excitonic dipole moment in GaN QDs, similar to the trend for the line widths from Fig. 5.2a, the absolute line widths values in the meV range cannot be explained. It was shown that the previously measured, rather broad zero phonon emission line widths of wurtzite GaN QDs cannot be modeled without the inclusion of spectral diffusion, as solely considering the exciton

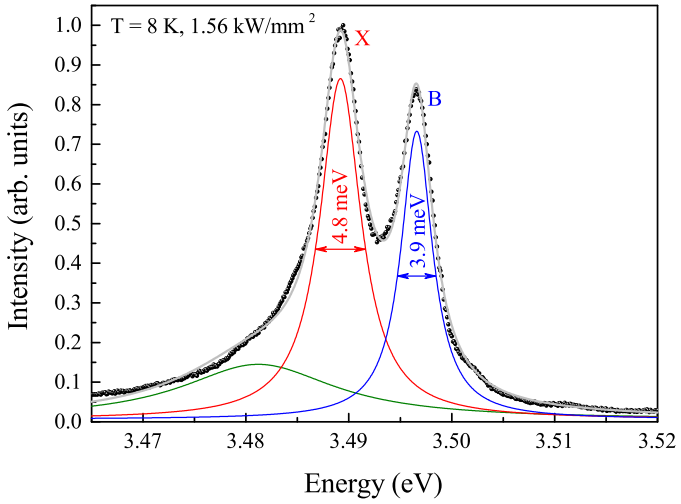

Figure 5.3: μ-PL spectrum extracted from Fig. 4.2. At an excitation power of 1.56 kW/mm^2 the excitonic and biexcitonic emissions dominate the spectrum. Spectral diffusion induces an emission line width broadening, which is more pronounced for the exciton (X) than for the biexciton (B) as clearly illustrated in the spectrum. The solid lines represent fits to the data.

acoustic phonon interaction strongly underestimates the measured FWHM [68].

5.2 Identification of excitonic complexes based on emission line broadening

Fig. 5.2 introduced a particular scaling behavior between the emission line widths and the excitonic dipole moment μ_X, which also has a direct consequence for emission line widths of higher excitonic complexes as e.g. biexcitons. As a direct result, one obtains a simple, straightforward additional tool in order to support the identification of excitonic complexes as described in Chap. 4, page 39. However, for the emission line widths of multiexcitons only relative dipole moments $\Delta\mu$ and not absolute dipole moments μ need to be taken into account, because only the change in the dipole moment upon decay of the excitonic complex determines the measurable emission line widths [38]. Naturally, this statement includes the assumption that the decay time of the excitonic complexes is small in regard to the integration time of the experimental acquisition process that yields the final μ-PL spectra [89,129,137]. Only for the exciton one obtains $\Delta\mu_X = \mu_X$, while the $\Delta\mu$ values of higher and charged excitonic complexes diminish in regard to $\Delta\mu_X$ as deduced for wurtzite GaN QDs in Ref. [38].

Fig. 5.3 illustrates a μ-PL spectrum that was extracted from Fig. 4.2 for an excitation power of 1.56 kW/mm^2 at a temperature of 8 K. The two most prominent emission lines correspond to excitonic (X) and biexcitonic (B) emission as identified by the excitation power dependent μ-PL series from Sec. 4.2 and a multitude of further experimental techniques as e.g. μ-TRPL and correlations spectroscopy [40]. The

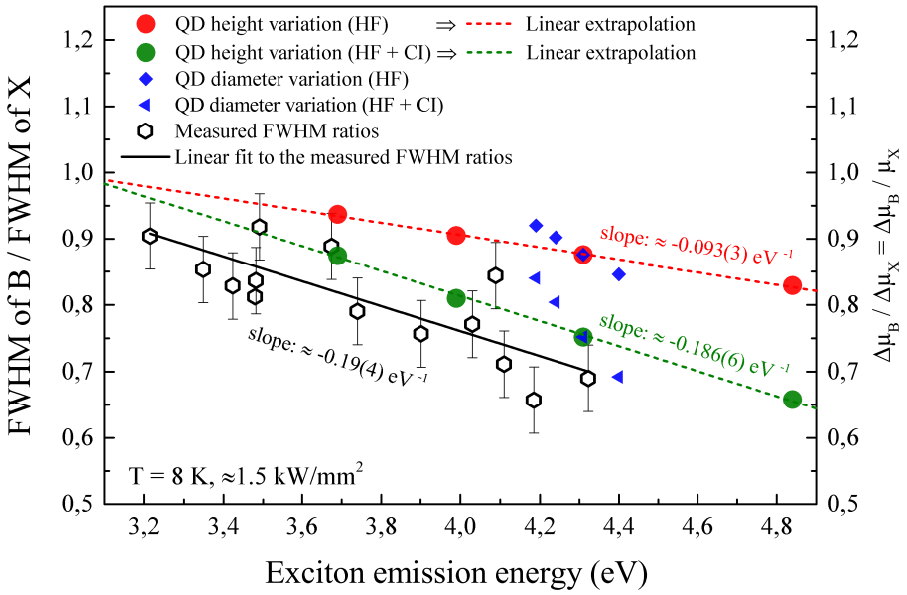

Figure 5.4: Compilation of emission line width ratios based on the FWHM of excitonic (X) and biexcitonic (B) emissions originating from individual GaN quantum dots (QDs). With increasing QD emission energy, the corresponding ratio is decreasing. A direct comparison to calculated relative dipole moment ratios for X and B facilitates an understanding of the measured trend. Here, 8-band k·p calculations in combination with a Hartree-Fock (HF) approach come into play, which are additionally amended by considering the configuration interaction (HF+CI). Occurring deviations between experiment and theory can be explained by QD geometry variations. Please see the text for details.

emission of X exhibits a FWHM of 4.8(1) meV, while the corresponding B emission exhibits a significantly lower line widths of 3.9(1) meV, yielding a FWHM ratio of 0.81.

A compilation of such emission line width ratios based on the FWHM of X and B emission can be found in Fig. 5.4. Please note that all the illustrated experimental FWHM ratios correspond to QDs, which were characterized by the full set of available experimental techniques that also formed the basis for the biexciton binding energy determination published in Ref. [40] (see Chap. 8, page 118). The inclusion of theoretical results in Fig. 5.4 based on the multi-particle 8-band k·p approach introduced in Chap. 3, allows for a successful description of the experimental results. Here, Fig. 5.4 considers two theoretical approximations, namely the Hartree-Fock (HF) and the Hartree-Fock approach in combination with the correlation interaction (HF+CI) calculations (see Sec. 3.2.3, page 31). Already the Hartree-Fock approach yields a diminishing trend for the relative dipole moment ratios of X and B as previously published in Ref. [38] with a slope of $-0.093(3)$ eV^{-1}, cf. Fig. 5.4. The inclusion of additional carriers to the multiexcitonic complexes is reducing the average electron-hole occupation probability density distances by the renormalization

effects that the Hartree-Fock approach considers in contrast to single-particle states that neglect any carrier interactions. However, a linear fit to the experimental results yields a slope of $-0.19(4)$ eV^{-1}, thus a clear discrepancy to the theoretical data.

The underlying QD dimensions for the presented calculations were again chosen in agreement with Chap. 2, page 16, considering a QD height and a diameter variation series. For the QD height series the aspect ratio was again set to 0.2 yielding QD dimensions that were also utilized for the theoretical data shown in Fig. 5.2. Again, the fluctuation of the experimental datapoints arises from QD geometry variations as considered by introducing a QD diameter variation series in Fig. 5.4 with a constant QD height of 1.2 nm.

The obvious discrepancy between the experimental datapoints and the Hartree-Fock results shown in Fig. 5.4 originates from disregarding the CI. If the CI calculations are seeded by Hartree-Fock wavefunctions as described in Sec. 3.2.3, page 31 then the slope of the experimental results can well be matched with a theoretical slope of -0.186(6) eV^{-1}. Only a minor absolute offset between the experimental and theoretical results remains evident in Fig. 5.4, which can be explained by the rather broad aspect ratio distribution of the wurtzite GaN QDs. The presented agreement between experiment and theory does not only demonstrate that the applied wavefunctions achieve an unmatched precise modeling of the carriers inherent to the QDs, but also constitutes a novel type of emission line assignment. Simply by comparing emission line widths, a basic emission line assignment can be undertaken for the case of strongly polar QDs with wurtzite GaN QDs embedded in AlN as a natural representative.

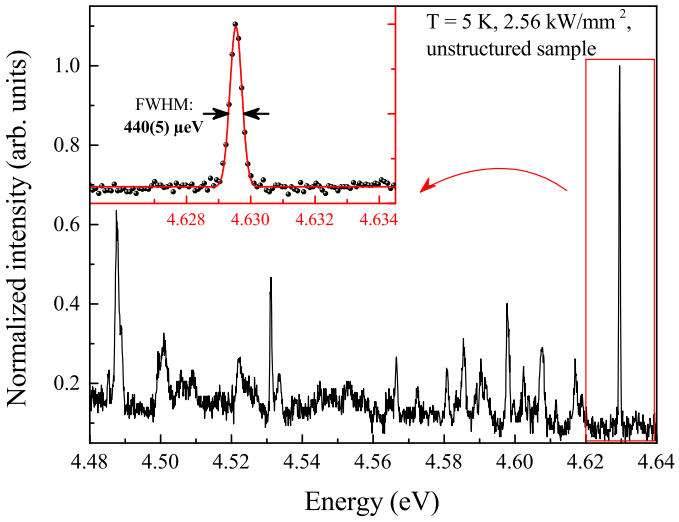

Figure 5.5: Overview μ-PL spectrum of a planar sample comprising wurtzite GaN quantum dots (QDs) embedded in AlN. Single emission lines are already accessible without applying any mesa structuring. Recent growth advances have enabled such QD densities in the $10^8\,\mathrm{cm}^{-2}$ regime, exhibiting emission line widths down to 440(5) μeV as shown in the inset.

5.3 Towards ultra narrow emission line widths

Recent growth advances in the research group of Prof. A. Strittmatter, aiming towards the growth of smaller, wurtzite GaN QDs as suggested in Sec. 5.1.3, have enabled the observation of even narrower emission below the presented limit of 2 meV as depicted in Fig. 5.2. The μ-PL spectrum of such a planar GaN QD sample is shown in Fig. 5.5, while details regarding the growth procedure are described in Chap. 2.1, page 16. Single QDs can already be addressed on this sample by μ-PL spectroscopy without any mesa structuring due to the exceptional QD density scaling in the low $10^8\,\mathrm{cm}^{-2}$ regime. In the inset of Fig. 5.5 a particularly narrow emission line is shown, exhibiting a FWHM of 440(5) μeV. Such narrow emission line width presents todays record (early 2015) for a planar GaN QD sample and constitutes the basis for future advanced spectroscopy.

5.4 Summary

In summary, the scaling behavior of the median excitonic emission line widths (8.2 - 3.3 meV) in wurtzite GaN QDs was related to an exceptionally strong decrease of the excitonic dipole moments with rising QD emission energy (3.4 - 4.2 eV). This general correlation was derived based on > 200 μ-PL spectra measured by an automatized spatial mapping setup. Multi-particle 8-band k·p calculations of excitonic wavefunctions yield exceptionally large excitonic dipole moments scaling between 1.55 e·nm and 0.47 e·nm for the analyzed, realistic QD height interval. The presented proportionality between the emission line widths and the dipole moments strongly suggests spectral diffusion as most dominating origin for the emission line broadening in wurtzite GaN QDs and explains the rare observation of emission line widths < 2 meV. The average electric field strength that causes this spectral diffusion phenomenon is estimated with ≈ 2 MV/m. Other dipole moment dependent line width broadening mechanisms like exciton acoustic phonon coupling were excluded. The presented chapter facilitates an in-detail understanding of emission line widths broadening, not only for wurtzite GaN QDs, but for any other strongly polar QD material system. A similar most general result is obtained by establishing an emission line widths comparison as a potent tool for an emission line identification that is from an experimentally point of view extremely easy to achieve. Having such an additional identification method at hand is most valuable, because no experimental technique can achieve a truly valid emission line assignment by itself. The effectiveness of this new identification method is approved by identifying more than 10 emission pairs associated to excitonic and biexcitonic emission in direct agreement with standard identification methods as e.g. excitation power dependent μ-PL, TRPL, and correlation spectroscopy. Additionally, future prospects for the QD growths are identified and already partially realized yielding todays (early 2015) record emission line width for a wurtzite GaN QD of 440(5) μeV. This recent progress will pave the way towards a technological relevance of nitrides, not only for light emitting diodes and laser diodes, but also for integrated quantum light sources.

6 Statistical analysis of the exciton-LO-phonon coupling

This chapter presents a detailed analysis of the coupling between single excitons inherent to wurtzite GaN QDs and longitudinal-optical-phonons (LO-phonons) over the spectral range that already formed the basis for the emission line width analysis introduced in Chap. 5, page 62. The Stokes-shifted luminescence traces of >200 QDs are analyzed, yielding a decreasing trend for the Huang-Rhys factor as a measure of the exciton-LO-phonon coupling strength with increasing exciton emission energy. Based on an adiabatic approximation applying multi-particle 8-band k·p wavefunctions, the Huang-Rhys factor be can calculated in good agreement with the experimental results. Such calculations reveal the QD height as the most vital parameter for the exciton-LO-phonon coupling strength in wurtzite GaN QDs. All geometric QD parameters applied for the calculations are confirmed by scanning transmission electron microscopy (STEM). The individual LO-phonon energies are determined for a significant number of QDs, scaling from the bulk LO-phonon energies of the QD material (GaN) towards the correspondingly higher energies of the matrix material (AlN) with rising QD emission energy. This chapter presents a unique conjunction of STEM, an extended μ-PL analysis, and calculations yielding a first spherical approximation of the exciton-LO-phonon interaction volume in wurtzite GaN QDs.

The results presented in this chapter have not been published to date, but are under review in Physical Review B. The multi-particle 8-band k·p wavefunctions were provided by G. Hönig [48] in order to finally derive the Huang-Rhys factor by a Fourier transformation performed by Dr. A. Schliwa, who has also performed all calculations regarding Gaussian envelope functions. The STEM analysis was undertaken at the "Leibniz-Institut für Kristallzüchtung" by Dr. T. Markurt in the research group of Dr. M. Albrecht. Only this unrivaled union of experimental and theoretical techniques facilitates the final, indirect *measurement* of the interaction range between excitons in individual GaN QDs and LO-phonons.

6.1 Exciton-phonon coupling - from bulk materials to nanostructures

The coupling between phononic and electronic excitations strongly influences most fundamental physical processes as e.g. light absorption, carrier recombination and relaxation. One of the early evidences for this coupling was observed in the absorption spectra of strongly polar, alkali-halide, bulk crystals exhibiting highly localized carrier recombination centers in the form of vacancies, the so called F-centers [138–140]. To a certain extent similar electronic systems such as excitons bound to impurities in II-VI materials like CdS were also rapidly confirmed to couple with lattice vibrations due to their significant level of localization [141–143]. A measure for the related coupling strength [140] was soon agreed to be expressed by the Huang-Rhys factor. In these early studies it was mostly a weighted balance between the crystal polarity, the localization depth of the emission centers, and the crystal quality that facilitated an increasing understanding of the coupling mechanism between phononic and electronic excitations. The accompanying, rapid evolution of the theoretical description for this exciton-phonon interaction within an adiabatic limit [144, 145], along with numerous experimental confirmations, has nowadays led to a fairly established understanding of such coupling processes in bulk materials, quantum wells, and nanowires [146–148]. Interestingly, the exciton-phonon coupling in quantum dots (QDs) still remains a most lively debated topic [68, 135, 136, 149, 150], not only because of its technologically relevance, but also for the following two reasons.

First of all, even though the QDs' zero-dimensionality resembles the early situation in F-centers and bound excitons, the opportunity to gradually tune the carrier confining potential by the QD dimensions is remarkable. As a direct result, the excitonic wavefunctions are altered, with strong impact on the exciton-phonon coupling strength [147] that becomes tunable as well. However, an even more fundamental second difference between the exciton phonon coupling related to point defects and the corresponding mechanism in structures that only mimic zero-dimensionality as QDs, is given by completely altered volume ratios. In QDs the spatial extent of the excitons' binding center is not anymore infinitesimally small in comparison to the adjacent matrix material hosting the bulk phonons. This situation raises the question, whether the exciton phonon coupling is still exclusively governed by vibrations native to the matrix material or the individual QD itself, as lively, but still inconclusively debated for As-based QDs [136, 151, 152].

Here, once more, QDs based on a strongly polar material systems as wurtzite GaN and AlN constitute a blessing in order to advance the understanding of the exciton-phonon coupling. The large excitonic dipole moments [38, 46] native to GaN QDs

embedded in AlN (see Chap. 5, page 62) facilitate a strong coupling to e.g. naturally polar longitudinal-optical-phonons (LO-phonons), yielding Huang-Rhys factors of up to ≈ 0.5. As a result, the traces of the exciton-LO-phonon coupling already clearly appear on a linear scale in μ-PL spectra [32] of single, wurtzite GaN QDs in contrast to e.g. As-based QDs with Huang-Rhys factors often just scaling in the 10^{-3} regime [136]. Hence, an extensive analysis of hundreds of single GaN QD spectra by means of μ-PL comes within reach as the most direct approach to not only precisely determine the coupling strength, but also the contributing phonon energies.

6.2 Phonon-assisted luminescence from single GaN quantum dots

Fig. 6.1a presents a μ-PL spectrum of the so labeled, individual GaN QD 1, whose emission is dominated by excitonic (X) and at higher energies biexcitonic (B) emission spectrally situated at $\approx 3.4\,\mathrm{eV}$. At the low energy side of these so called zero-LO-phonon emission lines, one can observe the evenly spaced one- and two-LO-phonon replica emission. These LO-phonon replicas exhibit an energetic spacing of $E_{LO} \approx 94\,\mathrm{meV}$, close to the common unstrained values for the two bulk GaN LO-phonon energies $A_1(LO) = 91.3\,\mathrm{meV}$ and $E_1(LO) = 92.2\,\mathrm{meV}$ at cryogenic temperatures [88]. The trend for the corresponding peak area I_{area} sequence based on Gaussian fitting functions for the individual emission lines is illustrated in Fig. 6.1b. It is found that such Gaussian fitting functions can well approximate all occurring emission line profiles because of the influence of spectral diffusion [46], cf. Chap. 5, page 62. This defect-induced phenomenon dominates the observed emission line shapes and evokes their widths even though LO-phonon replicas in bulk material can exhibit particularly asymmetric line shapes [41].
The peak area distribution shown in Fig. 6.1b can be approximated based on the following function [140, 144, 145]:

$$I_n = I_0 S^n e^{-S}/n! \tag{6.1}$$

Accordingly, the underlying adiabatic treatment in an independent phonon model [153] predicts a Poisson distribution at absolute zero temperature for the occurring intensities I_n that must be substituted by the emission peak area (I_{area}) of the individual phonon replica n. As a result of such an adiabatic approximation within the frame of the strong confinement regime [145] one obtains the Huang-Rhys factor S as a measure of the exciton-LO-phonon coupling strength [140]. An in-detail discussion supporting this adiabatic treatment is given in Sec. 6.5.1 along with a discussion regarding the two-LO-phonon replica. Hence, for QD 1 $S_X = 0.17(2)$

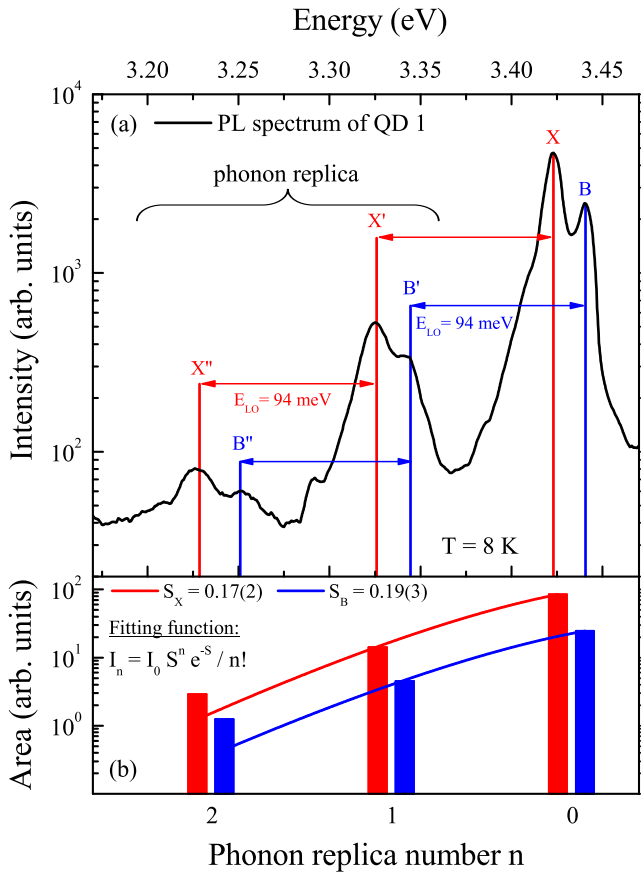

Figure 6.1: (a) μ-PL spectrum of the single GaN QD 1 showing excitonic (X) and biexcitonic (B) emission along with the associated individual LO-phonon replicas of first and second order. The corresponding emission lines are evenly spaced by a LO-phonon energy of ≈ 94 meV. (b) Manual peak fitting based on Gaussian functions (not shown) yields the illustrated peak area distribution that can be fitted by the denoted fitting function resulting the Huang-Rhys factor (S) as a measure of the exciton-LO-phonon coupling strength. Numbers in parentheses are the corresponding errors.

and $S_B = 0.19(3)$ are obtained for the exciton and the biexciton, based on the I_{area} values of all associated emission lines up to the second LO-phonon replica.

6.2.1 Comment regarding the emission line identification

The identification of the dominant X and B emission lines in the μ-PL spectrum of QD 1 from Fig. 6.1a is based on numerous excitation power dependent μ-PL measurements as introduced in Chap. 4.2, page 40. The comparison of corresponding absolute emission line areas in regard to variations of the pump power yields the number of excitonic decay channels n for each excitonic complex [40, 43]. Within the spectral range around 3.5 eV one commonly observes e.g. $n_X \approx 1.0(1)$ and $n_B \approx 2.0(1)$ for wurtzite GaN QDs like QD 1, which strongly indicates the identification of X and B emission [39, 115, 119] as soon as non-radiative processes are sufficiently suppressed [40]. Besides, within the spectral range from Fig. 6.1 it is common for GaN QDs to exhibit the observed anti-binding B emission [115, 119]. The large spatial separation of the charge carriers in GaN QDs, originating from the built-in polarization fields parallel to the [0001]-direction, leads to a reduction of the binding terms in the B complex as in-detail described in Chap. 8, page 118.

Furthermore, the identification of the LO-phonon emissions is not only based on their presented particular intensity ratios leading to the determination of the Huang-Rhys factor S and the energetic spacings of the occurring emission lines yielding E_{LO}, but also on temperature-dependent μ-PL spectroscopy. Already at low temperatures $< 50\,\mathrm{K}$ one can observe a trace of LO-phonon absorption during the excitonic emission process appearing at higher emission energies with respect to the zero-LO-phonon emission line. As soon as the temperature is raised towards room temperature the luminescence feature of LO-phonon absorption gains in intensity, while the LO-phonon emission as presented in Fig. 6.1a is diminishing. Both luminescence features, the so-called Stokes- and anti-Stokes-shifted emissions [154], are evenly spaced by the particular E_{LO} value of the analyzed QD, which further supports the emission line interpretation applied throughout this chapter.

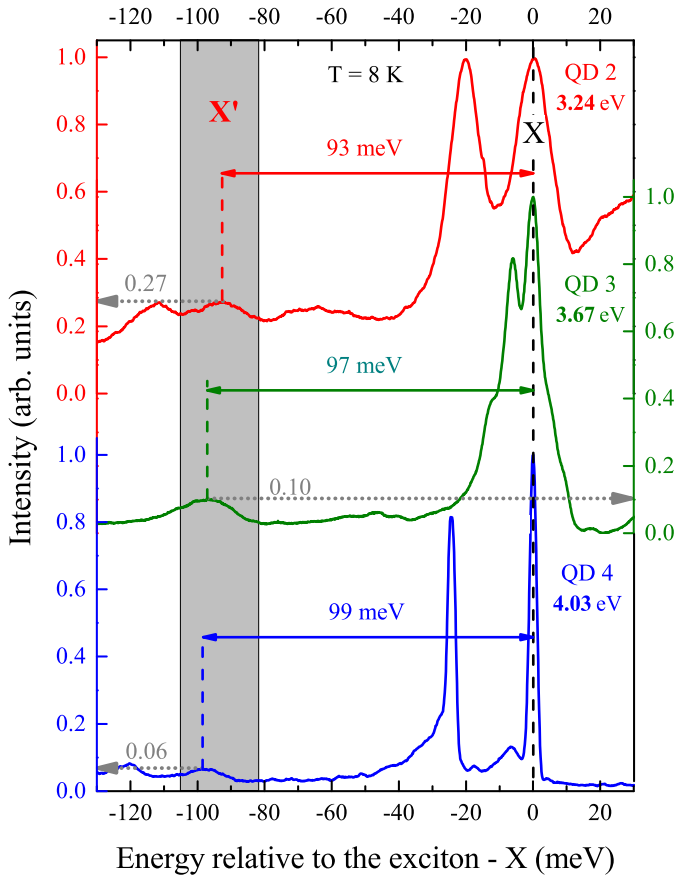

Figure 6.2: Normalized μ-PL spectra of three individual QDs emitting at 3.24, 3.67 and 4.03 eV as representatives for a large, a medium and a small GaN QD. The abscissa shows the energy relative to the exciton (X). On the Stokes-side of the X emission one observes the first LO-phonon replica (X') that diminishes in intensity with rising QD emission energy. In contrast, the LO-phonon energy is increasing with increasing QD emission energy, i.e. smaller QD size.

6.2.2 Fundamental scaling behaviors of the Huang-Rhys factor and the LO-phonon energy

Measuring E_{LO} and the Huang-Rhys factor S for a single QD like QD 1 is only of limited value if it comes to generally valid information affecting the entirety of GaN QDs as representatives of a strongly polar QD system. For example, geometric particularities, material composition, strain [35, 155] and varying defect environments [89, 129] could lead to quite particular characteristics for QD 1. Hence, more single GaN QD spectra need to be measured as shown in Fig. 6.2. The corresponding μ-PL spectra show the emission of individual QDs (QD 2 - 4) emitting at 3.24, 3.67 and 4.03 eV. Such an increase of the QD emission energy is mainly accompanied by a reduction in QD height [46] as theoretically shown in Sec. 6.2.3, which means that QD 2, 3 and 4 are representative for a large, a medium and a small GaN QD.

Interestingly, in the normalized spectra from Fig. 6.2 the maximal intensity I_{max} of the first phonon replica seems to scale with the QD size from 0.27, over 0.10 down to 0.06, pointing towards a reduction of the exciton-LO-phonon coupling strength. As apparent from the μ-PL spectra shown in Fig. 6.2, an in-detail analysis of I_{area} for the zero and first order LO-phonon replicas as demonstrated for QD 1 is extremely

difficult to achieve for QD 2 - 4 as various emission lines overlap in the spectral region of interest. As it is the aim to analyze many more single QD spectra in order to reveal QD size and shape dependent trends for S and E_{LO}, one must resort to a less error-prone and generally simpler I_{max} determination in order to analyze the exciton-LO-phonon coupling strength. If no pronounced broadening of the phonon replicas would occur with their rising order, then the determination of S is not predominantly influenced by either choosing an I_{area} or I_{max} based approach. However, as most clearly seen in Fig. 6.1 the phonon replicas indeed broaden. For instance, the excitonic emission of QD 1 the emission line width scales from 12.0, over 19.3, to 30.7 meV with a factor of ≈ 1.5. Due to the increased excitonic dipole moment of the B complex [38] this broadening is even more pronounced for the B-related emissions shown in Fig. 6.1, which broaden from 7.6, over 14.1, to 30.7 meV with a comparable larger scaling factor of ≈ 2.0. An exclusively on I_{max} based determination of such a reduced S' for the excitonic complexes of QD 1 (see Fig. 6.1) yields $S'_X = 0.11(1)$ and $S'_B = 0.14(1)$ in contrast to the naturally larger on I_{area} based values of $S_X = 0.17(2)$ and $S_B = 0.19(3)$, cf. Fig. 6.1. Hence, an I_{max}-based determination of a S', which is less effected by surrounding emission lines and consequently less error-prone, is well suited for the determination of general trends but it underestimates the exciton-LO-phonon coupling strength by a factor of ≈ 1.5 for large GaN QDs emitting at around 3.5 eV. Generally, the phonon replica broadening phenomenon is attributed to composition variations as well as the particular strain distribution in the QDs [156], which is overlaid by a strong influence of spectral diffusion in wurtzite GaN QDs [46] clearly dominating the broadening mechanism as shown in Chap. 5, page 62.

As a consequence, one obtains that the I_{max}-based S' values scale from 0.40 for QD 2, via 0.11 for QD 3 towards 0.06 for QD 4 in Fig. 6.2. Here, the S' is just determined by the intensity ratio of the excitonic emission and the corresponding first LO-phonon emission line. This limitation to only two emission lines for the determination of the S' is caused by the limited recorded spectral range still yielding sufficient spectral resolution for a precise determination of E_{LO} with an error of ≤ 1 meV. Furthermore, it is found that the second phonon replica is frequently overestimated in intensity as shown in Fig. 6.1a, an observation that will be discussed in Sec. 6.5.1. The difference in the I_{max} based S' determination for e.g. QD 1 if only one $[S'^1_X = 0.11(1)]$ or two LO-phonon replicas $[S'^2_X = 0.09(1)]$ are considered is small and resides within the experimental error.

Hence, just measuring I_{max} for excitonic emission lines and their associated first LO-phonon replicas is well suited for the following analysis of hundreds of single GaN QDs, especially with respect to a precise determination of E_{LO}. The determination of E_{LO} is straightforwardly achieved based on the first derivative of the recorded

μ-PL spectra. As a result one obtains an increase of E_{LO} from 93 meV for QD 2, via 97 meV for QD 3 towards 99 meV for QD 4, while S'_X simultaneously decreases, cf. Fig. 6.2. In parallel to the decrease of S'_X from QD 2 towards QD 4 one observes an additional effect in the corresponding μ-PL spectra. The observed excitonic FWHM is also decreasing with rising QD emission energy in good agreement with a reduction of the inherent excitonic dipole moment [38, 46] as previously introduced in Chap. 5, page 62.

6.2.3 Theoretical dependencies for the Huang-Rhys factor

The strong correlation between S and the exciton emission energy shown in Fig. 6.2 can be modeled based on an adiabatic approximation applying 8-band k·p wavefunctions. The justification for this adiabatic modeling of the exciton-LO-phonon interaction in wurtzite GaN QDs is discussed in-detail in Sec. 6.5.1. The exciton-LO-phonon interaction strength expressed by S can be calculated by employing the following expression [84, 157] in the Hartree-Fock approximation:

$$S = \frac{f_0^2}{(2\pi)^3(\hbar E_{LO})^2} \int \frac{1}{|\mathbf{k}|^2} \mid \mathcal{F}(|\psi_e|^2 - |\psi_h|^2) \mid^2 d^3\mathbf{k} \tag{6.2}$$

The Fröhlich constant [84, 158] is denoted by f_0 (see Eq. 6.3 in Sec. 6.5.1), $\mathcal{F}$ describes the 3D Fourier transformation, whereas $|\psi_e\rangle$ and $|\psi_h\rangle$ are the self-consistent electron and hole wavefunctions. Note, that S vanishes for an electron and a hole, occupying the same space ($|\psi_e|^2 \equiv |\psi_h|^2$), meaning that no interaction with the lattice occurs [159]. In a first attempt one can substitute E_{LO} with the bulk $A_1(LO)$ value of GaN [88] at cryogenic temperature and apply the static and the high-frequency dielectric constants of GaN [160] for the determination of f_0 [84], cf. Sec. 6.5.1. The wavefunctions (ψ_e and ψ_h) are again derived by performing numerical calculations based on the 8-band k·p envelope function theory, thus including the effects of QD shape, strain, piezo- and pyroelectricity, as also the Coulomb and exchange interaction [35] (see Chap. 3, page 21) in the determination of S based on Eq. 6.2. For instance, for a series of hexagonal GaN QDs with a constant base length of 16 nm the height is varied between 0.8 and 2.4 nm as shown in Fig. 6.3a. As a consequence of the strong inherent piezo- and pyroelectric built-in fields, the electron and hole parts of the resulting exciton wavefunctions become vertically separated as function of the QD height causing a drastic increase of the inherent excitonic dipole moments [38, 46]. Such a carrier separation evoked by a field induced band bending (see Chap. 3.7, page 37), does not only lead to a red-shift of the luminescence for taller QDs due to the linear quantum confined Stark effect (QCSE) [85, 86] but also has a drastic effect on the interaction between an exciton and generally polar phonons like the LO-phonons experimentally witnessed in Fig. 6.1 and 6.2.

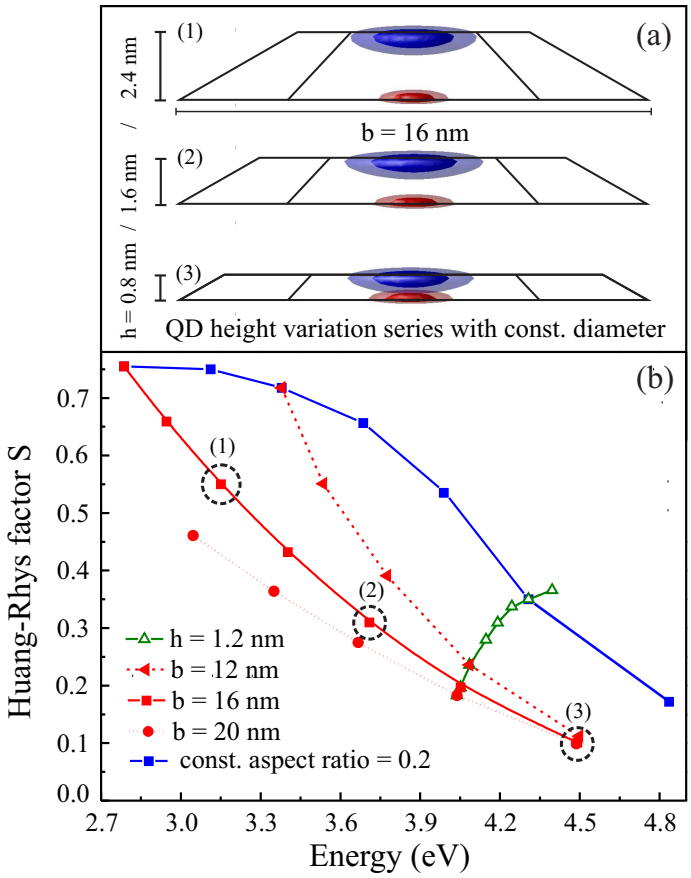

Figure 6.3: (a) Electron (blue) and hole (red) wavefunctions shown for three GaN QDs (1 - 3) of different height h (0.8 - 2.4 nm) but constant diameter b (16 nm). (b) Calculated Huang-Rhys factors S for three different QD series: red - QD height variation series for three different fixed base lengths (12, 16, 20 nm), blue - constant aspect ratio (AR = 0.2) QD series, and green - constant height (h = 1.2 nm).

The numerical results for various QD dimensions and shapes are displayed in Fig. 6.3b. The excitonic 8-band k·p envelope functions derived for three main QD series and calculated the corresponding S dependencies. Fig. 6.3b shows in red a QD height variation series (dashed red: 0.8 - 2.4 nm, solid red: 0.8 - 3.2 nm, dotted red: 0.8 - 2.4 nm) for three different fixed base lengths (b = 12, 16, and 20 nm), in blue a constant aspect ratio series (AR = 0.2), and in green a constant height QD series (h = 1.2 nm). For the QD height variation series the QD height was gradually reduced in steps of 0.4 nm in order to tune the QD emission wavelength all across the experimentally determined range. Accordingly, the QD bottom diameter was tuned from 16 nm down to 4 nm in steps of 2 nm for the constant aspect ratio QD series yielding a similar QD emission range as for the QD height variation series. In order to obtain a transition between the QD emission energies of the two former QD series (red and blue) a constant height series (green), exhibiting QD diameters scaling from 5.5 nm up to 8.6 nm, was calculated (see Fig. 6.3b). Interestingly, only the QD height variation series (red) and the constant aspect ratio series (blue) exhibit a decreasing trend for S with increasing QD emission energy as also experimentally observed for QD 2 - 4 in Fig. 6.2. However, both trends vary significantly if their first derivative is considered. The strongest reduction of S is observed for the larger QDs of the

height series emitting at lower energies. In contrast, the constant aspect ratio series only exhibits a comparably minor reduction of S in a comparable emission interval. However, for smaller QDs an inverted behavior can be observed if it comes to the slopes of both dependencies. While the constant aspect ratio QD series shows a drastic reduction of S, the corresponding trend for the QD height variation series flattens towards higher QD emission energies. In contrast to the experimental results shown in Fig. 6.2, the constant height QD series (green) shows an increase of S with rising excitonic emission energy due to the increasing lateral charge carrier confinement. So far the experimental evidence based on Fig. 6.2 is not sufficient in order to differ between such specific trends for S or to derive any generally valid information. Hence, many more μ-PL spectra of single, wurtzite GaN QDs are required in order to derive an in detail S dependence.

6.3 Statistical analysis of the Huang-Rhys factor and the LO-phonon energy

In order to obtain *generally valid* information, not only for the evolution of S with the QD emission energy but also for the opposing scaling behavior for E_{LO}, one needs to measure a significant number of single QD μ-PL spectra exhibiting LO-phonon-induced emissions. In order to realize such measurements the μ-PL setup was equipped with an automated mapping function that first locates and consequently measures the μ-PL spectra of mesa structures containing individual GaN QDs [46], cf. Chap. 2, page 16. The applied constant excitation power of $0.1\,\mathrm{kW/mm^2}$ mostly still yields dominant emission lines that exhibit an excitonic character with linearly scaling power dependencies [115, 119] and a corresponding fine structure splitting [43]. Hence, the effects of charged and neutral multi-excitonic complexes [38, 107, 114] with deviating excitonic dipole moments as introduced in Chap. 5, page 62 and therefore also deviating exciton-LO-phonon coupling strengths [152], can be neglected in the following analysis. Measuring such large numbers of μ-PL spectra (>200) further restricts the conducted measurements and subsequent data analysis to the intensity maxima of the zero- and one-phonon emission lines.
Fig. 6.4a illustrates the emission energy dependence of S' values extracted from single GaN QD μ-PL spectra. The clear trend of a lowering of the overall exciton-LO-phonon coupling strength towards larger emission energies as already suggested by Fig. 6.2 can be confirmed. Furthermore, the data indicates that the absolute slope of the S' dependence decreases towards higher emission energies in good agreement with the theoretical results for the QD height variation series from Fig. 6.3. As described in Sec. 6.2.2 the experimental determination of S' for hundreds of individual GaN QDs is only feasible if the maximal peak intensities of the zero- and one-phonon

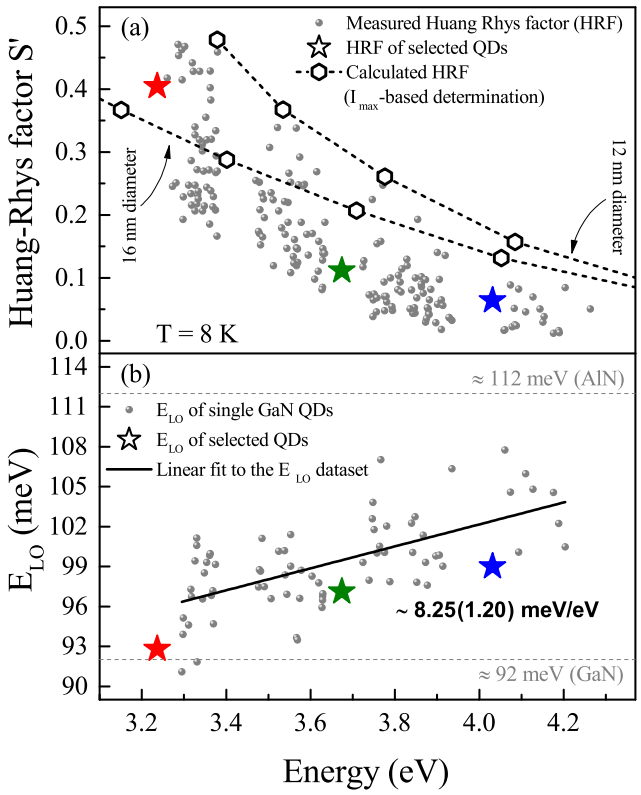

Figure 6.4: (a) Decreasing trend for the reduced Huang-Rhys factor S' with rising exciton emission energy measured for hundreds of wurtzite GaN QDs. The dashed lines connecting the hexagonal symbols illustrate the corrected theoretical dependence of S' from the QD height variation series. (b) Values for the LO-phonon energy E_{LO} extracted from the zero- and one-phonon emission lines. A linear fit to the dataset yields a slope of 8.25(1.20) meV/eV. The S' and E_{LO} values for QD 2 - 4 from Fig. 6.2 are depicted with star-shaped symbols, proving their S' and E_{LO} values as representative for the given emission energy.

lines are considered. In order to compare the experimental data with the theoretical data from Fig. 6.3 the correction factor of 1.5 needs to be applied for the theoretical dataset in order to account for the broadening phenomenon of the phonon replicas as described in 6.2.2. Hence, the best agreement between the experimental and theoretical results is found for the QD height series with a constant QD diameter of 12 and 16 nm as plotted along with the experimental data in Fig. 6.4a.

The general trend of S' in the measured emission energy interval is well reproduced for the QD height variation series considering a QD diameter of 12 nm. However, the corresponding absolute S' values only appear to agree with their maximal measured counterparts. Here, the second QD height variation series illustrated in Fig. 6.4a (QD diameter of 16 nm) yields S' values that are well comparable to the experimental values just the overall absolute slope of the S' dependence seems to be underestimated. Interestingly, the measured S' distribution seems to narrow from lower towards higher QD emission energies as also noticeable for the two calculated QD height variation series, cf. Fig. 6.4a. Hence, the experimental and theoretical Huang-Rhys factors are clearly less affected by QD diameter variations if it comes to smaller QDs emitting at higher energies. The widths of the measured S' distribution can be approximated by the two theoretical QD height variation series assuming a QD diameter span from 12 - 16 nm as confirmed in Sec. 6.4 by STEM-HAADF

(high-angle annular dark field) imaging. Deviations between the experimental and theoretical Huang-Rhys factors, especially for smaller QDs emitting at $\approx 4\,\mathrm{eV}$, can be explained by alloying effects in the vicinity of the charge carriers as outlined in Sec. 6.4, resulting further shape variations of the wavefunctions as subsequently discussed in Sec. 6.5.2.

The datapoint distribution of S' from Fig. 6.4a appears as split into four segments due to the applied automated tracking and mapping function of the μ-PL setup. In order to achieve a sufficient spectral resolution for a precise E_{LO} determination one needs to reduce the spectral widths of the detection window. While the measured absolute intensities in each spectral window are well comparable and applicable for the determination of S', the intensity comparison between several spectral windows is naturally more error-prone due to slight drifts in the positioning on each individual mesa structure over time. Hence, no S' values are considered in Fig. 6.4a that would comprise zero- and one-phonon lines from different spectral windows as their absolute intensity comparison would be flawed. Generally, based on hundreds of μ-PL spectra one can estimate an upper limit of the error for each datapoint shown in Fig. 6.4a yielding $\approx 10\,\%$. Hence, the contribution of the error of S' is minor in regard to the overall widths of the datapoint distribution caused by geometric variations of the QDs, cf. Chap. 6.5.2. Naturally, not *all* LO-phonons contributing to Fig. 6.4a could be identified by the entirety of indicators described in Sec. 6.2.1, meaning that the shown trend only preserves its significances based on the large number of datapoints.

For a limited number of data points from Fig. 6.4a one can even precisely obtain the energetic splitting between the zero- and one-phonon line E_{LO} based on the first derivative of the corresponding μ-PL spectra as shown in Fig. 6.4b. Here, a clearly inverse trend is observed for E_{LO} in regard to the emission energy. Larger E_{LO} values are observed for smaller QDs as already earlier on indicated by Fig. 6.2. A linear fit to the energetic dependence of E_{LO} yields a slope of $8.25(1.20)\,\mathrm{meV/eV}$. The star-shaped symbols in Fig. 6.4a and b illustrate the particular S' and E_{LO} values, which are extracted from the μ-PL spectra shown in Fig. 6.2. Finally, the trends suggested by Fig. 6.2 are indeed common for the analyzed GaN QDs, which has now been confirmed based on the statistical μ-PL analysis shown in Fig. 6.4. Interestingly, the observed trend for the E_{LO} dependence illustrated in Fig. 6.4b scales in between the LO-phonon energies of GaN and AlN at cryogenic temperatures [88]. This observation motivates high resolution STEM-HAADF imaging in order to analyze the GaN/AlN interfaces in regard to a possible $Al_xGa_{1-x}N$ alloying effect.

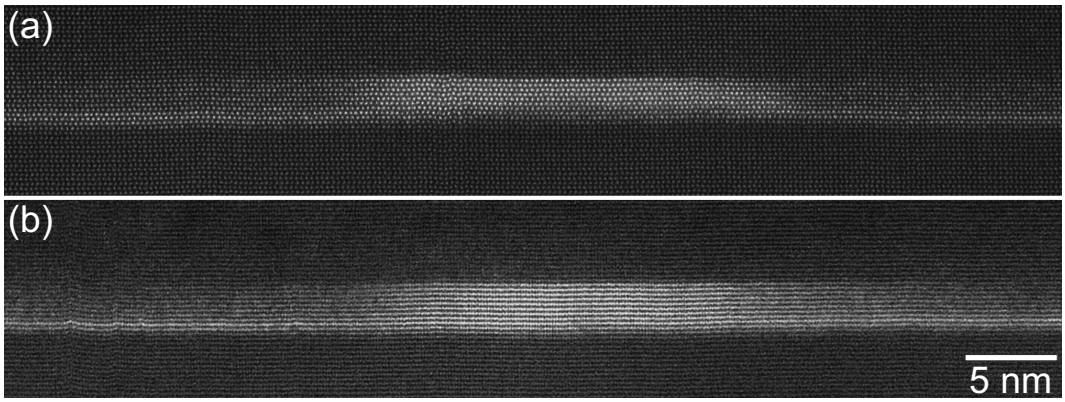

Figure 6.5: Cross-sectional STEM-HAADF images of GaN QDs embedded in an AlN matrix in the (a) $\langle 11\bar{2}0\rangle$ and (b) $\langle 1\bar{1}00\rangle$ projection, respectively. An AlGaN-alloying effect is visible on the QD base and the side facets. Both images exhibit the same length scale. Please see the text for any statistical results.

6.4 Microscopic analysis of alloying effects

Fig. 6.5 shows cross-sectional STEM-HAADF images of GaN QDs. Because of the higher atomic number the GaN QDs and the wetting layer appear brighter if compared to the AlN matrix. The wetting layer typically consists of 2 - 3 monolayers of GaN. By analyzing 15 QDs it was found that they indeed have the shape of a truncated pyramid as illustrated in Fig. 6.3a with a bottom widths scaling between 6 - 22 nm and a height including the wetting layer of 8 - 12 monolayers. These dimensions are in good agreement with the QD dimensions that were assumed for the multi-particle 8-band k·p calculations, cf. Chap. 3, page 21. Concerning a possible $Al_xGa_{1-x}N$-alloying effect an atomically sharp (0001) top facet is observed for all analyzed GaN QDs. However, the GaN/AlN (0001) interface directly at the bottom of the QDs and the corresponding lower wetting layer interface in between the GaN QDs appears to be not abrupt in the HAADF images, cf. Fig. 6.5.

Concerning the side facets of the GaN QDs one observes that the HAADF intensity is not abruptly diminishing but is gradually decreasing over more than 10 nm rather independent from the individual QD size. This effect was observed in both relevant wurtzite projections as illustrated in Fig. 6.5 for QDs recorded in the $\langle 11\bar{2}0\rangle$ and $\langle 1\bar{1}00\rangle$ zone axis direction, respectively. Additionally, the HAADF intensity of atomic columns fluctuates more strongly in the region next to the GaN QDs. One can determine the standard deviation and the mean value of the HAADF intensity of atomic columns in Fig. 6.5a for 3 different regions: in the center of the GaN QD, in the AlN matrix above and below the QD, and in the regions which laterally surround the GaN QD. For each region 180 atomic columns were analyzed. Long-ranged intensity gradients e.g. due to variation of the TEM specimen thickness have

been subtracted before the evaluation of the standard deviation. The ratio of the standard deviation and the mean intensity yields ≈ 0.06 in the region of the GaN QD and the AlN matrix material, while it amounts up to 0.10 in the region that laterally surrounds the GaN QD.
All these STEM-HAADF results indicate that the GaN QDs are horizontally embedded in an AlN matrix but are laterally surrounded by an $Al_xGa_{1-x}N$ alloy, whose AlN mole fraction x gradually increases with the distance from the QD. An $Al_xGa_{1-x}N$ alloy explains both, the increased mean HAADF intensity, as well as the stronger intensity fluctuation of atomic columns caused by statistical composition fluctuations of atomic columns in the alloy-region at the QD side facets. Such composition fluctuations fading along the growth direction are evoked by the 2-step overgrowth procedure described in Chap. 2.1, page 16), which is mandatory in order to maintain the QD formation during overgrowth by AlN. A projection effect (2D image of a 3D QD embedded in a matrix) can be ruled out as the reason for the observed contrast features as approved by the two recorded STEM-HAADF projections.

6.5 Concept of the exciton-phonon interaction volume

The following three possible reasons for the increase of the E_{LO} phonon energy with increasing QD emission energy as shown in Fig. 6.4b can be discussed based on the STEM analysis from Sec. 6.4:

(i) A QD size dependent $Al_xGa_{1-x}N$ alloying effect could shift the LO-phonon frequencies towards the values for AlN if mainly matrix material LO-phonons contribute to the exciton-LO-phonon interaction.

(ii) An increasing e.g. biaxial stress for decreasing QD size could originate an increase of the observed E_{LO} energy with increasing QD emission energy.

(iii) The exciton-LO-phonon interaction could average over the GaN QD and the AlN matrix material resulting in an increased LO-phonon energy for smaller GaN QDs due to a strengthened influence of the surrounding matrix material.

Even though an $Al_xGa_{1-x}N$ alloying effect is observed in Sec. 6.4, it mainly occurs at the side facets of the QDs where no charge carriers are situated, cf. Fig. 6.3a. Hence, a strong influence of the facet alloying on the exciton-LO-phonon interaction and the corresponding E_{LO} energy can be excluded even if, at a first glance, the extent of the exciton-LO-phonon interaction regime is limited by the exciton dimension. The surrounding of the electron is dominated by pure GaN and AlN material separated

by an atomically sharp interface, excluding a strong influence of intermixing effects on the exciton-LO-phonon interaction. Only the alloying at the QD bottom (see Sec. 6.4) could affect the exciton-LO-phonon interaction via the hole, resulting in generally lower E_{LO} values due to the $Al_xGa_{1-x}N$ environment. However, no clear QD size dependence was evident during the STEM-HAADF measurements for the widths of this particular alloying region that exhibits a composition gradient. Hence, an overall dominant influence of the $Al_xGa_{1-x}N$-alloying effect as suggested in point (i) can be refused.

An increase of the biaxial stress in the QD center towards larger emission energies as described in point (ii) can directly be calculated as described in Chap. 3.2.1, page 27 based on the theoretical approach relying on finite differences on regular grids [131]. The largest stress interval is observed for the QD height variation series for the case of biaxial stress considering a QD diameter of 12 nm, which also yields a good agreement with the experimental results in regard to the overall trend of S' with the emission energy, cf. Fig. 6.4a. At an emission energy of ≈ 3.38 eV such a 12 nm wide GaN QD is biaxially compressed by 9.0 GPa in its center due to the lattice mismatch to the underlying AlN. If the QD dimensions are now reduced, yielding a QD emission energy of ≈ 4.22 eV, then this biaxial stress rises up to 11.0 GPa with a direct effect on the LO-phonon frequencies for the $A_1(LO)$ and $E_1(LO)$ modes of the QD material (GaN). The calculated biaxial stress values can now be combined with the published phonon pressure coefficients for GaN [61] in order to determine the effect of the QD size on the LO-phonon energies. Note that published phonon pressure coefficients to date are only valid for room temperature but the slight hardening of the phonon frequencies towards cryogenic temperatures [88] can be neglected for the following estimations as the resulting deviation lies well within the widths of the measured E_{LO} distribution, cf. Fig. 6.4b. The predicted increasing stress towards smaller QDs is directly mirrored by the energy of the polar A_1(LO) and E_1(LO) modes with rising QD emission energy as shown in Fig. 6.6a. However, the stress-induced change of the LO-mode energies [$A_1(LO)$: 0.53 meV/eV, $E_1(LO)$: 0.65 meV/eV] cannot explain the measured trend for the E_{LO} energy dependence. The linear fit to the E_{LO} dataset from Fig. 6.4b is illustrated in Fig. 6.6a and differs by a factor of up to 15 for the $A_1(LO)$ mode.

Any more detailed stress variations over the extent of the QDs as reported by Grundmann et al. [131] are neglected in the given analysis as the exciton-LO-phonon interaction naturally averages over volumes that at least circumferences the exciton extent. In addition, the change of the biaxial stress in the QD center with emission energy is rather unaffected by such particular stress gradients. Only the absolute stress values can be flawed due to such averaging effects over an interaction volume. Hence, the general statement that the measured E_{LO} trend cannot exclusively be

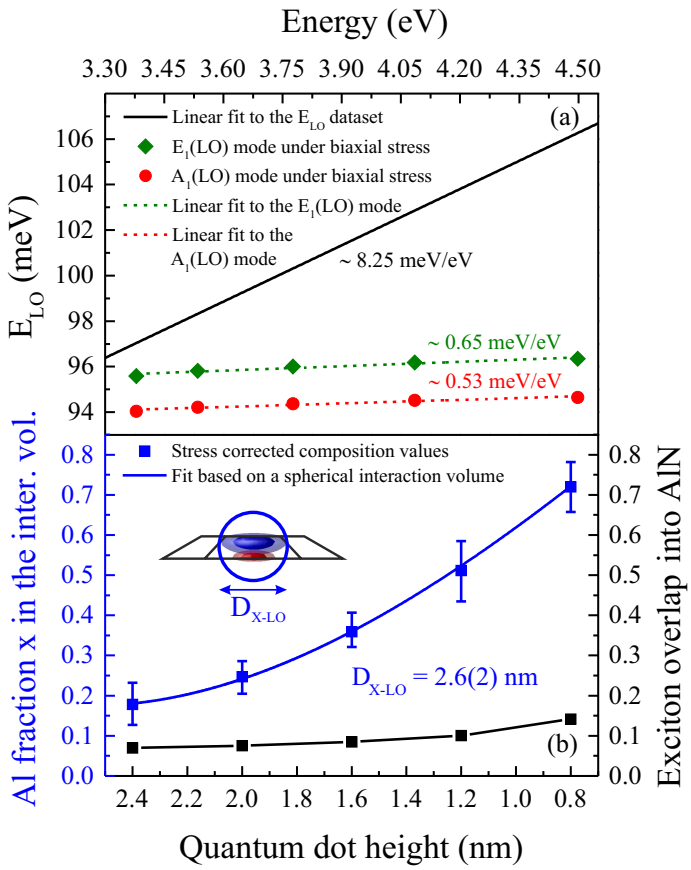

Figure 6.6: a) Linear fit to the E_{LO} dataset extracted from Fig. 6.4b along with the shifting behavior of the $A_1(LO)$ and $E_1(LO)$ modes under the influence of biaxial stress [61] induced by a quantum dot height reduction (2.4 - 0.8 nm, 12 nm diameter). b) Resulting Al mol fraction x in the exciton-LO-phonon interaction volume around the GaN QD center (inset) that leads to the E_{LO} dataset based on the stress-induced shifting of the $A_1(LO)$ mode. The fit to the data yields an estimate for the diameter of this interaction volume [$D_{X-LO} = 2.6(2)$]. Numbers in parentheses are the errors.

explained by a stress variation is maintained, no matter if just the QD center, or any larger volumes including the matrix material are considered.

Generally, the consideration of two LO-phonon modes [$A_1(LO)$ and $E_1(LO)$] is a main characteristic of the wurtzite lattice [161] as introduced in Chap. 3.1.3, page 25. The $A_1(LO)$ mode is based on oscillations of the Ga- vs. the N-sublattice in the direction of the c-axis, matching the geometry of the light detection in the μ-PL experiments, while the $E_1(LO)$ originates from corresponding oscillations perpendicular to the c-axis. Hence, the measured E_{LO} energy dependence should be dominated by coupling to the $A_1(LO)$ mode under quasi-resonant excitation. From this point onwards the discussion will be focused on the $A_1(LO)$ mode, keeping in mind that the stress induced shifting behavior of the $E_1(LO)$ mode does not significantly deviate if compared to the experimental data, cf. Fig. 6.6a.

The overall observed stress-induced shift rates are small in comparison to the slope of this E_{LO} dependence clearly demonstrating the negligible influence of the biaxial stress as described in point (ii). Based on the given discussion for point (i) and (ii) one now needs to discuss point (iii), the only plausible explanation left among the presented selection in order to explain the measured E_{LO} energy dependence.

In order to describe the measured E_{LO} energy dependence it is most feasible to

assume that the exciton-LO-phonon interaction averages over the GaN QD and the AlN matrix material resulting in an increased LO-phonon energy due to a strengthened influence of the surrounding AlN matrix material for smaller GaN QDs. The corresponding interaction volume can be approximated with a sphere as illustrated in the inset of Fig. 6.6b. Depending on the diameter D_{X-LO} of this spherical interaction volume, the exciton-LO-phonon interaction can now exclusively take place in the GaN material of the QD or it can overlap into the adjacent AlN matrix material yielding larger LO-phonon energies. The linear combination of the strain-induced $A_1(LO)$ mode position related to the GaN QD [GaN - $A_1(LO)$: 91.3 meV] and the corresponding, as unstrained approximated value for AlN at cryogenic temperatures [AlN - $A_1(LO)$: 110.8 meV] can now yield the measured E_{LO} values for each calculated QD emission energy. As a result, one obtains a composition ratio for all QD emission energies and the corresponding QD heights as illustrated in Fig. 6.6b. This composition dependence can now be fitted based on a simple geometric approach that assumes a constant exciton-LO-phonon interaction volume, while the QD height varies in between e.g. 0.8 and 2.4 nm. This approximation can now be used in order to estimate D_{X-LO} based on the present unique conjunction of theoretical and experimental data. Interestingly, by calculating the difference between the QD volume (truncated, hexagonal pyramid) and the interaction sphere one can indeed find a fixed value [D_{X-LO} = 2.6(2) nm] that well describes the calculated composition dependence as illustrated in Fig. 6.6b for the QD height series with a constant diameter of 12 nm. The second QD height series (16 nm QD diameter) that also relatively closely matched the experimental results from Fig. 6.4a, yields a within the error identical D_{X-LO} value.

This value for D_{X-LO} represents the first estimate for an exciton-LO-phonon interaction volume based on a significant number of single GaN QD spectra that revealed the underlying particular trend for the E_{LO} values. For large GaN QDs with a height of 2.4 nm the exciton-LO-phonon interaction volume can already be estimated by the extent of the exciton that overlaps into the matrix material, cf. Fig. 6.6b. However, with the reduction of the QD height from 2.4 to 0.8 nm the exciton overlap into the AlN matrix just scales from 6.9 % to 14.2 %, clearly demonstrating its negligible influence for the diameter of the exciton-LO-phonon interaction volume manifested by the measured E_{LO} values. Hence, for smaller QDs the origin of the determined interaction volume extent seems to be dominated by the regime of the phononic interaction and not by the excitonic extent and overlap into the matrix material. Please see Fig. 3.4 and 3.5 in Chap. 3, page 21 for an illustration of the corresponding electron and hole overlap into the matrix material for the QD center that diminishes as soon as the QD side facets are approached.

Furthermore, it was found that the best fit for the composition dependence shown

in Fig. 6.6b is obtained by introducing a constant composition offset of $\approx 17\,\%$. This offset value is motivated by the situation in QDs exhibiting a height that approaches the determined interaction volume diameter of 2.6(2) nm. Here, it appears that the interaction volumes starts to be more heavily influenced by the exciton extent with an overlap into the matrix material of 6.9 % for a QD with a height of 2.4 nm and a width of 12 nm. The fact that a larger offset is observed based on the fitting routine can additionally be well understood keeping the STEM results from Sec. 6.4 in mind. Here, a weak alloying effect was observed in the vicinity of the hole that now seems to be additionally confirmed by the extended μ-PL analysis in terms of a composition offset in access of the exciton overlap into the matrix material. Again, the results are consistent if compared to the second QD height series exhibiting QD diameters of 16 nm, cf. Fig. 6.4a. For instance a 2 nm high QD from this series exhibits an emission energy of 3.4 eV and a exciton overlap into the matrix material of 8.3 % approaching a constant composition offset of $\approx 14\,\%$ as obtained from a fit similar to the one shown in Fig. 6.6b. Furthermore, in the close vicinity of the QD the matrix material is also stressed, an effect that would further globally alter the determined aluminum fraction shown in Fig. 6.6b along with the composition offset. The assumption of a spherical shape for the exciton-LO-phonon interaction volume is motivated by its simplicity and the well agreement regarding the experimental results, cf. Fig. 6.6b. Since the electric dipole field beyond the excitonic charge distribution is diminishing with $\sim 1/r^3$, a spherical description of the exciton-LO-phonon interaction volume seems feasible. Clearly, the shape of this interaction volume should be influenced by geometric anisotropies and the different lateral expanses of the electron and hole wavefunctions as well as the particular nature of the contributing LO-phonons. However, any more complicated shape approximations (e.g. elliptical shape), introducing more fit parameters, are by no means appropriate for the number of data points shown in Fig. 6.6b. A detailed modeling of the exciton LO-phonon interaction volume remains a task for future work. The determined interaction volume diameter of 2.6(2) nm also explains why the QD facet alloying observed in Fig. 6.5 does not predominantly affect the exciton-LO-phonon coupling for the analyzed QD widths in contrast to the weak alloying effect in the vicinity of the hole. However, it can be assumed that fluctuations in the corresponding composition gradients cause the widths of the measured E_{LO} distribution shown in Fig. 6.4b.

6.5.1 Applicability of the spherical approximation and discussion

An improved agreement between the experimental and theoretical results shown in Fig. 6.4a can be obtained if the particular LO-phonon energies along with their emission energy dependence are considered. This energy dependence directly affects Eq. 6.2 via the Fröhlich constant comprising E_{LO} as described by the following formula [84]:

$$f_0 = \sqrt{2\pi e^2 \hbar E_{LO} \left(\frac{1}{\epsilon_\infty} - \frac{1}{\epsilon_0} \right)} \tag{6.3}$$

Hence, based on Eq. 6.2 and 6.3 one obtains $S \sim 1/E_{LO}$ for the Huang-Rhys factor. As the measured trend for E_{LO} resides above the bulk value of GaN and rises with the QD emission energy ($\sim 8.25(1.20)$ meV/eV) towards the bulk values of AlN, a lowering of the calculated S values from Fig. 6.4a could be obtained. Consequently, both QD height series illustrated in Fig. 6.4a (QD diameter of 12 and 16 nm) would achieve a better agreement with the experimental results. However, for the sake of clarity the application of any of such additional corrections is avoided in Fig. 6.4a. Hence, the theoretical results show S values based on a constant E_{LO} value (bulk GaN $A_1(LO)$ mode: 91.3 meV), which already yields a good agreement in comparison to the measured values. Over the emission energy interval Fig. 6.4a this correction scales in between 5 - 10 %, well within the limits of the experimental error and significantly below the overall widths of the datapoint distribution for S. The observation of the first and second LO-phonon replicas in Fig. 6.1 facilitates a general statement concerning the applicability of the chosen adiabatic approximation for calculating the Huang-Rhys factor in Sec. 6.2.3. The measured LO-phonon energies are not negligible in comparison to the electronic level spacings [91] or the related multiexcitonic level separations [39, 115, 119], possibly leading to a strong contribution of phonon-mediated scattering processes that are neglected in the adiabatic Huang-Rhys approach [84]. For InAs/GaAs QDs it was predicted that these non-adiabatic contributions should yield a strong enhancement of the second LO-phonon replicas by around 2 orders of magnitude if compared to the Huang-Rhys model [162]. However, already Dufåker et al. only observed an enhancement of the second LO-phonon intensity by a factor of 3 - 4 in InGaAs/GaAs QDs [156], clearly demonstrating a less dramatic significance of non-adiabatic effects. Interestingly, in wurtzite GaN/AlN QDs the ratio between the size of the e.g. electronic level spacings and the occurring huge LO-phonon energies is even more extreme in regard to possible phonon mediated scattering events. However, based on the presented analysis one can only observe an overestimation of the second LO-phonon replica by a factor of 2 - 3 in comparison to the Huang-Rhys-based peak area distribution [140, 144, 145] as shown in Fig. 6.1b along with the corresponding fitting function.

This observation substantiates the adiabatic treatment of the exciton LO-phonon coupling applied in this work, demonstrating only a small influence of non-adiabatic effects in wurtzite GaN QDs.
The long lasting debate in e.g. As-based QDs [136, 151, 152], whether the confined exciton in a QD interacts with LO-phonons of the QD material or the matrix material can considerably be advanced based on the observations from Fig. 6.4b. As discussed in Sec. 6.6, a natural transition is observed regarding the contribution of LO-phonons dominated by the QD (GaN) or matrix material (AlN). The predicted exciton LO-phonon interaction averages over a volume that includes a certain fraction of the QD and the matrix material, yielding the measured LO-phonon energy trend. In addition, the role of the exciton overlap into the matrix material along with the influence of weak alloying effects at the QD bases was demonstrated as supported by the STEM study from Sec. 6.4.
Finally, it should be pointed out that the small dielectric contrast at the QD interfaces (GaN/AlN) suppresses any strong coupling contribution related to optical interface modes and excitons [152,163–165] that could alter the measured Huang-Rhys factors and LO-phonon energies in the accessible QD height regime (1.2 - 2.4 nm). It is even expected that the lower-frequency interface optical-phonon modes exhibit a stronger Fröhlich coupling if compared to their higher-frequency counterparts residing in the frequency regime of the measured LO-phonon replica [165]. Hence, the μ-PL spectra from Fig. 6.2 already dissent any dominant contribution of optical interface modes, however, minor contributions cannot totally be ruled out and remain a challenging task for future work as their spectral regime is additionally affected by the LO-phonon traces related to the excited-state luminescence of GaN QDs (cf. QD2 and QD3 in Fig. 6.2). Additionally, a dominating effect of phonon confinement [166,167] cannot directly be witnessed in the extended μ-PL analysis of hundreds of individual GaN QDs. Almost all measured LO-phonon energies shown in Fig. 6.4b exceed the bulk value of the QD material [GaN: $A_1(LO)$: 91.3 meV], clearly supporting contributions of the matrix material and the related averaging phenomenon as the most dominant effect that explains the measurements.

6.5.2 The Huang-Rhys factor in strongly and weakly polar quantum dot systems - arsenides vs. nitrides

The huge difference in the magnitude of the Huang-Rhys factor S between wurtzite GaN/AlN QDs ($S \leq 0.8$, see Fig. 6.3b) and zincblende InAs/GaAs QDs ($S \leq 0.02$ [145]) is discussed in this chapter. Both QD systems act as representatives for a strongly and a weakly polar QD system and are similar concerning the spatial QD dimensions but essentially differ in two aspects:

(i) Owing to the hugely different band-gaps (GaN: 3.51 eV [168] vs. InAs: 0.417 eV [169]) the effective charge carrier masses differ by almost an order of magnitude leading to very different exciton Bohr radii (GaN: 3 nm / InAs: 35 nm) in both QD systems with a strong effect on the achievable charge carrier confinement.

(ii) The second aspect refers to the underlying lattice being zincblende in the case of InAs/GaAs and wurtzite for the GaN/AlN QD system. Both lattices lack inversion symmetry leading to piezoelectric fields in the case of strain. Their magnitudes, however, are much larger in the case of GaN QDs. Furthermore, a spontaneous polarization of the lattice that is unique to the wurtzite system causes the so called pyroelectric effect introduced in Chap. 3.1.1, page 22. Altogether, both effects lead to internal fields with a magnitude of up to several MV/cm in case of c-plane GaN/AlN QDs [46], which is at least 10 times larger than for InAs(111)/GaAs QDs [155].

In the case of c-plane GaN QDs the consequences for the ground-state exciton are a generally small extent of the electron and the hole wavefunction in the c-direction due to a strong confinement along the c-axis and a weak confinement in perpendicular directions. This observation is particularly true for the wavefunction of the hole that is laterally only weakly confined, cf. Fig. 6.3a. Hence, the overall lateral exciton extent is limited by the electron-hole Coulomb interaction rather than the confinement. For InAs/GaAs QDs, by contrast, the extent of the electron and the hole wavefunction is determined by the QD size. Moreover, due to its smaller effective mass the electron exhibits a stronger barrier penetration than the heavier hole, leading to an even larger spatial extent of the electron wavefunction. Hence, the vertical electron-hole dipole moment in InAs/GaAs QDs is comparatively small and mainly determined by In composition gradients within the QDs [132].
In order to compare these two systems with their dissimilar internal fields and effective masses, one can even resort to a more intuitive, analytical model using Gaussian functions as wavefunction replacements. The latter is strongly motivated by Eq. 6.2 showing that the Huang-Rhys factor S only depends on material properties such

as dielectric constants [160, 170] embedded in the Fröhlich constant f_0 [158], the LO-phonon energy E_{LO}, and on the wavefunctions' extent and separation. Hence, the following normalized ($\int g^2 dV = 1$) Gaussian function can be employed:

$$g(x,y,z) = \frac{e^{-[(x-\mu_x)^2/4\sigma_x^2+(y-\mu_y)^2/4\sigma_y^2+(z-\mu_z)^2/4\sigma_z^2]}}{(2\pi)^{\frac{3}{4}}\sigma_x\sigma_y\sigma_z}. \tag{6.4}$$

The vertical separation of the electron and hole wavefunctions is considered by the parameter $\mu_z^{e/h}$ with the separation $d = \mu_z^e - \mu_z^h$ as also depicted in Fig. 6.7. All wavefunctions (electron: $\psi_e = g_e$ and hole: $\psi_h = g_h$) are treated as oblate-shaped Gaussian functions with $\sigma_z < \sigma_x = \sigma_y$ in good agreement with 8-band k·p simulations for both QD systems [38,155]. In the context of the GaN QDs three parameters are varied, namely, (i) the vertical electron-hole separation, (ii) the lateral, and (iii) the vertical wavefunction extent as shown in Fig. 6.7a - c and described in the following:

(i) Vertical electron-hole separation. The Huang-Rhys factor S increases with increasing vertical electron-hole separation d reaching sizable values of about $S > 1.0$ for d approaching 5 nm, cf. Fig. 6.7(a). Comparable large QD heights have been found in the presented STEM analysis in Sec. 6.4 and are confirmed by the experimental results shown in Fig. 6.4a.

(ii) Lateral wavefunction extent. With increasing QD base length, both, electron and hole wavefunctions can expand up to the limit set by the Coulomb interaction. Accordingly, as shown in Fig. 6.7(b), S decreases with increasing lateral electron and hole extension for a fixed electron-hole separation d.

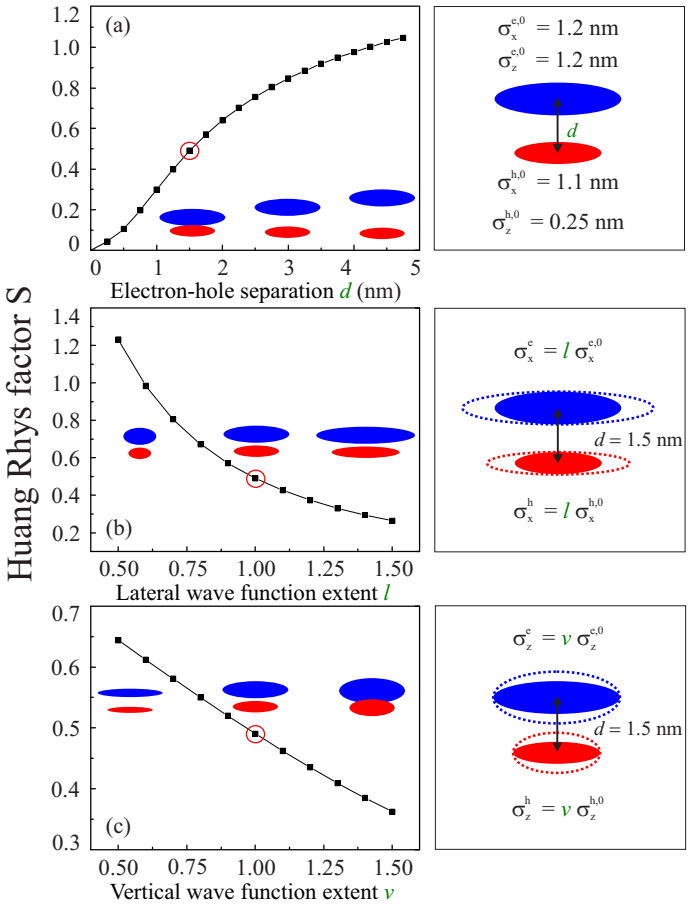

Figure 6.7: The influence of (a) the vertical electron-hole separation, (b) the lateral, and (c) the vertical wavefunction extent on the Huang-Rhys factor S based on the material parameters for GaN [160, 170]. The starting point of the calculations are electron and hole wavefunctions that were chosen to match the corresponding two-particle 8-band k·p wavefunctions of wurzite GaN quantum dots.

(iii) Vertical wavefunction extent. As result of an QD interface alloying, the vertical wavefunctions size may increase as described by the scaling parameter v in Fig. 6.7(c). Even though the QDs' top facets appeared as atomically flat in the STEM analysis (Sec. 6.4) an interface alloying at the QDs' bottoms can be observed, affecting the vertical wavefunction extent of the holes. As a result of such a change in the vertical wavefunction extent S can decrease with increasing vertical electron and/or hole extension for a fixed electron-hole distance d. This observation is particularly interesting in regard to Fig. 6.4a showing an overestimation of the theoretical values for S especially for smaller QDs in regard to the experimental counterparts, even though the detailed 8-band k·p modeling included QD dimensions in good agreement with the STEM results. Hence, the theoretical overestimation for S apparent in Fig. 6.4a could be caused by the interface alloying in the vicinity of the hole wavefunction that would increase its penetration into the QD matrix material causing a rise of the excitonic dipole moment scaling with the Huang-Rhys factor.

Additionally, the latter two cases (ii) and (iii) may well explain the experimentally observed scatter in the Huang-Rhys factors for a given exciton energy caused by

variations in the QD diameters and the interface roughening at the QDs' bottoms. For the case of InAs/GaAs QDs it is only feasible to differ between the following two cases due to the occurring small dipole moments, namely (iv) the overall exciton size and (v) the electron hole size ratio:

(iv) Variation of exciton size. The given variation in Fig. 6.8(a) links the GaN/AlN QD excitons with their inherently small electron/hole extent to the much larger excitons in the InAs/GaAs system. This case specifically aims at the differently sized electron and hole wavefunctions in InGaAs/GaAs QDs with their small intrinsic dipole moments. For a given set $(\sigma_i^e, \mu_i^e; \sigma_i^h, \mu_i^h)$ a transformation of the exciton size is performed by scaling $(\sigma_i, \mu_i) \longmapsto (x\,\sigma_i, x\,\mu_i)$, thus, connecting the size range of a wurtzite GaN/AlN exciton with the one of a InAs/GaAs exciton. Inspection of Eq. 6.2 shows that S scales with the inverse of the scaling factor x, $S \longmapsto (1/x)\,S$, meaning, that for a doubling of the exciton size S is halved, cf. Fig. 6.8(a). This scaling effect already accounts for large parts of the deviations between the two QD systems. As soon as the exciton size is decreased a strong rise for S can be observed even for the InAs/GaAs QD system, a situation that is permanently present in wurtzite GaN QDs.

(v) Electron/hole size ratio. Due to the asymmetric effective masses of the electron and the hole the electron's spatial extension is larger than that of the hole counterpart. The QD shape and internal fields, however, can override this asymmetry effect by e.g. forcing the hole wavefunction into the corners of the QD exhibiting minima in the piezoelectric potential, leading to complicated mutual size relations [145]. In order to account for this phenomenon in the present analytical model the electron wavefunction extent is varied between one half and three halves of an actual, fixed hole size, while the electron-hole separation also remains constant at $d = 0.3\,\mathrm{nm}$ as shown in Fig. 6.8(b). For evenly sized charge carriers the trend for the Huang-Rhys factor S exhibits a distinguished minimum that is exclusively affected by the inherent dipole extent d. As soon as the electron wavefunction deviates in size, the Huang-Rhys factor reaches sizable values of up to $S > 0.1$ even in the InAs/GaAs QD system, which is well comparable to the experimental results for small wurtzite GaN/AlN QDs shown in Fig. 6.4a.

The presented analytical model facilitates an understanding of the large Huang-Rhys factor variation observed for GaN QDs and its significant energy dependence in terms of the height-dependent size separation and the related QCSE-induced energy shift. Moreover, detailed insight was provided regarding the very different magnitudes of the Huang-Rhys factor found for the wurtzite GaN/AlN and the

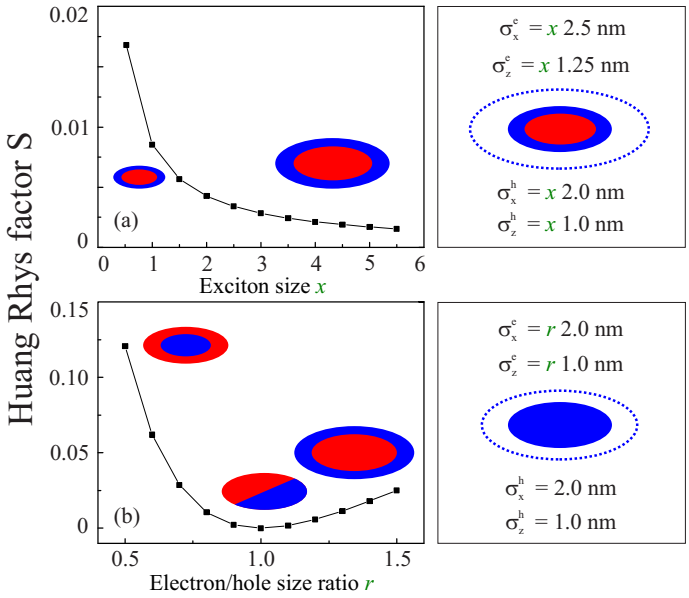

Figure 6.8: The influence of (a) the variation of exciton size and (b) the electron-hole size ratio on the Huang-Rhys factor S based on the material parameters for InAs [155]. Initially, the Gaussian-shaped electron and hole wavefunctions were matched to the corresponding 8-band k·p wavefunctions of zincblende InAs/GaAs quantum dots.

zincblende InAs/GaAs system. By applying Gaussian wavefunctions it was feasible to undertake a more detailed parameter study if compared to the 8-band k·p results. Furthermore, in the future all the described Gaussian wavefunctions can be applied by other research groups for an even more advanced modeling of the exciton-LO-phonon coupling with focus on the interaction volume, as they are based on the initial 8-band k·p calculations that achieved the present well agreement with the experimental data.

6.6 Summary

In summary, the luminescence traces of the exciton-LO-phonon interaction in hundreds of single, wurtzite GaN/AlN QDs were analyzed. General trends for the Huang-Rhys factor and the LO-phonon energy were identified by analyzing the Stokes-shifted LO-phonon replicas of first order. An increase of the QDs' emission energy from 3.2 to 4.2 eV leads to a decrease of the vital Huang-Rhys factor by over an order of magnitude ($\approx$ 0.5 - 0.01). By applying an adiabatic approximation residing on two-particle 8-band k·p wavefunctions, the Huang-Rhys factor was calculated for various QD dimensions in good agreement with the experimental trends. An analysis of the second LO-phonon replicas validates this adiabatic treatment even for strongly polar QD systems as represented by GaN QDs in contrast to theoretical reports from the literature. Based on this comparison between hundreds of measured Huang-Rhys factors and the corresponding theoretical trends it was shown that the QD height dominates all other QD geometry variations in such a strongly polar QD material system. The LO-phonon energy as the second fundamental parameter for

the exciton-LO-phonon interaction increases with rising QD emission energy, continuously scaling from the LO-phonon energies of the QD material (GaN) towards the corresponding values of the matrix material (AlN). It is shown that the slope of this measured LO-phonon energy trend [$\sim 8.25(1.20)$ meV/eV] cannot straightforwardly be explained by stress or composition variations affecting the QDs and their surroundings. A detailed STEM analysis proves that the measured LO-phonon energy variation is not predominantly caused by any alloying effects due to the specific field-induced localization of excitons in nitride QDs. Also the stress calculations cannot solely explain the measured LO-phonon energies, suggesting an averaging volume for the exciton-LO-phonon interaction, whose diameter can even surpass the individual QD height. For larger GaN QDs the diameter of this exciton LO-phonon interaction volume seems to well agree with the exciton extent overlapping into the AlN matrix material. However, for smaller GaN QDs the diameter of this interaction volume is not further dominated by the extent of the exciton but by the phononic contribution limiting its diameter. Novel general insight concerning the origin of the LO-phonons that contribute to the exciton LO-phonon interaction in embedded QDs is obtained as an averaging effect between the QD and the matrix material phonons is witnessed.

Based on the unique conjunction between the extended μ-PL analysis and the 8-band k·p based two-particle calculations, one obtains a first estimate for the diameter of an exciton-LO-phonon interaction volume yielding 2.6(2) nm for wurtzite GaN QDs. The determination of this value is facilitated by the strong exciton-LO-phonon interaction in nitride QDs revealing general trends for the Huang-Rhys factor and the LO-phonon energy as measures of the exciton-LO-phonon interaction. Such dependencies are commonly obscured in less-polar QD systems based on e.g. zincblende InAs/GaAs as additionally explained based on a straightforward analytical model.

7 Analysis of photon statistics: From one- to two-photon emission

A combined experimental and theoretical study of two-photon emission from the biexciton cascade in single, wurtzite GaN QDs is presented in this chapter. By changing the biexciton binding energy, pump power and temperature, the balance between the one- and two-photon decay processes is controlled in this 4-level system, which drastically affects the photon statistics of the resulting emission. As a most pronounced feature of this interplay one observes a bunching phenomenon and a transition from sub- to super-Poissonian photon statistics, originating from the complex nature of the biexciton cascade. It is demonstrated how photon-statistics can be steered between one- and two-photon processes towards an increased, bunched two-photon emission probability up to 50 K providing the perspective of photon pair generation in the ultraviolet spectral range. Furthermore, temperature-dependent correlation spectroscopy attests phonon-induced dephasing processes directly related to Chap. 6, page 74, while the in this chapter applied emission line assignment is based on Chap. 4, page 74.

The results presented in this chapter are published in Ref. [39]. The numerics that solve the quantum-state tomography of the biexciton cascade were developed and implemented in the research group of Prof. Dr. A. Knorr by Dr. A. Carmele. Only the joint efforts of experiment and theory finally lead to an intuitive explanation of the bunching phenomenon as presented within this chapter, confirming an efficient two-photon emission from the biexciton cascade in single, wurtzite GaN QDs.

7.1 Introduction to the bunching phenomenon

The search for quantum light sources exhibiting two-photon emission is related directly to applications in quantum information processing, cryptography and imaging [6, 171]. Prominent examples for two-photon emission involve parametric down-conversion and highly-pumped semiconductor quantum wells [172], or either atomic or semiconductor quantum dot (QD) based 4-level systems [173,174]. In contrast to single photon processes, which are bound to sub-Poissonian distributions, the statistics of a two-photon emission varies from non-classical (sub-Poissonian) to even

chaotic (super-Poissonian) behavior. For example, polarization-entangled photon pairs generated by a light-emitting diode can exhibit a sub-Poissonian distribution [173,175]. However, two-photon emission in the case of single emitters is not always solely associated with sub-Poissonian distributions.

In the following, controllable photon emission statistics are presented featuring a unique bunching phenomenon, which arises from the biexciton cascade emission from a single QD. Most interestingly, this system must theoretically be described by a 4-level system and not by most commonly applied independent 2-level system approaches, as substantiated by varying the biexciton binding energy, pump power and temperature during the photon correlation measurements. GaN QDs appear as an ideal semiconductor-based candidate for a study of such photon emission statistics because two significant parameters, namely the fine structure splitting of the excitonic bright-states [37] and the biexciton binding energy [75,83,119], can efficiently be tuned close to, or even across zero depending on the QD size. As a result, the photon-statistics are drastically altered, which is e.g. expressed by the observation of a different degree of bunched two-photon emission. Depending on the electronic configuration of the QD, the reported two-photon emission can deteriorate the antibunched single photon emission property of an exciton as long as the biexciton state is still populated, in addition to e.g. various types of commonly assumed background luminescence [176,177]. It is experimentally and theoretically shown that depending on the configuration of the QD's electronic states, the number of contributing decay processes changes drastically and shifts the weight between one- and two-photon processes, favoring either anti-bunched or bunched emission. The presented results contribute to the fundamental understanding of few photon emission events and highlight the importance of measuring the photon-statistics in order to probe exciton-correlations involved in the emission process. The observed tunable stream of bunched photons is inherently related and applicable to previously as non-classical considered effects [178], such as e.g. sub-wavelength interference [179] and ghost imaging [180].

7.2 Influence of the biexciton binding energy

Fig. 7.1a presents a scheme of the employed Hanbury-Brown & Twiss (HBT) correlation setup with indicators for the applied bandpass configurations (I., II., III.) and detected excitonic complexes (exciton - X, and/or biexciton - B). The corresponding μ-PL spectrum of a single GaN QD with X and anti-binding B emission is illustrated in Fig. 7.1b. Due to a large inscribed dipole moment, single GaN QD emission is affected by spectral diffusion [32,37] as previously introduced in Chap. 5, page 62 and acoustic phonon coupling [68]. The combination of both effects yields the ob-

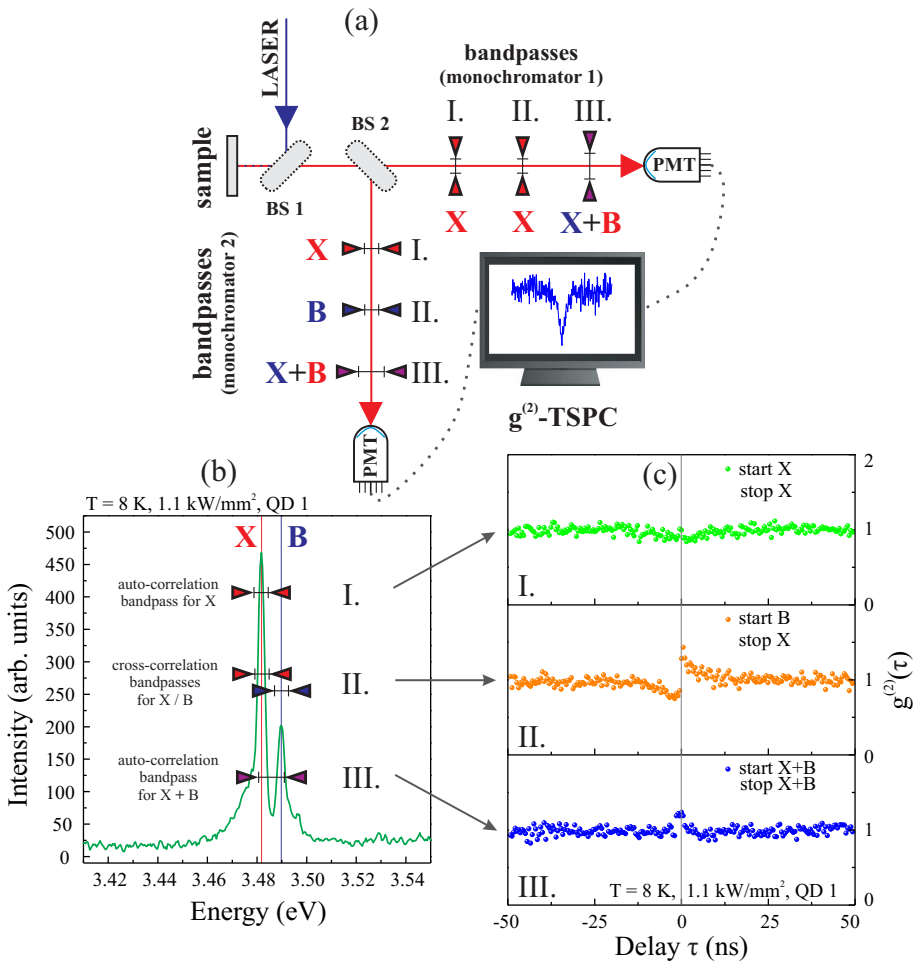

Figure 7.1: (a) Hanbury-Brown & Twiss setup for photon correlation measurements. Three different bandpass configurations (I., II., III.) are illustrated along with the detected excitonic complex (exciton - X and/or biexciton - B). (b) μ-PL spectrum of a single GaN quantum dot showing X and anti-binding B emission. The spectral width of the bandpasses for the auto- and cross-correlation measurements is depicted. (c) Auto-correlation measurement of X, cross-correlation measurement of B / X, wide bandpass auto-correlation measurement of X + B. Bandpass configuration III. indicates bunching with $g^{(2)}(0) = 1.23$.

served FWHM of X and B emission in the meV range, which stands in contrast to the corresponding radiative decay times, which are of the order of several ns for QD 1 - 3 as approved by time resolved μ-PL measurements, cf. Chap. 4.4, page 50. For instance, QD 1 yields a radiative decay time of 7.7 ns for X and 4.4 ns for B. The different applied bandpass configurations correspond to an auto-correlation measurement of X (I.), a cross-correlation measurement of B and X (II.), and a wide bandpass auto-correlation measurement that collects *both* complexes in *both* detection channels (III.). As a result, a weak $[g^{(2)}(0) = 0.90]$ antibunching is observed in Fig. 7.1c for the bandpass configuration I.

Such an incomplete antibunching feature can be explained as follows. In a low-pump situation a pronounced antibunching for similar wurtzite GaN QDs [31, 32] can be observed. However, for rising excitation power the influence of the occupied biexciton state on the overall emission statistics is strengthened, which is particularly valid for low biexciton binding energies (see Sec. 7.3 for further details). The common signature of a cross-correlation measurement of B and X, i.e. antibunching for negative delay times (τ) followed by bunching for positive τ, appears for bandpass configuration II. In contrast, for the wide bandpass auto-correlation measurement (III.) a definite [$g^{(2)}(0) = 1.23$] and around $\tau = 0$ symmetric bunching feature is observed.

In order to explore the origin of this bunching feature a large number of single GaN QDs was analyzed in order to locate QDs with varying biexciton binding energies E^B_{bind} around an emission energy of 3.5 eV. Exemplary μ-PL spectra of 3 GaN QDs (QD 1 - 3) are illustrated in Fig. 7.2a. QD 1 exhibits spectrally resolved X and antibinding B emission with a biexciton binding energy of $E^X - E^B = E^B_{bind} = -8.1$ meV. QD 2 and 3 exhibit E^B_{bind} below the FWHM of the envelope of the X and B emission. In contrast to QD 1, only one dominant emission line composed by X and B emission is observed. Based on a common FWHM value of $\gtrsim 5.0$ meV for X emitting at around 3.5 eV, an estimate of E^B_{bind} can be obtained for QD 2 and 3, which yields $|E^B_{bind}| \leq |-2.0|$ meV and $|E^B_{bind}| \leq |-0.3|$ meV, respectively. Auto-correlation measurements of the dominant emission of QD 3 with a bandpass as illustrated in Fig. 7.2a allows the observation of a strong bunching with $g^{(2)}(0) = 3.10$ as shown in Fig. 7.2b. An increase of the detuning E^B_{bind} between the X and B transition via QD 2 towards QD 1 now reduces the observed bunching effect down to $g^{(2)}(0) = 1.23$ as depicted in Fig. 7.2b and later on plotted in Fig. 7.3b.

The identification of the emission lines in the μ-PL spectra (Fig. 7.1b and 7.2a) of the GaN QDs originates from numerous excitation power dependent μ-PL and $g^{(2)}$-correlation function measurements on spectrally resolved and overlaying exciton (X) and biexction (B) emission peaks as exemplarily represented by QD 1 - 3. The comparison of absolute emission line areas in regard to variations of the pump power yields the scaling factor n for each excitonic complex [43] as introduced in Chap. 4, page 39. Within the spectral range around 3.5 eV one commonly observes e.g. $\mu_X = 1.1(1)$ and $\mu_B = 2.0(1)$ for GaN QDs like QD 1, which strongly indicates the identification of X and B emission [115, 119]. Also, the typical signature of a cross-correlation measurement as obtained for B and X (Fig. 7.1c) demonstrates a cascade process and hence further supports the given emission line identification [117].

Before turning towards the interpretation of the bunching phenomenon, some facts concerning the unusual biexcitonic structure of wurtzite GaN QDs will subsequently be summarized in order to substantialize the given emission line assignment before

a detailed explanation is given in Chap. 8, page 118. Within the analyzed spectral range at around 3.5 eV it is common for GaN QDs to exhibit the observed anti-binding B emission [115, 119]. The large spatial separation of the charge carriers in GaN QDs, originating from the built-in polarization fields parallel to the [0001]-axis, leads to a reduction of the binding terms in the B complex. For modeling this balance between binding and anti-binding terms in the B complex, the Coulomb, exchange and correlation interactions need to be taken into account [36, 75] as described in Chap. 8, page 118. Interestingly, for $\approx 2\,\%$ of the GaN QDs emitting at around 3.5 eV, as derived from a large (> 200) number of μ-PL measurements, the compensation between the binding and anti-binding terms in the B complex leads to a strong reduction of the absolute value of the biexciton binding energy $|E^B_{bind}|$ as e.g. observed for QD 2 and 3. As a consequence, no clear spectral separation between the X and B emission lines can be observed based on the occurring FWHM values and bunching in the $g^{(2)}$-correlation function occurs for selected QDs, cf. Fig. 7.2b. The statistical μ-PL analysis has shown for the analyzed sample that an average $E^B_{bind} \approx -8$ meV is common for GaN QDs emitting at around 3.5 eV, an observation previously introduced in Chap. 4.2, page 40. However, mainly due to diameter fluctuations of the QDs in the sample of interest, one can also observe $|E^B_{bind}|$ values well below the commonly observed FWHM value of $\gtrsim 5.0$ meV for X (see lower quartile of the line widths distribution from Fig. 5.2, page 66). Consequently, excitation power dependent μ-PL measurements yield scaling factors of $n_{X+B} = 1.4(1)$ e.g. for QD 2 and 3 suggesting a spectral overlay between the X and B emission for those QDs.

7.3 The quantum-state tomography of the biexcitonic decay

The explanation of the observed bunching phenomenon will be addressed in this section. Bunching in the $g^{(2)}$-correlation function itself is not an uncommon feature in QD spectroscopy and is e.g. assigned to spectral diffusion [137, 181] or weakly pumped biexcitons [182]. However, such origins for the reported bunching phenomenon can be excluded as explained in Sec. 7.5. Especially the E^B_{bind}-dependence of the bunching phenomenon does not allow its straight-forward simulation based on typical rate equation approaches [5, 183] and realistic parameters for wurtzite GaN QDs embedded in AlN [43, 45]. As a consequence, the quantum-state tomography of the biexciton cascade [149, 184] can numerically be solved in order to account for the quantum mechanical particularities of the analyzed system.

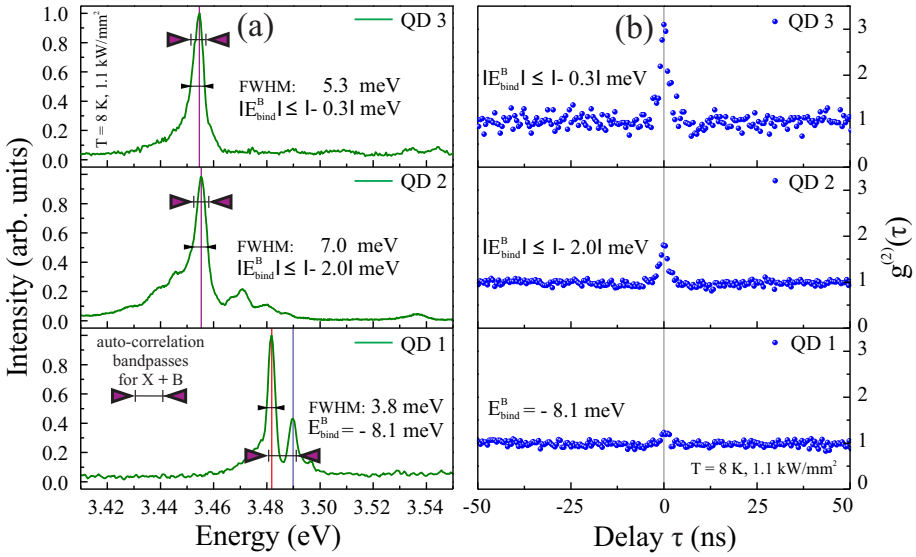

Figure 7.2: (a) Exemplary μ-PL spectra of GaN QDs 1 - 3 showing spectrally resolved exciton (X) and biexciton (B) emission (QD 1) or corresponding spectrally overlapping X + B emission (QD 2 and 3). The FWHM and the biexciton binding energy (E^B_{bind}) are shown along with applied auto-correlation bandpasses. (b) Auto-correlation measurements for the corresponding quantum dots illustrate the inverse scaling behavior between the photon bunching strength $g^{(2)}(0)$ and the detuning E^B_{bind}.

The corresponding Hamilton operator within the rotating wave and dipole approximation, still without the system-environment coupling, reads:

$$\begin{aligned} H &= \hbar \sum_k \omega_k^0 c_k^\dagger c_k - \hbar \sum_{j=H,V} M_k (G^\dagger X_j c_k^\dagger + X_j^\dagger B c_k^\dagger) + \text{H.c.} \\ &\quad + \hbar\omega_B \; B^\dagger B \; + \hbar\omega_H \; X_H^\dagger X_H + \hbar\omega_V \; X_V^\dagger X_V . \end{aligned} \tag{7.1}$$

Here, the Coulomb interaction between the horizontally and vertically polarized excitons (H, V) is incorporated in the ground-state $G^\dagger$, the exciton $X^\dagger_{H/V}$ and the biexciton $B^\dagger$ operators with the eigenenergies $\hbar\omega_{B/H/V}$, determined by the fine-structure splitting of the excitonic bright states $E^X_{FSS} = \hbar(\omega_H - \omega_V)$ and E^B_{bind}. The precise value for E^X_{FSS} does not change the theoretical results if chosen as just sufficiently small in comparison to E^B_{bind}, which is typical for GaN QDs emitting at around 3.5 eV [37]. Hence, for simplicity $\omega_H = \omega_V$ is assumed for the following explanation, cf. Fig. 7.3a and d. The ground-state energy is chosen as zero and the electron-photon coupling element M_k couples equally strong to both polarizations (H, V), while the photon-creation and -annihilation operators are denoted with $c_k^\dagger$ and c_k. The system dynamics based on the Hamiltonian from Eq. 7.1 describe very complex emission dynamics into free space, i.e. a photon mode continuum with wavenumber k [150, 185]. Since the experiment only detects photons in reso-

nance with the exciton-biexciton state transition ($X^\dagger_{H/V}B$) and the ground-exciton state transition ($G^\dagger X_{H/V}$), the complex dynamics can be reduced to two modes k_B and k_X. Therefore, only two polarization-independent modes in resonance are assumed with the exciton-ground state transition $\omega^0_X = c_0 k_X = \omega_{H/V}$ and the biexciton-exciton state transition $\omega^0_B = c_0 k_B = \omega_B - \omega_{H/V}$, while $c^\dagger_{X/B}$ denotes the corresponding photon-creation and -annihilation operators in agreement with the experimental limitations.

Concerning the loss of photons and excitonic coherence due to the system-environment coupling, a Markovian approximation is applied. This is possible, since the time-scale of the observed emission processes leading to a bunching signature is within the nanosecond regime and, clearly, losses such as pure dephasing dominate the dynamics. In order to consistently introduce such losses, the Born-Markov approach in the Lindblad-form was chosen for a system operator A ($\mathcal{L}[A]\rho := 2A\rho A^\dagger - A^\dagger A\rho - \rho A^\dagger A$), which takes into account photon mode loss κ, incoherent pumping P [186], radiative decay Γ_{rad}, and phenomenological pure dephasing γ_{pure} (LA-phonon-based, band diagonal pure dephasing mechanism [149]) based on their corresponding rates. Finally, the complete dynamics is calculated within the density matrix ρ approach ($\dot\rho = \frac{i}{\hbar}[\rho, H] + \mathcal{L}\rho$) comprising a dissipative Liouvillian $\mathcal{L}$ and parameters that assure the weak coupling limit ($\kappa + \gamma_{pure} \gg M$) in order to prevent any induced emission dynamics, clearly not present in the experiment. As a result of the introduced simplifications, the theoretical description does not allow a full quantitative discussion of the bunching phenomenon, but still provides an essential qualitative description and successfully reveals the underlying physics. The following dissipative Liouvillian $\mathcal{L}$ is applied:

$$\begin{aligned}\mathcal{L}\rho \;:=\; & \frac{\kappa}{2}\sum_{i=X,B}\mathcal{L}[c_i]\rho + P\sum_{j=H,V}\mathcal{L}[X_j^\dagger G]\rho + \mathcal{L}[B^\dagger X_j]\rho \\ & + \Gamma_{rad}\sum_{j=H,V}\mathcal{L}[G^\dagger X_j]\rho + \mathcal{L}[X_j^\dagger B]\rho - \sum_{k=G,X,B}\gamma_k\left(T_k\rho T_k - \rho\right)\end{aligned} \tag{7.2}$$

Here, ρ denotes the density matrix while κ, P, Γ_{rad}, and γ_{pure} are the rates for the mode loss, the incoherent pumping [186, 187], the radiative decay and the phenomenological pure dephasing [149]. The pure dephasing part of $\mathcal{L}$ is defined with $T_G = X^\dagger_H X_H + X^\dagger_V X_V - G^\dagger G$, $T_X = B^\dagger B - X^\dagger_H X_H - X^\dagger_V X_V$, as also $T_B = B^\dagger B - G^\dagger G$ for the three possible population differences and $\gamma_G = \gamma_X = \gamma_{pure}$, $\gamma_B = 2\gamma_{pure}$ as the dephasing constants.

Based on the described model one can derive the stationary correlation function $g^{(2)}(0) = \langle c^\dagger_B c^\dagger_X c_X c_B\rangle / \langle c^\dagger_X c_X\rangle\langle c^\dagger_B c_B\rangle$ (see Sec. 7.3.2 for all resulting equations). Bunching processes yielding $g^{(2)}(0) > 1$ (see Fig. 7.2b and 7.3b) trivially confirm that the intensity-intensity correlation (IIC) is larger than the intensity itself,

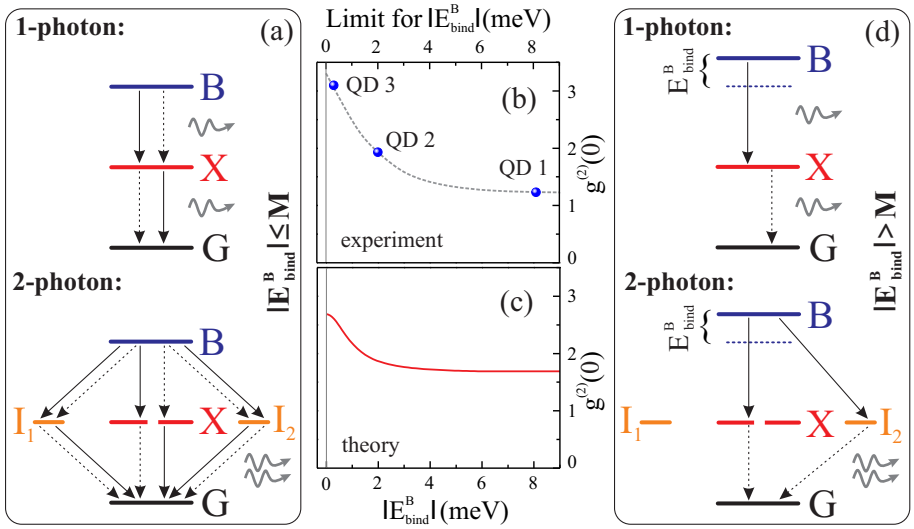

Figure 7.3: (a) Level scheme of the biexciton cascade for the resonant case with a biexciton binding energy $|E^B_{bind}| \leq M$. Biexciton, exciton, intermediate-states and ground-state are denoted with B, X, $I_{1/2}$, and G, while M is the electron-photon coupling element. Dashed/solid arrows denote the exciton/biexciton photon modes. (b) + (c) Theoretical and experimental $g^{(2)}(0)$ values for varying E^B_{bind} (dashed line → guide to the eye) d) Level scheme of the biexciton cascade for the non-resonant case $|E^B_{bind}| > M$.

hence two-photon processes dominate their one-photon counterparts resulting in: $\langle c^\dagger_B c^\dagger_X c_X c_B\rangle > \langle c^\dagger_X c_X\rangle\langle c^\dagger_B c_B\rangle$. As a consequence of the measured E^B_{bind} dependence of $g^{(2)}(0)$ (Fig. 7.2b and 7.3b) one now needs to elucidate the E^B_{bind}-affected balance between the intensity and the IIC. Contributions from all decay processes involved in the generation of the intensity and the IIC facilitate the calculation of $g^{(2)}(0, E^B_{bind})$ as shown in Fig. 7.3c. This theoretical result agrees well with the trend of the experimental data from Fig. 7.3b.

7.3.1 Intuitive explanation of the bunching phenomenon

In order to intuitively explain the measured and calculated asymmetric effect of E^B_{bind} on the intensity and the IIC, a straightforward description of the bunching phenomenon based on the level schemes shown in Fig. 7.3a and d is possible. Here two scenarios with respect to the ratio between the biexciton binding energy E^B_{bind} and the electron-photon coupling element M are classified; the resonant case $|E^B_{bind}| \leq M$ (see Fig. 7.3a) and the non-resonant case $|E^B_{bind}| > M$ (Fig. 7.3d). Only most dominating, i.e. resonantly contributing, decay processes are depicted with dashed or solid arrows for the exciton and biexciton photon modes k_X and k_B.

The source of the intensity are the photon-assisted B-X and X-G state transitions as depicted in Fig. 7.3a and d (top). For $|E^B_{bind}| \leq M$ all state transitions are in resonance with the modes of the emitted light field k_X and k_B and hence four

transition processes originate the intensity in Fig. 7.3a (top). However, as soon as $|E^B_{bind}| > M$ occurs, only two processes still resonantly contribute to the intensity as shown in Fig. 7.3d (top), due to the existing mismatch e.g. between the B-X state transition and the k_X mode.

In contrast to the intensity, the IIC is genuinely a two-photon process, which is first of all fed by a generally larger number of radiative decay processes as illustrated in Fig. 7.3a and d (bottom). For $|E^B_{bind}| \leq M$ the B-X and X-G state transitions are in resonance with the k_X and k_B modes, and a large number of decay processes arises. The B-X state transition can either populate the one-photon X states (vertical arrows) or the correlated two-photon intermediate (I) states (diagonal arrows), which are either density- (I_1) or polarization-like (I_2). Please see Sec. 7.3.2 for a more detailed description of both two-photon states. These two-photon I states are a particular feature of the 4-level system and are essential for the description of the bunching phenomenon that arises from the biexciton cascade [149, 175]. Subsequently, the system evolves via the one-photon X and the intermediate two-photon states I_1 and I_2 into the two-photon G state by emission of a photon pair. As a result there are ten possible two-photon decay processes towards G in Fig. 7.3a (bottom), eight via the two-photon I states and two via the one-photon X state if the weak coupling regime is assumed. Please note the break in the X state visible in Fig. 7.3a and d (bottom), which just illustrates that no twofold population of the same mode is possible in the IIC schemes.

Again, with a larger detuning $|E^B_{bind}| > M$ the situation changes significantly. Due to the lifted resonance condition only two two-photon decay processes survive and contribute efficiently to the IIC as expressed by the remaining bunching in Fig. 7.3b and c for larger detunings. All other eight processes become off-resonant and hence negligible as shown in Fig. 7.3d (bottom). Only one residual process still resonantly populates the polarization-like two-photon I_2 state and another one the X state, which then still allows the formation of a photon pair. Hence, the reduction of the number of contributing decay processes is 10→2 for the IIC, which is in clear contrast to the case of the intensity, where the reduction of the contributing decay processes is just 4→2. This asymmetry in the E^B_{bind} dependence of the $g^{(2)}(0)$-function based on the number of contributing decay channels for the intensity and the IIC explains the detuning dependence of the bunching phenomenon. Only the absolute detuning value $|E^B_{bind}|$ is relevant for steering the photon statistics between one- and two-photon processes (intensity ↔ IIC) as the detuning dependence of $g^{(2)}(0)$ is symmetric, i.e. only the energetic difference between $|E^B_{bind}|$ and M tunes the bunching strength.

Considering the particular nature of a 4-level system it is now also possible to understand the comparable [32] weak antibunching feature of the excitonic emission

of QD 1 in Fig. 7.1c [$g^{(2)}(0) = 0.90$]. Even though the X and B emission are spectrally separated, there is just weak indication for an antibunching dip due to a residual overlay with the two-photon process induced bunching, which is neglected in frequently applied 2-level based models [5, 31, 183]. Not only commonly assumed background luminescences deteriorate such single photon emission [176, 177], also two-photon processes play a dominant role if the biexciton state is initially occupied. This matter is demonstrated by the residual bunching in Fig. 7.3b and c, even for larger E^B_{bind} exceeding the FWHM of the related emission lines. For particular, large E^B_{bind} values of e.g. around $-35\,\mathrm{meV}$ [32] one can observe much smaller $g^{(2)}(0)$ values compared to QD 1 for even up to 200 K due to a negligible influence of 2-photon processes, cf. Fig. 7.3b. Please note that the theory also predicts a strong influence of E^X_{FSS} on the bunching phenomenon as soon as it approaches the quantity of M. Hence, for particular and on the analyzed sample rare QD shapes and sizes it is even possible to observe smaller $g^{(2)}(0)$ values than for QD 1 with comparable E^B_{bind} but consequently deviating and not negligible E^X_{FSS}. By choosing typical GaN QDs emitting at around 3.5 eV, based on analyzing a statistical valid number of QDs, one frequently observes QDs with negligible E^X_{FSS} in regard to M and E^B_{bind}. Hence, for smaller GaN/AlN QDs emitting at higher energies, or even for QDs based on other material systems such as e.g. InAs/GaAs, one would have to take the unique balance of E^B_{bind} and E^X_{FSS} into account in order to estimate the strength of the 2-photon processes that induce the bunching phenomenon.

7.3.2 One- and two-photon processes in the biexciton cascade

The explanation of the bunching phenomenon is mainly based on the number of decay processes, which either contribute to the intensity or the intensity-intensity-corellation (IIC) representing the denominator and nominator of the $g^{(2)}$-correlation function, respectively. Distinction between the resonant case ($|E^B_{bind}| \leq M$) and the non-resonant case ($|E^B_{bind}| > M$) is achieved by comparing $|E^B_{bind}|$ with the electron-photon coupling element M. Even though the given explanation based on level schemes (Fig. 7.3a and d) might be intuitive, it cannot account for all the details of such a complex 4-level system as the biexciton cascade.

In detail one can e.g. describe the level schemes, which illustrate the generation of the intensity (one-photon processes) in Fig. 7.3a and d (top) via the decay of the biexciton density $\langle B^\dagger B\rangle$ by spontaneous emission, as shown in the following:

$$
\begin{aligned}
&(1) \quad \left\langle B^\dagger B\right\rangle \overset{\Delta}{\rightarrow} \left\langle X^\dagger B c_X^\dagger\right\rangle \overset{\Delta}{\rightarrow} \left\langle c_X^\dagger c_X\right\rangle \\
&(2) \quad \left\langle B^\dagger B\right\rangle \rightarrow \left\langle X^\dagger B c_B^\dagger\right\rangle \rightarrow \left\langle c_B^\dagger c_B\right\rangle \\
&(3) \quad \left\langle X^\dagger X\right\rangle \overset{\Delta}{\rightarrow} \left\langle G^\dagger X c_B^\dagger\right\rangle \overset{\Delta}{\rightarrow} \left\langle c_B^\dagger c_B\right\rangle \\
&(4) \quad \left\langle X^\dagger X\right\rangle \rightarrow \left\langle G^\dagger X c_X^\dagger\right\rangle \rightarrow \left\langle c_X^\dagger c_X\right\rangle
\end{aligned}
$$

Decay path 1 and 3 (black) are influenced by the absolute value of a detuning $\Delta = |E_{bind}^B|$ and vanish for rising $|E_{bind}^B|$, whereas decay path 2 and 4 (red) are maintained even for larger detunings. Here the ground-state, the exciton and the biexciton operators are again denoted with $G^\dagger$, $X^\dagger$, and $B^\dagger$, while the photon creation and annihilation operators are consistently denoted with $c_{X/B}^\dagger$ and $c_{X/B}$. For the resonant case all 4 decay processes contribute to the intensity but as soon as the non-resonant case is reached, only 2 decay processes remain and contribute to the denominator of the $g^{(2)}$-correlation function. However, for the IIC as the numerator of the $g^{(2)}$-correlation function, 10 decay processes contribute to the resonant case that is reduced to 2 dominant decay processes (red) for the non-resonant case with larger detuning $\Delta = E_{bind}^B$. The resulting decay processes (two-photon processes) for the IIC are illustrated in Fig. 7.3a and d (bottom) and can be summarized to:

$$
\begin{aligned}
&(1) : I_2 \quad \langle B^\dagger B\rangle \overset{\Delta}{\rightarrow} \left\langle X^\dagger B c_X^\dagger\right\rangle \overset{\Delta}{\rightarrow} \left\langle G^\dagger B c_X^\dagger c_B^\dagger\right\rangle \overset{\Delta}{\rightarrow} \left\langle G^\dagger X c_X^\dagger c_B^\dagger c_X\right\rangle \overset{\Delta}{\rightarrow} \left\langle c_B^\dagger c_X^\dagger c_X c_B\right\rangle \\
&(2) : I_2 \quad \langle B^\dagger B\rangle \overset{\Delta}{\rightarrow} \left\langle X^\dagger B c_X^\dagger\right\rangle \overset{\Delta}{\rightarrow} \left\langle G^\dagger B c_X^\dagger c_B^\dagger\right\rangle \rightarrow \left\langle G^\dagger X c_X^\dagger c_B^\dagger c_B\right\rangle \rightarrow \left\langle c_B^\dagger c_X^\dagger c_X c_B\right\rangle \\
&(3) : X \quad \langle B^\dagger B\rangle \overset{\Delta}{\rightarrow} \left\langle X^\dagger B c_X^\dagger\right\rangle \overset{\Delta}{\rightarrow} \left\langle X^\dagger X c_X^\dagger c_X\right\rangle \overset{\Delta}{\rightarrow} \left\langle G^\dagger X c_X^\dagger c_B^\dagger c_X\right\rangle \overset{\Delta}{\rightarrow} \left\langle c_B^\dagger c_X^\dagger c_X c_B\right\rangle \\
&(4) : I_1 \quad \langle B^\dagger B\rangle \overset{\Delta}{\rightarrow} \left\langle X^\dagger B c_X^\dagger\right\rangle \rightarrow \left\langle X^\dagger X c_X^\dagger c_B\right\rangle \rightarrow \left\langle G^\dagger X c_X^\dagger c_B^\dagger c_X\right\rangle \overset{\Delta}{\rightarrow} \left\langle c_B^\dagger c_X^\dagger c_X c_B\right\rangle \\
&(5) : I_1 \quad \langle B^\dagger B\rangle \overset{\Delta}{\rightarrow} \left\langle X^\dagger B c_X^\dagger\right\rangle \rightarrow \left\langle X^\dagger X c_X^\dagger c_B^\dagger\right\rangle \overset{\Delta}{\rightarrow} \left\langle G^\dagger X c_X^\dagger c_B^\dagger c_B\right\rangle \rightarrow \left\langle c_B^\dagger c_X^\dagger c_X c_B\right\rangle \\
&(6) : I_2 \quad \langle B^\dagger B\rangle \rightarrow \left\langle X^\dagger B c_B^\dagger\right\rangle \rightarrow \left\langle G^\dagger B c_X^\dagger c_B^\dagger\right\rangle \overset{\Delta}{\rightarrow} \left\langle G^\dagger X c_X^\dagger c_B^\dagger c_X\right\rangle \overset{\Delta}{\rightarrow} \left\langle c_B^\dagger c_X^\dagger c_X c_B\right\rangle \\
&(7) : I_2 \quad \langle B^\dagger B\rangle \rightarrow \left\langle X^\dagger B c_B^\dagger\right\rangle \rightarrow \left\langle G^\dagger B c_X^\dagger c_B^\dagger\right\rangle \rightarrow \left\langle G^\dagger X c_X^\dagger c_B^\dagger c_B\right\rangle \rightarrow \left\langle c_B^\dagger c_X^\dagger c_X c_B\right\rangle \\
&(8) : X \quad \langle B^\dagger B\rangle \rightarrow \left\langle X^\dagger B c_B^\dagger\right\rangle \rightarrow \left\langle X^\dagger X c_B^\dagger c_B\right\rangle \rightarrow \left\langle G^\dagger X c_X^\dagger c_B^\dagger c_B\right\rangle \rightarrow \left\langle c_B^\dagger c_X^\dagger c_X c_B\right\rangle \\
&(9) : I_1 \quad \langle B^\dagger B\rangle \rightarrow \left\langle X^\dagger B c_B^\dagger\right\rangle \overset{\Delta}{\rightarrow} \left\langle X^\dagger X c_X^\dagger c_B\right\rangle \overset{\Delta}{\rightarrow} \left\langle G^\dagger X c_X^\dagger c_B^\dagger c_B\right\rangle \rightarrow \left\langle c_B^\dagger c_X^\dagger c_X c_B\right\rangle \\
&(10) : I_1 \quad \langle B^\dagger B\rangle \rightarrow \left\langle X^\dagger B c_B^\dagger\right\rangle \overset{\Delta}{\rightarrow} \left\langle X^\dagger X c_X^\dagger c_B\right\rangle \rightarrow \left\langle G^\dagger X c_X^\dagger c_B^\dagger c_X\right\rangle \overset{\Delta}{\rightarrow} \left\langle c_B^\dagger c_X^\dagger c_X c_B\right\rangle
\end{aligned}
$$

As an example for the resulting complex set of equations, the equation of motion for the photon-assisted ground-biexciton state transition is given:

$$
\begin{aligned}
&\partial_t \left\langle G^\dagger B C_B^{m,n} C_X^{p,q} \right\rangle \\
&= -i \left(\omega_B - (m-n)\omega_B^0 - (p-q)\omega_X^0\right) \left\langle G^\dagger B C_B^{m,n} C_X^{p,q} \right\rangle \\
&\quad - \kappa(m+n+p+q) \left\langle G^\dagger B C_B^{m,n} C_X^{p,q} \right\rangle \\
&\quad - (2P + 2\gamma_{pure} + 2\Gamma_{rad}) \left\langle G^\dagger B C_B^{m,n} C_X^{p,q} \right\rangle \\
&\quad + i\ M \sum_{i=H,V} \left\langle X_i^\dagger B\ C_B^{m,n+1} C_X^{p,q} \right\rangle + \left\langle X_i^\dagger B\ C_B^{m,n} C_X^{p,q+1} \right\rangle \\
&\quad - i\ M \sum_{i=H,V} \left\langle G^\dagger X_i\ C_B^{m,n+1} C_X^{p,q} \right\rangle + \left\langle G^\dagger X_i\ C_B^{m,n} C_X^{p,q+1} \right\rangle \\
&\quad + i\ M \sum_{i=H,V} m\ \left\langle X_i^\dagger B\ C_B^{m-1,n} C_X^{p,q} \right\rangle + p\ \left\langle X_i^\dagger B\ C_B^{m,n} C_X^{p-1,q} \right\rangle
\end{aligned}
\tag{7.3}
$$

with $C_B^{m,n} := c_B^{\dagger m} c_B^n$ and $C_X^{p,q} := c_X^{\dagger p} c_X^q$ and m, n, p, q as integers. Since, the observable is calculated in the spontaneous emission limit, only ground-biexciton state transitions with $m+p=2$ and $n=q=0$ contribute. As an example, Eq. 7.4 shows the resulting important polarization-like intermediate-state transition with $m=2$ and $p=0$:

$$
\begin{aligned}
&\partial_t \left\langle G^\dagger B C_B^{2,0} C_X^{0,0} \right\rangle \\
&= -i \left(\omega_B - 2\omega_B^0\right) \left\langle G^\dagger B C_B^{2,0} C_X^{0,0} \right\rangle \\
&\quad - 2\left(\kappa + P + \gamma_{pure} + \Gamma_{rad}\right) \left\langle G^\dagger B C_B^{2,0} C_X^{0,0} \right\rangle \\
&\quad + i\ 2\ M \sum_{i=H,V} \left\langle X_i^\dagger B\ C_B^{1,0} C_X^{0,0} \right\rangle
\end{aligned}
\tag{7.4}
$$

Finally, the stationary, adiabatic limit is of interest, hence, the biexciton energy must be written as $\omega_B = \omega_B^0 + \omega_X^0$ in order to obtain

$$
\left\langle G^\dagger B C_B^{2,0} C_X^{0,0} \right\rangle = i\ 2\ M \sum_{i=H,V} \frac{\left\langle X_i^\dagger B\ C_B^{1,0} C_X^{0,0} \right\rangle}{i E_{bind}^B + 2\left(\kappa + P + \gamma_{pure} + \Gamma_{rad}\right)}. \tag{7.5}
$$

Note: $\omega_B - 2\omega_B^0 = \omega_B^0 + \omega_X^0 - 2\omega_B^0 = \omega_X^0 - \omega_B^0 = -E_{bind}^B$ with $\omega_B^0 = \omega_X^0 + E_{bind}^B$. Consequently, for this important transition that is feeding the cross-correlation, one observes a strong effect of E_{bind}^B and γ_{pure}, which is for the latter case twice as large as for the one-photon transitions. The full set of parameters used for the calculation

of the bunching phenomenon and its E^B_{bind}, pump rate, and temperature dependence is listed in Tab. 7.1.

The two remaining decay processes 7 and 8 (red) for the non-resonant case decay via the polarization-like two-photon intermediate I_2 and the X state and are not effectively influence by the detuning $\Delta = E^B_{bind}$, cf. Fig. 7.3d (bottom). The decay processes via the intermediate two-photon I_1 or I_2 states are either density- or polarization-like, as expressed by the notation of the processes given in either 4, 5, 9, and 10 or 1, 2, 6, and 7. The processes 3 and 8 represent decay processes via the X state and are classical in case of 8 (first generation of a B photon then of an X photon) or clearly non-classical as for case 3 (first generation of an X photon then of a B photon). Please note that only the absolute value of the detuning $\Delta = |E^B_{bind}|$ has an impact on the contribution of the decay processes to the intensity and the IIC as only the energetic state offset influences the computed dynamics.

7.4 Excitation power and temperature dependence

Further parameter studies of the pump power and the temperature dependence were conducted in order to confirm the given interpretation by a comparison of the trends for the experimentally and theoretically derived $g^{(2)}(0)$-values. Fig. 7.4a illustrates the power dependence of the bunching phenomenon for QD 2 at 25 K, showing a reduction of the bunching towards higher pump powers (Fig. 7.4b). The evolution of the bunching phenomenon with temperature is shown in Fig. 7.5a. At 6 K a strong bunching is observed for QD 2, which is reduced upon the rise of temperature towards 50 K and finally vanishes at ≤ 70 K (see Fig. 7.5b). For the smallest experimentally accessible pump powers and temperatures, two-photon processes can well compete with one-photon processes. Consequently, a bunched photon emission is observed as long as the biexciton state is still sufficiently populated.

Both, the pump power and the temperature dependence of the bunching phe-

Table 7.1: Set of essential parameters applied for the quantum-state tomography calculations of the biexciton cascade in wurtzite GaN quantum dots.

Parameter description:	**Value**
electron-photon coupling element M	$0.06\,\mathrm{ps}^{-1}$
pump rate P	$M\times 0.025$
mode loss rate κ	$M\times 16$
radiative decay rate Γ_{rad}	$1.5\,\mathrm{ns}^{-1}$
pure dephasing rate γ_{pure}	$0.32\,\mathrm{ps}^{-1}$
fine structure splitting E^X_{FSS}	4 μeV

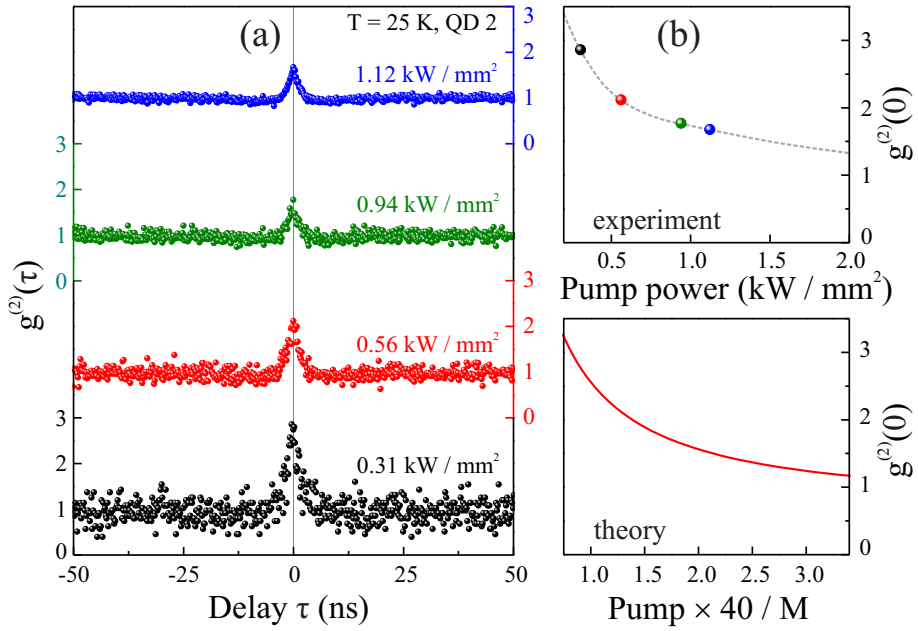

Figure 7.4: (a) Excitation power dependence of the $g^{(2)}$-correlation function for QD 2 at a temperature of 25 K. (b) Corresponding power dependence of the resulting $g^{(2)}(0)$ values shows a decrease of the bunching phenomenon with increasing excitation power that can be modeled based on the presented theoretical approach (please see the text for details). Dashed lines are guides to the eye.

nomenon can be understood within the frame of the model if the pure and the excitation-induced dephasing are considered. Most two-photon processes, which e.g. relax via the intermediate I states, are twice as sensitive [186,187] to such dephasings ($-2\gamma_{pure}$, $-2P$) in regard to their one-photon counterparts (see Sec. 7.3.2). Hence, an increased pumping or temperature simply reduces the number of participating two-photon decay processes more drastically, if compared to the one-photon case in accordance with the E^B_{bind} detuning dependence, cf. Fig. 7.3. The measured $g^{(2)}(0)$-dependencies are in good qualitative agreement with the corresponding theoretical results in Fig. 7.4b and Fig. 7.5b, which well supports the overall given interpretation. The rising temperature also strongly affects the FWHM of the bunching peak τ_b, which is reduced from 2.7 to 0.4 ns in the temperature interval from 6 to 50 K, cf. Fig. 7.5b. This speeding up of the bunching phenomenon demonstrates the rapid dephasing of the two-photon process by acoustic phonons, while the one-photon process remains stable up to a temperature of at least 70 K (Fig. 7.5b) and above in GaN QDs [32] due to the deep confinement potential.

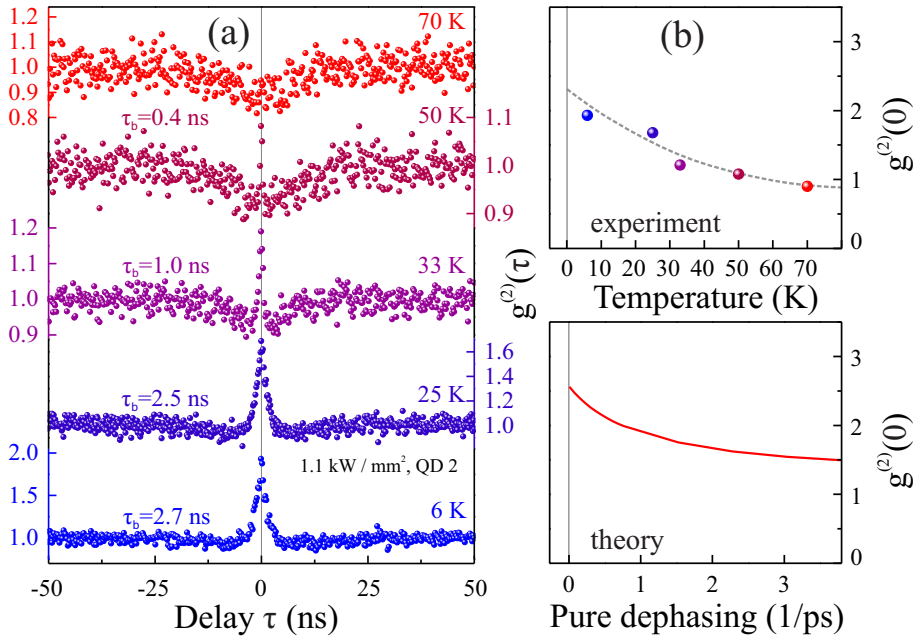

Figure 7.5: (a) Temperature dependence of the $g^{(2)}$-correlation function for QD 2 up to a temperature of 70 K at a constant excitation power of 1.1 kW/mm^2. The $g^{(2)}(0)$ value decreases upon rise of temperature as shown in (b) for the experimental data and the applied modeling, while the FWHM of the bunching part in the $g^{(2)}$-correlation function narrows as expressed by τ_b. Dashed lines are guides to the eye.

7.5 Alternative origins of the bunching phenomenon

The given interpretation of the bunching phenomenon well explains its biexciton binding energy, pump power and temperature dependencies and is further supported by the provided in-detail emission line identification. However, bunching in the $g^{(2)}$-correlation function can also occur mainly due to the following two alternative effects that must be ruled out in order to proof the reported observation of two-photon emission based bunching.

First, spectral diffusion as an origin of the reported bunching phenomenon must be excluded. Due to the huge built-in dipole moments in wurtzite GaN QDs up to 2 e·nm and a surrounding defect rich AlN matrix material one observes a drastic emission line broadening previously introduced in Chap. 5, page 62. The defect-rich AlN matrix material induces a fluctuating Coulomb field in the vicinity of a GaN QD that constantly alters the emission energy of the inherent excitonic complexes. As a result, spectral emission line jitter, emission line broadening [68], and a particular excitation power dependence of the emission line widths [43, 89] can be observed. Fig. 7.6 shows auto-correlation measurements of the bunched emission from QD 2 for two bandpass configurations A and B as illustrated in the attributed inset. Commonly, such variation of the applied bandpass widths and spectral positions drasti-

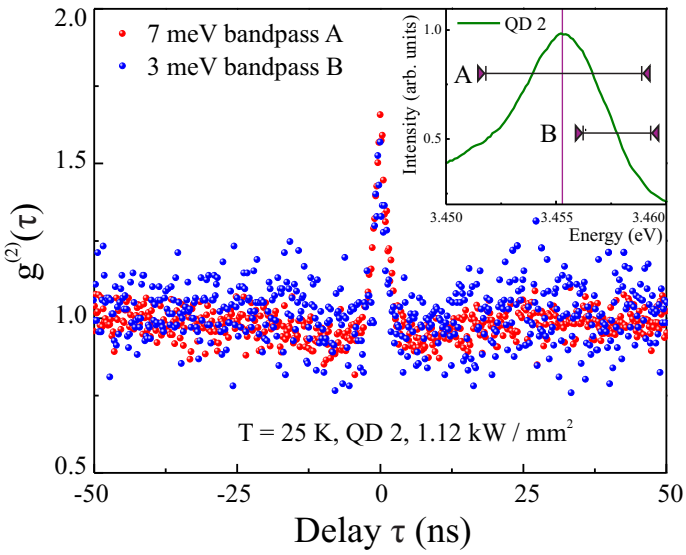

Figure 7.6: Auto-correlation measurements of QD 2 based on different bandpass configurations (A and B) with varying spectral widths (7 and 3 meV) and position as illustrated in the inset showing the related μ-PL spectrum. Altering the bandpass configuration does not drastically affect the bunching signature, which allows to exclude spectral diffusion as the origin of the bunching phenomenon.

cally alters the strength of the bunching if originated by spectral diffusion [137,181]. For a bandpass configuration comprising the full QD emission (bandpass A), a comparably weak bunching should occur in case of spectral diffusion on a ns time scale. In contrast, the bunching in the $g^{(2)}$-correlation function should strengthen as soon as the bandpass width for the auto-correlation measurement is reduced and spectrally shifted towards coverage of one half of the emission line (bandpass B). Due to the limited spectral diffusion time the e.g. excitonic emission remains in the energy range of bandpass B for a time period in excess of the radiative decay time, which results in a bunched photon stream. However, altering the bandpasses does not drastically affect the bunching strength or the general shape of the $g^{(2)}$-correlation function as shown in Fig. 7.6. This observation proves that the homogenous emission line does not remain within one half of the broadened emission line on a ns time scale. For bandpass B even a weak reduction of the bunching phenomenon is observed in Fig. 7.6 due to the residual small spectral separation between the X and B emission for QD 2, cf. Fig. 7.3b. Hence, the observed bunching phenomenon for QD 1 - 3 does not originate from spectral diffusion.

However, as a second alternative interpretation one needs to consider that even spectrally pure biexcitonic emission can originate a bunching in the $g^{(2)}$-correlation function for low pump powers as shown by Kiraz et al. [182]. Although, the emission line assignment contradicts the observation of purely biexcitonic emission for QD 2 and 3, the entire matter is discussed in order to further support the interpretation of the bunching phenomenon as a particular overlay between one- and two-photon processes. An exclusively by biexcitons induced bunching in the $g^{(2)}$-correlation function occurs at $\tau \neq 0$ and is commonly overlaid by a temporarily narrower anti-bunching feature at $\tau = 0$ in contrast to the results for e.g. QD 2, cf. Fig. 7.6. The

experimental observation of a biexciton induced bunching at low pump powers [182] can well be modeled based on rate equations for X and B emission [43], yielding a most pronounced bunching at $\tau \neq 0$, whereas the maximum in the $g^{(2)}$-correlation function for the reported bunching phenomenon occurs at $\tau = 0$, cf. Fig. 7.6. One could argue that due to the limited time resolution of the applied HBT setup the antibunching dip in the $g^{(2)}$-correlation function measurement of B could be omitted. However, a variation of the pump power commonly tunes the temporal width of an antibunching trace [31, 43], which is not evident in Fig. 7.4a, nor has ever been observed in this study. Hence, a purely biexcitonic origin of the bunching phenomenon must be excluded and clearly separated from the given interpretation based on varying numbers of one- and two-photon processes.

Finally, none of the alternative interpretations for the experimental results, namely spectral diffusion or a biexciton-induced bunching in the $g^{(2)}$-correlation function at $\tau \neq 0$, explain the particular biexciton binding energy dependence of the bunching phenomenon. Hence, the provided interpretation of the experimental data is further strengthened, identifying a unique balance between one- and two-photon processes as the origin of the reported photon-bunching phenomenon.

7.6 Summary

In summary, this chapter showed that the two-photon emission from the biexciton cascade of a single quantum dot, as a representative of a 4-level system, can exhibit a super-Poissonian photon distribution in contrast to the sub-Poissonian statistics of e.g. polarization-entangled photon pairs [173, 175]. In particular, it was experimentally and theoretically demonstrated how bunched two-photon emission from a single GaN QD can be tuned by means of the biexciton binding energy, pump power and temperature up to 50 K. Alteration of these parameters enables control over the emission from sub-Poissonian one- to super-Poissonian two-photon processes, as explicitly expressed by the reported bunching phenomenon. Alternative common interpretations for a bunching signature in the $g^{(2)}$-correlation function based on purely biexcitonic single photon emission or spectral diffusion have been ruled out, demonstrating the importance of two-photon processes in the biexciton cascade. Moreover, it was outlined that the antibunching in the $g^{(2)}$-correlation function of a "single" photon emitter can be overlaid by the reported bunched two-photon process as long as the biexciton state is still populated. All results prove that the full nature of the 4-level system must not be neglected as in 2-level based approaches, which evidently only consider one-photon processes.

8 Manifestation of unconventional biexciton states

After having established the exceptionally strong exciton-LO-phonon coupling in Chap. 6 (page 74) and the particular influence of the biexciton binding energy regarding the photon statistics in Chap. 7, page 100, it is the aim of this chapter to introduce a novel biexciton model [40]. This so called hybrid-biexciton model deviates from the common biexciton perception and originates highly unconventional emission characteristics. The recent discovery of this novel type of quasiparticle will not only explain the observed anti-binding nature of biexcitons for certain wurtzite GaN QD sizes, but will also explain the experimentally confirmed distinct transition from anti-binding to binding biexcitons [119].
Generally, the strong internal piezo- and pyroelectric fields native to wurtzite GaN QDs embedded in AlN separate the electron- from the hole-subsystem, causing a very distinct confinement in the growth-direction (c-axis) for both charge carrier types, cf. Sec 3.7, page 37. Along lateral directions the electrons are still subject to a strong confinement, in contrast to the weakly confined holes with their large effective hole mass. Consequently, no significant orbital structure for holes can be present anymore, facilitating the generation of the hybrid-biexciton complex, in which Coulomb forces, in particular the hole-hole repulsion and the exchange interaction, become most significant. Hence, laterally separated hole states with parallel spins are energetically more favorable than those exhibiting anti-parallel spins as common for the case of strong confinement in all spatial directions. In contrast to the conventional-biexciton complex with a net spin of $s = 0$, the hybrid-biexciton exhibits $s = \pm 3$ leading to completely different photoluminescence signatures as shown in this chapter along with drastically enhanced charge carrier binding energies. An efficient biexciton cascade via the excitonic dark states will be attestable, benefitting from the generally strong exciton-phonon coupling in such QDs, as already indicated in Chap. 6, page 74, with a spin flip process as a key element.

The results presented in this chapter are published in Ref. [40]. G. Hönig theoretically developed the presented hybrid-biexciton concept, implemented the particle interaction algorithms and calculated, as well as evaluated the numerical data shown in this chapter. Dr. A. Schliwa developed the multi-excitonic rate equation model

that facilitates an understanding of the temperature and excitation power dependent luminescence results. The unique phalanx of experiment and theory described in the following confirms the hybrid-biexciton concept, yielding a coherent description for this first member in the novel class of hybrid-quasiparticles.

8.1 From anti-binding to binding biexcitons

The biexcitonic emission (B) described in Chap. 4, page 39 appeared on the high energy side of the exciton (X) emission at an energy of around 3.5 eV in good agreement with the results from Chap. 6, page 74. However, in Chap. 7, page 100 a reduction of the difference between the X and B emission, the so called biexciton binding energy (E^B_{bind}), is observed, scaling from -8.1 meV towards -0.3 meV with a striking effect on the photon statistics. The observation of this scaling behavior is

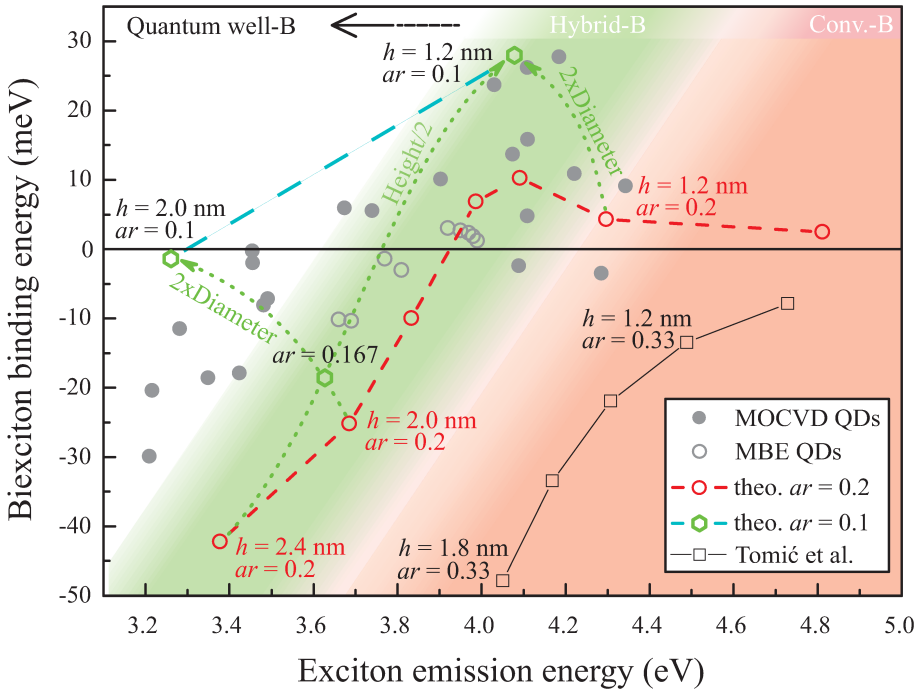

Figure 8.1: The biexciton (B) binding energy is plotted versus the exciton (X) emission energy. The red circles show calculated values based on the hybrid-B model for GaN QDs with a constant aspect ratio of ar = 0.2 and reduced height (h) towards larger emission energies. The grey dots depict the experimental data for quantum dots (QDs) grown by metalorganic chemical vapor deposition (MOCVD), while grey circles show the corresponding molecular beam epitaxy (MBE) values [119]. The inclusion of theoretical data points with ar = 0.1 (green hexagons) spans a data grid that encloses the experimental data point spread in well agreement with microscopic studies. Theoretical results for the conventional-B model from Tomić et al. [75] are indicated by black squares. Please see the text for further details. Adopted from Ref. [40].

in good agreement with the results from Simeonov et al. [119] for single, wurtzite GaN/AlN QDs grown by molecular beam epitaxy (MBE). At elevated emission energies one can even observe a transition from anti-binding ($E^B_{bind} < 0$) to binding biexcitons ($E^B_{bind} > 0$), an observation that will be explained in the following along with all its consequences for the optical signature of B for the particular case of wurtzite GaN QDs with varying emission energy. Fig. 8.1 summarizes experimental E^B_{bind} values for QDs grown by metalorganic chemical vapor deposition (MOCVD - this work and Ref. [32]) as well as MBE-grown (Ref. [119]), single, wurtzite GaN QDs (grey dots and circles).

The transition from anti-binding to binding biexcitons is evident in Fig. 8.1 along with an astonishing magnitude of the absolute E^B_{bind} values. In addition, Fig. 8.1 shows the theoretical results based on the hybrid-B model in well agreement with the experimental data. The theoretical results for a QD aspect ratio of 0.2 (red circles) nicely match the results for MBE-grown QDs and reproduce the sign change of the B binding energy, while they slightly deviate from the results for QDs grown by MOCVD. However, QD growth kinetics and the resulting QD geometries are known to be different between MBE and MOCVD growth [188] due to fundamentally different segregation temperatures. The apparent spread of the MOCVD results can be well described by doubling the QD diameter towards an aspect ratio of 0.1 (green hexagons), as marked by green arrows and the blue line in Fig. 8.1, indicating a data-grid for future explorations. Atomic force microscopy (AFM) and scanning transmission electron microscopy (STEM) studies confirm such QD aspect ratio interval between 0.1 and 0.2 [43] for wurtzite GaN QDs as outlined in Chap. 2, page 16. Therefore, the assumption of $ar = 0.2$ represents a lower limit for common B binding energies in Fig. 8.1 for MOCVD-grown, wurtzite GaN QDs. Previously published calculations by Tomić et al. [36, 75] still failed to predict such a transition from anti-binding to binding biexcitons as shown in Fig. 8.1 (black squares), constituting the need for a detailed consideration of the interaction energies inherent to the biexciton complex as described in the following section and Chapter 3.2, page 26. Here, also the transition from conventional-biexcitons to quantum well-biexcitons via the hybrid-B will be discussed as already indicated by the color fading in Fig. 8.1.

8.1.1 Particle interaction energies in excitonic complexes

As depicted in Fig. 8.2a, the spatial separation of confined electrons and holes, which is common to wurtzite GaN QDs (see Sec. 3.7, page 37), reduces their charge-related, attractive Coulomb interaction (blue) and their spin-related, repulsive exchange interaction (red). For the conventional-B shown in Fig. 8.2b, additional repulsive/attractive (red/blue) Coulomb interactions between the charge carriers exist as indicated by the depicted arrows. However, the simulations of the B reveal

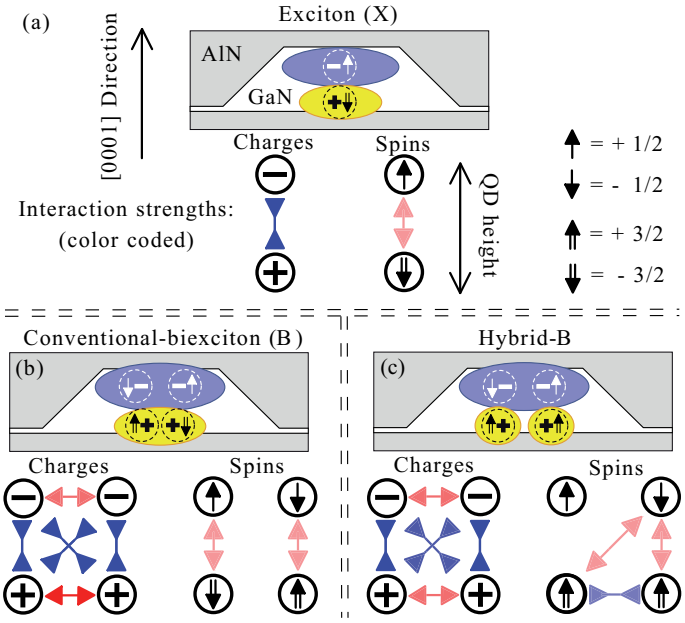

Figure 8.2: Schematic arrangement of electron and hole orbitals inside of a wurtzite GaN quantum dot along with their corresponding attractive (blue) and repulsive (red) interactions within (a) the exciton (X) and the biexciton (B) complexes (b) and (c). Compared to the conventional-B model, a hybrid-B with a reduced repulsive direct Coulomb and an additional attractive exchange force is energetically more favorable, altering the optical signature. Adopted from Ref. [40].

a Coulomb repulsion that overcomes the lateral confinement of the holes, leading to a separated localization of the hole wavefunctions at the bottom of the QD, cf. Fig. 8.2c. Accordingly, the B forms a hybrid system of two electrons sharing one orbital at the top of the QD and two spatially separated holes at the bottom of the QD. In this configuration the holes can exhibit parallel spins, thus reducing the energy of the so called hybrid-B via the hole-hole exchange interaction (blue). Due to the reduced hole-hole Coulomb repulsion and the additional attractive hole-hole exchange interaction illustrated in Fig. 8.2, the total energy of the hybrid-B is drastically decreased, rendering it more energetically favorable.

Calculations within the conventional-B model assuming antiparallel hole spins for small QDs with an aspect ratio of 0.33 as shown in Fig. 8.1 could not explain the zero-crossing of the B binding energies [39], not to mention positive B binding energies of up to 30 meV and beyond for even flatter QDs. All hybrid-B calculations presented in Fig. 8.1 use the material parameters listed in the supplementary material of Ref. [40], which are identical to the values assumed in Refs. [36, 75] for the conventional-B, however, without any artificial reductions of the built-in polarization fields as suggested therein. Nevertheless, due to the large aspect ratios of the model QDs discussed in Refs. [36, 75], these QDs correspond to the conventional-B regime of strong confinement, i.e. antiparallel hole spins. The applied non-restricted Hartree-Fock calculations (see Chap. 3.2.3, page 31) in combination with the experimental evidence, predict different biexcitonic regimes, which are marked by colored

areas in Fig. 8.1: First, the conventional-B regime (red) for QD diameters $\lesssim$ 6 nm, followed by the hybrid-B regime (green) with weakly confined holes for QD diameters $\gtrsim$ 6 nm. For QD diameters $\gtrsim$ 12 nm the electrons *and* holes encounter weak lateral confinement followed by a transition into the quantum-well-B regime (white) without significant lateral confinement. However, please note that the depicted B-regimes lack well defined border lines (indicated by the color fading in Fig. 8.1) due to the apparent wide range of structural QD parameters and are meant for rough orientation only. The height of the QD can additionally influence this most pivotal QD diameter approximation, since a smaller electron-hole separation leads to a stronger lateral confinement of the holes by the attraction of the electrons.
Prior two-dimensional studies of electron interactions in QDs [189–193] raised the question, whether a Wigner molecule (of electrons) is reliably described within the unrestricted Hartree-Fock method, allowing for symmetry-broken solutions [194]. The presented calculations use such a, here three-dimensional, Hartree-Fock method, which predicts a Wigner molecule like *hole separation* within the hybrid-B model. Therefore, the presented theoretical method might underestimate the minimum QD diameters required for the observed lateral hole separation. However, the striking agreement between the theoretical and experimental data confirms the entire hybrid-B concept as substantiated in the following. Although, the situation with one strongly and one weakly confined charge carrier type is similar to the situation found in type II QDs [195]; a negative B binding energy (relative to the dark X) would prevent the formation of a B in such QDs in strong contrast to the case of wurtzite GaN QDs.

8.2 Hybrid-biexciton decay cascade - experimental evidences

The in-parallel aligned hole spins of the hybrid-B cause a total spin of $s = \pm 3$ if band intermixing effects are neglected. Therefore, the hybrid-B can radiatively decay into the dark X states exhibiting total spins of ± 2 via the emission of photons with an angular momentum of ± 1, cf. Fig. 8.3a and b. As the electron-hole exchange interaction of symmetry-broken wavefunctions does not lead to a splitting of the dark X states, in contrast to the bright X states, such dark X states are expected to show a significantly smaller splitting than the bright X states of wurtzite GaN QDs (with measured bright X fine-structure splittings of 2 - 7 meV [37]). Therefore, the emitted photons of the hybrid-B show a smaller energetic splitting than expected for a conventional-B, commonly showing the same splitting as the bright X states [90, 196–200]. Due to the large total spin of $s = \pm 3$, future μ-PL experiments within magnetic fields should reveal a field strength dependent four-

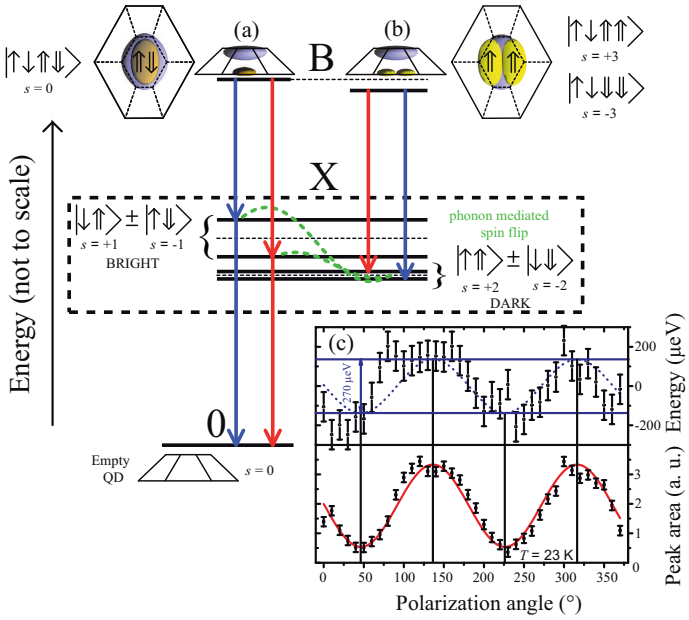

Figure 8.3: The conventional-biexciton (B) decay scheme is illustrate in (a), while (b) shows the hybrid-B decay comprising a spatial hole density separation (see the corresponding isosurfaces), due to a small lateral hole confinement native to GaN quantum dots. The separated holes align their spins in-parallel, reducing the hybrid-B energy by the hole-hole exchange interaction. Compared to the conventional-B ($s = 0$), the hybrid-B has total spins of $s = \pm 3$. Therefore, this complex decays into the dark exciton (X) states ($s = \pm 2$) via the emission of photons. An efficient mechanism in order to depopulate the dark X states is a phonon-mediated spin flip into the bright X states (green). (c) A polarization-dependent μ-PL analysis of the B emission of a quantum dot with a bright X splitting of 4.3(2) meV (compare Fig. 8.4a) reveals a small energetic drift of 270(50) μeV due to the dark X splitting. Adopted from Ref. [40].

fold splitting of the hybrid-B emission line, caused by the splitting of the hybrid-B states and the dark X states, which will become optically active. Observing such a splitting will be challenging due to the large emission linewidths [46] introduced in Chap. 5, page 62, but seems achievable based on recent growth advances indicated in Chap. 5.3, page 72. However, even without the application of a magnetic field one can already indirectly witness the anomalous cascade process via the dark states by a straight-forward polarization-dependent μ-PL measurement. A careful analysis of such spectra yields a polarization-dependent shift of the hybrid-B emission line (see Fig. 8.3c) along with a periodic intensity variation, yielding an estimate for the dark X splitting of 270(50) μeV. The corresponding bright X states show an approximately 16 times larger splitting of 4.3(2) meV as most directly shown in Fig. 8.4a.

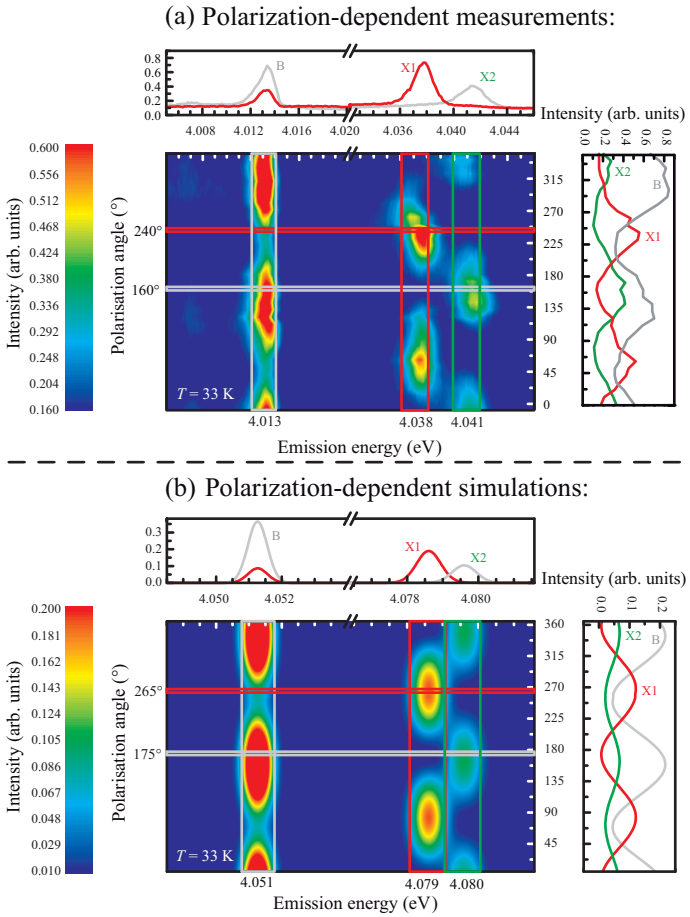

Figure 8.4: Experimentally recorded (a) and calculated (b), color-coded polarization-dependent μ-PL spectra are compared to each other, yielding a well agreement due to the applied multi-particle calculations. A reduction of the quantum dot aspect ratio towards 0.1 (see Fig. 8.1) yields biexciton (B) binding energies that approach $\approx 30\,\mathrm{meV}$ as reproduced in the comparison shown. The fine-structure splitting between the bright exciton doublets (X1, X2) is influenced by the amount of anisotropy within the quantum dot structure. Adopted from Ref. [40].

8.2.1 Polarization-dependent luminescence traces

A direct comparison between the experimental and theoretical results concerning the polarization of the emission is shown in Fig. 8.4 for a QD with an emission energy of around 4 eV. The depicted contour plots show experimental (a) and theoretical (b) μ-PL spectra as a function of the polarization angle. On top of each contour plot two single spectra for orthogonal polarization angles are plotted vs. the emission energy, demonstrating the fully linear polarization of the bright X states luminescence (X1, X2). The intensities for the corresponding emission lines are plotted vs. the polarization angle on the right side of each contour plot for a better identification of the polarization angle dependent emission maxima. The overlap of two fully cross-polarized B emission lines in Fig. 8.4a is mimicking a single, partially polarized emission line [37]. This observation can directly be confirmed by the simulated spectra shown in Fig. 8.4b belonging to a QD structure with an aspect ratio of 0.1 and a B binding energy of $\approx 28\,\mathrm{meV}$ at an emission energy of 4.08 eV, which corresponds to the upmost theoretical data point in Fig. 8.1 (green hexagon). The observation of such a striking agreement between experiment and theory already supports the identification of the hybrid-B and the underlying model and is further strengthened

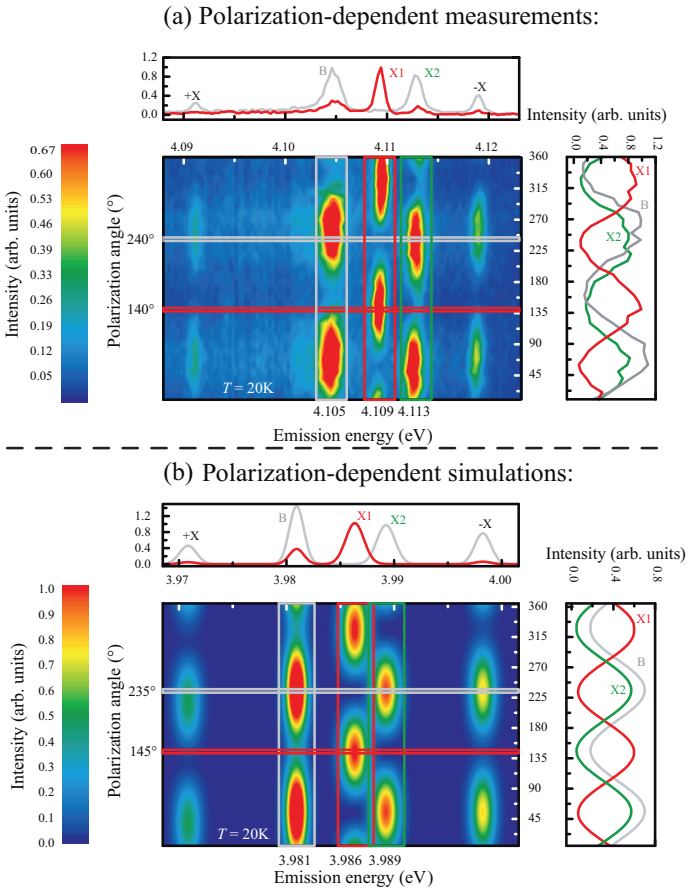

Figure 8.5: Experimental (a) and theoretical (b), color-coded, polarization-dependent μ-PL spectra are compared to each other yielding a good quantitative agreement of polarization degrees, angles and energetic spacings. Besides the excitonic (X1, X2) and biexcitonic (B) emission lines, also additional luminescence of charged excitons (+X, -X), can be assigned based on a direct comparison between the experimental result and the calculated spectra. A good agreement between experiment and theory regarding the B binding energy is achieved by increasing the quantum dot aspect ratio from 0.1 (see Fig. 8.4) to 0.2.

by additional measurements as shown in the following.

The only parameters that had to be approached regarding the experiment for the simulation shown in Fig. 8.4 are the emission line width induced by spectral diffusion [38,46], the particular excitation power, and the temperature dependencies that vary the intensity balance between X1, X2, and B. Neither material, nor geometric QD parameters were varied in order to match the individual measurement, causing the apparent slight discrepancies for the luminescence energies. Therefore, also the bright X states show a QD anisotropy-dependent smaller fine-structure splitting of $\approx 1\,\mathrm{meV}$ in the simulations and a slightly larger hybrid-B binding energy. The visible emission energy variations of the measured emission lines in Fig. 8.4a during the polarization angle scan are caused by the spectral diffusion phenomenon, which can be suppressed by lowering the temperature but sacrificing the intensity balance of the bright exciton states as explained in the following.

In some of the single QD spectra additional emission lines were found, which can tentatively be assigned to positively (+X) or negatively (-X) charged excitonic complexes by comparison to the modeled polarization spectra shown in Fig. 8.5. Here, the measurements result a spectrum with a significantly smaller hybrid-B binding

energy of $\approx 4\,\mathrm{meV}$, if compared to Fig. 8.4, and a well comparable bright X splitting of $\approx 4\,\mathrm{meV}$. However, the overall emission energy is not significantly varied, meaning that the electron-hole wave function anisotropy and overlap are maintained, while the QD aspect ratio must have been increased, cf. Fig. 8.1. Increasing the QD aspect ratio from 0.1 to 0.2, well within the limits determined by the AFM and STEM techniques [43] as described in Chap. 2, page 16, yields an artificial PL spectrum as shown in Fig. 8.5b. Based on the striking agreement between experiment and theory regarding the optical finger print one cannot only identify the X and B emissions but also the optical traces of charged exciton luminescence, so called trions.
Generally, such pronounced charged exciton emission is only rarely observed in the analyzed QD samples and emission characteristics as depicted in Fig. 8.4 are more common. For instance, structural defects in the close vicinity of a QD can affect its charge neutrality by charges that tunnel in between the defect and the QD potential. The occurrence of +X *and* -X in Fig. 8.5 hints the tunneling of one charge carrier type either (electron/hole) out of the QD into the defect potential (hybrid-B $\rightarrow$ +/-X) and backwards from the charged defect into the QD potential (X $\rightarrow$ -/+X). Hence, the measured intensities of the charged exciton emissions are not predominantly governed by the calculated oscillator strengths but by the charge transfer rates between the QD and the surrounding defect environment. In order to achieve a reasonable comparison between experiment and theory in Fig. 8.5, the calculated oscillator strengths of both charged excitons had to be reduced by 70 %. Naturally, the +X is expected to exhibit the same spatial hole separation as the hybrid-B. Therefore, all hole and electron spins are expected to align in parallel to each other, due to the exchange interaction. The two possible +X ground states with total spins of $s = \pm 1/2 \pm 3/2 \pm 3/2 = \pm 3.5$ are degenerate and exhibit a high resistance against spin dephasing, which makes the +X in GaN QDs extremely interesting for quantum computing applications. The preparation and reading of the +X spin states observed in Fig. 8.5 should be possible in future polarized photon absorption and emission experiments. Nevertheless, the assumption of parallel hole spins allows a precise modeling of the experimental line separations as well as polarization directions and degrees.

8.2.2 Temperature dependence of the luminescence

Temperature-dependent μ-PL measurements (Fig. 8.6) reveal the thermal activation of the bright exciton states (X1, X2) due to phonon-mediated spin-flip processes [108] transferring the carriers between the dark and the bright exciton states. By comparing the overall exciton intensity with its biexciton counterpart in an Arrhenius plot (Fig. 8.7a), one determines an activation energy (E_{DB}) of 1.0(3) meV, resembling the average excitonic dark-bright (DB) splitting. Interestingly, the sole

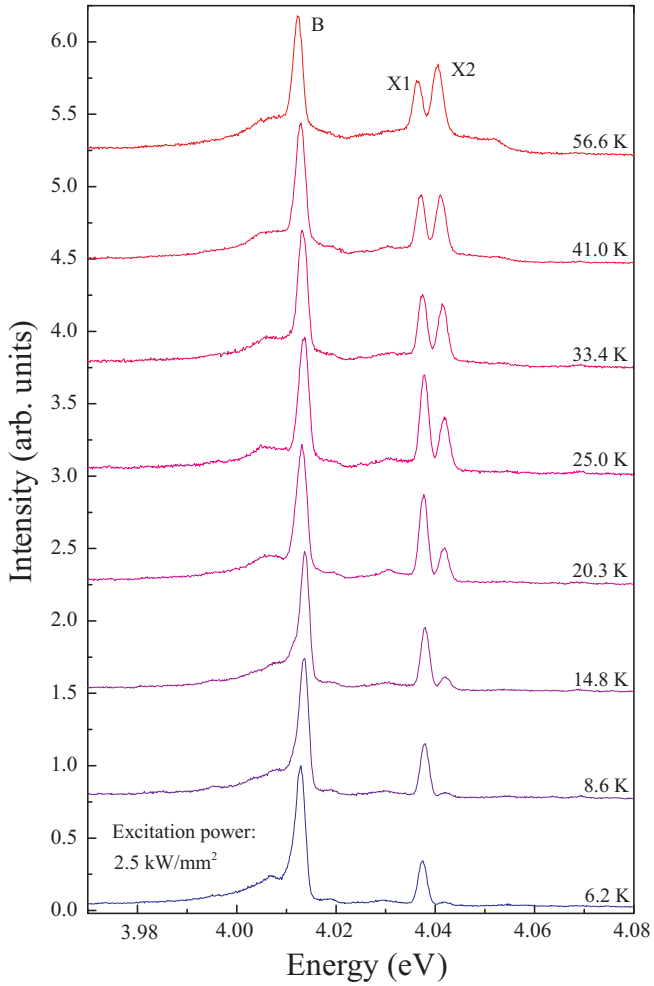

Figure 8.6: Vertically stacked μ-Photoluminescence spectra showing the bright excitonic (X1, X2) and hybrid-biexciton (B) emissions depending on temperature at a constant excitation power of $2.5\,\mathrm{kW/mm^2}$. With rising temperature, a thermal activation process strengthens not only the emission of X2, but also the overall luminescence intensity of the exciton (X1 + X2). The corresponding Arrhenius plots can be found in Fig. 8.7. Adopted from Ref. [40].

thermal activation of X2 in regard to X1 is a two-step process as shown in Fig. 8.7b. Based on a two-step Arrhenius fit [201] one can extract two activation energies: $E_{\mathrm{DB}^*} = 0.9(4)$ meV, again matching the average excitonic dark-bright splitting; and $E_{\mathrm{BB}} = 5.1(8)$ meV, implying the much larger fine-structure splitting of the bright exciton states. Therefore, both Arrhenius plots independently deduce E_{DB}, in-line with the theoretical prediction of an average dark-bright splitting of 0.81 meV, strongly scaling with the QD volume.

The thermal activation of the excitonic emission lines evidences the existence of efficient phonon-mediated spin-flip processes [108] within GaN QDs. This explains the stronger X1 emission in comparison to the X2 emission at a temperature of 33 K in Fig. 8.4, despite the much larger oscillator-strength of X2 depending on the amount of fine-structure splitting between X1 and X2 [37]. Additionally, this unbalance in the oscillator strengths explains the observations of E_{DB^*} in the low temperature regime of Fig. 8.7b. The dark X states as the final states of the hybrid-B are expected to be long-time stable until additional carriers are captured by the

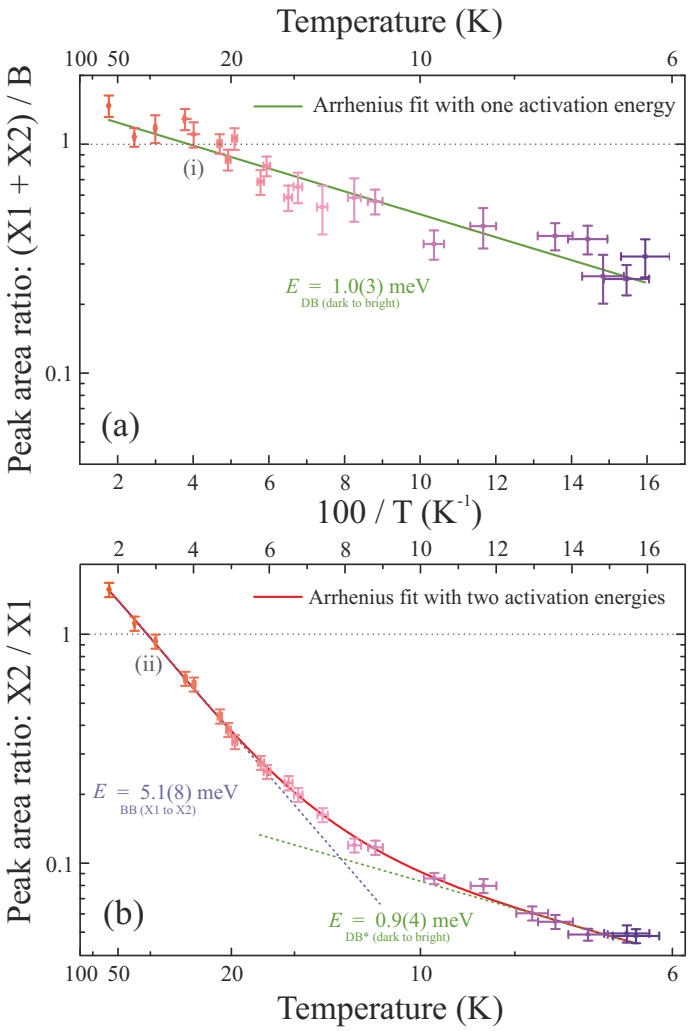

Figure 8.7: (a) Arrhenius plot belonging to Fig. 8.6 showing the overall thermal activation process of X1 + X2 in regard to B fitted (solid line) with one activation energy. (b) Arrhenius plot with two activation energies illustrating the thermal activation process of X2 in regard to X1. As a result, the depicted fits yield the thermal activation energies $E_{\mathrm{DB}^{(*)}}$ and E_{BB} matching the energetic splitting between the dark and bright exciton states. All intensities correspond to peak areas extracted from a fitting routine applying Gaussian fitting functions. The intersection points (i) and (ii) are further described in Sec. 8.2.5, page 131. Numbers in parentheses indicate the error. Adopted from Ref. [40].

QD or a phonon-mediated spin-flip to a bright X state takes place, cf. Fig. 8.3b. The latter process must be efficient in order to explain the occurrence of an intense X emission besides the hybrid-B emission. This presumption is strongly supported by excitonic spin-flip times on the order of ps that were already observed in QDs [202] in addition to the generally strong coupling between excitons and phonons in GaN QDs [68, 69] as partially treated in Chap. 6, page 74.

8.2.3 Temperature-dependent second-order correlation analysis

The most direct and suggestive proof for the occurrence of phonon-mediated spin-flip processes arises from temperature-dependent second-order correlation measurements. At a temperature of 30 K (see Fig. 8.8a) one observes the typical signature of a cascade process arising from the decay of the hybrid-B (start) to the ground-state via the dark and bright X states (stop). By lowering the temperature towards 8 K (see Fig. 8.8b) it becomes feasible to efficiently suppress the phonon-mediated

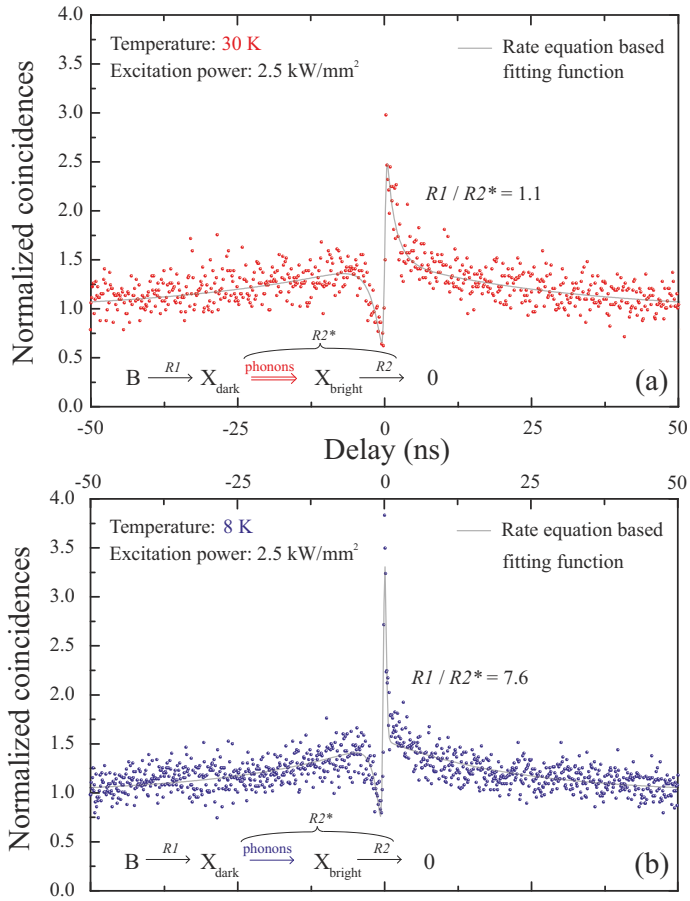

Figure 8.8: Both histograms show the photon cross-correlation analysis comprising the hybrid-biexciton (start) and both bright exciton complexes (stop). By lowering the temperature from 30 K (a) to 8 K (b) at a constant excitation power one observes the transition from a typical biexciton cascade (a) towards the signature of a spin-blockaded biexciton cascade (b). The weighting between the corresponding rates $R1$ and $R2^*$ obtained from a fitting procedure (solid line, see text) is correspondingly altered, clearly demonstrating the influence of the phonon-mediated dark to bright exciton transitions. Adopted from Ref. [40].

spin-flip processes, yielding the typical cross-correlation signature of a B cascade via an additional intermediate level [203] that governs the decay dynamics. Here, the hybrid-B decay rate ($R1$) is enhanced in comparison to the exciton decay rate ($R2^*$), which is limited by the spin-flip rate from the dark into the bright X states. Identical excitation conditions at 30 K almost equalize $R1$ and $R2^*$, proving the existence of a phonon-limited hybrid-B cascade, including a transition from the dark to the bright X states.

The apparent temporally broad [$\approx 25\,(3)$ ns] bunching phenomenon noticeable in both correlation functions, arises from spectral diffusion [38, 46] as described by Sallen et al. [129, 137]. The limited biphoton time resolution of the applied HBT setup (225 ps) is considered by a convoluted fitting routine [43] along with the effect of spectral diffusion, yielding the fitting functions shown in Fig. 8.8a and b. Consequently, a phonon-limited hybrid-B $\rightarrow$ dark X $\rightarrow$ bright X $\rightarrow$ empty QD emission cascade is witnessed, which is activated upon rise of temperature.

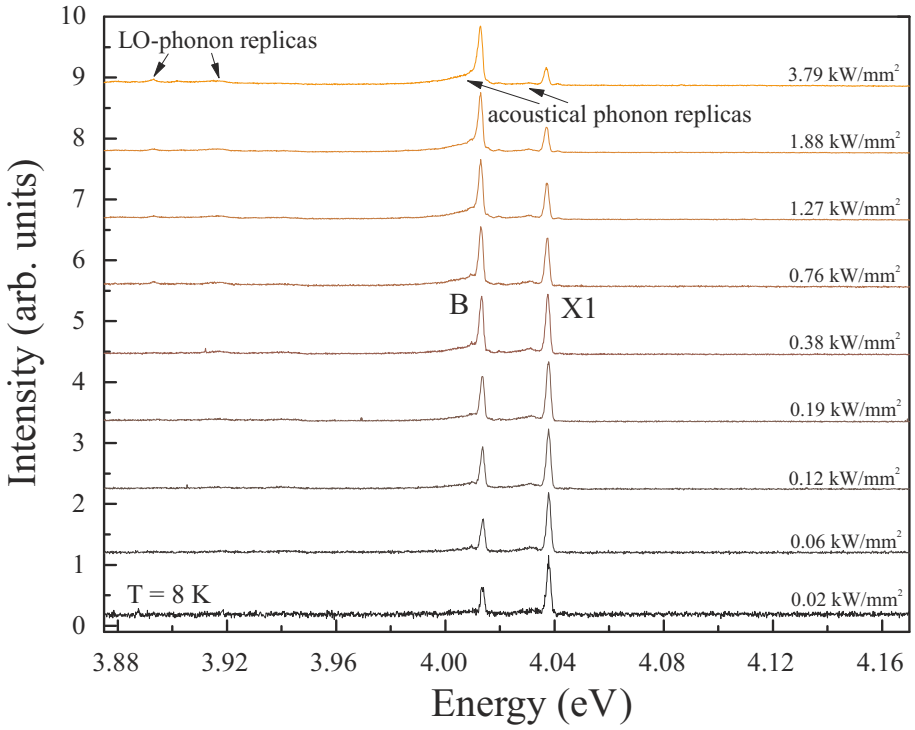

Figure 8.9: Excitation power dependent μ-PL overview spectra of B and X1 (a) support the identification of the biexcitonic and excitonic emissions by analyzing their intensity scaling behaviors that strongly dependent on the number of charge carriers involved. The spectra show a broad energy range of $\approx 300\,\text{meV}$ without *any* additional strong luminescence traces. Only the acoustic and longitudinal-optical (LO) phonon replica are noticeable, while X2 at the higher energy side of X1 is only weakly present at the given temperature of 8 K.

8.2.4 Excitation power dependent measurements

By raising the excitation power at a constant temperature of 8 K, the biexcitonic complex with twice the number of particles if compared to the exciton is increasingly populated as shown by the μ-PL overview spectra from Fig. 8.9. Please note that no other dominant emission lines are noticeable in these overview μ-PL spectra along with X1 and B except of the corresponding LO-phonon replica [32,68]. The emission of X2 at the higher energy side of X1 (see Fig. 8.6) is still sufficiently suppressed at the given temperature. The weak overall shift of X1 and B towards lower energies upon rise of excitation power is caused by the phenomenon of spectral diffusion [43, 89].

Gaussian fit functions applied to the emission lines yield the peak areas plotted in Fig. 8.10 versus the excitation power on a double logarithmic scale. Already the application of a simplified rate equation model [43,45], which neglects the dark exciton states, fits the experimental data yielding the commonly extracted exponent n [32] as described in Sec. 4.2, page 40. However, an extension of the modeling towards a

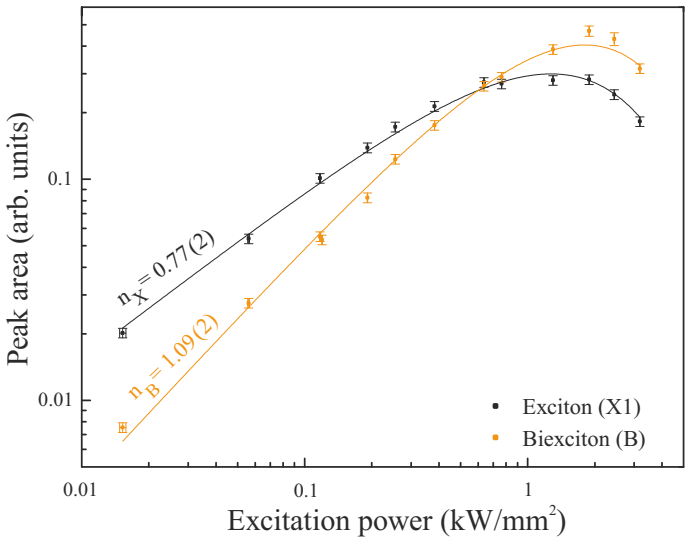

Figure 8.10: Plotting the peak areas of the emission X1 and B shown in Fig. 8.9 in a double logarithmic plot directly illustrates the deviating power dependences as described by the exponent $n_{X/B}$ involved in the depicted standard fitting model (solid line). Please see Chap. 4.2, page 40 for further details regarding the fitting process. Numbers in parentheses indicate the error.

more advanced rate equation model as outlined in Sec. 8.2.5, page 131, will introduce numerous additional fitting parameters, clearly rendering the fitting function over-parametrized in regard to the experimental data. A similar observation is true for the fitting of the photon correlation results evidencing the cascade process presented in Sec. 8.2.3. Already a simplified fitting model based on a three-level system [32,43,183,204], i. e. neglecting the dark exciton states, facilitates sufficient fit results (see Fig. 8.8) for each individual temperature. However, the entire temperature dependence of the photon correlation results clearly demonstrates the contribution of the dark exciton states as expressed by the altered rate ratio $^{R1}/_{R2^*}$ extracted from the fitting procedure applied in Fig. 8.8. Similar to the case of the power-dependent μ-PL results, the inclusion of additional rates considering the occurring spin-flip processes, would over-parametrize the individual fitting function, which can only be encountered by recording additional temperature steps and applying concatenated fitting routines taking *all temperature steps simultaneously* into account. Such more detailed analysis remains a motivating task for future work.

8.2.5 Multi-excitonic rate equation model

An independent multi-excitonic rate equation model [43] is briefly outlined in the following in order to introduce the reader to the complexity of the rate balance describing the excitation power and temperature dependence of the hybrid-B cascade introduced in Secs. 8.2.2 and 8.2.4. Such a model is characterized by the following properties as depicted in Fig. 8.11a:

- The model includes the ground-state $|0\rangle$, two dark exciton $|XD1\rangle$, $|XD2\rangle$ and two bright exciton states $|XB1\rangle$, $|XB2\rangle$, the three relevant biexciton states $|B(\pm 3)\rangle$, $|B(0)\rangle$, and larger multi-excitonic complexes depicted in the level

scheme of Fig. 8.11a. These higher order multi-excitonic complexes mainly serve as reservoir in order to achieve an accurate description of the biexcitonic occupation at elevated pump rates.

- The hybrid-B ($|B(\pm 3)\rangle$) with $s = \pm 3$ constitutes the degenerate biexciton ground-states and the conventional-B $|B(0)\rangle$ with $s = 0$ the excited-state. Their splitting equals 25 meV as supported by the particle interaction calculations for a QD aspect ration of 0.1, cf. Fig. 8.4.

- All further relevant energetic splittings of the hybrid-B cascade are taken from the temperature-dependent μ-PL spectra illustrated in Fig. 8.6.

- Radiative transitions between the states occur upwards with the pump rate Π , and downwards with the decay rate γ. Therefore, deviating individual optical decay rates for specific excitonic complexes are neglected in this first approach, allowing a straightforward qualitative description of the measurements.

- Phonon-assisted processes are considered among the four exciton states, between the hybrid- and conventional-biexcitons, and between the ground (-A) and excited states (-B) of higher order multi-excitonic complexes. The phonon creation rate is proportional to the phonon density, and the complementary phonon annihilation rate accounts for the temperature-dependent phonon occupation, hence, the Bose statistics as already applied in Fig. 8.4 and 8.5. Generally, the exciton phonon interaction strength is significantly larger in the nitride than in the arsenide QD system [68, 69] as introduced in Chap. 6, page 74, due to large deformation potentials as well as piezoelectric constants, and the directly related pronounced electron-hole dipole of the excitonic complexes [38, 46] as introduced in Chap. 5, page 62.

Application of the rate equation model yields the results depicted in Fig. 8.11b - d. At low temperatures (≤ 10 K) only $|XB1\rangle$ shows a significant occupation probability as a function of the excitation power, cf. Fig. 8.11b and 8.6. The onset of this dominance of $|XB1\rangle$ at low excitation powers can also directly be observed in the excitation power dependent μ-PL spectra presented in Fig. 8.9. The occupation probability of the conventional-B [$|B(0)\rangle$] always remains very small upon rising pump rate due to its large energetic spacing (25 meV) in regard to the hybrid-B [$|B(\pm 3)\rangle$], which gets increasingly populated as demonstrated in Fig. 8.11b. The temperature dependence of the occupation probabilities shown in Fig. 8.11c predicts several intersection points for the illustrated dependencies, which can also directly be found in the corresponding intensity trends from Fig. 8.11d. For fixed excitation conditions ($\Pi/\gamma = 0.6$) the temperature-dependent intensity trends intersect at characteristic temperatures marked by (i) and (ii) in Fig. 8.11d. Exactly these two

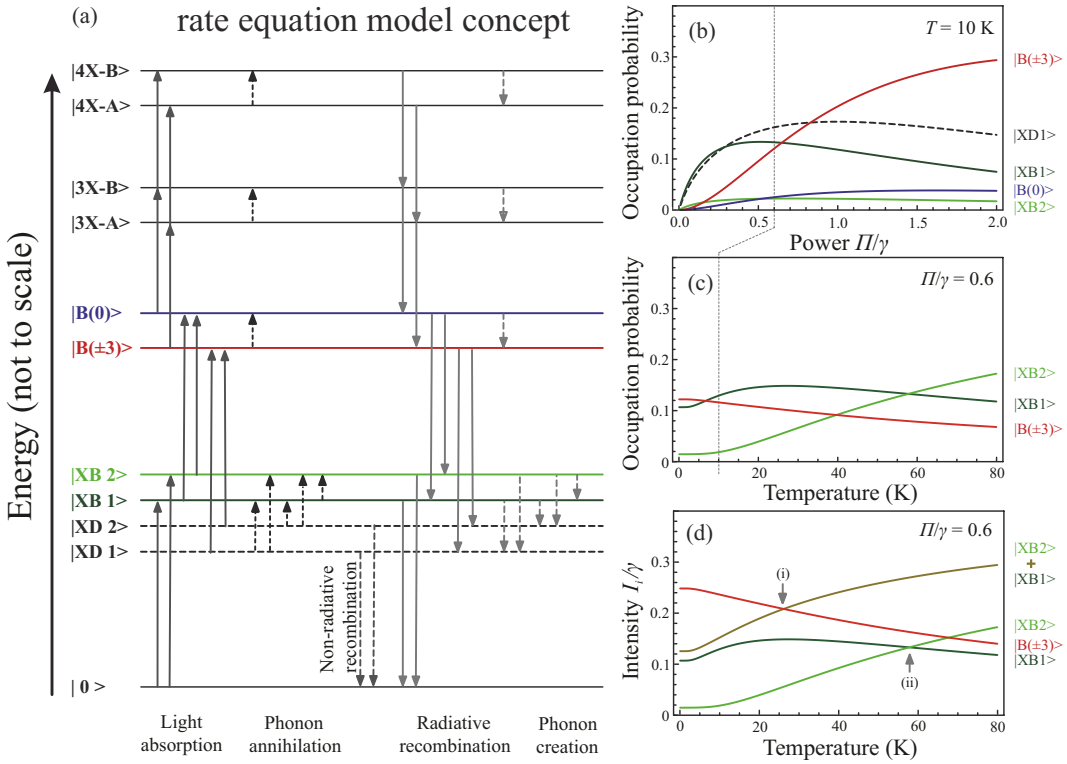

Figure 8.11: (a) Scheme of the multi-excitonic rate equation model based on a level diagram. $|B(\pm 3)\rangle$ denotes the degenerate hybrid-biexcitons with $s = \pm 3$ and $|B(0)\rangle$ the conventional biexciton with $s = 0$. (b) Occupation probabilities of the two bright excitons ($|XB1\rangle$: dark green, $|XB2\rangle$: light green), the dark excitons $|XD1\rangle$ and $|XD2\rangle$ (black dotted line) and the hybrid-biexciton $|B(\pm 3)\rangle$ (red line) depending on the pump to decay rate ratio Π/γ. The temperature dependence of the occupation probabilities is shown in (c) and the intensities of the corresponding radiative decay-channels are illustrated in (d). The colors in the diagrams match the level scheme coloring. Please see the text for further details.

intersection points (i) and (ii) are also marked in the experimental results (Arrhenius plots) shown in Fig. 8.7 and are further analyzed in the following:

(i) Here, $|XB1\rangle + |XB2\rangle$ and $|B(\pm 3)\rangle$ intersect upon rise at a temperature of $\approx 25\,\mathrm{K}$ in accordance with the experiment ($\approx 26\,\mathrm{K}$, see Fig. 8.6 and 8.7). The sole occupation probabilities of $|XB1\rangle$ and $|XB2\rangle$ match at a temperature of 58 K, with $|XB1\rangle$ dominating at low temperatures and $|XB2\rangle$ gaining towards elevated temperatures as shown in Fig. 8.11d.

(ii) This latter crossing point deviates from its experimental counterpart ($\approx 36\,\mathrm{K}$, see Fig. 8.2.2, page 126) due to the neglection of individual optical rates for $|XB1\rangle$ and $|XB2\rangle$. More correctly, $|XB2\rangle$ exhibits an increased oscillator strength in comparison to $|XB1\rangle$, which is weighted by the excitonic fine-structure splitting [37].

However, an in-detail consideration of such individual optical rates would spoil the deeper physical insight provided by the applied rate equation model based on its simplicity and must remain a task for future work.

Beyond the experimental observations, the presented model also predicts a high occupation probability of the dark-exction states for large excitation powers at the given temperature. The overall deviation of the exponents $n_X = 0.77(2)$ and $n_B = 1.09(2)$ in Fig. 8.10 from the, in a first approach, ideal values of $n_X = 1$ and $n_B = 2$ (see Chap. 4, page 39) indicates non-radiative decay channels with the long-lived dark-exciton states as most probable starting points.

8.3 Summary

In conclusion, the theoretical and experimental evidence is given for the existence of a hybrid-biexciton, featuring a net spin of $s = \pm 3$. It is exactly this particular spin configuration that causes the crossing between the bright excitons and the hybrid-biexcitons in the corresponding μ-PL spectra. The strong repulsive dipole-dipole interaction in the hybrid-biexciton complex can be counterbalanced by the hole-hole exchange interaction and large correlation effects as approved by the provided agreement between calculations and experiment. Hence, due to angular momentum conservation, the commonly anticipated radiative decay sequence of such biexcitons is heavily altered in contrast to the classic counterpart with $s = 0$. The intermediate state of the cascade of the hybrid-biexciton is not any longer a bright exciton state with $s = \pm 1$ but a dark exciton state with $s = \pm 2$. As a most direct consequence of this deviating cascade, a spin reversal is necessary in order to proceed towards the second stage of the cascade, the decay of a bright exciton that finally leaves an empty GaN QD behind. The most striking evidence for this hybrid-biexciton is provided by the conjunction of polarization-, excitation-, and temperature-dependent μ-PL, in combination with correlation spectroscopy. On the basis of this unique phalanx of experimental techniques it is not only feasible to comprehend the cascade process, but also all energetic level spacings of the biexciton cascade can be derived. For the first time, the bright and the dark exciton splitting are experimentally accessible in a single QD along with the dark-bright splitting and the biexciton binding energy. As all these experimental parameters compare well regarding theory, the first coherent description for this novel member in the class of hybrid-quasiparticles is obtained.

9 Summary

The central results of this thesis establish a fundamental understanding regarding the optical signatures of single, wurtzite GaN quantum dots (QDs) embedded in AlN. A wide range of topics is encompassed, treating fundamental effects as the generation of multiexcitons, carrier dynamics, the exciton-phonon coupling, advanced photon statistics, unconventional quasiparticles, and even the interaction of QD excitons with their defect environment. In contrast to common QD systems based on e.g. selenides and arsenides, the analysis of nitride QDs is still a rather novel topic and its results often challenge existing established conceptions based on comparable, weakly polar QD materials. However, this unique opportunity to question time-honored models and understandings comes at the price of very challenging and elaborate single QD spectroscopy in the ultraviolet spectral range.

In order to overcome this challenge, the first aim of this thesis was to design and build a fully automated, extremely stable, and highly efficient micro-Photoluminescence (μ-PL) setup with time-resolved and correlation capabilities, second to none if compared to the international competition. All experimental results clearly demonstrate the unique capabilities of this setup sketched in the Appendix and speak for themselves. However, the entire set of original experimental results can only find its complete physical interpretation if an equally strong modeling is applied. A significant share of all the related modeling endeavors are based on 8-band k·p calculations in combination with a Hartree-Fock approach and correlation interaction calculations, allowing a successful description of excitons inherent to GaN QDs.

This experimentally focused thesis introduces the reader to common techniques of emission line assignment, which are further developed towards a successful identification of multiexcitonic complexes. An entire zoo of multiexcitonic emission lines is, for the first-time, identified in a GaN QD, boasting previously unobtainable level of detail, while also raising fundamental questions regarding complex binding energies and spin alignments. Exactly these challenges are again treated in the last chapter of this thesis, which describes an entire class of novel quasiparticles featuring so called hybrid-states. In this sense, the early description of extended multiexcitons establishes a common thread aiming towards the final thesis chapter that establishes such hybrid-quasiparticles. Following this common thread, the reader is introduced to the interaction of excitons with their defect environment yielding a

prominent emission line widths broadening, to the exciton-phonon coupling, and to highly unconventional photon statistics arising from the biexciton cascade.
While the identification of an exciton and a biexciton inherent to a single GaN QD has already been reported, the observation of excited state related luminescence situated ≈ 53 meV higher in energy represents a novel research result. In addition, various multi-excitonic complexes up to the sext-exciton are identified, which is not only an astonishing achievement regarding nitride QDs, but for any other QD system as well. For excitonic complexes up to the quart-exciton it was even possible to reveal their accompanying excited multiexcitonic transitions. As a result, not only all occurring multiexcitonic binding energies are reported, but also radiative decay and relaxation times are extracted. Hence, by combining excitation power dependent measurements scaling over ≈ 6 orders of magnitude with time-resolved μ-PL measurements, a large variety of multiexcitons can be observed, which invariably challenge any modeling approaches ever reported. The sheer size of the GaN QDs limits the theoretical treatment to an 8-band k·p approach combined with Hartree-Fock and correlation interaction calculations. However, even such an elaborated tool for the description of excitons struggles with complexes beyond the biexciton, emphasizing the importance of the presented experimental analysis. Nevertheless, the particular case of the biexciton still allows a direct comparison between experiment and theory, yielding a so far unprecedented agreement. The determined radiative decay times for the ground-state multiexcitons range from 7.73(28) ns to 1.97(04) ns, scaling with the number of participating electron-hole pairs, which determines the amount of available decay channels. The fact that no corresponding rise-time is observable within the experimental limits (≈ 5 ps) stands in good agreement with an Auger-electron-dominated relaxation process from the electronic matrix material or wetting layer states into the QD states that initially still overcomes the phonon-bottleneck effect. However, this particular balance scales with the number of free carriers, whose concentration rapidly decays after the laser-induced excitation. After the initial carrier population is established inside of the QD, further intra-QD relaxation is indeed limited by the efficiency of multi-phonon processes. This particular shift in the weighted balance between Auger- and multi-phonon-induced carrier relaxation is directly monitored by the conducted time-resolved μ-PL measurements. As a result, relaxation times scaling from 51(27) ps to 155(17) ps can be observed for a single GaN QD emitting at around 3.5 eV. Hence, despite the strong coupling between polar phonons and excitons in GaN QDs, a significant phonon-bottleneck is evident for the intra-QD relaxation, which naturally limits achievable, future device performance.

Any more detailed analysis of the multiexcitonic complexes by e.g. correlation spectroscopy is hindered by a particular emission line-width broadening phenomenon common for wurtzite GaN QDs. As a result, the median emission line width scales with the QD height from 8.2 meV at an emission energy of 3.45 eV down to 3.3 meV at 4.15 eV as derived by a statistical analysis of emission line widths based on hundreds of individual GaN QDs. Only rarely emission line widths below 1 meV can be observed and only recent growth advances allow entering the sub-meV range with record emission line width of just 440(5) μeV as shown in this thesis. Charge fluctuation in the close vicinity of the QDs along with huge dipole moments scaling from 1.55 e·nm down to 0.47 e·nm for the analyzed QD emission range cause a particular vulnerability of wurtzite GaN QDs to spectral diffusion, yielding the observed emission line broadening. However, this phenomenon does not only hinder more in-detail spectroscopic endeavors, it even enables novel pathways for an emission line assignment. Here, this particular correlation between the emission line width broadening and relative multiexcitonic dipole moments is applied for an identification of excitons and biexcitons in several GaN QDs in good agreement with the theoretical predictions. Furthermore, an estimate of the electric field strength that causes the emission line widths broadening can be obtained, yielding ≈ 2 MV/m along with an average distance of ≈ 8 nm in between the QD center and the particular, fluctuating, charged defect.

As a statistical analysis of emission line widths broadening presents such a beneficial tool, it is only natural to apply the same experimental concept focussing on the coupling between excitons and longitudinal-optical (LO) phonons in hundreds of single GaN QDs. Huge Huang-Rhys factors are observed as a measure of the related coupling strength, scaling from values of ≈ 0.5 down to below 0.05. While the Huang-Rhys factor decreases with increasing QD emission energy, i.e. diminishing QD height, the corresponding LO-phonon energies increase. A precise statistical analysis of contributing LO-phonon energies exhibits a gradual progression in between the bulk LO-phonon energies of the QD material (GaN) and the matrix material (AlN) with a slope of 8.25(1.20) meV/eV. As a result, a unique approximation of an exciton-LO-phonon interaction volume is obtained, yielding a diameter of 2.6(2) nm. Hence, the exciton-LO-phonon interaction regime overlaps into the QDs' matrix material and therefore even surpasses the exciton extent.

Multiexcitons and their most simplistic representative the biexciton can serve as ideal sources for advanced photon statistics. The biexciton cascade for GaN QDs at approximately an energy of 3.5 eV benefits from small excitonic fine-structure splittings, which enable an efficient contribution of two-photon processes. Such two-photon processes account for a bunching phenomenon observed in the corresponding $g^{(2)}(\tau)$ correlation functions. At $\tau = 0$ a striking bunching effect is noticeable, which

reaches well up to $g^{(2)}(0) = 3.1$. Hence, the biexciton cascade in single, wurtzite GaN QDs represents an ideal candidate for the generation of photon-pairs. For particularly small biexciton binding energies and negligible excitonic fine-structure splittings, it is even feasible to observe an excitation- and/or temperature-induced dephasing of the two-photon states. Hence, the presented measurements detail the first demonstration of an optically driven UV-two-photon source up to a temperature of 50 K. Exactly quantum light sources of such kind are described as a key requirement for quantum cryptography ultimately leading to truly secure data transmission [6]. By providing a numerical solution of the quantum state tomography related to the biexciton cascade, a unique understanding of the balance between one- and two-photon processes can be established. Additionally, an intuitive model is developed in order to explain the complex underlying quantum physics, facilitating a fundamental understanding based on level schemes depicting decay channels.
The analysis of the exciton interaction with its charge and phononic environment, along with the correlation analysis finally culminates in the description of hybrid-quasiparticles. As a first member of this novel class of hybrid-quasiparticles, the biexciton is experimentally analyzed by the entire set of experimental techniques. As a result, an astonishing agreement with the presented calculations is achieved, which predict an experimentally confirmed novel spin alignment for certain biexcitonic complexes. Depending on the the QDs' emission energy that is affected by their size, the biexciton in GaN QDs can either exhibit a classical spin configuration (antiparallel hole and electron spins) or a hybrid spin configuration featuring *parallel* hole spins. Consequently, the emission characteristics and statistics are heavily altered, showing unknown polarization patterns and the signature of a spin-blockade biexcitonic cascade at a temperature of 8 K. However, raising the temperature towards 30 K enables the entire biexcitonic cascade, evidencing a phonon-mediated spin-flip process from the dark-exciton states into their bright counterparts. A unique combination of temperature- and polarization-dependent luminescence studies even directly results all important parameters of the underlying biexciton cascade in-line with the theoretical results, featuring a biexciton binding energy of $> 25(1)$ meV, an exciton bright-state splitting of 4.3(2) meV, an exciton dark-state splitting of 270(50) μeV, and an exciton bright-dark-splitting of $\approx 1.0(3)$ meV at an emission energy of around 4.0 eV. Finally, the high hole masses native to wurtzite GaN QDs facilitate their spatial separation that enables the parallel hole spin configuration. Similar configurations can be expected for the experimentally observed species-rich zoo of multiexcitons, rendering their simulation and further analysis a compelling, future task. Hybrid-quasiparticles appear not only as highly promising for future quantum-computing and bit storage applications, but also for more fundamental spectroscopy under the influence of magnetic fields.

10 Publications

The presented thesis includes results that have already been published in the following papers marked with an asterisk (*). All other publications not directly related to the topic of the thesis just reflect the author's many-sided particular research interests. Some of these additional publications marked with a dagger (†) include fundamental parameters for bulk GaN, AlN, and ZnO that have already partly been considered in reference books as the "Landolt-Börnstein - Group III Condensed Matter".

Articles

(36) **Emission energy dependent line width variations of excitons and biexcitons inherent to single, wurtzite GaN quantum dots**
G. Hönig, G. Callsen, A. Bokov, S. Kalinowski, and A. Hoffmann,
Phys. Stat. Sol (RRL) (manuscript in preparation based on Chap. 5, page 62)

(35) **Multi-excitons in single, wurtzite GaN quantum dots**
G. Callsen, G. Hönig, A. Bokov, S. Kalinowski, and A. Hoffmann,
Phys. Rev. B. (manuscript in preparation based on Chap. 4, page 39)

(34) **Stability and excitation channels of nitrogen acceptor related DAP transitions in highly N doped ZnO**
M. R. Wagner, J. S. Reparaz, G. Callsen, C. Nenstiel, S. Lautenschlaeger, B. K. Meyer, A. Hoffmann, and M. R. Phillips,
Appl. Phys. Letters (manuscript in preparation)

(33) **Germanium, the superior dopant in n-type GaN**
C. Nenstiel, M. Bügler, G. Callsen, F. Nippert, S. Fritze, A. Dadgar, H. Witte, A. Rohrbeck, A. Krost, and A. Hoffmann,
submitted to Phys. Stat. Sol (RRL).

(32) **Influence of Blue Luminescence and QCSE in green InGaN/GaN QWs**
F. Nippert, A. Nirschl, I. Pietzonka, T. Schulz, M. Albrecht, S. Westerkamp, T. Kure, C. Nenstiel, G. Callsen, M. Strassburg, and A. Hoffmann,
submitted to Appl. Phys. Letters.

(31) **Desorption induced GaN quantum dots on (0001) AlN by MOVPE**
K. Bellmann, F. Tabataba-Vakili, T. Wernicke, A. Strittmatter, G. Callsen, A. Hoffmann, and M. Kneissl,
submitted to Appl. Phys. Letters.

(30) **Direct evidence of quantum dot emission from GaN islands at threading dislocations using scanning transmission electron microscope cathodoluminescence**
G. Schmidt, C. Berger, P. Veit, S. Metzner, F. Bertram, A. Dadgar, A. Strittmatter, G. Callsen, A. Hoffmann, and J. Christen,
submitted to Appl. Phys. Letters.

(29) **Resonant phonon and exciton dynamics in ZnO**
M. R. Wagner, J. S. Reparaz, S. Werner, R. Kirste, G. Callsen, C. Thomsen, and A. Hoffmann,
submitted to Phys. Rev. B.

(28) **Mimicking nature: ZnO nanotrees to boost light harvesting**
I. Gonzalez-Valls, F. Güell, B. Ballesteros, M. R. Wagner, G. Callsen, A. Hoffmann, J. S. Reparaz, and M. Lira-Cantu,
Under review in Solar Energy Materials & Solar Cells.

(27) **Analysis of the exciton-LO-phonon coupling in single, wurtzite GaN quantum dots**
G. Callsen, G. Hönig, S. Kalinowski, C. Kindel, J. Settke, J. Brunnmeier, A. Bokov, C. Nenstiel, T. Kure, F. Nippert, A. Schliwa, T. Markurt, T. Schulz, M. Albrecht, S. Kako, M. Arita, Y. Arakawa, and A. Hoffmann,
Under review in Phys. Rev. B (based on Chap. 6, page 74).

(26*) **Manifestation of unconventional biexciton states in quantum dots**
G. Hönig, G. Callsen, A. Schliwa, S. Kalinowski, C. Kindel, S. Kako, Y. Arakawa, D. Bimberg, and A. Hoffmann,
Nat. Commun. **5**, 5721 (2014), *"G. H. and G. C. contributed equally to the manuscript (see author contributions)"*.

(25†) **Phonon pressure coefficients and deformation potentials of wurtzite AlN determined by uniaxial pressure-dependent Raman measurements**
G. Callsen, M. R. Wagner, J. S. Reparaz, F. Nippert, T. Kure, S. Kalinowski, A. Hoffmann, M. J. Ford, M. R. Phillips, R. F. Dalmau, R. Schlesser, R. Collazo, and Z. Sitar,
Phys. Rev. B **90**, 205206 (2014).

(24) **Dependence on pressure of the refractive indices of wurtzite ZnO, GaN, and AlN**
A. R. Goni, F. Kaess, J. S. Reparaz, M. I. Alonso, M. Garriga, G. Callsen, M. R. Wagner, A. Hoffmann, and Z. Sitar,
Phys. Rev. B **90**, 045208 (2014).

(23*) **Spectral diffusion in nitride quantum dots: Emission energy dependent linewidths broadening via giant built-in dipole moments**
C. Kindel, G. Callsen, S. Kako, T. Kawano, H. Oishi, G. Hönig, A. Schliwa, Y. Arakawa, and A. Hoffmann,
Phys. Stat. Sol (RRL) **8**, 408 (2014), *"the first and the second author equally contributed to the manuscript (see Acknowledgement)"*.

(22) **Non-polar GaN quantum dots integrated into high quality cubic AlN microdisks**
M. Bürger, G. Callsen, T. Kure, A. Hoffmann, A. Pawlis, D. Reuter, and D. J. As,
Phys. Stat. Sol (c) **11**, 790 (2014).

(21) **Effects of strain on the valence band structure and exciton-polariton energies in ZnO**
M. R. Wagner, G. Callsen, J. S. Reparaz, R. Kirste, A. Hoffmann, A. V. Rodina, A. Schleife, F. Bechstedt, and M. R. Phillips,
Phys. Rev. B **88**, 235210 (2013).

(20) **Identification of electric dipole moments of excitonic complexes in nitride-based quantum dots**
G. Hönig, S. Rodt, G. Callsen, I. A. Ostapenko, T. Kure, A. Schliwa, C. Kindel, D. Bimberg, A. Hoffmann, S. Kako, and Y. Arakawa,
Phys. Rev. B **88**, 045309 (2013).

(19) **Lasing properties of non-polar GaN quantum dots in cubic aluminum nitride microdisk cavities**
M. Bürger, G. Callsen, T. Kure, A. Hoffmann, A. Pawlis, D. Reuter, and D. J. As,
Appl. Phys. Lett. **103**, 021107 (2013).

(18) **Spatial mapping of exciton lifetimes in single ZnO nanowires**
J. S. Reparaz, G. Callsen, M. R. Wagner, F. Güell, J. R. Morante, C. M. Sotomayor Torres, and A. Hoffmann,
APL Mat. **1**, 012103 (2013).

(17*) **Steering photon statistics in single quantum dots: From one- to two-photon emission**
G. Callsen, A. Carmele, G. Hönig, C. Kindel, J. Brunnmeier, M. R. Wagner, E. Stock, J. S. Reparaz, A. Schliwa, S. Reitzenstein, S. Kako, Y. Arakawa, A. Knorr, and A. Hoffmann,
Phys. Rev. B **87**, 245314 (2013), *"editors choice"*.

(16) **Structural and optical investigation of non-polar (1-100) GaN grown by the ammonothermal method**
D. Gogova, P. P. Petrov, M. Bügler, M. R. Wagner, C. Nenstiel, G. Callsen, M. Schmidbauer, R. Kucharski, M. Zajac, R. Dwilinski, M. R. Phillips, A. Hoffmann, and R. Fornari,
J. Appl. Phys. **113**, 203513 (2013).

(15) **Probing local strain and composition in Ge nanowires by means of tip-enhanced Raman scattering**
J. S. Reparaz, N. Peica, R. Kirste, A. R. Goni, M. R. Wagner, G. Callsen, M. I. Alonso, M. Garriga, I. C. Marcus, A. Ronda, I. Berbezier, J. Maultzsch, C. Thomsen, and A. Hoffmann,
Nanotechnology **24**, 185704 (2013).

(14) **Fermi Level Control of Point Defects During Growth of Mg-Doped GaN**
Z. Bryan, M. Hoffmann, J. Tweedie, R. Kirste, G. Callsen, I. Bryan, A. Rice, M. Bobea, S. Mita, J. Xie, Z. Sitar and R. Collazo,
J. Elec. Mat. **42**, 815 (2013).

(13) **Compensation effects in GaN:Mg probed by Raman spectroscopy and photoluminescence measurements**
R. Kirste, M. P. Hoffmann, J. Tweedie, Z. Bryan, G. Callsen, T. Kure, C. Nenstiel, M. R. Wagner, R. Collazo, A. Hoffmann, and Z. Sitar,
J. Appl. Phys. **113**, 103504 (2013).

(12) **Signature of the two-dimensional phonon dispersion in graphene probed by double-resonant Raman scattering**
P. May, M. Lazzeri, P. Venezuela, F. Herziger, G. Callsen, J. S. Reparaz, A. Hoffmann, F. Mauri, and J. Maultzsch,
Phys. Rev. B **87**, 075402 (2013).

(11) **Structural investigations of silicon nanostructures grown by self-organized island formation for photovoltaic applications**
M. Roczen, M. Schade, E. Malguth, G. Callsen, T. Barthel, O. Gref, J. A. Töfflinger, A. Schöpke, M. Schmidt, H. S. Leipner, F. Ruske, M. R. Phillips, A. Hoffmann, L. Korte, and B. Rech,
Appl. Phys. A **108**, 719 (2012).

(10) **Optical signature of Mg-doped GaN: Transfer processes**
G. Callsen, M. R. Wagner, T. Kure, J. S. Reparaz, M. Bügler, J. Brunnmeier, C. Nenstiel, M. Hoffmann, J. Tweedie, Z. Bryan, S. Aygun, R. Kirste, R. Collazo, Z. Sitar, and A. Hoffmann,
Phys. Rev. B **86**, 075207 (2012).

(9) **Optical signatures of nitrogen acceptors in ZnO**
S. Lautenschlaeger, S. Eisermann, G. Haas, E. A. Zolnowski, M. N. Hofmann, A. Laufer, M. Pinnisch, M. R. Wagner, J. S. Reparaz, G. Callsen, A. Hoffmann, A. Chernikov, S. Chatterjee, V. Bornwasser, M. Koch, and B. K. Meyer,
Phys. Rev. B **85**, 235204 (2012).

(8) **Temperature dependent photoluminescence of lateral polarity junctions of metal organic chemical vapor deposition grown GaN**
R. Kirste, R. Collazo, G. Callsen, M. R. Wagner, T. Kure, J. S. Reparaz, S. Mita, J. Xie, A. Rice, J. Tweedie, Z. Sitar, and A. Hoffmann,
J. of Appl. Phys. **110**, 093503 (2011).

(7) **Titanium-assisted growth of silica nanowires: from surface-matched to free-standing morphologies**
G. Callsen, J. S. Reparaz, M. R. Wagner, A. Vierck, M. R. Phillips, C. Thomsen, and A. Hoffmann,
Nanotechnology **22**, 405604 (2011).

(6) **Bound excitons in ZnO: Structural defect complexes versus shallow impurity centers**
M. R. Wagner, G. Callsen, J. S. Reparaz, J.-H. Schulze, R. Kirste, M. Cobet, I. A. Ostapenko, S. Rodt, C. Nenstiel, M. Kaiser, and A. Hoffmann,
Phys. Rev. B **84**, 035313 (2011).

(5†) **Phonon deformation potentials in wurtzite GaN and ZnO determined by uniaxial pressure dependent Raman measurements**
G. Callsen, J. S. Reparaz, M. R. Wagner, R. Kirste, C. Nenstiel, M. R. Phillips, and A. Hoffmann,
Appl. Phys. Lett. **98**, 061906 (2011).

(4) **Recombination dynamics in ZnO nanowires: Surfaces states versus mode quality factor**
J. S. Reparaz, F. Guell, M. R. Wagner, G. Callsen, R. Kirste, S. Claramunt, J. R. Morante, and A. Hoffmann,
Appl. Phys. Lett. **97**, 133116 (2010).

(3) **Excited state properties of donor bound excitons in ZnO**
B. K. Meyer, J. Sann, S. Eisermann, S. Lautenschlaeger, M. R. Wagner, M. Kaiser, G. Callsen, J. S. Reparaz, and A. Hoffmann,
Phys. Rev. B **82**, 115207 (2010).

(2) **Lithium related deep and shallow acceptors in Li-doped ZnO nanocrystals**
C. Rauch, W. Gelhoff, M. R. Wagner, E. Malguth, G. Callsen, R. Kirste, B. Salameh, A. Hoffmann, S. Polarz, Y. Aksu, and M. Driess,
J. of Appl. Phys. **107**, 024311 (2010).

(1) **Nitrogen incorporation in homoepitaxial ZnO CVD epilayers**
S. Lautenschlaeger, S. Eisermann, B. K. Meyer, G. Callsen, M. R. Wagner, and A. Hoffmann,
Phys. Stat. Sol. (RRL) **3**, 16 (2009).

11 Conference contributions

Invited talks:

(12) **Steering the optical properties of nitride quantum dots**
G. Callsen, A. Carmele, G. Hönig, C. Kindel, A. Schliwa, A. Knorr, S. Kako, Y. Arakawa, and A. Hoffmann
METANANO 2014, Varadero, Cuba.

(11) **Optical properties of single GaN/AlN quantum dots**
G. Callsen, G. Hönig, A. Carmele, C. Kindel, T. Markurt, S. Kalinowski, T. Kure, J. Brunnmeier, A. Schliwa, S. Kako, Y. Arakawa, A. Knorr, M. Albrecht, and A. Hoffmann
Graduate Lecture 2014, Paderborn, Germany.

(10) **Steering the optical properties of nitride quantum dots**
G. Callsen, G. Hönig, A. Carmele, C. Kindel, S. Kalinowski, T. Kure, J. Brunnmeier, A. Schliwa, S. Kako, Y. Arakawa, A. Knorr, and A. Hoffmann
SemiconNano 2013, Lake Arrowhead, USA.

Contributed talks:

(09) **Multiexcitonic complexes and excited states in single wurtzite GaN/AlN quantum dots**
G. Callsen, G. Hönig, A. Carmele, C. Kindel, S. Kalinowski, T. Kure, J. Brunnmeier, A. Schliwa, S. Kako, Y. Arakawa, A. Knorr, and A. Hoffmann
10th International Conference on Nitride Semiconductors, 2013, Washington DC, USA.

(08) **The effects of large electric dipole moments in GaN QDs**
G. Callsen, G. Hönig, J. Brunnmeier, D. Bostanjoglo, S. Kalinowski, A. Schliwa, S. Sako, Y. Arakawa, and A. Hoffmann
Research Seminar - Christen, Krost, Goldhahn - 2013, Magdeburg, Germany.

(07) **Photoluminescence analysis of wurtzite GaN quantum dots up to non-cryogenic temperatures**
G. Callsen, G. Hönig, A. Carmele, J. Brunnmeier, D. Bostanjoglo, S. Kalinowski, T. Kure, M. R. Wagner, A. Schliwa, S. Sako, Y. Arakawa, A. Knorr, and A. Hoffmann
EMRS 2013, Strasbourg, France.

(06) **Giant exciton-phonon coupling in single wurtzite GaN quantum dots**
G. Callsen, J. Settke, T. Markurt, J. Brunnmeier, T. Kure, M. R. Wagner, G. Hönig, C. Kindel, S. Kako, M. Albrecht, A. Schliwa, Y. Arakawa, and A. Hoffmann
International Workshop on Nitrides (IWN), Sapporo, Japan.

(05) **Two-photon emission from single GaN quantum dots**
G. Callsen, J. Brunnmeier, G. Hönig, C. Kindel, E. Stock, J. Settke, A. Schliwa, S. Kako, Y. Arakawa, and A. Hoffmann
76th DPG Spring Meeting 2012, Berlin, Germany.

(04) **Phonon deformation potential determination in GaN, AlN and ZnO for strain tailoring applications**
G. Callsen, J. S. Reparaz, M. R. Wagner, R. Kirste, M. Bügler, M. Hoffmann, R. Collazo, Z. Sitar, A. R. Goni, and A. Hoffmann
EMRS 2011, Nice, France.

(03) **Detailed Photoluminescence study of the magnesium related acceptor states in GaN**
G. Callsen, T. Kure, M. R. Wagner, R. Kirste, J. S. Reparaz, M. Hoffmann, S. Aygun, J. Tweedie, R. Collazo, Z. Sitar, C. Nenstiel, M. R. Phillips, and A. Hoffmann
Spie Photonics West 2011, San Francisco, USA.

(02) **Uniaxial stress dependent analysis of the optical and vibrational properties of high quality ZnO substrates**
G. Callsen, M. R. Wagner, R. Kirste, J.-H. Schulze, and A. Hoffmann
74th DPG Spring Meeting 2010, Regensburg, Germany.

(01) **Influence of uniaxial strain on the optical and vibrational properties of high quality ZnO substrates**
G. Callsen, M. R. Wagner, R. Kirste, J.-H. Schulze, and A. Hoffmann
73rd DPG Spring Meeting 2009, Dresden, Germany.

Posters:

(P1) **Exciton-Phonon coupling in single wurtzite GaN quantum dots**
G. Callsen, A. Schliwa, S. Kako, G. Hönig, I. A. Ostapenko, J. Brunnmeier, J. Settke, C. Kindel, E. Stock, Y. Arakawa, and A. Hoffmann
QD 2012, Santa Fe, USA.

12 Appendix

The scheme of the μ-PL setup introduced by Fig. 2.2 (page 18) in Chap. 2 illustrates a strong simplification of the entire μ-PL system, which also suits luminescence techniques beyond the scope of the present thesis. Due to the complexity of the entire constructed μ-PL system it is better illustrated by three separate figures. Hence, Fig. 12.1, Fig. 12.2, and Fig. 12.3, depict the "Excitation", the "Main μ-PL", and the "Detection" part of the entire μ-PL system that are directly connectable via the sketched beam paths.

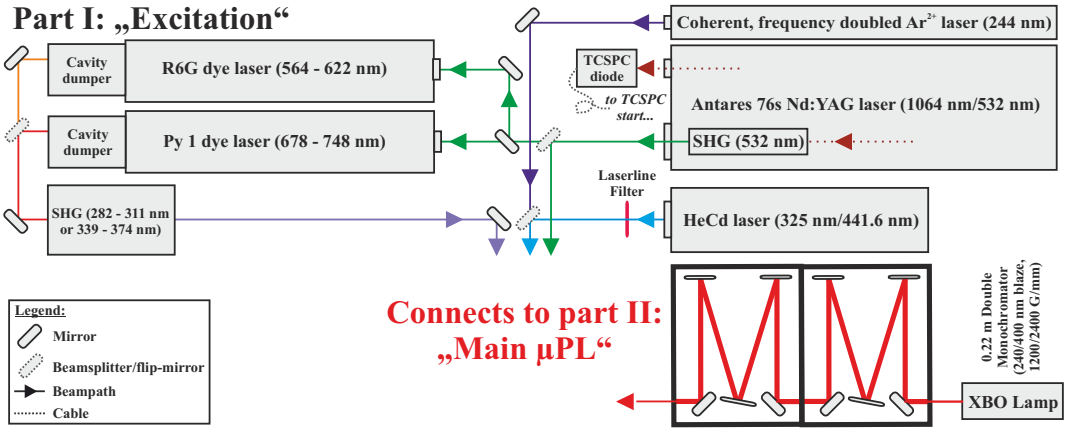

Figure 12.1: Illustration of the "Excitation" part I of the constructed μ-PL system featuring a large variety of different pulsed and continuous-wave laser sources along with a monochromatized XBO lamp. The section shown directly connects to the "Main μ-PL system" in Fig. 12.2 via the sketched light beam paths. Please see the text for details.

Nearly all experimental results presented in this thesis are based on continuous wave (cw) laser sources like a frequency doubled Ar^{2+}-laser (244 nm, Coherent, Innova 300 FreD) and a HeCd laser (325 nm, Melles Griot, Series 74) as shown in Fig. 12.1. An extra-cavity frequency-quadrupled (2+2), pulsed Nd:YAG laser (266 nm, Coherent, Antares 76 s) was applied for the μ-TRPL measurements providing $\approx$55 ps wide laser pulses with a repetition rate of 76 MHz based on the principle of active mode locking. However, also several additional alternative laser sources are available in the constructed μ-PL setup and are intended for future measurements as additionally illustrated in Fig. 12.1, showing the entire "Excitation" part of the μ-PL system along with an XBO lamp attached to a double monochromator featuring various

gratings for future photoluminescence excitation (PLE) measurements.

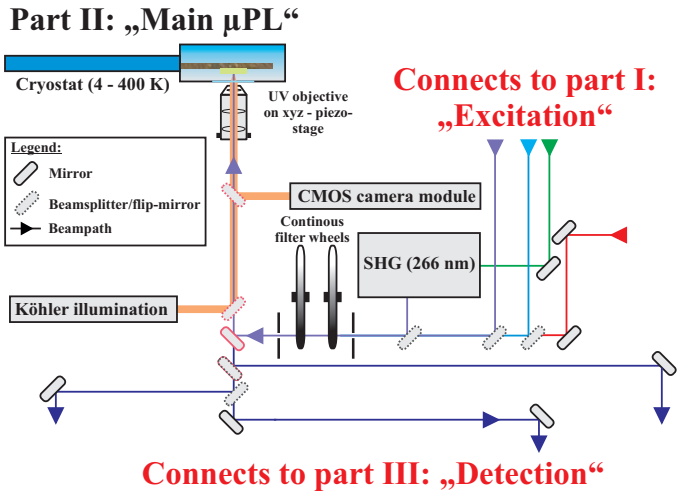

Figure 12.2: The "Main μ-PL" setup section is shown, connecting the experimental sections from Fig. 12.1 and Fig. 12.3. The sample is situated in the helium flow cryostat and a microscope lens [specialized for the ultraviolet (UV) spectral range] focusses the laser of choice onto the sample. The luminescence light is gathered by the same microscope lens and is consequently transferred to the detection section. Please see the text for details.

The directly to Fig. 12.1 connected "Main μ-PL part" is illustrated in Fig. 12.2. The e.g. GaN/AlN quantum dot (QD) sample is situated in a helium flow cryostat (Janis ST-500 microscope cryostat, 4 - 400 K) and the laser light of choice is focussed onto the sample surface by a microscope lens [N.A. 0.4 - 0.65, magnification 20x - 50x, several manufactures, ultraviolet (UV) transmission]. In order to facilitate μ-PL mapscans over the sample's surface the microscope lens is mounted on a closed-loop, 3-axis, piezo actuator with a travel range of 100 μm (Physik Instrumente, P-611.3 cube). Due to space restrictions, the final second harmonic generation step (SHG), leading to the extra-cavity quadrupling of the pulsed Nd:YAG laser, is implement in this section of the μ-PL setup. In order to e.g. locate mesa structures on the GaN/AlN QD sample surface with a diameter of down to 200 nm by a microscope lens with the listed comparable low magnifications, one needs to take special care on the microscope illumination and final imaging on a 1/2" CMOS monochrome camera (iDS, UI-5240SE-M-GL). Therefore, a fully customized Köhler illumination along with a matching CMOS camera modul were constructed. Fully automatized continuous neutral density filter wheels allow precise control of the excitation power over up to 6 orders of magnitude.

The light collected from the sample of choice is finally guided towards the "Detection" section of the μ-PL system as shown in Fig. 12.2. As most straightforward detection choice, a single monochromator (Spex 1704, focus length of 1 m, various gratings) is available reaching an optical resolution of below 100 μeV at a central

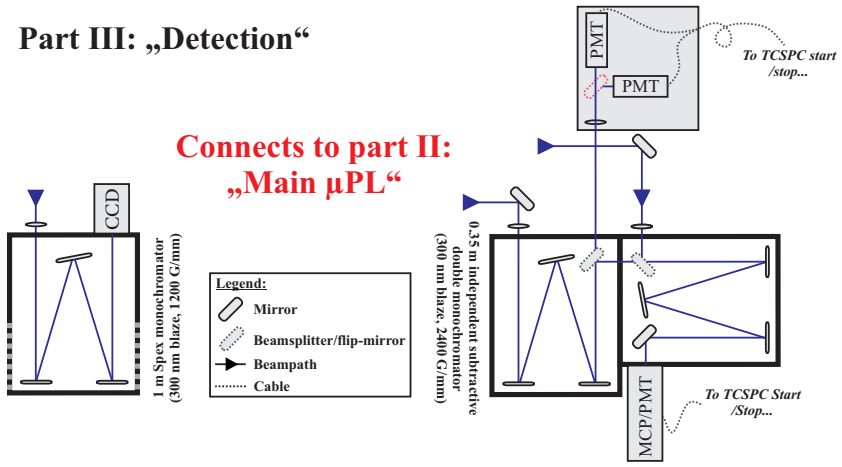

Figure 12.3: Illustration of the "Detection" section of the μ-PL system directly connecting to the experimental setup shown in Fig. 12.2. For standard μ-PL measurements a monochromator equipped with a charge-coupled device (CCD) is available and for μ-TRPL a subtractive double monochromator can be applied. Auto- and cross-correlation measurements can be performed with the illustrated Hanburry-Brown & Twiss (HBT) setup. Please see the text for details.

wavelength of ≈ 300 nm if higher (e.g. 2nd) grating orders are applied. The system is equipped with a 2048 pixel wide, UV-enhanced charge-coupled device (CCD, Princeton Instruments, SPEC-10) and a large variety of edge filters can be used in order to reach the desired straight light level reduction in the corresponding monochromator. As an alternative, the luminescence light can also be guided towards an independently drivable, subtractive, double monochromator (McPherson, 2035, focus length of 0.35 m, various gratings). If the entire subtractive double monochromator is used in combination with a multichannel plate photomultiplier (e.g. Hamamatsu, R3809U-50, S20 cathode) and one of the various pulsed laser sources then μ-TRPL measurements can be performed. Therefore, the time-correlated single photon counting technique (TSPC) is applied in combination with a suitable two-channel TSPC measurement card (Becker & Hickl, SPC-130 modul) and a fast photodiode modul (Becker & Hickl, PHD-400), cf. Fig. 12.1. As a result, one obtains an ideal time resolution of down to ≈ 30 ps if one of the dye lasers (Fig. 12.1) is applied. If additional deconvolution techniques are applied then even a time resolution of below 10 ps is achievable [47], depending on the signal to noise ratio of the measured signal. The most outstanding subsection of the constructed μ-PL system is the Hanburry-Brown & Twiss (HBT) setup, cf. Fig. 12.3. Due to the independently driven subtractive double monochromator one can perform auto- and cross-correlation measurements down to a wavelength of ≈ 250 nm. Photomultiplier tubes (Hamamatsu, H10721-210) are used as detectors in the HBT setup, exhibiting a measured biphoton time

resolution of down to 225 ps.
The entire μ-PL system described by Fig. 12.1 - 12.3 is controlled by a Labview program, operating the monochromators, the UV-enhanced CCD, the piezo stage, the cryostat mount, and the TSPC measurement card. Additionally, motor-driven, fully UV-capable $\lambda/2$-plates and linear polarizers can be mounted into the beam path of choice in order to allow polarization angle resolved μ-PL scans.

Bibliography

[1] Y. Arakawa and H. Sakaki, "Multidimensional quantum well laser and temperature dependence of its threshold current," *Applied Physics Letters*, vol. 40, pp. 939–941, June 1982.

[2] R. Dingle and C. H. Henry, "Quantum effects in heterostructure lasers." US Patent Office, 1976.

[3] M. Asada, Y. Miyamoto, and Y. Suematsu, "Gain and the threshold of three-dimensional quantum-box lasers," *IEEE Journal of Quantum Electronics*, vol. 22, pp. 1915–1921, Sept. 1986.

[4] D. Bimberg, N. Kirstaedter, N. N. Ledentsov, Z. I. Alferov, P. S. Kop'ev, and V. M. Ustinov, "InGaAs-GaAs quantum-dot lasers," *IEEE Journal of Selected Topics in Quantum Electronics*, vol. 3, pp. 196–205, Apr. 1997.

[5] P. Michler, A. Imamoğlu, M. D. Mason, P. J. Carson, G. F. Strouse, and S. K. Buratto, "Quantum correlation among photons from a single quantum dot at room temperature," *Nature*, vol. 406, no. 6799, pp. 968–970, 2000.

[6] P. Zoller, T. Beth, D. Binosi, R. Blatt, H. Briegel, D. Bruss, T. Calarco, J. I. Cirac, D. Deutsch, and J. Eisert, "Quantum information processing and communication," *The European Physical Journal D-Atomic, Molecular, Optical and Plasma Physics*, vol. 36, no. 2, pp. 203–228, 2005.

[7] Y. Shirasaki, G. J. Supran, M. G. Bawendi, and V. Bulović, "Emergence of colloidal quantum-dot light-emitting technologies," *Nature Photonics*, vol. 7, pp. 13–23, Dec. 2012.

[8] D. Bimberg, M. Grundmann, and N. N. Ledentsov, *Quantum dot heterostructures*. Wiley, Dec. 1998.

[9] X. Peng, L. Manna, W. Yang, J. Wickham, E. Scher, A. Kadavanich, and A. P. Alivisatos, "Shape control of CdSe nanocrystals," *Nature*, vol. 404, pp. 59–61, Mar. 2000.

[10] R. Rossetti, J. L. Ellison, J. M. Gibson, and L. E. Brus, "Size effects in the excited electronic states of small colloidal CdS crystallites," *Journal Of Chemical Physics*, vol. 80, no. 9, p. 4464, 1984.

[11] E. Koroknay, W.-M. Schulz, M. Eichfelder, R. Roßbach, M. Jetter, and P. Michler, "InP quantum dots for applications in laser devices and future solid-state quantum gates," *Journal of Physics: Conference Series*, vol. 245, p. 012077, Sept. 2010.

[12] N. Koshida, "Device Applications of Silicon Nanocrystals and Nanostructures," *Device Applications of Silicon Nanocrystals and Nanostructures:*, 2009.

[13] V. A. Shchukin, N. N. Ledentsov, P. S. Kop'ev, and D. Bimberg, "Spontaneous Ordering of Arrays of Coherent Strained Islands," *Physical Review Letters*, vol. 75, pp. 2968–2971, Oct. 1995.

[14] S. B. Nam, D. C. Reynolds, C. W. Litton, R. J. Almassy, T. C. Collins, and C. M. Wolfe, "Free-exciton energy spectrum in GaAs," *Physical Review B*, vol. 13, pp. 761–767, Jan. 1976.

[15] K. Takahashi, A. Yoshikawa, and A. Sandhu, *Wide bandgap semiconductors*. Berlin, Heidelberg, New York: Springer, 2007.

[16] B. G. Levi, "Nobel Prize in Physics recognizes research leading to high-brightness blue LEDs," *Physics Today*, vol. 67, pp. 14–17, Dec. 2014.

[17] E. F. Schubert, T. Gessmann, and J. K. Kim, *Light emitting diodes*. Cambridge University Press, 2 ed., 2005.

[18] B. K. Meyer, *AlN: excitonic energy gaps, exciton binding energies and lifetime*, vol. 44A of *Landolt-Börnstein - Group III Condensated Matter*. New Data and Updates for I-VII, 2009.

[19] W. Yang, J. Li, Y. Zhang, P.-K. Huang, T.-C. Lu, H.-C. Kuo, S. Li, X. Yang, H. Chen, D. Liu, and J. Kang, "High density GaN/AlN quantum dots for deep UV LED with high quantum efficiency and temperature stability," *Scientific Reports*, vol. 4, June 2014.

[20] C. Himwas, R. Songmuang, L. S. Dang, J. Bleuse, L. Rapenne, E. Sarigiannidou, and E. Monroy, "Thermal stability of the deep ultraviolet emission from AlGaN/AlN Stranski-Krastanov quantum dots," *Applied Physics Letters*, vol. 101, no. 24, p. 241914, 2012.

[21] S. Tanaka, S. Iwai, and Y. Aoyagi, "Self-assembling GaN quantum dots on AlGaN surfaces using a surfactant," *Applied Physics Letters*, vol. 69, no. 26, p. 4096, 1996.

[22] B. Daudin, F. Widmann, G. Feuillet, Y. Samson, M. Arlery, and J. L. Rouviere, "Stranski-Krastanov growth mode during the molecular beam epitaxy of highly strained GaN," *Physical Review B*, vol. 56, p. 7069, Sept. 1997.

[23] M. Jetter, V. Pérez-Solórzano, A. Gröning, H. Gräbeldinger, M. Ubl, and H. Schweizer, "Carrier dynamics in sitecontrolled GaInN quantum dots," *physica status solidi (c)*, vol. 3, no. 6, pp. 2060–2064, 2006.

[24] I. A. Ostapenko, G. Hönig, C. Kindel, S. Rodt, A. Strittmatter, A. Hoffmann, and D. Bimberg, "Large internal dipole moment in InGaN/GaN quantum dots," *Applied Physics Letters*, vol. 97, p. 063103, 2010.

[25] F. Widmann, J. Simon, B. Daudin, G. Feuillet, J. L. Rouviere, N. T. Pelekanos, and G. Fishman, "Blue-light emission from GaN self-assembled quantum dots due to giant piezoelectric effect," *Physical Review B*, vol. 58, no. 24, pp. 15989–15992, 1998.

[26] L. Dang, G. Fishman, H. Mariette, C. Adelmann, E. Martinez, J. Simon, B. Daudin, E. Monroy, N. Pelekanos, J. Rouviere, and Y. Cho, "GaN quantum dots: Physics and applications," *Journal Of The Korean Physical Society*, vol. 42, pp. S657–S661, 2003.

[27] S. Kako, M. Miyamura, K. Tachibana, K. Hoshino, and Y. Arakawa, "Size-dependent radiative decay time of excitons in GaN/AlN self-assembled quantum dots," *Applied Physics Letters*, vol. 83, no. 5, p. 984, 2003.

[28] T. Bretagnon, S. Kalliakos, P. Lefebvre, P. Valvin, B. Gil, N. Grandjean, A. Dussaigne, B. Damilano, and J. Massies, "Time dependence of the photoluminescence of GaN/AlN quantum dots under high photoexcitation," *Physical Review B*, vol. 68, no. 20, p. 205301, 2003.

[29] K. Hoshino, S. Kako, and Y. Arakawa, "Formation and optical properties of stacked GaN self-assembled quantum dots grown by metalorganic chemical vapor deposition," *Applied Physics Letters*, vol. 85, p. 1262, 2004.

[30] D. Simeonov, E. Feltin, J. F. Carlin, R. Butté, M. Ilegems, and N. Grandjean, "Stranski-Krastanov GaN/AlN quantum dots grown by metal organic vapor phase epitaxy," *Journal Of Applied Physics*, vol. 99, p. 3509, Apr. 2006.

[31] C. Santori, S. Götzinger, Y. Yamamoto, S. Kako, K. Hoshino, and Y. Arakawa, "Photon correlation studies of single GaN quantum dots," *Applied Physics Letters*, vol. 87, no. 5, p. 051916, 2005.

[32] S. Kako, C. Santori, K. Hoshino, S. Goetzinger, Y. Yamamoto, and Y. Arakawa, "A gallium-nitride single-photon source operating at 200K," *Nature Materials*, vol. 5, no. 11, pp. 887–892, 2006.

[33] M. J. Holmes, K. Choi, S. Kako, M. Arita, and Y. Arakawa, "Room-temperature triggered single photon emission from a III-Nitride site-controlled nanowire quantum dot," *Nano Letters*, 2014.

[34] A. D. Andreev and E. P. O'Reilly, "Theory of the electronic structure of GaN/AlN hexagonal quantum dots," *Physical Review B*, vol. 62, no. 23, p. 15851, 2000.

[35] M. Winkelnkemper, A. Schliwa, and D. Bimberg, "Interrelation of structural and electronic properties in InGaN / GaN quantum dots using an eight-band kp model," *Physical Review B*, vol. 74, no. 15, p. 155322, 2006.

[36] S. Tomić and N. Vukmirović, "Excitonic and biexcitonic properties of single GaN quantum dots modeled by 8-band kp theory and configuration interaction method," *Physical Review B*, vol. 79, no. 24, p. 245330, 2009.

[37] C. Kindel, S. Kako, T. Kawano, H. Oishi, Y. Arakawa, G. Hönig, M. Winkelnkemper, A. Schliwa, A. Hoffmann, and D. Bimberg, "Exciton fine-structure splitting in GaN/AlN quantum dots," *Physical Review B*, vol. 81, no. 24, p. 241309, 2010.

[38] G. Hönig, S. Rodt, G. Callsen, I. A. Ostapenko, T. Kure, A. Schliwa, C. Kindel, D. Bimberg, A. Hoffmann, S. Kako, and Y. Arakawa, "Identification of electric dipole moments of excitonic complexes in nitride-based quantum dots," *Physical Review B*, vol. 88, p. 045309, July 2013.

[39] G. Callsen, A. Carmele, G. Hönig, C. kindel, J. Brunnmeier, M. R. Wagner, E. Stock, J. S. Reparaz, A. Schliwa, S. Reitzenstein, A. Knorr, A. Hoffmann, S. Kako, and Y. Arakawa, "Steering photon statistics in single quantum dots: From one- to two-photon emission," *Physical Review B*, vol. 87, p. 245314, June 2013.

[40] G. Hönig, G. Callsen, A. Schliwa, S. Kalinowski, C. Kindel, S. Kako, Y. Arakawa, D. Bimberg, and A. Hoffmann, "Manifestation of unconventional biexciton states in quantum dots," *Nature Communications*, vol. 5, 2014.

[41] C. F. Klingshirn, *Semiconductor optics*. Berlin: Springer, 1995.

[42] C. Yu, *Cardona - Fundamentals of Semiconductors - 2010*. Heidelberg: Springer, Sept. 2011.

[43] C. H. Kindel, *Study on Optical Polarization in Hexagonal Gallium Nitride Quantum Dots*. PhD thesis, University of Tokyo, July 2010.

[44] M. Miyamura, K. Tachibana, and Y. Arakawa, "High-density and size-controlled GaN self-assembled quantum dots grown by metalorganic chemical vapor deposition," *Applied Physics Letters*, vol. 80, no. 21, pp. 3937–3939, 2002.

[45] S. Kako, *Optical Properties of Gallium Nitride Self-Assembled Quantum Dots And Application to Generation of Non-Classical Light*. PhD thesis, University of Tokyo, Feb. 2007.

[46] C. Kindel, G. Callsen, S. Kako, T. Kawano, H. Oishi, G. Hönig, A. Schliwa, A. Hoffmann, and Y. Arakawa, "Spectral diffusion in nitride quantum dots: Emission energy dependent linewidths broadening via giant builtin dipole moments," *Phys Status Solidi - Rapid Research Letters*, vol. 8, no. 5, pp. 408–413, 2014.

[47] D. V. O'Connor, W. R. Ware, and J. C. Andre, "Deconvolution of fluorescence decay curves. A critical comparison of techniques," *Journal Of Physical Chemistry*, vol. 83, no. 10, pp. 1333–1343, 1979.

[48] G. Hönig, *Mehrteilchenzustände in Halbleiter-Quantenpunkten*. PhD thesis, Technische Universität Berlin, Berlin, Mar. 2015.

[49] M. J. Paisley, Z. Sitar, J. B. Posthill, and R. F. Davis, "Growth of cubic phase gallium nitride by modified molecular-beam epitaxy," *American Vacuum Society*, vol. 7, pp. 701–705, June 1989.

[50] P. Perlin, C. Jauberthie-Carillon, J. P. Itie, A. San Miguel, I. Grzegory, and A. Polian, "Raman scattering and x-ray-absorption spectroscopy in gallium nitride under high pressure," *Physical Review B*, vol. 45, no. 1, p. 83, 1992.

[51] M. Ueno, A. Onodera, O. Shimomura, and K. Takemura, "X-ray observation of the structural phase transition of aluminum nitride under high pressure," *Physical Review B*, vol. 45, no. 17, p. 10123, 1992.

[52] J. Simon, N. Pelekanos, C. Adelmann, E. Martinez-Guerrero, R. Andre, B. Daudin, L. Dang, and H. Mariette, "Direct comparison of recombination dynamics in cubic and hexagonal GaN/AlN quantum dots," *Physical Review B*, vol. 68, no. 3, p. 035312, 2003.

[53] V. A. Fonoberov and A. A. Balandin, "Excitonic properties of strained wurtzite and zinc-blende GaN / AlGaN quantum dots," *Journal Of Applied Physics*, vol. 94, no. 11, pp. 7178–7186, 2003.

[54] J. P. Garayt, J. M. Gérard, F. Enjalbert, L. Ferlazzo, S. Founta, E. Martinez-Guerrero, F. Rol, D. Araujo, R. Cox, and B. Daudin, "Study of isolated cubic GaN quantum dots by low-temperature cathodoluminescence," *Physica E - Low-Dimensional Systems and Nanostructures*, vol. 26, no. 1, pp. 203–206, 2005.

[55] S. Sergent, S. Kako, M. Bürger, and D. J. As, "Narrow spectral linewidth of single zinc-blende GaN/AlN self-assembled quantum dots," *Applied Physics Letters*, vol. 103, p. 151109, 2013.

[56] F. J. Manjón, D. Errandonea, A. H. Romero, N. Garro, J. Serrano, and M. Kuball, "Lattice dynamics of wurtzite and rocksalt AlN under high pressure: Effect of compression on the crystal anisotropy of wurtzite-type semiconductors," *Physical Review B*, vol. 77, no. 20, p. 205204, 2008.

[57] O. Lagerstedt and B. Monemar, "Variation of lattice parameters in GaN with stoichiometry and doping," *Physical Review B*, vol. 19, pp. 3064–3070, Mar. 1979.

[58] S. Iwama, K. Hayakawa, and T. Arizumi, "Ultrafine powders of TiN and AlN produced by a reactive gas evaporation technique with electron beam heating," *Journal Of Crystal Growth*, vol. 56, pp. 265–269, Jan. 1982.

[59] O. Ambacher, J. Majewski, C. Miskys, A. Link, M. Hermann, M. Eickhoff, M. Stutzmann, F. Bernardini, V. Fiorentini, V. Tilak, B. Schaff, and L. F. Eastman, "Pyroelectric properties of Al(In)GaN/GaN hetero- and quantum well structures," *Journal Of Physics-Condensed Matter*, vol. 14, pp. 3399–3434, Apr. 2002.

[60] F. Bernardini, V. Fiorentini, and D. Vanderbilt, "Spontaneous polarization and piezoelectric constants of III-V nitrides," *Physical Review B*, vol. 56, p. 1049163, Oct. 1997.

[61] G. Callsen, J. S. Reparaz, M. R. Wagner, R. Kirste, C. Nenstiel, A. Hoffmann, and M. R. Phillips, "Phonon deformation potentials in wurtzite GaN and ZnO determined by uniaxial pressure dependent Raman measurements," *Applied Physics Letters*, vol. 98, no. 6, p. 061906, 2011.

[62] L. Cláudio de Carvalho, A. Schleife, F. Fuchs, and F. Bechstedt, "Valence-band splittings in cubic and hexagonal AlN, GaN, and InN," *Applied Physics Letters*, vol. 97, no. 23, pp. 232101–232101–3, 2010.

[63] G. F. Koster, *Properties of the thirty-two point groups*. Cambridge: M.I.T. Press, 1 ed., June 2008.

[64] B. Gil, *Physics of Wurtzite Nitrides and Oxides: Passport to Devices*. Springer, 2014.

[65] M. R. Wagner, J.-H. Schulze, R. Kirste, M. Cobet, A. Hoffmann, C. Rauch, A. V. Rodina, B. K. Meyer, U. Roeder, and K. Thonke, "Gamma(7) valence band symmetry related hole fine splitting of bound excitons in ZnO observed in magneto-optical studies," *Physical Review B*, vol. 80, no. 20, p. 205203, 2009.

[66] R. Loudon, "The Raman effect in crystals," *Advances in Physics*, vol. 13, pp. 423–482, Oct. 1964.

[67] G. Callsen, M. R. Wagner, J. S. Reparaz, F. Nippert, T. Kure, S. Kalinowski, A. Hoffmann, M. J. Ford, M. R. Phillips, R. F. Dalmau, R. Schlesser, R. Collazo, and Z. Sitar, "Phonon pressure coefficients and deformation potentials of wurtzite AlN determined by uniaxial," *Physical Review B*, vol. 90, p. 205206, Nov. 2014.

[68] I. Ostapenko, G. Hönig, S. Rodt, A. Schliwa, A. Hoffmann, D. Bimberg, M. R. Dachner, M. Richter, A. Knorr, and S. Kako, "Exciton acoustic-phonon coupling in single GaN/AlN quantum dots," *Physical Review B*, vol. 85, no. 8, p. 081303, 2012.

[69] F. Rol, S. Founta, H. Mariette, B. Daudin, L. S. Dang, J. Bleuse, D. Peyrade, J. M. Gérard, and B. Gayral, "Probing exciton localization in nonpolar GaN/AlN quantum dots by single-dot optical spectroscopy," *Physical Review B*, vol. 75, p. 125306, Mar. 2007.

[70] P. Bruesch, *Phonons: Theory and experiments II. Volume 2.* Springer-Verlag New York Inc.,New York, NY, Jan. 1986.

[71] O. Stier, M. Grundmann, and D. Bimberg, "Electronic and optical properties of strained quantum dots modeled by 8-band kp theory," *Physical Review B*, vol. 59, no. 8, p. 5688, 1999.

[72] M. Hayne, J. Maes, S. Bersier, V. V. Moshchalkov, A. Schliwa, L. Müller-Kirsch, C. Kapteyn, R. Heitz, and D. Bimberg, "Electron localization by self-assembled GaSb/GaAs quantum dots," *Applied Physics Letters*, vol. 82, no. 24, p. 4355, 2003.

[73] A. Rastelli, S. Stufler, A. Schliwa, R. Songmuang, C. Manzano, G. Costantini, K. Kern, A. Zrenner, D. Bimberg, and O. Schmidt, "Hierarchical Self-Assembly of GaAs/AlGaAs Quantum Dots," *Physical Review Letters*, vol. 92, p. 166104, Apr. 2004.

[74] A. Schliwa, *Electronic Properties of Self-Organized Quantum Dots.* PhD thesis, Technische Universität Berlin, Mar. 2007.

[75] S. Tomić and N. Vukmirović, "Erratum: Excitonic and biexcitonic properties of single GaN quantum dots modeled by 8-band kp theory and configuration-interaction method," *Physical Review B*, vol. 86, no. 15, p. 159902, 2012.

[76] S. F. Borg, "Matrix-tensor Methods in Continuum Mechanics. (Based on a Preprint Edition, an Introduction to Matrix-tensor Methods in Theoretical and Applied Mechanics)," 1963.

[77] B. Gil, *Group III Nitride Semiconductor Compounds.* Physics and Applications, Oxford University Press on Demand, Jan. 1998.

[78] I. Vurgaftman and J. R. Meyer, "Band parameters for nitrogen-containing semiconductors," *Journal Of Applied Physics*, vol. 94, no. 6, pp. 3675–3696, 2003.

[79] F. Bernardini and V. Fiorentini, "First-principles calculation of the piezoelectric tensor of III–V nitrides," *Applied Physics Letters*, vol. 80, no. 22, pp. 4145–4147, 2002.

[80] D. Gershoni, C. H. Henry, and G. A. Baraff, "Calculating the optical properties of multidimensional heterostructures: Application to the modeling of quaternary quantum well lasers," *IEEE Journal of Quantum Electronics*, vol. 29, no. 9, pp. 2433–2450, 1993.

[81] G. Baraff and D. Gershoni, "Eigenfunction-expansion method for solving the quantum-wire problem: Formulation," *Physical Review B*, vol. 43, pp. 4011–4022, Feb. 1991.

[82] M. Winkelnkemper, *Electronic Structure of Nitride-based Quantum Dots*. PhD thesis, Technische Universität Berlin, Nov. 2008.

[83] S. Tomić and N. Vukmirović, "Excitonic and biexcitonic properties of single GaN quantum dots modeled by 8-band kp theory and configuration interaction method," *Physical Review B*, vol. 79, no. 24, p. 245330, 2009.

[84] O. Stier, *Electronic and Optical Properties of Quantum Dots and Wires*. PhD thesis, Technische Universität Berlin, Berlin, Oct. 2000.

[85] T. Nakaoka, S. Kako, and Y. Arakawa, "Quantum confined Stark effect in single self-assembled GaN/AlN quantum dots," *Physica E - Low-Dimensional Systems and Nanostructures*, vol. 32, no. 1-2, pp. 148–151, 2006.

[86] T. Nakaoka, S. Kako, and Y. Arakawa, "Unconventional quantum-confined Stark effect in a single GaN quantum dot," *Physical Review B*, vol. 73, no. 12, p. 121305, 2006.

[87] F. Bernardini and V. Fiorentini, "Polarization fields in nitride nanostructures: 10 points to think about," *Applied Surface Science*, vol. 166, pp. 23–29, Oct. 2000.

[88] V. Y. Davydov, Y. E. Kitaev, I. N. Goncharuk, A. N. Smirnov, J. Graul, O. Semchinova, D. Uffmann, M. B. Smirnov, A. P. Mirgorodsky, and R. A. Evarestov, "Phonon dispersion and Raman scattering in hexagonal GaN and AlN," *Physical Review B*, vol. 58, no. 19, p. 12899, 1998.

[89] A. Berthelot, I. Favero, G. Cassabois, C. Voisin, C. Delalande, P. Roussignol, R. Ferreira, and J. M. Gérard, "Unconventional motional narrowing in the optical spectrum of a semiconductor quantum dot," *Nature Physics*, vol. 2, pp. 759–764, Oct. 2006.

[90] V. Mlinar and A. Zunger, "Internal electronic structure and fine structure of multiexcitons in semiconductor quantum dots," *Physical Review B*, vol. 80, p. 205311, Nov. 2009.

[91] M. Winkelnkemper, R. Seguin, S. Rodt, A. Hoffmann, and D. Bimberg, "GaN/AlN quantum dots for single qubit emitters," *Journal Of Physics-Condensed Matter*, vol. 20, no. 45, p. 454211, 2008.

[92] B. Gil, O. Briot, and R.-L. Aulombard, "Valence-band physics and the optical properties of GaN epilayers grown onto sapphire with wurtzite symmetry," *Physical Review B*, vol. 52, pp. 94248–17031, Dec. 1995.

[93] B. Gil, P. Bigenwald, P. P. Paskov, and B. Monemar, "Internal structure of acceptor-bound excitons in wide-band-gap wurtzite semiconductors," *Physical Review B*, vol. 81, no. 8, p. 085211, 2010.

[94] U. Bockelmann and T. Egeler, "Electron relaxation in quantum dots by means of Auger processes," *Physical Review B (Condensed Matter)*, vol. 46, pp. 1398603–15577, Dec. 1992.

[95] A. L. Efros, V. A. Kharchenko, and M. Rosen, "Breaking the phonon bottleneck in nanometer quantum dots: Role of Auger-like processes," *Solid State Communications*, vol. 93, pp. 281–284, Jan. 1995.

[96] K. Mukai and M. Sugawara, "Optical characterization of quantum dots," *Semiconductors and Semimetals*, vol. 60, pp. 183–208, 1999.

[97] U. Bockelmann and G. Bastard, "Phonon scattering and energy relaxation in two-, one-, and zero-dimensional electron gases," *Physical Review B*, vol. 42, pp. 8947–8951, Nov. 1990.

[98] K. Mukai, N. Ohtsuka, H. Shoji, and M. Sugawara, "Phonon bottleneck in self-formed InGaAs/GaAs quantum dots by electroluminescence and time-resolved photoluminescence," *Physical Review B*, vol. 54, no. 8, p. R5243, 1996.

[99] R. Heitz, M. Veit, N. Ledentsov, A. Hoffmann, D. Bimberg, V. Ustinov, P. Kopev, and Z. Alferov, "Energy relaxation by multiphonon processes in InAs/GaAs quantum dots," *Physical Review B*, vol. 56, no. 16, pp. 10435–10445, 1997.

[100] F. Adler, M. Geiger, A. Bauknecht, F. Scholz, H. Schweizer, M. H. Pilkuhn, B. Ohnesorge, and A. Forchel, "Optical transitions and carrier relaxation in self assembled InAs/GaAs quantum dots," *Journal Of Applied Physics*, vol. 80, pp. 4019–4026, Oct. 1996.

[101] H. Yu, S. Lycett, C. Roberts, and R. Murray, "Time resolved study of self-assembled InAs quantum dots," *Applied Physics Letters*, vol. 69, pp. 4087–4089, Dec. 1996.

[102] T. Inoshita and H. Sakaki, "Electron relaxation in a quantum dot: Significance of multiphonon processes," *Physical Review B*, vol. 46, pp. 7260–7263, Sept. 1992.

[103] B. Ohnesorge, M. Albrecht, J. Oshinowo, A. Forchel, and Y. Arakawa, "Rapid carrier relaxation in self-assembled InGaAs/GaAs quantum dots," *Physical Review B*, vol. 54, no. 16, p. 11532, 1996.

[104] U. Bockelmann, W. Heller, A. Filoramo, and P. Roussignol, "Microphotoluminescence studies of single quantum dots. I. Time-resolved experiments," *Physical Review B*, vol. 55, pp. 4456–4468, Feb. 1997.

[105] Y. Arakawa, "Fabrication of Quantum Wires and Dots and Nanostructure Characterization," in *NATO ASI Series* (K. Eberl, P. Petroff, and P. Demeester, eds.), pp. 197–205, Springer Netherlands, 1995.

[106] N. Baer, S. Schulz, P. Gartner, S. Schumacher, G. Czycholl, and F. Jahnke, "Influence of symmetry and Coulomb correlation effects on the optical properties of nitride quantum dots," *Physical Review B*, vol. 76, p. 075310, Aug. 2007.

[107] E. Dekel, D. Gershoni, E. Ehrenfreund, D. Spektor, J. M. García, and P. M. Petroff, "Multiexciton spectroscopy of a single self-assembled quantum dot," *Physical Review Letters*, vol. 80, no. 22, pp. 4991–4994, 1998.

[108] F. Liu, L. Biadala, A. V. Rodina, D. R. Yakovlev, D. Dunker, C. Javaux, J.-P. Hermier, A. L. Efros, B. Dubertret, and M. Bayer, "Spin dynamics of negatively charged excitons in CdSe/CdS colloidal nanocrystals," *Physical Review B*, vol. 88, p. 035302, July 2013.

[109] S. G, A. Musiał, P. Podemski, and J. Misiewicz, "On the applicability of a few level rate equation model to the determination of exciton versus biexciton kinetics in quasi-zero-dimensional structures," *Journal Of Applied Physics*, vol. 108, p. 3507, Aug. 2010.

[110] M. Nakayama, K. Suyama, and H. Nishimura, "Biexciton formation in GaAs/AlAs type-II superlattices under extremely low excitation powers," *Physical Review B*, vol. 51, no. 12, p. 7870, 1995.

[111] J. Wagner and F. Bechstedt, "Phonon deformation potentials of alpha-GaN and -AlN: An ab initio calculation," *Applied Physics Letters*, vol. 77, no. 3, pp. 346–348, 2000.

[112] J. M. Wagner and F. Bechstedt, "Properties of strained wurtzite GaN and AlN: Ab initio studies," *Physical Review B*, vol. 66, p. 115202, Sept. 2002.

[113] E. Dekel, D. V. Regelman, D. Gershoni, E. Ehrenfreund, W. V. Schoenfeld, and P. M. Petroff, "Cascade evolution and radiative recombination of quantum dot multiexcitons studied by time-resolved spectroscopy," *Physical Review B*, vol. 62, no. 16, pp. 11–11, 2000.

[114] R. Seguin, S. Rodt, A. Strittmatter, L. Reissmann, T. Bartel, A. Hoffmann, D. Bimberg, E. Hahn, and D. Gerthsen, "Multi-excitonic complexes in single InGaN quantum dots," *Applied Physics Letters*, vol. 84, p. 4023, 2004.

[115] S. Amloy, K. H. Yu, K. F. Karlsson, R. Farivar, T. G. Andersson, and P. O. Holtz, "Size dependent biexciton binding energies in GaN quantum dots," *Applied Physics Letters*, vol. 99, no. 25, p. 251903, 2011.

[116] T. Kawano, S. Kako, C. kindel, and Y. Arakawa, "Annealing effect on spectral linewidth of hexagonal gallium nitride quantum dots," in *Nano-Optoelectronics Workshop, 2007. i-NOW '07. International*, pp. 120–121, Aug. 2007.

[117] C. Kindel, S. Kako, T. Kawano, H. Oishi, and Y. Arakawa, "Collinear Polarization of Exciton/Biexciton Photoluminescence from Single Hexagonal GaN Quantum Dots," *Japanese Journal of Applied Physics*, vol. 48, no. 4, p. 04C116, 2009.

[118] J. Simon, N. T. Pelekanos, C. Adelmann, E. Martinez-Guerrero, R. Andre, B. Daudin, and H. Mariette, "Direct comparison of recombination dynamics in cubic and hexagonal GaN/AlN quantum dots," *Physical Review B*, vol. 68, no. 3, p. 035312, 2003.

[119] D. Simeonov, A. Dussaigne, R. Butté, and N. Grandjean, "Complex behavior of biexcitons in GaN quantum dots due to a giant built-in polarization field," *Physical Review B*, vol. 77, p. 075306, Feb. 2008.

[120] P. Michler, "A Quantum Dot Single-Photon Turnstile Device," *Science*, vol. 290, pp. 2282–2285, Dec. 2000.

[121] G. Bester, S. Nair, and A. Zunger, "Pseudopotential calculation of the excitonic fine structure of million-atom self-assembled InGaAs/GaAs quantum dots," *Physical Review B*, vol. 67, no. 16, p. 161306, 2003.

[122] H. Htoon, M. Furis, S. A. Crooker, S. Jeong, and V. I. Klimov, "Linearly polarized 'fine structure'of the bright exciton state in individual CdSe nanocrystal quantum dots," *Physical Review B*, vol. 77, no. 3, p. 035328, 2008.

[123] N. Bloembergen, E. M. Purcell, and R. V. Pound, "Relaxation effects in nuclear magnetic resonance absorption," *Physical Review*, vol. 73, no. 7, p. 679, 1948.

[124] S. S. Sturniolo and M. M. Pieruccini, "An exact analytical solution for the evolution of a dipole-dipole interacting system under spherical diffusion in magnetic resonance experiments.," *Journal of Magnetic Resonance (1969)*, vol. 223, pp. 138–147, Sept. 2012.

[125] R. Flach, D. S. Hamilton, P. M. Selzer, and W. M. Yen, "Time-Resolved Fluorescence Line-Narrowing Studies in LaF 3: Pr3+," *Physical Review Letters*, vol. 35, no. 15, pp. 1034–1037, 1975.

[126] Y. Shen, T. M. Sweeney, and H. Wang, "Zero-phonon linewidth of single nitrogen vacancy centers in diamond nanocrystals," *Physical Review B*, vol. 77, no. 3, p. 33201, 2008.

[127] V. Türck, S. Rodt, O. Stier, R. Heitz, R. Engelhardt, U. W. Pohl, D. Bimberg, and R. Steingrüber, "Effect of random field fluctuations on excitonic transitions of individual CdSe quantum dots," *Physical Review B*, vol. 61, no. 15, p. 9944, 2000.

[128] L. Besombes, K. Kheng, L. Marsal, and H. Mariette, "Few-particle effects in single CdTe quantum dots," *Physical Review B*, vol. 65, no. 12, p. 121314, 2002.

[129] G. Sallen, A. Tribu, T. Aichele, R. André, L. Besombes, C. Bougerol, M. Richard, S. Tatarenko, K. Kheng, and J.-P. Poizat, "Subnanosecond spectral diffusion measurement using photon correlation," *Nature Photonics*, vol. 4, pp. 696–699, Oct. 2010.

[130] K. Kuroda, T. Kuroda, K. Watanabe, T. Mano, G. Kido, N. Koguchi, and K. Sakoda, "Distribution of exciton emission linewidth observed for GaAs quantum dots grown by droplet epitaxy," *Journal of Luminescence*, vol. 130, no. 12, pp. 2390–2393, 2010.

[131] M. Grundmann, O. Stier, and D. Bimberg, "InAs/GaAs pyramidal quantum dots: Strain distribution, optical phonons, and electronic structure," *Physical Review B*, vol. 52, no. 16, p. 11969, 1995.

[132] P. W. Fry, I. E. Itskevich, D. J. Mowbray, M. S. Skolnick, J. J. Finley, J. A. Barker, E. P. O'Reilly, L. R. Wilson, I. A. Larkin, and P. A. Maksym, "Inverted electron-hole alignment in InAs-GaAs self-assembled quantum dots," *Physical Review Letters*, vol. 84, no. 4, p. 733, 2000.

[133] M. Bayer and A. Forchel, "Temperature dependence of the exciton homogeneous linewidth in In0.60 Ga0.40 As/GaAs self-assembled quantum dots," *Physical Review B*, vol. 65, no. 4, p. 041308, 2002.

[134] M. Holmes, S. Kako, K. Choi, P. Podemski, M. Arita, and Y. Arakawa, "Measurement of an Exciton Rabi Rotation in a Single GaN/AlGaN Nanowire-Quantum Dot," *Physical Review Letters*, vol. 111, p. 057401, July 2013.

[135] B. Krummheuer, V. M. Axt, T. Kuhn, I. D'Amico, and F. Rossi, "Pure dephasing and phonon dynamics in GaAs- and GaN-based quantum dot structures: Interplay between material parameters and geometry," *Physical Review B*, vol. 71, no. 23, p. 235329, 2005.

[136] E. Stock, M. R. Dachner, T. Warming, A. Schliwa, A. Lochmann, A. Hoffmann, A. Toropov, A. Bakarov, I. Derebezov, and M. Richter, "Acoustic and optical phonon scattering in a single In(Ga)As quantum dot," *Physical Review B*, vol. 83, no. 4, p. 041304, 2011.

[137] G. Sallen, A. Tribu, T. Aichele, R. André, L. Besombes, C. Bougerol, M. Richard, S. Tatarenko, K. Kheng, and J.-P. Poizat, "Subnanosecond spectral diffusion measurement using photon correlation," *Nature Photonics*, vol. 4, pp. 696–699, Oct. 2010.

[138] R. W. Pohl, "Electron conductivity and photochemical processes in alkali-halide crystals," *Proceedings of the Physical Society*, vol. 49, no. 4S, p. 3, 1937.

[139] N. F. Mott, "Discussion of the papers by pohl, and by gurney and mott," *Proceedings of the Physical Society*, vol. 49, no. 4S, p. 36, 1937.

[140] K. Huang and A. Rhys, "Theory of light absorption and non-radiative transitions in F-centres," *Proceedings of the Royal Society of London. Series A. Mathematical and Physical Sciences*, vol. 204, no. 1078, pp. 406–423, 1950.

[141] D. G. Thomas and J. J. Hopfield, "Optical properties of bound exciton complexes in cadmium sulfide," *Physical Review*, vol. 128, no. 5, p. 2135, 1962.

[142] J. F. Scott, R. C. Leite, and T. C. Damen, "Resonant Raman effect in semiconductors," *Physical Review*, vol. 188, pp. 1285–1290, 1969.

[143] C. W. Litton, D. C. Reynolds, T. C. Collins, and Y. S. Park, "Exciton—LO-Phonon Interaction and the Anti-Stokes Emission Line in CdS," *Physical Review Letters*, vol. 25, no. 23, p. 1619, 1970.

[144] C. B. Duke and G. D. Mahan, "Phonon-broadened impurity spectra. I. Density of states," *Physical Review*, vol. 139, no. 6A, p. A1965, 1965.

[145] R. Heitz, I. Mukhametzhanov, O. Stier, A. Madhukar, and D. Bimberg, "Enhanced polar exciton-LO-phonon interaction in quantum dots," *Physical Review Letters*, vol. 83, no. 22, p. 4654, 1999.

[146] X. B. Zhang, T. Taliercio, S. Kolliakos, and P. Lefebvre, "Influence of electron-phonon interaction on the optical properties of III nitride semiconductors," *Journal Of Physics-Condensed Matter*, vol. 13, no. 32, p. 7053, 2001.

[147] S. Kalliakos, X. B. Zhang, T. Taliercio, P. Lefebvre, B. Gil, N. Grandjean, B. Damilano, and J. Massies, "Large size dependence of exciton-longitudinal-optical-phonon coupling in nitride-based quantum wells and quantum boxes," *Applied Physics Letters*, vol. 80, no. 3, p. 428, 2002.

[148] E. Binder, J. Schilp, and T. Kuhn, "LO-phonon quantum kinetics in photoexcited bulk semiconductors and heterostructures," *physica status solidi (b)*, vol. 206, no. 1, pp. 227–233, 1998.

[149] A. Carmele and A. Knorr, "Analytical solution of the quantum-state tomography of the biexciton cascade in semiconductor quantum dots: Pure dephasing does not affect entanglement," *Physical Review B*, vol. 84, no. 7, p. 075328, 2011.

[150] J. Kabuss, A. Carmele, M. Richter, and A. Knorr, "Microscopic equation-of-motion approach to the multiphonon assisted quantum emission of a semiconductor quantum dot," *Physical Review B*, vol. 84, no. 12, p. 125324, 2011.

[151] D. Dufåker, L. O. Mereni, K. F. Karlsson, V. Dimastrodonato, G. Juska, P.-O. Holtz, and E. Pelucchi, "Exciton-phonon coupling in single quantum dots with different barriers," *Applied Physics Letters*, vol. 98, no. 25, pp. 251911–251911–3, 2011.

[152] D. Dufåker, K. F. Karlsson, V. Dimastrodonato, L. O. Mereni, B. E. Sernelius, P.-O. Holtz, and E. Pelucchi, "Phonon replicas of charged and neutral exciton complexes in single quantum dots," *Physical Review B*, vol. 82, no. 20, p. 205421, 2010.

[153] G. D. Mahan, *Many-particle physics; 3rd ed.* Physics of Solids and Liquids, Boston: Springer, 2000.

[154] Y. P. Rakovich and J. F. Donegan, *Anti-Stokes photoluminescence in semiconductor nanocrystal quantum dots*. Semiconductor Nanocrystal Quantum Dots, Springer, 2008.

[155] A. Schliwa, M. Winkelnkemper, A. Lochmann, E. Stock, and D. Bimberg, "In(Ga)As/GaAs quantum dots grown on a (111) surface as ideal sources of entangled photon pairs," *Physical Review B*, vol. 80, no. 16, p. 161307, 2009.

[156] D. Dufåker, K. F. Karlsson, L. O. Mereni, V. Dimastrodonato, G. Juska, E. Pelucchi, and P.-O. Holtz, "Evidence of nonadiabatic exciton-phonon interaction probed by second-order LO-phonon replicas of single quantum dots," *Physical Review B*, vol. 87, no. 8, p. 085317, 2013.

[157] S. Nomura and T. Kobayashi, "Exciton–LO-phonon couplings in spherical semiconductor microcrystallites," *Physical Review B*, vol. 45, no. 3, p. 1305, 1992.

[158] S. Rudin and T. L. Reinecke, "Electron–LO-phonon scattering rates in semiconductor quantum wells," *Physical Review B*, vol. 41, no. 11, p. 7713, 1990.

[159] S. Schmitt-Rink, D. Miller, and D. S. Chemla, "Theory of the linear and nonlinear optical properties of semiconductor microcrystallites," *Physical Review B*, vol. 35, no. 15, p. 8113, 1987.

[160] A. R. Goni, H. Siegle, K. Syassen, C. Thomsen, and J. M. Wagner, "Effect of pressure on optical phonon modes and transverse effective charges in GaN and AlN," *Physical Review B*, vol. 64, no. 3, p. 035205, 2001.

[161] T. C. Damen, S. Porto, and B. Tell, "Raman effect in zinc oxide," *Physical Review*, vol. 142, no. 2, p. 570, 1966.

[162] O. Verzelen, R. Ferreira, and G. Bastard, "Excitonic polarons in semiconductor quantum dots," *Physical Review Letters*, vol. 88, no. 14, p. 146803, 2002.

[163] D. V. Melnikov and W. B. Fowler, "Electron-phonon interaction in a spherical quantum dot with finite potential barriers: The Fröhlich Hamiltonian," *Physical Review B*, vol. 64, no. 24, p. 245320, 2001.

[164] J. Gleize, M. A. Renucci, J. Frandon, and F. Demangeot, "Anisotropy effects on polar optical phonons in wurtzite GaN/AlN superlattices," *Physical Review B*, vol. 60, no. 23, p. 15985, 1999.

[165] J.-j. Shi, "Interface optical-phonon modes and electron–interface-phonon interactions in wurtzite GaN/AlN quantum wells," *Physical Review B*, vol. 68, no. 16, p. 165335, 2003.

[166] V. A. Fonoberov and A. A. Balandin, "Interface and confined optical phonons in wurtzite nanocrystals," *Physical Review B*, vol. 70, no. 23, p. 233205, 2004.

[167] L. Zhang, "Uniform description of polar optical phonon states and their Fröhlich electron–phonon interaction Hamiltonians in multi-layer wurtzite nitride low-dimensional quantum structures," *Superlattices and Microstructures*, vol. 53, pp. 113–129, 2013.

[168] I. Vurgaftman and J. R. Meyer, "Band parameters for nitrogen-containing semiconductors," *Journal Of Applied Physics*, vol. 94, no. 6, pp. 3675–3696, 2003.

[169] I. Vurgaftman, J. R. Meyer, and L. R. Ram-Mohan, "Band parameters for III–V compound semiconductors and their alloys," *Journal Of Applied Physics*, vol. 89, no. 11, pp. 5815–5875, 2001.

[170] M. E. Levinshtein, S. L. Rumyantsev, and M. S. Shur, *Properties of Advanced Semiconductor Materials: GaN, AIN, InN, BN, SiC, SiGe*. New York: John Wiley & Sons, Inc., 2001.

[171] D. V. Strekalov, A. V. Sergienko, D. N. Klyshko, and Y. H. Shih, "Observation of two-photon "ghost" interference and diffraction," *Physical Review Letters*, vol. 74, no. 18, pp. 3600–3603, 1995.

[172] A. Hayat, A. Nevet, P. Ginzburg, and M. Orenstein, "Applications of two-photon processes in semiconductor photonic devices: invited review," *Semiconductor Science And Technology*, vol. 26, no. 8, p. 083001, 2011.

[173] R. M. Stevenson, C. L. Salter, J. Nilsson, A. J. Bennett, M. B. Ward, I. Farrer, D. A. Ritchie, and A. J. Shields, "Indistinguishable Entangled Photons Generated by a Light-Emitting Diode," *Physical Review Letters*, vol. 108, no. 4, p. 040503, 2012.

[174] D. J. Gauthier, Q. Wu, S. E. Morin, and T. W. Mossberg, "Realization of a continuous-wave, two-photon optical laser," *Physical Review Letters*, vol. 68, no. 4, pp. 464–467, 1992.

[175] Y. Ota, S. Iwamoto, N. Kumagai, and Y. Arakawa, "Spontaneous two-photon emission from a single quantum dot," *Physical Review Letters*, vol. 107, no. 23, p. 233602, 2011.

[176] M. D. Wissert, B. Rudat, U. Lemmer, and H. J. Eisler, "Quantum dots as single-photon sources: Antibunching via two-photon excitation," *Physical Review B*, vol. 83, no. 11, p. 113304, 2011.

[177] M. M. Pelton, C. C. Santori, J. J. Vucković, B. B. Zhang, G. S. G. Solomon, J. J. Plant, and Y. Y. Yamamoto, "Efficient source of single photons: a single quantum dot in a micropost microcavity.," *Physical Review Letters*, vol. 89, pp. 233602–233602, Dec. 2002.

[178] A. Nevet, A. Hayat, P. Ginzburg, and M. Orenstein, "Indistinguishable Photon Pairs from Independent True Chaotic Sources," *Physical Review Letters*, vol. 107, no. 25, p. 253601, 2011.

[179] J. Xiong, D. Z. Cao, F. Huang, H. G. Li, X. J. Sun, and K. Wang, "Experimental observation of classical subwavelength interference with a pseudothermal light source," *Physical Review Letters*, vol. 94, no. 17, p. 173601, 2005.

[180] F. Ferri, D. Magatti, A. Gatti, M. Bache, E. Brambilla, and L. A. Lugiato, "High-resolution ghost image and ghost diffraction experiments with thermal light," *Physical Review Letters*, vol. 94, no. 18, p. 183602, 2005.

[181] W. Walden-Newman, I. Sarpkaya, and S. Strauf, "Quantum Light Signatures and Nanosecond Spectral Diffusion from Cavity-Embedded Carbon Nanotubes," *Nano Letters*, vol. 12, no. 4, p. 1934, 2012.

[182] A. Kiraz, S. Fälth, C. Becher, B. Gayral, W. V. Schoenfeld, P. M. Petroff, L. Zhang, E. Hu, and A. Imamoğlu, "Photon correlation spectroscopy of a single quantum dot," *Physical Review B*, vol. 65, no. 16, p. 161303, 2002.

[183] E. Moreau, I. Robert, L. Manin, V. Thierry-Mieg, J. Gérard, and I. Abram, "Quantum cascade of photons in semiconductor quantum dots," *Physical Review Letters*, vol. 87, no. 18, p. 183601, 2001.

[184] A. Carmele, F. Milde, M. R. Dachner, M. Harouni, R. Roknizadeh, M. Richter, and A. Knorr, "Formation dynamics of an entangled photon pair: A temperature-dependent analysis," *Physical Review B*, vol. 81, no. 19, p. 195319, 2010.

[185] E. del Valle, A. Gonzalez-Tudela, F. P. Laussy, C. Tejedor, and M. J. Hartmann, "Theory of frequency-filtered and time-resolved N-photon correlations," *Physical Review Letters*, vol. 109, no. 18, p. 183601, 2012.

[186] H. Carmichael, *Statistical Methods in Quantum Optics 1 - Master Equation and Fokker-Planck Equations*. Berlin Heidelberg New York: Springer, Jan. 1999.

[187] C. W. Gardiner and P. Zoller, *Quantum Noise*. Springer, Oct. 2004.

[188] V. A. Shchukin and D. Bimberg, "Spontaneous ordering of nanostructures on crystal surfaces," *Reviews of Modern Physics*, vol. 71, pp. 1125–1171, 1999.

[189] C. Yannouleas and U. Landman, "Spontaneous Symmetry Breaking in Single and Molecular Quantum Dots," *Physical Review Letters*, vol. 82, pp. 5325–5328, June 1999.

[190] C. Yannouleas and U. Landman, "Erratum: Spontaneous Symmetry Breaking in Single and Molecular Quantum Dots," *Physical Review Letters*, vol. 85, p. 2220, Sept. 2000.

[191] R. Egger, W. Häusler, C. H. Mak, and H. Grabert, "Crossover from Fermi liquid to Wigner molecule behavior in quantum dots," *Physical Review Letters*, vol. 82, no. 16, p. 3320, 1999.

[192] R. Egger, W. Häusler, C. H. Mak, and H. Grabert, "Erratum: Crossover from Fermi Liquid to Wigner Molecule Behavior in Quantum Dots," *Physical Review Letters*, vol. 83, p. 462, July 1999.

[193] S. M. Reimann, M. Koskinen, and M. Manninen, "Formation of Wigner molecules in small quantum dots," *Physical Review B*, vol. 62, pp. 8108–8113, Sept. 2000.

[194] B. Reusch, W. Häusler, and H. Grabert, "Wigner molecules in quantum dots," *Physical Review B*, vol. 63, p. 113313, Mar. 2001.

[195] M. Hayne, J. Maes, S. Bersier, V. V. Moshchalkov, A. Schliwa, L. Müller-Kirsch, C. Kapteyn, R. Heitz, and D. Bimberg, "Electron localization by self-assembled GaSb/GaAs quantum dots," *Applied Physics Letters*, vol. 82, no. 24, p. 4355, 2003.

[196] V. D. Kulakovskii, G. Bacher, R. Weigand, T. Kümmell, A. Forchel, E. Borovitskaya, K. Leonardi, and D. Hommel, "Fine Structure of Biexciton Emission in Symmetric and Asymmetric CdSe/ZnSe Single Quantum Dots," *Physical Review Letters*, vol. 82, pp. 1780–1783, Feb. 1999.

[197] O. Stier, M. Grundmann, and D. Bimberg, "Electronic and optical properties of strained quantum dots modeled by 8-band k.p theory," *Physical Review B*, vol. 59, pp. 5688–5701, Feb. 1999.

[198] S. Rodt, R. Heitz, A. Schliwa, R. L. Sellin, F. Guffarth, and D. Bimberg, "Repulsive exciton-exciton interaction in quantum dots," *Physical Review B*, vol. 68, p. 035331, July 2003.

[199] R. Seguin, A. Schliwa, S. Rodt, K. Pötschke, U. W. Pohl, and D. Bimberg, "Size-dependent fine-structure splitting in self-organized InAs/GaAs quantum dots," *Physical Review Letters*, vol. 95, no. 25, p. 257402, 2005.

[200] N. Akopian, N. H. Lindner, E. Poem, Y. Berlatzky, J. Avron, D. Gershoni, B. D. Gerardot, and P. M. Petroff, "Entangled photon pairs from semiconductor quantum dots," *Physical Review Letters*, vol. 96, no. 13, p. 130501, 2006.

[201] D. Bimberg, M. Sondergeld, and E. Grobe, "Thermal dissociation of excitons bounds to neutral acceptors in high-purity GaAs," *Physical Review B*, vol. 4, no. 10, p. 3451, 1971.

[202] I. Favero, G. Cassabois, C. Voisin, C. Delalande, P. Roussignol, R. Ferreira, C. Couteau, J. P. Poizat, and J. M. Gérard, "Fast exciton spin relaxation in single quantum dots," *Physical Review B*, vol. 71, p. 233304, June 2005.

[203] Y. Kodriano, E. Poem, N. H. Lindner, C. Tradonsky, B. D. Gerardot, P. M. Petroff, J. E. Avron, and D. Gershoni, "Radiative cascade from quantum dot metastable spin-blockaded biexciton," *Physical Review B*, vol. 82, p. 155329, Oct. 2010.

[204] A. J. Shields, "Semiconductor quantum light sources," *Nature Photonics*, vol. 1, pp. 215–223, Apr. 2007.

Acknowledgment

I am deeply indebted to the following people who accompanied me on my "bon voyage" through solid state physics aiming towards single quantum dot spectroscopy in the ultraviolett spectral range:

- Prof. Dr. Axel Hoffmann for having given me the opportunity to research in his group, not only on quantum dots but on any other topic that was of interest for me and within reach. Knowing that such "scientific freedom" is extremely rare nowadays, makes this a most valuable gift and a great thing to remember. Giving me the chance to build a lab and to measure without any constraints, was the most fundamental building block for all discoveries and publications. Also Prof. Dr. Axel Hoffmann's considerate nature and even-tempered kind have showed me how to deal with all sorts of challenging moments, presenting a valuable lesson for a young, inquisitive mind.

- Prof. Dr. Matthew Phillips for a great time in his lab, for proofreading and examining this thesis and for all his motivating and encouraging emails throughout the last years. Also I would like to express my gratitude for his willingness to fly to Berlin for several times in order to support my PhD endeavor and the entire "Cotutelle Doctoral Degree" program between the Technische Universität Berlin and the "University of Technology, Sydney".

- Prof. Dr. Janina Maultzsch for assessing this thesis, for bringing my tennis partner Dr. Emanuele Poliani to Berlin, and for her enduring support during the last years.

- Prof. Dr. Bernard Gil for carefully reviewing my thesis and for asking the most tantalizing questions on several conferences.

- Prof. Dr. Michael Lehmann for chairing my defense and for all his most valuable advice.

- Prof. Dr. Andreas Knorr for all his support related advanced photon statistics and two-photon processes, providing me a glimpse into the mind of a theoretical physicist.

- Prof. Dr. Donat As for having given me the chance to present my work at the physics department of the university of Paderborn. Also I wish to acknowledge the outstanding cubic GaN quantum dot samples that he has provided. Even though these samples are not discussed in this thesis, they will definitely be discussed in future publications.

- Prof. Dr. Yasuhiko Arakawa for providing an amazing sample that constitutes the foundation of most of the spectroscopic data that is shown in this thesis. Also I would like to thank him for having given me the unique opportunity to present my research at the university of Tokyo.

- Gerald Hönig for one of the best scientific cooperations I could have ever imagined. Our joint work serves as a perfect example for what can be achieved if a theoretical and experimental physicist join their research efforts. I will never forget all our discussions and countless emails that allowed us to encounter *any* physical challenge we found throughout our quantum dot journey. Also, and that speaks for itself, I so far had never ever seen a theoretical physicist in the laboratory, until I met Gerald Hönig... .

- Dr. Martin Albrecht for all his great (S)TEM images, motivating discussions, and challenging questions.

- Dr. Christian Kindel for his supervision throughout my quantum dot research episode and for all the great datasets that helped to set the focus for my own measurements. It was a true delight to work together with such a well-considered physicist, who never blenched when confronted with the numerous questions of mine.

- Dr. Alexander Carmele who has showed me that a pure theoretical physicist and an experimentalist like myself can indeed communicate after a while, if both sides slowly adapt each others vocabulary. I am really grateful for having met such a considerate and patient theoretical physicist, who has always tried to answer all my questions down to the last detail. Without Dr. Alexander Carmele all my work on photon statistics would have been much less productive.

- Dr. Andrei Schliwa for all his great effort regarding the calculations of the Huang-Rhys factor, his amazing general theoretical expertise that has always been a great support, and his refreshingly direct manner. Also I will never forget our time at the SemiconNano 2013 conference with lots of great discussions and the longest lineup of my life at the airport of Los Angeles.

- Dr. Toni Markurt for his (S)TEM analysis of the GaN quantum dots and his straightforward and absolutely clear physical explanations.

- Dr. Satoshi Kako for having supplied such a great GaN quantum dot sample to me. Also I will never forget the lab tour he gave in Tokyo along with a great dinner afterwards. I guess it is rare to meet a Japanese physicist who asks physical questions in such a precise and direct way, which makes it a real pleasure to cooperate.

- Dr. Markus Wagner and Dr. Juan Sebastian Reparaz for the most amazing times in the lab and a lot of fun evenings and conferences. Discussing physics with such great minds will always be a true pleasure!

- Dr. Erik Stock for his experimental support and commitment to the Labview programming.

- Christian Nenstiel, Ole Hitzemann, Thomas Kure, Felix Nippert, Max Bügler for all their support in the lab, for cheering me up when things got a bit tougher, and for productively criticizing my research, which has finally enabled numerous publications. Also we most definitely share plenty of great lab moments and I am glad that my "lab-equipment-healing-hands" could help you out from time to time.

- Juri Brunnmeier, Stefan Kalinowski, Dmitrij Bostanjoglo, and Andrey Bokov for their support during the construction of the UV-enhanced μ-Photoluminescence setup and for their willingness to work with me as their supervisor. It has been a great experience to discover the optical signature of GaN quantum dots with all of you.

- Dr. Harald Scheel for his general support regarding numerous technical challenges.

- Heiner Perls, Werner Kaczmarek, Lothar Kroll, and Nobert Zielinski as representatives of the "old guard", who have shown great patience while building and fixing lab equipment of all kind. Especially I would also thank Werner Kaczmarek for all his support with the uniaxial pressure apparatus that has finally lead to two great publications, which, however, are not discussed in more detail in this thesis.

- Ines Rudolph and Doreen Nitzsche for help with all kinds of administrative challenges. It is a real pleasure to have such an amazing support! Doreen Nitzsche is the best CRC (Collaborative Research Centre) secretary and colleague that I personally could ever imagine in my role as the scientific secretary of the CRC 787.

- All members of the "Feinmechanische Werkstatt" as there are Wolfgang Pieper, Rainer Noethen, Marco Haupt, Daniela Beiße, Andreas Ludewig, and Andreas Jank. Without their support it would have been impossible to set up and continuously improve our experiments. Due to their great ideas and an amazing dedication to details, our experimental setups have nowadays reached a fully functional operating mode. Based on my experience from "other" universities I extraordinarily wish to acknowledge the outstanding capabilities and the tremendous speed of our workshop.

I am grateful to all members of the research groups of Prof. Dr. Hoffmann, Prof. Dr. Thomsen, Prof. Dr. Matthew Phillips, and Prof. Dr. Janina Maultzsch for the productive, cheerful, and pleasant atmosphere. Also I appreciate great support from the "Cotutelle Doctoral Degree" program between the Technische Universität Berlin and the "University of Technology, Sydney".

Financial support is acknowledged from the German Research Foundation (DFG) within the Collaborative Research Center (CRC) 787 and the Australian Research Council (ARC, LP0990087), while working at the University of Technology, Sydney (UTS).

I would like to thank David Gadenne and Holger Schmeckebier for all their advice, highly appreciated thoughts, and for lending me their ears for all these years.

My deepest gratitude is devoted to my family for their unconditional and enduring support from the early on. Especially I feel indebted to my mother and father, who have not only helped me to overcome all kind of obstacles on my way to these last lines, but also made the entire endeavor a most pleasant and rewarding experience.

All my gratefulness is dedicated to Jacqueline Kimm, for her love, as well as inexhaustible support and sympathetic patience during my "doctoral" journey. There is not greater way of support than a reason to come home, making you forget everyday work.